A unified perspective on two-dimensional quantum turbulence and plasticity

Audun Skaugen

Thesis submitted for the degree of Philosophiae Doctor (PhD)

Department of Physics
Faculty of Mathematics and Natural Sciences
University of Oslo, Norway

August 1, 2018

Abstract

We investigate two-dimensional quantum turbulence and plasticity from a common mathematical perspective, focusing on topological defects as the most important degrees of freedom. Quantum turbulence features quantized vortices which tend to cluster into statistically self-similar structures as a result of the inverse energy cascade. Similarly, the strong interaction between dislocations in single crystals under load leads to characteristic patterns, suggesting a common way of studying the complex nonequilibrium dynamics of the two fields. In the field of turbulence, we benefit from a fruitful interplay between models at different scales, from microscopic quantum field theory, via the semiclassical Gross–Pitaevskii equation, to the more phenomenological point vortex models of larger systems, leading to novel statistical signatures of the self-similar structure of vortices in two-dimensional quantum turbulence. In plasticity, the phase-field crystal model plays a similar mesoscale role to the Gross–Pitaevskii equation in quantum turbu-lence, but there are some problems in applying it to realistic crystals. We attempt to alleviate some of these problems through a more detailed understanding of the elastic and plastic behavior of the phase-field crystal.

Acknowledgments

This research project was conducted during my time as a PhD student in the Physics of Geological Processes (PGP) group at the Department of Physics, University of Oslo. The PGP group is very friendly and welcoming, and benefits from a vibrant culture of cross-disciplinary research. I had the extremely good fortune to be supervised by the friendliest person of them all, Professor Luiza Angheluta. I first met Luiza when she was a postdoc lecturing a course on statistical mechanics, with an infectious passion for the theory of symmetry-breaking phase transitions, topological defects, and the Renormalization group. This course inspired me to specialize in the field of statistical mechanics, and when Luiza was awarded a permanent position with a freely defined PhD project, it was an easy choice to apply for this position. I was not disappointed: Luiza has guided me expertly and passionately through four years of cross-disciplinary research in quantum turbulence, which itself is a combination of two disciplines, and plasticity.

Our work on plasticity received a timely piece of inspiration when Jorge Viñals contacted Luiza from the University of Minnesota with some very interesting thoughts about momentum balance in the phase-field crystal. Since then we have worked together continually, at some points meeting weekly over video conference. Jorge always had insightful replies to my arguments, often spotting subtle problems long before I understood these subtleties.

Long research projects like this have a tendency to get bogged down into minute details that seemingly have little to do with the research goals. In such times, I have been able to fall back to my hobby of performing music, taking my mind temporarily off those details. A big thank you to all my musical friends in Føyka Big Band, the choir Vox Humana, and the student orchestra Bjørneblæs. You help me stay sane when nothing seems to work.

Thank you to my family, for all their inspiration towards science, music, and life in general. A heartfelt thank you to Irene for her loving support through this process and for always being there for me.

List of papers

Paper I: *Vortex clustering and universal scaling laws in two-dimensional quantum turbulence*
Audun Skaugen and Luiza Angheluta
Physical Review E **93**, 032106 (2016)
Reference: [1]

Paper II: *Velocity statistics for nonuniform configurations of point vortices*
Audun Skaugen and Luiza Angheluta
Physical Review E **93**, 042137 (2016)
Reference: [2]

Paper III: *Origin of the inverse energy cascade in two-dimensional quantum turbulence*
Audun Skaugen and Luiza Angheluta
Physical Review E **95**, 052144 (2017)
Reference: [3]

Paper IV: *Dislocation dynamics and crystal plasticity in the phase-field crystal model*
Audun Skaugen, Luiza Angheluta and Jorge Viñals
Physical Review B **97**, 054113 (2018)
Reference: [4]

Paper V: *Mesoscale model of dislocation motion and crystal plasticity*
Audun Skaugen, Luiza Angheluta and Jorge Viñals
Submitted to Physical Review Letters, arXiv:1807.10245
Reference: [5]

Contents

Part I

Thesis

Chapter 1

Introduction

Water flowing slowly through a pipe is governed by a simple linear relation between the fluid flow rate Q and the pressure difference ΔP that drives the flow. This relation is known as the Poiseuille equation [6], and is given by

$$\Delta P = \frac{8\mu L Q}{\pi R^4},\qquad(1.1)$$

where μ is the dynamic viscosity, L is the pipe length, Q is the volumetric flow rate, and R is the pipe radius. The equation can be derived by assuming laminar flow in the Navier–Stokes equation. However, when the flow rate exceeds a given threshold, laminar flow gives way to large fluctuations in the flow field, leading a sharp increase in the resistance to flow [7]. This strongly fluctuating state is known as *turbulence*. More recently, the concept of turbulence has also been applied to quantum fluids, such as superfluid helium and laser-cooled atomic Bose–Einstein condensates. These systems feature similar phenomenology to the classical case, with the crucial difference that vorticity is quantized.

Materials under small loads feature a simple linear relation between loading force and deformation, known as a stress–strain relationship [8],

$$e_{ij} = C_{ijkl}\sigma_{kl},\qquad(1.2)$$

where the strain e_{ij} measures the relative deformation of the crystal, and the stress σ_{kl} is the applied force in the direction k per unit area with normal vector components n_l. However, when the strain exceeds some threshold, the material starts to fail. The exact point of failure is quite predictable in large samples, but as the sample size decreases the picture becomes more complicated, featuring many small-

3

scale yielding events which can be seen as serrations in the measured stress–strain relation [9]. Understanding this yielding transition is the subject of *plasticity*.

These two subjects seem to have little in common, since one is concerned with fluids in sustained motion, while the other is concerned with crystal structures at rest, with applied forces resisted by the stiffness of the material. However, as we will see, there are some deep mathematical similarities between the two problems when looked at in a certain way. This thesis project is concerned with exploring some of these similarities in the hope of shedding light on both problems.

The thesis is structured as follows: In this introductory chapter, we explore the high-level, qualitative similarities between modeling approaches and key physical phenomena in turbulence and plasticity. In chapter 2, we give an overview of the field of fully developed classical turbulence, with a particular emphasis on motivating the introduction of physical quantities that we make use of in this thesis project. In chapter 3, we study the nonequilibrium behavior of two-dimensional weakly interacting Bose–Einstein condensates, and discuss how turbulent states can develop in this system, as well as how these states can shed light on the behavior of classical turbulent states. We also summarize our three publications (papers I–III) contributing to this area of research. Chapter 4 introduces the basic concepts of elasticity and plasticity, as well as the phase-field crystal model for mesoscopic crystal plasticity. We also summarize our publications IV–V, which study the nonequilibrium properties of this model. We provide a brief discussion of the numerical methods employed in this project in chapter 5. Finally, we make some general observations about the interplay between the two fields and conclude in chapter 6. The four published papers I–IV and the submitted paper V are included in part II.

1.1   2D turbulence and the point vortex model

Turbulence is a state of fluid flow where strong velocity fluctuations coexist on a wide separation of scales, resulting in a rapid dissipation of kinetic energy from the fluid. In 3D, this complicated flow arises because energy is added to the system at a rate that is much faster than the available viscous dissipation, which is more efficient at dissipating smaller-scale fluctuations. As a result, large fluctuations in the flow can grow while removing energy from the mean flow. This fluctuation can then break down into smaller fluctuations, which develop still smaller fluctuations, and so on. The resulting steady-state flow removes energy from the system as fast

as it is added by transferring this energy into smaller and smaller scales in a self-similar process, until a scale is reached that is small enough for viscous dissipation to be efficient in removing the injected energy. This is known as the Richardson energy cascade.

In 2D, it turns out that the kinetic energy flows in the opposite direction, towards larger and larger scales. This is known as the *inverse energy cascade*, and results in large-scale rotational flows spanning the entire system. Unlike the clear qualitative picture of the Richardson cascade, the mechanism for the backwards transfer of energy is not fully understood. As part of modeling efforts to gain a detailed understanding of the inverse energy cascade, the flow was simplified into a collection of point-like vortices carrying units of circulation. These vortices are then subject to phenomenological merging and annihilation rules, and by studying the statistical behavior of how vortices are distributed relative to each other, one can hopefully gain some insight into the mechanism for the backwards transfer of energy. Similarly, 3D quantum turbulence has been applied to gain insights into problems related to the conservation of helicity in 3D turbulence.

The description of 2D flow as resulting from a collection of point-like vortices, while constituting an approximation in the field of classical turbulence, is much closer to reality in quantum fluids, where quantized vortices are the only carriers of fluid rotation. This has resulted in great interest in the field of quantum turbulence, where one studies fluctuating flow regimes in quantum fluids both theoretically, numerically and experimentally, to gain physical insight into the behavior of point-like vortices (in 2D) or line-like vortex filaments (in 3D). There are, however, some important differences between the vortices of quantum fluids and the point vortices studied in classical turbulence — in particular, vortex merging is not a common feature of quantum turbulence. The field of quantum turbulence therefore deserves to be studied in its own right, in addition to as a way of understanding classical turbulence. In papers I–III, we explore and relate different scale-free statistical signatures associated with the statistical behavior of vortices in 2D quantum turbulence.

1.2   Plasticity and dislocations

Plasticity occurs when crystal structures fail due to applied loads, causing a reorganization of the crystal lattice and irreversible deformations. Naively, one might expect this to occur when the applied load is sufficient to break all the bonds hold-

ing two crystal planes together. This assumption, however, leads to computations of crystal strengths that are orders of magnitude higher than the actual measured values. Instead, the applied stresses will concentrate on weaknesses in the crystal leading to localized deformations near these weaknesses. A particular kind of essential crystal weaknesses are dislocations, which are places where the lattice symmetry does not quite fit. Dislocations tend to move under applied load, and the result is a crystal that can continuously deform without whole planes slipping over each other. The interaction of dislocations, however, means that this process is complicated, characterized by large structures of dislocations which suddenly depin in avalanche-like events [9].

Thus, like in turbulence, the statistical behavior of line-like structures in 3D, or point-like structures in 2D is essential in studying plasticity. This suggests that it might be helpful to study both fields from a common perspective. However, modeling the behavior of large-scale ensembles of dislocations, known as discrete dislocation dynamics, requires phenomenological rules such as dislocation mobility and annihilation rules, which are difficult to justify without empirical input. These processes could be studied with the help of a *mesoscale* model that can explicitly model the breakdown of the crystal lattice near the dislocation core, while still being able to access the relatively slow timescales of plastic deformation. One such model is the phase-field crystal model (PFC), which models the atomic density on a coarse-grained level where fast elastic interactions are averaged out. Unfortunately, the resulting dynamical equation does not correctly reproduce the separation of timescales between fast elastic deformations and slow plastic deformations. In paper IV, we develop a new formalism to study the elastic and plastic behavior of the PFC, which we employ in paper V in order to quantitatively demonstrate the problem, as well as presenting a solution.

1.3   Notation

The notational convention varies between our published papers, but we employ a consistent notation throughout this thesis. Here we give the most important conventions.

Vectors are written in boldface (e.g. $\mathbf{v}$), as opposed to scalars which use the standard font weight (e.g. x). The norm of a vector $\mathbf{v}$ is denoted by its standard equivalent, $v = |\mathbf{v}|$, while its Cartesian components are denoted by Latin subscript indices v_i. The coordinate vector is $\mathbf{r}$, with components x, y and z. This

leads to some ambiguity in the context of the phase-field crystal, because we use the symbol r for the quench depth parameter. We therefore refrain from using this symbol for denoting the radius $|\mathbf{r}|$ when discussing the phase-field crystal, hopefully avoiding some confusion.

Given a collection of N topological defects, we use Greek letters for indexing into this set, thus the positions of quantized vortices in 2D quantum turbulence are denoted by $\{\mathbf{r}_\alpha\}_{\alpha=1}^N$. This index is raised when we need to refer to the components of such vectors, thus the i'th coordinate of vortex α is denoted by r_i^α. The Einstein summation convention is used only for the components of vectors and tensors, thus the expression $r_i^\alpha v_i^\alpha$ is equivalent to the dot product $\mathbf{r}_\alpha \cdot \mathbf{v}_\alpha$ without summation over α.

The gradient operator is ∇, and its Cartesian components are referred to by the short-hand $\partial_i = \frac{\partial}{\partial r_i}$. Similarly, differentiation with respect to time is be denoted by $\partial_t = \frac{\partial}{\partial t}$, in addition to the dot notation $\dot{\psi} = \partial_t \psi$. We use the convention that differential operators bind tightly to the symbol to their right, thus $\partial_x f \partial_y g = (\partial_x f)(\partial_y g)$, not $\partial_x (f \partial_y g)$. The Levi–Civita symbol is denoted by ϵ, thus the curl of a vector $\mathbf{v}$ in 3D has i'th component given by $\epsilon_{ijk} \partial_j v_k$.

The imaginary unit is i. This will hopefully not lead to confusion with the Latin subscript indices, since we never use them as anything other than subscripts. Thus ik_i is the imaginary unit times the i'th component of the wave vector $\mathbf{k}$.

The Fourier and inverse Fourier transforms are denoted by $F[-]$ and $F^{-1}[-]$, respectively. Fourier-transformed quantities are also indicated by a tilde above the original symbol. We use the asymmetric normalization where the inverse transform is divided by 2π, thus

$$\tilde{\psi}(\mathbf{k}) = F[\psi](\mathbf{k}) = \int \psi(\mathbf{r}) e^{-i\mathbf{k}\cdot\mathbf{r}} \mathrm{d}^d\mathbf{r},$$

$$\psi(\mathbf{r}) = F^{-1}\left[\tilde{\psi}\right](\mathbf{r}) = \frac{1}{(2\pi)^d} \int \tilde{\psi}(\mathbf{k}) e^{i\mathbf{k}\cdot\mathbf{r}} \mathrm{d}^d\mathbf{k},$$

where d is the number of dimensions. We will make use of the following properties of Fourier transforms, which are readily proven by manipulating the above definitions:

- Spectral differentiation,

$$F[\partial_i \psi](\mathbf{k}) = ik_i \tilde{\psi}(\mathbf{k}); \tag{1.3}$$

- the shift property,

$$F^{-1}[\tilde{\psi}(\mathbf{k} - \mathbf{g})](\mathbf{r}) = e^{i\mathbf{g}\cdot\mathbf{r}}\psi(\mathbf{r});$$ (1.4)

- the convolution theorems,

$$F\left[\int f(\mathbf{r}')g(\mathbf{r} - \mathbf{r}')\mathrm{d}^d\mathbf{r}'\right](\mathbf{k}) = \tilde{f}(\mathbf{k})\tilde{g}(\mathbf{k}),$$

$$F^{-1}\left[\int \tilde{f}(\mathbf{k}')\tilde{g}(\mathbf{k} - \mathbf{k}')\mathrm{d}^d\mathbf{k}'\right](\mathbf{r}) = (2\pi)^d f(\mathbf{r})g(\mathbf{r}).$$ (1.5)

Chapter 2

Turbulence

Turbulence is the tendency of fast fluid flows to develop large fluctuations leading to rapid dissipation of energy. This is characterized by the dimensionless *Reynolds number*, $\mathrm{Re} = \frac{UL}{\nu}$, where U is the typical fluid velocity, L is the typical length scale of the system, and ν is the kinematic viscosity [7]. One can think of this number as describing the balance between inertial effects causing disturbances to spread through the system by advection with U, and dissipative effects which tend to dampen out these disturbances. For low Reynolds numbers, small disturbances tend to dissipate out before they can spread, so that laminar flow has a high degree of stability. As the Reynolds number increases, disturbances get more and more long-lived, leading to a transition to turbulence around $\mathrm{Re} \sim 2000 - 3000$ or so [7, 10], although the precise transition point depends sensitively on the geometry.

The transition to turbulence at these intermediate Reynolds numbers is a much studied subject with complicated phenomenology (see for example [11, 12]), but here we will be more interested in the nonequilibrium steady state of *fully developed* turbulence at very high Reynolds numbers, where energy is injected into the system by some driving process at a constant rate ϵ, and then dissipated out by viscous forces at the same rate. This is a state where the entire fluid field has large fluctuations at a wide range of spatial scales, which is important because it leads to a much larger energy dissipation compared to a laminar flow with the same mean flow rate. In this chapter, we will introduce Kolmogorov's classical 1941 theory of fully developed three-dimensional turbulence [13], before discussing how the picture changes in two dimensions. We will then discuss how outstanding problems in the field of two-dimensional turbulence can be studied from the perspective of quantum turbulence.

2.1 The direct energy cascade

Any theoretical understanding of turbulence starts with the Navier–Stokes equation describing the momentum balance of a velocity field $\mathbf{V}$ with density ρ [10], (ignoring body forces),

$$\rho(\partial_t \mathbf{V} + \mathbf{V} \cdot \nabla \mathbf{V}) = \nabla \cdot \boldsymbol{\sigma}, \qquad (2.1)$$

where the stress tensor $\boldsymbol{\sigma}$ contains an isotropic pressure term and a term linearly dependent on velocity shear to model momentum diffusion,

$$\sigma_{ij} = -P\delta_{ij} + \mu \left[\partial_i V_j + \partial_j V_i - \frac{2}{3}\delta_{ij}\partial_k V_k \right]. \qquad (2.2)$$

The parameter μ is called the dynamic viscosity and the pressure P is determined from a thermodynamical equation of state. Alternatively, if we assume that the fluid is incompressible, we can take the density to be constant and determine the pressure from the condition that $\partial_i V_i = 0$. Inserting the stress into the momentum balance, we find for incompressible flow that

$$\partial_t \mathbf{V} + \mathbf{V} \cdot \nabla \mathbf{V} = -\nabla p + \nu \nabla^2 \mathbf{V}, \qquad (2.3)$$

where $p = \frac{P}{\rho}$ is the rescaled pressure and $\nu = \frac{\mu}{\rho}$ is the kinematic viscosity. The pressure is determined by taking the divergence of this equation and using the incompressibility assumption, giving

$$\nabla^2 p + \nabla \cdot (\mathbf{V} \cdot \nabla \mathbf{V}) = 0. \qquad (2.4)$$

This equation along with equation (2.3) gives a closed system of equations describing the fluid flow.

In principle, the Navier–Stokes equation is fully deterministic. However, due to the nonlinear nature of the equation, small-scale fluctuations can tend to grow unboundedly, reducing the usefulness of a deterministic description. The first step to accounting for turbulent noise is through the Reynolds-averaged Navier–Stokes equation, which is derived by decomposing the velocity field $\mathbf{V} = \mathbf{U} + \mathbf{v}$ into a mean flow $\mathbf{U} = \langle \mathbf{V} \rangle$ averaged over the noise, and a fluctuating velocity $\mathbf{v}$ with $\langle \mathbf{v} \rangle = 0$. By taking the average of the Navier–Stokes equation with respect to this

ensemble, we find

$$\partial_t \mathbf{U} + \langle (\mathbf{U} + \mathbf{v}) \cdot \nabla(\mathbf{U} + \mathbf{v}) \rangle = -\nabla p + \nu \nabla^2 \mathbf{U}$$
$$\partial_t \mathbf{U} + \mathbf{U} \cdot \nabla \mathbf{U} = -\nabla p + \nu \nabla^2 \mathbf{U} - \nabla \cdot \langle \mathbf{v} \otimes \mathbf{v} \rangle \qquad (2.5)$$

where we have used $\langle \mathbf{U} \rangle = \mathbf{U}$, $\langle \mathbf{v} \rangle = 0$, and exploited the commutation of derivatives with expectation values to write $\langle \mathbf{v} \cdot \nabla \mathbf{v} \rangle = \nabla \cdot \langle \mathbf{v} \otimes \mathbf{v} \rangle$. This allows us to express the effect of a fluctuating velocity field as resembling a stress term $\sigma_{ij}^R = -\langle v_i v_j \rangle$, known as the *Reynolds stress*. Since this tensor is negative-definite, it results in a loss of energy from the mean flow. Note that, since this equation depends on the second moment of the fluctuating velocity, it does not give a closed equation for the mean velocity field. One can derive an equation for this second moment by multiplying the Navier–Stokes equation with $\mathbf{V}$ before averaging, but this equation will again depend on third moments of $\mathbf{v}$. Continuing in this manner one derives an infinite sequence of equations for higher and higher moments of $\mathbf{v}$. A common modeling approach is to truncate this sequence at some order by introducing a closure assumption, essentially an assumption about how certain high-order moments behave [10]. We will not consider such assumptions here.

We can estimate the relative importance of the viscous dissipation versus the Reynolds stress by dimensional analysis. If both the mean and fluctuating velocities have typical magnitude U going to zero over the system size L, then the ratio between the two terms has size given by

$$\frac{[\nabla \cdot \langle \mathbf{v} \otimes \mathbf{v} \rangle]}{[\nu \nabla^2 U]} = \frac{U^2/L}{\nu U/L^2} = \frac{UL}{\nu} = \text{Re}, \qquad (2.6)$$

giving the Reynolds number. This argument shows that, in fully developed turbulence with high Reynolds numbers, the Reynolds stress is much more efficient at removing energy from the mean flow than viscous dissipation. However, the Reynolds stress must still conserve energy, so the energy from the mean flow must be transferred into fluctuations which are presumably characterized by a length scale slightly smaller than that of the mean flow. We can then repeat a similar argument to the above for these largest-scale fluctuations, which will lead to a similar Reynolds stress term that transfers energy into still smaller-scale fluctuations, but now over a smaller length scale leading to a smaller Reynolds number. One might then expect this process to repeat in a self-similar manner until the Reynolds number is small enough that viscous effects become important. This
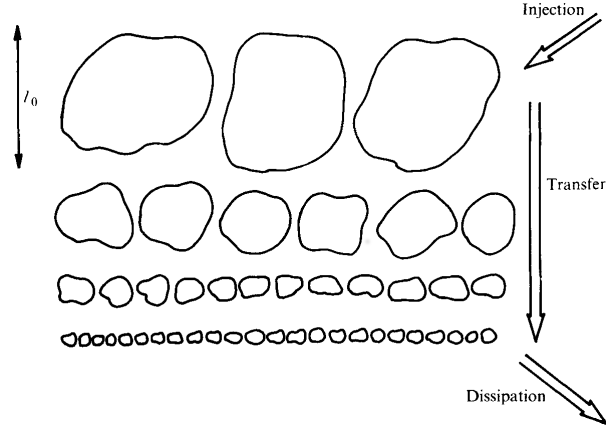
Figure 2.1: Qualitative picture of the Richardson cascade, where turbulent eddies are broken up into smaller eddies in a self-similar process. Reprinted from ref. [14] with permission from Cambridge university press.

qualitative picture of the turbulent steady-state is known as the *Richardson cascade* (see figure 2.1), and the range of length scales where energy transfer dominates over viscous dissipation is known as the *inertial range*.

This qualitative picture of an energy cascade across length scales suggests that we should study velocity structures coherent across a given distance $r = |\mathbf{r}|$. One way of doing this is by generalizing the Reynolds stress to two-point correlations in fluctuating velocity field, $U_{ij}(\mathbf{r}, \mathbf{r}') = \langle v_i(\mathbf{r}')v_j(\mathbf{r}' + \mathbf{r}) \rangle$. It is common to assume statistical homogeneity, which means that U_{ij} only depends on its first argument $\mathbf{r}$, as well as statistical isotropy, which means that U_{ij} only depends on the norm r of $\mathbf{r}$. If the system is large, we can replace the ensemble average by an average over the volume V, giving U_{ij} the form of a convolution $U_{ij}(\mathbf{r}) = \frac{1}{V} \int v_i(\mathbf{r}')v_j(\mathbf{r}' + \mathbf{r})\mathrm{d}^2\mathbf{r}'$, which will be simplified by taking the Fourier transform. By the convolution theorem, we find

$$\tilde{U}_{ij}(\mathbf{k}) = \int U_{ij}(\mathbf{r})e^{-i\mathbf{k}\cdot\mathbf{r}}\mathrm{d}^3\mathbf{r} = \frac{1}{V}\tilde{v}_i(-\mathbf{k})\tilde{v}_j(\mathbf{k}), \qquad (2.7)$$

where $\tilde{v}_i(\mathbf{k})$ are the Fourier components of the fluctuating velocity field. Integrating the trace $\tilde{U}_{ii}$ over all of reciprocal space, we recover the mean fluctuating kinetic energy density $E_k = \frac{1}{2}\rho \langle v^2 \rangle$,

$$\frac{1}{(2\pi)^3}\int \tilde{U}_{ii}(\mathbf{k})\mathrm{d}^3\mathbf{k} = U_{ii}(\mathbf{0}) = \frac{1}{V}\int v_i(\mathbf{r})v_i(\mathbf{r})\mathrm{d}^3\mathbf{r} = \frac{2E_k}{\rho}. \qquad (2.8)$$

Since we are only interested in how energy depends on the magnitude $k = |\mathbf{k}|$ of the wave vector, we integrate out the directional dependence by

$$
\begin{aligned}
E_k &= \frac{1}{2}\frac{\rho}{(2\pi)^3}\int_0^\infty \left[\int_{|\mathbf{k}|=k} \tilde{U}_{ii}(\mathbf{k})\mathrm{d}S\right]\mathrm{d}k \\
&= \frac{\rho}{(2\pi)^3}\int_0^\infty \left[\int_{|\mathbf{k}|=k} \frac{1}{2V}\tilde{v}_i(-\mathbf{k})\tilde{v}_i(\mathbf{k})\mathrm{d}S\right]\mathrm{d}k = \frac{\rho}{(2\pi)^3}\int_0^\infty E(k)\mathrm{d}k, \quad (2.9)
\end{aligned}
$$

where the $\mathrm{d}S$ integral is taken across a sphere of constant $|\mathbf{k}|$. This equation defines the *kinetic energy spectrum* $E(k)$, which quantifies the kinetic energy of turbulent structures coherent across a length scale $L = 2\pi/k$. If the system is statistically isotropic so that $U_{ij}(\mathbf{r}) = U_{ij}(r)$ is independent of the direction of $\mathbf{r}$, we also have that $\tilde{U}_{ij}(\mathbf{k}) = \tilde{U}_{ij}(k)$ is independent of the direction of $\mathbf{k}$. In that case, the directional integral simply gives a factor $4\pi k^2$ from the measure, or $2\pi k$ in 2D. Using that $\tilde{v}_i(-\mathbf{k}) = \tilde{v}_i(\mathbf{k})^*$ since $\mathbf{v}$ is real, the energy spectrum simplifies to

$$
E(k) = \frac{2\pi}{V}k^2|\tilde{\mathbf{v}}(\mathbf{k})|^2 \quad \text{(3D)}, \qquad E(k) = \frac{\pi}{V}k|\tilde{\mathbf{v}}(\mathbf{k})|^2 \quad \text{(2D)}. \qquad (2.10)
$$

The picture of a self-similar energy cascade suggests that this energy does not depend on the details of the system, but only on the constants describing the whole self-similar process and on the length scale itself. Given that the energy dissipation rate ϵ also quantifies the transfer of energy between scales, we should expect the form $E(k) = C_E\epsilon^a k^b$ where C_E is a dimensionless constant. Noting that the energy spectrum has units of $L^3 T^{-2}$ and the dissipation rate $L^2 T^{-3}$, dimensional analysis gives the estimate

$$
E(k) = C_E\epsilon^a k^b, \quad [E(k)] = L^{2a-b}T^{-3a} = L^3 T^{-2}, \qquad (2.11)
$$

which requires $a = \frac{2}{3}$ and $\frac{4}{3} - b = 3 \Leftrightarrow b = -\frac{5}{3}$. The result is the famous *Kolmogorov energy scaling*,

$$
E(k) = C_E\epsilon^{2/3}k^{-5/3}, \qquad (2.12)
$$

which can also be motivated by similar arguments of self-similarity in physical space [10, 13]. In practice, this simple scaling law will be modified by intermittent effects related to the random variation of the energy flux ϵ_k across a given wavenumber [14, 15]. These effects are most easily observed in higher moments

13

of longitudinal velocity differences, $\delta v_r(\mathbf{r}) = [\mathbf{v}(\mathbf{r'}+\mathbf{r}) - \mathbf{v}(\mathbf{r})] \cdot \mathbf{r}/r$, which define the structure functions $S_p(\mathbf{r}) = \langle \delta v_r(\mathbf{r})^p \rangle$.

As we have argued, the self-similar scaling in the energy spectrum should be accompanied by a transfer of energy from larger to smaller scales. This transfer can be studied quantitatively by the spectral energy flux, which is derived by differentiating the definition of $\tilde{U}_{ij}(\mathbf{k})$ with time and using the Navier–Stokes equation in spectral space to show that [10]

$$\frac{\mathrm{d}E(k)}{\mathrm{d}t} = D(k) + T(k) + F(k), \quad D(k) = -\nu k^2 E(k), \qquad (2.13)$$

where $D(k)$ is due to viscous dissipation, $T(k)$ is related to the nonlinear term giving rise to three-point correlations in velocity,

$$T(k) = -2\pi\rho k^2 P_{ijm}(\mathbf{k}) \int \mathrm{Im}\left[\langle \tilde{u}_i(\mathbf{k})\tilde{u}_j(\mathbf{k'})\tilde{u}_k(\mathbf{k}-\mathbf{k'})\rangle\right] \mathrm{d}^3\mathbf{k'}, \qquad (2.14)$$

and $P_{ijm}(\mathbf{k})$ is a function of the wave vector $\mathbf{k}$ only. It can also be shown that $\int_0^\infty T(k)\mathrm{d}k = 0$, which means that the nonlinear term can only redistribute energy between scales, as we have argued from more general grounds above. The $F(k)$ term is added to account for the injection of energy balancing the dissipation $D(k)$, and is usually assumed to be localized around some characteristic wavenumber k_i. We can study how energy is moved from wavenumbers smaller than k to those larger than k by integrating $T(k)$, giving a quantity called the *spectral energy flux*,

$$\Pi(k) = \int_k^\infty T(k')\mathrm{d}k' = -\int_0^k T(k')\mathrm{d}k'. \qquad (2.15)$$

This quantity is important in studying the energy cascade because it gives direct evidence as to the direction of energy flux across scales. For the Richardson cascade described above, it is expected to be positive across the inertial range. Indeed, assuming a steady-state where $E(k)$ is independent of time, we find for wavenumbers $k > k_i$ such that $F(k) = 0$,

$$\Pi(k) = -\int_0^k T(k')\mathrm{d}k' = \int_0^\infty F(k)\mathrm{d}k - 2\nu \int_0^k k'^2 E(k')\mathrm{d}k', \qquad (2.16)$$

where the integral of $F(k)$ equals the energy injection rate ϵ. Inserting the Kol-

14

mogorov scaling law for $E(k)$, this is equivalent to

$$\Pi(k) = \epsilon - \frac{3}{2}\nu C_E \epsilon^{2/3} k^{4/3} + \int_0^{k_i} k'^2 E(k') \mathrm{d}k', \qquad (2.17)$$

where the last term is related to the behavior at scales larger than the onset k_i of the energy cascade, and will be much smaller than the other terms. Thus, the spectral flux is approximately constant and equal to the energy injection and dissipation rate until k is such that viscous effects become important, at which point the energy cascade stops in favor of viscous dissipation. We can estimate the small-scale limit of the inertial range by finding the wavenumber k_d where this happens by setting $\Pi(k_d) = 0$, giving the *Kolmogorov microscale* wavenumber

$$k_d \sim \left(\frac{\epsilon}{\nu^3}\right)^{1/4}, \qquad (2.18)$$

which is the only combination of ϵ and ν that gives the dimension L^{-1} of a wavenumber. For scales smaller than this microscale ($k > k_d$), we expect the energy spectrum to stop following the $k^{-5/3}$ form and instead decay rapidly to zero, along with $T(k)$.

2.2 Two-dimensional turbulence

In two-dimensional systems, turbulent states look very different from their three-dimensional counterpart. The 3D Richardson cascade leads to the coexistence of fluctuations across a wide set of spatial scales all the way down to the Kolmogorov microscale k_d, which is typically very small, so the visual image of the turbulent state has no discernible structure. By contrast, 2D turbulence is characterized by spectacular coherent rotational structures on large scales. This is visible in quasi-2D atmospheric flows (see figure 2.2), as well as in experiments in confined fluid flows such as soap films [16, 17]. Direct numerical solution of the Navier–Stokes equation in 2D also reproduces such structures [10].

One important difference between the 2D and 3D cases can be found by looking at the equation of motion for vorticity $\boldsymbol{\omega} = \nabla \times \mathbf{V}$. Taking the curl of the Navier–Stokes equation, rewriting $\mathbf{V} \cdot \nabla \mathbf{V} = \frac{1}{2}\nabla(V^2) - \mathbf{V} \times \boldsymbol{\omega}$, and using incompressibility, we find

$$\partial_t \boldsymbol{\omega} + \mathbf{V} \cdot \nabla \boldsymbol{\omega} = \boldsymbol{\omega} \cdot \nabla \mathbf{V} + \nu \nabla^2 \boldsymbol{\omega}, \qquad (2.19)$$

Figure 2.2: Processed view of the north polar region of Jupiter as seen by NASA's Juno spacecraft. Swirling storms and coherent vortices are seen on very large scales. Public domain, obtained from the Bruce Murray Space Image Library [18].

which is a simple advection–diffusion equation with an additional source term $\boldsymbol{\omega} \cdot \nabla \mathbf{V}$ called the *vortex stretching* term. This term is an important source of velocity fluctuations because it tends to stretch areas of vorticity into smaller and more intense vortices. In two dimensions, since the vorticity is always oriented along the z direction while $\mathbf{V}$ is independent of z, this term is zero. Thus, vorticity in 2D satisfies a simple advection–diffusion equation. This motivates the introduction of another conserved scalar quantity known as *enstrophy*,

$$\Omega = \left\langle \frac{1}{2}\omega^2 \right\rangle = \frac{1}{2V}\int |\nabla \times \mathbf{v}|^2 \mathrm{d}^2\mathbf{r}. \tag{2.20}$$

This quantity needs to be accounted for in the same way as energy, with enstrophy added to the system on a characteristic forcing scale and dissipated out most efficiently on small scales. Batchelor [19] suggested that, as the turbulent velocity field mixes the vorticity field, vorticity gradients increase and thus the enstrophy moves to smaller scales in a similar way as the kinetic energy does in 3D.

We can study this enstrophy cascade in spectral space using similar techniques as for the kinetic energy in 3D. Considering the vorticity correlation function $\Omega(\mathbf{r}) = \frac{1}{2}\langle \omega(\mathbf{r}')\omega(\mathbf{r}' + \mathbf{r})\rangle$, we find that its Fourier transform takes the form

$$\tilde{\Omega}(\mathbf{k}) = \frac{1}{2V}\epsilon_{ij}\epsilon_{ik}[-ik_i\tilde{v}_j(-\mathbf{k})][ik_i\tilde{v}_k(\mathbf{k})] = \frac{1}{2V}k^2|\tilde{\mathbf{v}}(\mathbf{k})|^2, \tag{2.21}$$

so integrating over a shell of constant $\mathbf{k}$, we find that the enstrophy spectrum is related to the energy spectrum by

$$\tilde{\Omega}(k) = \frac{1}{2V}k^2 \int_{|\mathbf{k}|=k} |\tilde{\mathbf{v}}(\mathbf{k})|^2 \mathrm{d}S = k^2 E(k), \tag{2.22}$$

where $E(k)$ is the 2D kinetic energy spectrum defined in equation (2.10). This ties the energy and enstrophy spectra together, as they differ only by a factor k^2.

Now assume that the system is forced at a characteristic length scale given by the wavenumber k_i, with an energy injection rate ϵ. This corresponds to an enstrophy injection rate $\beta = k_i^2\epsilon$, and a self-similar enstrophy cascade should be associated with an enstrophy spectrum, and therefore an energy spectrum, which only depends on β and k. Applying the same kind of dimensional analysis as we did for the energy cascade, we see that $[\beta] = L^{-2}[\epsilon] = T^{-3}$, so writing $E(k) = C_\Omega \beta^a k^b$ we must have $L^{-b}T^{-3a} = [E(k)] = L^3 T^{-2}$, giving $a = \frac{2}{3}, b = -3$. Thus the enstrophy cascade is characterized by an energy spectrum following the power
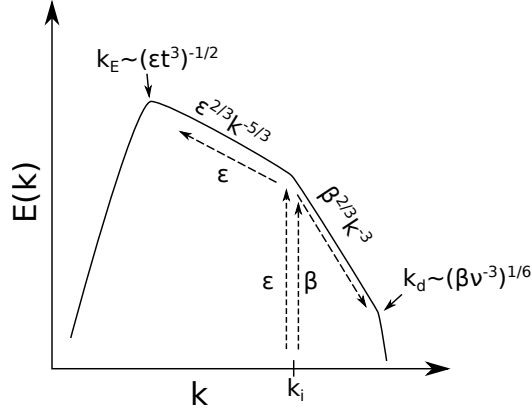
Figure 2.3: Schematic illustration of the dual cascades of 2D turbulence in a log-log plot where power laws look like straight lines. Energy is injected at rate ϵ at wavenumber k_i and enstrophy at rate $\beta = k_i^2 \epsilon$, shown as vertical dashed arrows. The enstrophy cascades down to smaller scales causing a self-similar k^{-3} energy spectrum, while the energy cascades to larger scales causing a $k^{-5/3}$ energy spectrum. This energy therefore piles up on larger and larger scales, moving the peak up and to the left and increasing the width of the inertial range until the system size is reached. After a similar illustration by Lesieur [10].

law

$$E(k) = C_\Omega \beta^{2/3} k^{-3} = C_\Omega k_i^{4/3} \epsilon^{2/3} k^{-3}, \tag{2.23}$$

although in practice this power law must be corrected by a logarithmic factor $(\ln \frac{k}{k_i})^{-1/3}$ [20]. This spectral signature should be accompanied by a positive *enstrophy flux*, given by

$$Z(k) = \int_k^\infty k^2 T(k) \mathrm{d}k, \tag{2.24}$$

where $T(k)$ is the spectral energy transfer function from equation (2.13). Applying a similar argument as that leading to equation (2.17), we can show that

$$Z(k) = \beta - 2\nu \int_0^k k'^4 E(k') \mathrm{d}k' \sim \beta - 2\nu C_\Omega \beta^{2/3} k^2, \tag{2.25}$$

which gives the Kolmogorov microscale of the enstrophy cascade as $k_d \sim \left(\frac{\beta}{\nu^3}\right)^{1/6}$.

Consider now what happens to the kinetic energy in the inertial range $k_i < k < k_d$ of the enstrophy cascade. By the above argument, the transfer function $T(k) = -\frac{1}{k^2}\frac{\mathrm{d}Z}{\mathrm{d}k}$ goes like k^{-1} in the inertial range, while it should go to zero for

18

$k > k_d$. The spectral energy flux $\Pi(k) = -\int_k^{k_d} T(k)$ should therefore go like $\Pi \sim -\ln k_d/k$, which is negative. As a result, the presence of the enstrophy cascade prevents the kinetic energy injected at k_i from transferring down to smaller scales. Kraichnan [21] therefore proposed that the kinetic energy goes in the opposite direction, towards *larger* scales in 2D. This *inverse energy cascade* would then be signaled by a $k^{-5/3}$ energy spectrum at $k < k_i$ by the same dimensional analysis as we used to show equation (2.12), while the spectral energy flux $\Pi(k)$ would be negative in the same range. This situation is illustrated in figure 2.3.

Assuming that there is no efficient energy dissipation mechanism at large scales, this will cause the energy to build up on larger and larger scales. For example, assume that the inverse energy cascade extends over an inertial range $k_E < k < k_i$, so that $E(k) = C_I \epsilon^{2/3} k^{-5/3}$ in this range and then falls rapidly to zero for $k < k_E$. The energy contained in scales larger than the injection scale k_i is then approximately given by

$$E_I = \int_0^{k_i} E(k)\mathrm{d}k \approx C_I \epsilon^{2/3} \int_{k_E}^{k_i} k^{-5/3}\mathrm{d}k = \frac{3}{2}C_I \epsilon^{2/3}\left(k_E^{-2/3} - k_i^{-2/3}\right). \quad (2.26)$$

With energy being added to this system at a rate ϵ, E_I needs to grow at this rate, which is only possible if k_E decreases with time. Setting $\frac{\mathrm{d}E_I}{\mathrm{d}t} = \epsilon$, we find

$$\frac{\mathrm{d}(k_E^{-2/3})}{\mathrm{d}t} \sim \epsilon^{1/3}, \quad k_E \sim \epsilon^{-1/2}t^{-3/2} = \frac{1}{\sqrt{\epsilon t^3}}, \quad (2.27)$$

which is the only combination of ϵ and time with the dimension L^{-1}. Thus, the inertial range of the inverse energy cascade widens until k_E gets close to the system size, where further transfer of energy to larger scales is blocked. The result is typically that energy piles up at small wavenumbers, breaking the self-similarity of the cascade. This is the phenomenon of energy condensation, which manifests itself as a few large, system-spanning rotational structures in the flow. In this way, we have obtained an *ordered state* of a few large vortices by *adding* energy to the system, which is an unexpected outcome.

Alternatively, one can obtain forced steady-states in 2D turbulence if there is an efficient dissipation mechanism at the largest scales. Such a dissipation mechanism is often added to numerical simulations through an additional term in the Navier–Stokes equation of the form $\nu_L \nabla^{-2}\mathbf{V}$ [22, 23] (meaning formally that we determine a field $\mathbf{W}$ by $\nabla^2\mathbf{W} = \mathbf{V}$ and add a term $\nu_L\mathbf{W}$), which varies with scale like k^{-2} and is therefore important only at the largest scales. This allows for

studying statistical properties of the inverse energy cascade by taking long time-averages in the steady-state regime. In lab experiments, large-scale damping can for example be due to linear drag with the vertical boundary in quasi-2D flows [22].

2.3   The point vortex model

In 3D turbulence, the Richardson picture of large eddies breaking up into smaller eddies gave an intuitive, if quantitatively imprecise, picture of how energy is transferred from large scales to small. The picture in 2D is much less clear. Kraichnan [24] gave a picture where small-scale vorticity structures, when sheared by some large-scale flow, tends to elongate and lose energy to the larger-scale strain. Energy is therefore transferred to larger scales, while the small-scale vortical structure itself becomes smaller, transferring enstrophy to smaller scales. This picture has been borne out by numerical and experimental studies [22, 23].

A seemingly completely different mechanism for the condensation of energy at large scales was provided by Onsager [25] by decomposing the 2D flow into a discrete collection of point-like, singular vortices. Such a picture naturally emerges when studying the stream function for incompressible flows with vanishing viscosity [26]. The incompressibility of $\mathbf{v}$ means that it can be represented by a stream function ψ, with $v_i = \epsilon_{ij}\partial_j\psi$, from which $\nabla \cdot \mathbf{v} = 0$ is satisfied identically. The stream function can be determined from a given vorticity field $\omega(\mathbf{r})$ by the relation

$$\omega = \epsilon_{ij}\partial_i v_j = \epsilon_{ij}\epsilon_{jk}\partial_{ik}\psi = -\nabla^2\psi, \tag{2.28}$$

giving a Poisson equation for the stream function, which is conveniently solved by the Green's function method. The 2D Laplacian in an infinite plane has a Green's function given by

$$G(\mathbf{r}, \mathbf{r}') = \frac{1}{2\pi}\ln|\mathbf{r} - \mathbf{r}'|, \quad \nabla^2 G = \frac{1}{2\pi}\nabla^2\ln|\mathbf{r} - \mathbf{r}'| = \delta(\mathbf{r} - \mathbf{r}'), \tag{2.29}$$

so the stream function can be expressed as

$$\psi(\mathbf{r}) = -\int G(\mathbf{r}, \mathbf{r}')\omega(\mathbf{r}')\mathrm{d}^2\mathbf{r}' = -\frac{1}{2\pi}\int \omega(\mathbf{r}')\ln|\mathbf{r} - \mathbf{r}'|\mathrm{d}^2\mathbf{r}'. \tag{2.30}$$

By analogy to the point charges of elementary particles in electromagnetism, one now considers the vorticity field as represented by a discrete set of point-like

sources located at $\mathbf{r}_\alpha$, with a continuous distribution of circulation strength given by $2\pi s_\alpha$. Hence $\omega(\mathbf{r}) = 2\pi \sum_\alpha s_\alpha \delta(\mathbf{r} - \mathbf{r}_\alpha)$, from which we find

$$\psi(\mathbf{r}) = -\sum_\alpha s_\alpha \ln |\mathbf{r} - \mathbf{r}_\alpha|. \tag{2.31}$$

The velocity field due to such a collection of vortices is now given by

$$v_i = \epsilon_{ij}\partial_j \psi, \quad v_x = -\sum_\alpha s_\alpha \frac{y - y_\alpha}{|\mathbf{r} - \mathbf{r}_\alpha|^2}, \quad v_y = \sum_\alpha s_\alpha \frac{x - x_\alpha}{|\mathbf{r} - \mathbf{r}_\alpha|^2}, \tag{2.32}$$

from which one can verify that the circulation integral satisfies

$$\oint_C \mathbf{v} \cdot \mathrm{d}\mathbf{l} = 2\pi \sum_{\mathbf{r}_\alpha \in C} s_\alpha, \tag{2.33}$$

where the sum runs over all vortices contained inside the given loop C. Setting $\rho = 1$ and computing the kinetic energy of this velocity field, we find

$$\frac{1}{2} \int v_i v_i \mathrm{d}^2\mathbf{r} = \frac{1}{2} \sum_{\alpha,\beta} s_\alpha s_\beta \int \nabla \ln |\mathbf{r} - \mathbf{r}_\alpha| \cdot \nabla \ln |\mathbf{r} - \mathbf{r}_\beta| \mathrm{d}^2\mathbf{r}, \tag{2.34}$$

where we used that the 2D Levi–Civita tensor satisfies $\epsilon_{ij}\epsilon_{ik} = \delta_{jk}$. For terms in this sum where $\alpha = \beta$, we can perform the integral in polar coordinates relative to the vortex position, giving

$$\frac{1}{2} \sum_\alpha 2\pi (s_\alpha)^2 \int_a^R (\nabla \ln r)^2 r \mathrm{d}r = \pi \sum_\alpha (s_\alpha)^2 \ln \frac{R}{a}, \tag{2.35}$$

where a and R are lower and upper cutoff length scales introduced to control the logarithmic divergence of this energy at both small and large scales. Ignoring these diverging terms, we can proceed with the sum over different indices. Applying an integration by parts and ignoring another logarithmic divergence from the boundary term, we find

$$H = -\frac{1}{2} \sum_{\alpha \neq \beta} s_\alpha s_\beta \int \ln |\mathbf{r} - \mathbf{r}_\alpha| \nabla^2 \ln |\mathbf{r} - \mathbf{r}_\beta| \mathrm{d}^2\mathbf{r} = -\pi \sum_{\alpha \neq \beta} s_\alpha s_\beta \ln r_{\alpha\beta}, \tag{2.36}$$

where we used that $\nabla^2 \ln r = 2\pi \delta(\mathbf{r})$, and the intervortex distance is denoted by $r_{\alpha\beta} = |\mathbf{r}_{\alpha\beta}| = |\mathbf{r}_\alpha - \mathbf{r}_\beta|$. This expression is known as the point vortex Hamil-
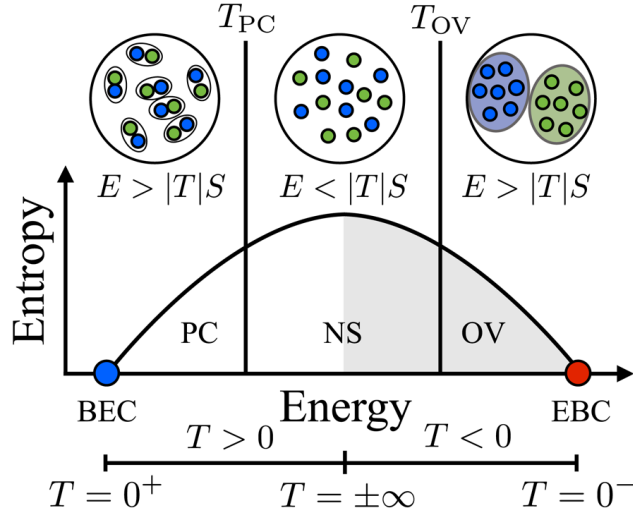
Figure 2.4: Qualitative illustration of the density of states $\Omega(E)$ of the point vortex Hamiltonian as a function of energy, with examples of positive, infinite, and negative temperature states. Reprinted figure with permission from [27]. Copyright 2014 by the American Physical Society.

tonian; indeed it turns out that the dynamics of inviscid point vortices satisfy a Hamiltonian system of equations given by H. By equation (2.19), we see that 2D vorticity is simply advected by the velocity field at $\nu = 0$. Applying this principle to point vortices, we must have that $\dot{x}_\alpha = \partial_y \psi^{(\alpha)}(\mathbf{r}_\alpha)$, $\dot{y}_\alpha = -\partial_x \psi^{(\alpha)}(\mathbf{r}_\alpha)$, where the (α) superscript indicates that we remove the contribution to ψ from the vortex α, which is singular at $\mathbf{r}_\alpha$. By evaluating this derivative, we can show that the dynamics of point vortices is equivalent to a Hamiltonian system of equations given by

$$2\pi s_\alpha \dot{x}_\alpha = \frac{\partial H}{\partial y_\alpha}, \quad \dot{y}_\alpha = -\frac{\partial H}{\partial(2\pi s_\alpha x_\alpha)}, \tag{2.37}$$

with the extra factor of 2 coming from the symmetry of the Hamiltonian under the interchange $\mathbf{r}_\alpha \leftrightarrow \mathbf{r}_\beta$. Hence, we see that $2\pi s_\alpha x_\alpha$ and y_α are the conjugate coordinates in the Hamiltonian, which is highly unusual. Hamiltonian dynamics of typical systems in classical mechanics has a momentum coordinate $\mathbf{p}$ as conjugate to the physical coordinates $\mathbf{r}$. The fact that such a momentum coordinate is missing here is because vortices have no inertia, simply following the velocity field passively.

This simple fact has dramatic consequences for the equilibrium behavior of a

bounded vortex gas. In a bounded system, the Green's function of the Laplacian is modified to satisfy the no-flux boundary condition on the velocity field, but the general structure of the system is preserved [26]. In particular, the phase space still consists of the vortex coordinate variables weighted by circulation strength, which are now confined to the area A of the system. Hence, the phase space $\mathbb{P}$ of N vortices has volume

$$|\mathbb{P}| = \prod_\alpha \int \mathrm{d}(2\pi s_\alpha x_\alpha)\mathrm{d}y_\alpha = (2\pi A)^N \prod_\alpha s_\alpha, \tag{2.38}$$

which is a finite number. The energy, meanwhile, takes values from $-\infty$ to ∞, but the density of states $D(E)$ at a given energy E must have a bounded integral $\int_{-\infty}^{\infty} D(E)\mathrm{d}E = |\mathbb{P}|$. This is only possible if $D(E)$ has a maximum $D'(E_{\mathrm{crit}}) = 0$, from which it asymptotically decreases to 0, giving $D'(E > E_{\mathrm{crit}}) < 0$. Thus the microcanonical inverse temperature,

$$\beta = \frac{\mathrm{d}S}{\mathrm{d}E} \propto \frac{\mathrm{d}\ln D}{\mathrm{d}E} = \frac{D'}{D}, \tag{2.39}$$

is *negative* for $E > E_{\mathrm{crit}}$ [25], which means that an increase in energy leads to an ordered low-entropy state. This tendency of the system to become ordered when energy is added is exactly what we observed in the case of energy condensation due to the inverse energy cascade. Indeed, if we consider a system where like-signed vortices are clustered together into large coherent structures (see figure 2.4), we see that an increase in energy is associated with the clusters packing more tightly together, leading to a decrease in the typical intervortex distance $r_{\alpha\beta}$ and a higher energy $-\ln r_{\alpha\beta}$. Tighter vortex clusters have a smaller available phase-space volume, hence these vortex clusters have negative temperature. A similar argument shows that a system of tightly coupled vortex dipoles has positive temperature, while the critical energy where $\Omega'(E_{\mathrm{crit}}) = 0$ is associated with a free gas of vortices not strongly coupled to other vortices with infinite temperature $T = 1/\beta$.

From the above discussion we see that, if the point vortex model is a good approximation of 2D turbulent states, the phenomenon of energy condensation can be explained as the tendency of like-signed vortices to cluster together into large coherent structures. However, the equilibrium arguments performed by Onsager are insufficient in investigating the nonequilibrium state of the inverse energy cascade and the forward enstrophy cascade, where turbulent energy fluxes and viscosity are important. In classical fluid flows, the most important effect of viscosity

is that vortices have a core structure of size a, within which the vorticity field decays smoothly to zero [28]. The core region is subject to the diffusion term in equation (2.19), causing the core radius to increase like $a \sim \sqrt{t}$. Vortices whose core regions come into contact are then subject to merging rules, giving rise to a new vortex with a different circulation and core radius [29]. Such dissipative point vortex models have reproduced the k^{-3} energy spectrum associated with the enstrophy cascade, which is associated with a scale-free distribution of vortex core sizes. Similarly, the $k^{-5/3}$ energy spectrum of the inverse energy cascade has been reproduced by adding a phenomenological small-scale driving mechanism to the point vortex model [30].

The fact that the energy of the system of vortices only depends on their position means that energetic properties like the energy spectrum are purely dependent on the spatial configuration of vortices. Novikov [31] derived an expression for the energy spectrum given by

$$E(k) = \frac{\pi}{k} \left(\sum_{\alpha} s_{\alpha}^2 + \sum_{\alpha \neq \beta} s_{\alpha} s_{\beta} J_0(k r_{\alpha\beta}) \right), \qquad (2.40)$$

and then went on to consider the behavior of this function in a cluster of vortices of the same circulation $s_{\alpha} = 1$, in which case the energy spectrum only depends on the intervortex distance. Upon averaging, this leads to a dependence on the vortex pair correlation function $g(\mathbf{r}) = \frac{A}{N^2} \sum_{\alpha \neq \beta} \langle \delta(\mathbf{r} - \mathbf{r}_{\alpha\beta}) \rangle$, given by

$$\langle E(k) \rangle = \frac{N\pi}{k} \left(1 + \frac{N}{A} \int J_0(kr) g(\mathbf{r}) \mathrm{d}^2 \mathbf{r} \right), \qquad (2.41)$$

providing a relationship between the structure of the vortex cluster as measured by pair correlations and the energy spectrum. Novikov then argued that a self-similar energy cascade should be related to a self-similar scaling of the pair correlation, leading to the ansatz $g(\mathbf{r}) - 1 \propto r^{-\alpha}$, from which a $k^{\alpha-3}$ energy spectrum follows. An $r^{-4/3}$ scaling in the vortex pair correlation is associated with the $k^{-5/3}$ energy spectrum of the inverse energy cascade, suggesting that 2D turbulence features fractal vortex clusters with self-similar structure. This hypothesis is the starting point for many analytic and numerical studies of point vortex turbulence, including our papers II and III, which we will discuss more thoroughly in the next chapter on quantum turbulence.

Thus we find a qualitative picture of the inverse energy cascade that is very different from the picture of vortex stretching, which we mentioned in the begin-

ning of this section. It is an open question whether the two pictures are equivalent in some way, or whether they describe qualitatively different processes which are expressed in different systems.

Onsager also mentioned that the point vortex model might be a more accurate representation of rotating superfluids, where such point-like vortices appear as the only carriers of vorticity. This simple observation has led to considerable interest in the turbulent behavior of superfluids, due to the potential for experimental investigation of the point vortex model. However, the point vortices of superfluids have some important differences from their classical counterparts, such as the quantization of vortex circulation, and the nondiffusive vortex core structure. Turbulent states in superfluids are therefore subject to intense study in their own right, in a field known as *quantum turbulence*. This is the field to which we turn our attention in the next chapter.

Chapter 3

Quantum turbulence

Quantum turbulence is a state of rapidly fluctuating flow similar to classical turbulence, but occurring in a quantum fluid or superfluid [32]. Superfluids are macroscopic quantum states of matter where the wavefunctions of many particles overlap, leading to counterintuitive phenomena, such as vanishing viscosity and the quantization of vorticity. One might wonder whether turbulence could even exist given these differences. However, both numerical and experimental work has proved the existence of an energy cascade in 3D [33, 34], which is associated with vortex lines breaking up into smaller vortex rings, leading to a complex tangle of vortices [35, 36]. Work on 3D quantum turbulence has focused on superfluid helium, which is modeled phenomenologically by the coexistence of a normal fluid component obeying the Navier–Stokes equation, and a superfluid component that is represented phenomenologically as a collection of interacting vortex filaments coupled to the normal fluid through viscous drag with the vortex core [37].

In the previous chapter on classical turbulence, we saw how outstanding problems in 2D turbulence can be informed by studies of vortices in 2D quantum turbulence. Two-dimensional superfluids can be realized experimentally as dilute atomic Bose–Einstein condensates in a laser-cooled trap, which are strongly confined in the vertical direction to give a quasi-2D state [38]. Since these systems are dilute, the interactions between atoms located at $\mathbf{r}_\alpha$ and $\mathbf{r}_\beta$ can be approximated by contact interactions, $V(\mathbf{r}_\alpha - \mathbf{r}_\beta) = g\delta(\mathbf{r}_\alpha - \mathbf{r}_\beta)$. In this chapter we introduce the semiclassical Gross–Pitaevskii equation (GPE) to study the basic properties of these systems. We show how the equation can be interpreted as describing a superfluid velocity field obeying a hydrodynamic equation, and how quantized vortices arise as singularities in the complex phase of the wavefunction. From this, we derive the point vortex model as an effective description of the motion

when compressible effects are small. We then describe observations of the inverse energy cascade in quantum turbulence and how they relate to the spatial structure of quantized vortices. Finally, we summarize our contributions investigating this spatial structure in papers I–III.

3.1 The Gross–Pitaevskii equation

A Bose–Einstein condensate (BEC) is a system of N particles of mass m obeying Bose–Einstein statistics, where the temperature is cold enough that a macroscopic number N_0 of particles remain in the ground state of the trapping potential. Weakly interacting Bose gases are typically modeled by a second-quantized Hamiltonian for the particle annihilation and creation operators $\hat{\Psi}(\mathbf{r})$, $\hat{\Psi}^\dagger(\mathbf{r})$ trapped by an external potential $V(\mathbf{r})$, given by [39]

$$H = \int \left[\frac{\hbar^2}{2m} \nabla \hat{\Psi}^\dagger \cdot \nabla \hat{\Psi} + V(\mathbf{r}) \hat{\Psi}^\dagger \hat{\Psi} + \frac{1}{2} g \hat{\Psi}^\dagger \hat{\Psi}^\dagger \hat{\Psi} \hat{\Psi} \right] \mathrm{d}^d \mathbf{r}, \qquad (3.1)$$

where g is the strength of the contact interaction between particles in the gas. In the Heisenberg picture, the particle operator $\hat{\Psi}$ obeys the Heisenberg equation of motion, given by

$$i\hbar \partial_t \hat{\Psi} = [\Psi, H] = -\frac{\hbar^2}{2m} \nabla^2 \hat{\Psi} + V \hat{\Psi} + g \hat{\Psi}^\dagger \hat{\Psi} \hat{\Psi}. \qquad (3.2)$$

The particle operator is then decomposed into $\hat{\Psi} = \hat{\psi} + \hat{\phi}$, where $\hat{\psi}$ is the ground state and $\hat{\phi}$ represents excitations. Due to Bose–Einstein condensation, the occupation number of the ground state $N_0 = \left\langle \hat{\psi}^\dagger \hat{\psi} \right\rangle \gg 1$ is large compared to the commutator $[\hat{\psi}, \hat{\psi}^\dagger] = 1$. Thus the particle operators of the ground state approximately commute, and we can treat it as a classical field in what is known as a Bogoliubov approximation [39]. Also neglecting the excitations $\hat{\phi}$, which are of order $N - N_0 \ll N_0$, we obtain the time-dependent Gross–Pitaevskii equation

$$i\hbar \partial_t \psi(\mathbf{r}) = -\frac{\hbar^2}{2m} \nabla^2 \psi(\mathbf{r}) + V(\mathbf{r}, t)\psi + g|\psi(\mathbf{r})|^2 \psi(\mathbf{r}), \qquad (3.3)$$

where ψ is a complex order parameter that represents the ground state wavefunction. Since stationary states oscillate with the chemical potential μ (similar to how single-particle states oscillate with their energy), it is useful to transform to

the comoving frame $\psi \mapsto \psi e^{-i\mu t/\hbar}$, which leads to an additional term $-\mu\psi$ on the right-hand side,

$$i\hbar\partial_t\psi = -\frac{\hbar^2}{2m}\nabla^2\psi - \left(\mu - V - g|\psi|^2\right)\psi. \tag{3.4}$$

This corresponds to considering the conserved dynamics of the grand canonical Hamiltonian $\mathcal{H} = H - \mu N$, using a classical version of the Hamiltonian in equation (3.1),

$$\mathcal{H} = \int \mathrm{d}^d\mathbf{r}\left[\frac{\hbar^2}{2m}|\nabla\psi|^2 + V|\psi|^2 + \frac{\mu^2}{2g}\left(\frac{g}{\mu}|\psi|^2 - 1\right)^2\right], \quad i\hbar\partial_t\psi = \frac{\delta\mathcal{H}}{\delta\psi^*}, \tag{3.5}$$

where we completed the square in the expression $\frac{g}{2}|\psi|^4 - \mu|\psi|^2$ and ignored an unimportant additive energy constant. We can verify that this conserves energy as long as the confining potential is constant by taking functional derivatives,

$$\partial_t\mathcal{H} = \int \mathrm{d}^d\mathbf{r}\left(\frac{\delta\mathcal{H}}{\delta\psi}\partial_t\psi + \frac{\delta\mathcal{H}}{\delta\psi^*}\partial_t\psi^* + \frac{\delta\mathcal{H}}{\delta V}\partial_t V\right)$$
$$= \int \mathrm{d}^d\mathbf{r}\left(\frac{\delta\mathcal{H}}{\delta\psi}\frac{1}{i\hbar}\frac{\delta\mathcal{H}}{\delta\psi^*} - \frac{\delta\mathcal{H}}{\delta\psi^*}\frac{1}{i\hbar}\frac{\delta\mathcal{H}}{\delta\psi} + |\psi|^2\partial_t V\right) = \int |\psi|^2\partial_t V \mathrm{d}^d\mathbf{r}. \tag{3.6}$$

By contrast, a time-dependent potential can add or remove energy from the system, as we will exploit below.

3.2 The Thomas–Fermi ground state

A simple understanding of the stationary lowest-energy state of the Gross–Pitaevskii equation can be found using the Thomas–Fermi approximation. In this approximation, we assume that the kinetic energy term $\frac{\hbar^2}{2m}\nabla^2\psi$ of the ground state is small compared to the other terms, leading to a slowly varying state. Thus, ignoring this term and looking for stationary states by setting $\partial_t\psi_{TF} = 0$, we find

$$(\mu - V - g|\psi_{TF}|^2)\psi_{TF} = 0, \quad \Leftarrow \quad \psi_{TF} = 0 \quad \text{or} \quad \psi_{TF} = \sqrt{\frac{\mu - V}{g}}, \tag{3.7}$$

where the solution can be multiplied with an arbitrary constant phase factor, and we take $\psi_{TF} = 0$ when $V > \mu$. For example, if the confining potential is harmonic with $V = \frac{1}{2}m\omega^2 r^2$, we find that the condensate should extend approximately out

to the Thomas–Fermi radius given by

$$\frac{1}{2}m\omega^2 R_{TF}^2 = \mu, \quad \Leftarrow \quad R_{TF} = \sqrt{\frac{2\mu}{m\omega^2}}, \qquad (3.8)$$

and within this radius the solution takes the shape of a hemisphere, given by

$$\psi_{TF} = \sqrt{\frac{\mu - \frac{1}{2}m\omega^2 r^2}{g}} = \sqrt{\frac{\mu}{g}\left(1 - \frac{r^2}{R_{TF}^2}\right)}. \qquad (3.9)$$

This solution has rapid variations near R_{TF}, so the Thomas–Fermi approximation breaks down here, with the balance between potential and distortion energies determining a smoother approach to $\psi = 0$ at $r \sim R_{TF}$. It is still a good approximation away from R_{TF}. We therefore use this solution as an initial condition in paper I.

3.3 Dissipation

At small but finite temperatures, the low-energy state described by the condensate wavefunction is not fully populated, with some atoms being thermally excited to higher-energy states. The interaction between the low-energy condensate and higher-energy excitations leads to dissipation of energy from the condensate. This can be modeled explicitly by considering the states above some energy cutoff to be in thermal equilibrium, yielding a grand canonical description of the condensate [40]. The result is the Stochastic Projected Gross–Pitaevskii equation (SPGPE), which effectively results in the addition of a dissipating term to the time development,

$$i\hbar\partial_t\psi = (1 - i\gamma)\left[-\frac{\hbar^2}{2m}\nabla^2\psi(\mathbf{r}) + V(\mathbf{r}, t)\psi - \mu\psi + g|\psi(\mathbf{r})|^2\psi(\mathbf{r})\right], \quad (3.10)$$

with γ related to the temperature [40]. That this term causes energy to dissipate can be seen from its effect on the Hamiltonian,

$$\begin{aligned}
\partial_t \mathcal{H} &= \int \mathrm{d}^d \mathbf{r} \left(\frac{\delta \mathcal{H}}{\delta \psi} \partial_t \psi + \frac{\delta \mathcal{H}}{\delta \psi^*} \partial_t \psi^* + \frac{\delta \mathcal{H}}{\delta V} \partial_t V \right) \\
&= \int \mathrm{d}^d \mathbf{r} \left(\frac{\delta \mathcal{H}}{\delta \psi} \frac{1 - i\gamma}{i\hbar} \frac{\delta \mathcal{H}}{\delta \psi^*} - \frac{\delta \mathcal{H}}{\delta \psi^*} \frac{1 + i\gamma}{i\hbar} \frac{\delta \mathcal{H}}{\delta \psi} + |\psi|^2 \partial_t V \right) \\
&= -\frac{\gamma}{\hbar} \int d^d \mathbf{r} \left| \frac{\delta \mathcal{H}}{\delta \psi^*} \right|^2 + \int d^d \mathbf{r} |\psi|^2 \partial_t V,
\end{aligned} \tag{3.11}$$

where the first term is negative, dissipating energy. If the confining potential also varies with time, we can obtain a nonequilibrium steady state driven by the competition between a net influx of energy from the time-dependent potential, and the energy dissipation due to the γ term. We use this technique in paper I in order to generate a forced turbulent steady-state. In particular, the potential $V(\mathbf{r}, t) = V_t(\mathbf{r}) + V_g(\mathbf{r}, t)$ consists of a constant harmonic trapping potential $V_t = \frac{1}{2} m \omega^2 r^2$, and a small Gaussian obstacle with peak $V_0 > \mu$ that moves around a circle with a given speed. Since $V_0 > \mu$, the wavefunction will go to zero around the obstacle, and as it moves it will push a compression wave in front of it, while leaving a diluted wake behind it. Thus, the density $|\psi|^2$ is higher in front of the obstacle where the potential increases with time and is lower behind it where the potential decreases, giving a positive second term of equation (3.11). In this way, the stirring obstacle adds energy to the system, leading to a nonequilibrium steady-state determined by the balance between forcing and dissipation.

For such numerical work as well as ease of analysis, it is useful to introduce dimensionless units. The natural scale of the energy is set by the chemical potential μ, while the global phase rotation $e^{-i\mu t/\hbar}$ gives rise to a time scale $\tau = \hbar/\mu$. The chemical potential along with the atomic mass gives a speed $\sqrt{\frac{\mu}{m}}$, which we will see below corresponds to the speed of sound. Finally, the distance that sound can travel during one phase rotation is the coherence length, $\xi = c\tau = \frac{\hbar}{\sqrt{m\mu}}$. Indeed, a disturbance over a length scale ξ is associated with a kinetic energy penalty of order $\frac{\hbar^2}{m\xi^2}$, which is permissible as long as it stays below the chemical potential μ; hence $\xi = \frac{\hbar}{\sqrt{m\mu}}$ sets the typical length scale of distortions in the BEC. Rescaling time, space and potential energy by these units, we obtain the dimensionless form

$$i\partial_t \psi = (1 - i\gamma) \left[-\frac{1}{2} \nabla^2 \psi + \left(V - 1 + \frac{g}{\mu} |\psi|^2 \right) \psi \right]. \tag{3.12}$$

31

The interaction parameter $\frac{g}{\mu}$ can be absorbed into the wavefunction by $\psi \mapsto \sqrt{\frac{g}{\mu}}\psi$, which requires another rescaling of time by g/μ. Thus we obtain a fully dimensionless equation with the dissipation parameter γ as the only adjustable constant,

$$\partial_t \psi = (i + \gamma)\left[\frac{1}{2}\nabla^2\psi + (1 - V - |\psi|^2)\psi\right],\qquad(3.13)$$

which corresponds to the dimensionless Hamiltonian given by

$$\mathcal{H} = \int\left[\frac{1}{2}|\nabla\psi|^2 + V|\psi|^2 + \frac{1}{2}\left(|\psi|^2 - 1\right)^2\right]\mathrm{d}^d\mathbf{r}.\qquad(3.14)$$

3.4 Hydrodynamics

While the Gross–Pitaevskii equation resembles the Schrödinger equation with an extra nonlinearity, it can also be transformed into hydrodynamical equations describing the superfluid flow in the condensate. This is done through the Madelung transformation $\psi(\mathbf{r}) = \sqrt{\rho(\mathbf{r})}e^{i\phi(\mathbf{r})}$, where $\rho = |\psi|^2$ represents the particle density and ϕ the complex phase. The current density of ρ is as usual given by $\mathbf{J} = \frac{\hbar}{2mi}\left(\psi^*\nabla\psi - \nabla\psi^*\psi\right) = \frac{\hbar}{m}\rho\nabla\phi$, allowing us to identify the superfluid velocity $\mathbf{v} = \frac{\hbar}{m}\nabla\phi$. We note that as a gradient, this superfluid velocity is irrotational. Inserting the Madelung transformation into the SPGPE, multiplying with the conjugate and taking real and imaginary parts, we find [40]

$$\partial_t \rho + \nabla \cdot (\rho\mathbf{v}) = \frac{2\rho\gamma}{\hbar}(\mu - U_{\text{eff}}),\qquad(3.15)$$

$$\hbar\partial_t\phi = \mu - U_{\text{eff}} + \frac{\hbar\gamma}{2\rho}\nabla \cdot (\rho\mathbf{v}),\qquad(3.16)$$

$$U_{\text{eff}} = \frac{m\mathbf{v}^2}{2} + V + g\rho - \frac{\hbar^2}{2m}\frac{\nabla^2\sqrt{\rho}}{\sqrt{\rho}}.\qquad(3.17)$$

The first equation shows that the particle number $N = \int\rho\mathrm{d}^d\mathbf{r}$ is not conserved, but is driven towards chemical equilibrium with the thermal excitations, defined by $U_{\text{eff}} = \mu$. The last term in the effective potential U_{eff} is called the quantum pressure, which is small unless the density changes rapidly, that is, far away from vortices and R_{TF}. Taking the gradient of the ϕ equation and ignoring the quantum pressure and other terms related to the rapid variation of ρ, one derives a Navier–

Stokes-like equation for the velocity field [40],

$$\partial_t \mathbf{v} + \mathbf{v} \cdot \nabla \mathbf{v} = -\frac{1}{m}(V + g\rho) + \frac{\hbar\gamma}{2m}\nabla^2\mathbf{v}. \tag{3.18}$$

This shows that the superfluid velocity behaves effectively like a classical velocity field with kinematic viscosity $\nu_q = \hbar\gamma/2m$ proportional to the dissipation parameter γ, except for effects related to the quantum pressure near vortex cores.

In light of this, it is interesting to see how the Hamiltonian transforms under the Madelung transformation. Inserting $\psi = \sqrt{\rho}e^{i\phi}$ into (3.5), the Hamiltonian decomposes nicely into four terms,

$$\mathcal{H} = \int \left[\frac{1}{2}\rho\mathbf{v}^2 + \frac{\hbar^2}{4m}\frac{|\nabla\rho|^2}{\rho} + V\rho + \frac{\mu^2}{2g}\left(\frac{g}{\mu}\rho^2 - 1\right)^2 \right] \mathrm{d}^d\mathbf{r}. \tag{3.19}$$

This decomposition includes the kinetic energy $T = \frac{1}{2}\rho\mathbf{v}^2$, a distortion energy related to density variations $\nabla\rho$, potential energy $V\rho$, and a term balancing the contact interaction with the chemical potential.

As any fluid, superfluids have compression waves, or sound waves, as their elementary excitations. Ignoring the confining potential for simplicity, we see that the ground state of equations (3.15–3.16) is the Thomas–Fermi solution $\rho = \frac{\mu}{g}$ at constant $\phi = 0$, corresponding to the $\mathbf{v} = 0$ solution of equation (3.18). Sound waves are found as small deviations from this state, $\rho = \frac{\mu}{g} + \delta\rho$ with $\delta\rho$ and ϕ small, leading to linearized equations for $\delta\rho$ and ϕ given by

$$\partial_t \delta\rho + \frac{\hbar\mu}{mg}\nabla^2\phi = -\frac{2\gamma\mu}{\hbar}\left(\delta\rho - \frac{1}{4}\xi^2\nabla^2\delta\rho\right),$$

$$\hbar\partial_t\phi = -g\delta\rho + \frac{1}{4}g\xi^2\nabla^2\delta\rho + \frac{\hbar^2\gamma}{2m}\nabla^2\phi. \tag{3.20}$$

If we consider distortions that vary slowly compared to the coherence length ξ, we can ignore the quantum pressure term $\xi^2\nabla^2\delta\rho$. Hence, at $\gamma = 0$ we can differentiate the ϕ equation with time to obtain

$$\partial_{tt}\phi - \frac{\mu}{m}\nabla^2\phi = 0, \tag{3.21}$$

which is a wave equation describing compression waves moving with speed $c = \sqrt{\frac{\mu}{m}}$, justifying why it is called the speed of sound. This result was also found by Pismen [41], with a factor $\sqrt{2}$ in the speed of sound due to their different

33

convention for the GPE, where they leave out the factor $\frac{1}{2}$ in front of the Laplacian in equation (3.13). On the other hand, if the dissipation dominates with $\gamma \gg 1$, the two equations decouple into an exponential decay for $\delta\rho$ and a diffusion equation for ϕ,

$$\partial_t \delta\rho = -\frac{2\gamma\mu}{\hbar}\delta\rho, \quad \partial_t \phi = \nu_q \nabla^2 \phi, \tag{3.22}$$

with the diffusion constant given by the kinematic viscosity $\nu_q = \frac{\hbar\gamma}{2m}$, and the exponential decay rate characterized by the phase rotation time scale $\tau = \hbar/\mu$. This shows that conservative behavior is associated with ballistic degrees of freedom, while the dissipative behavior is associated with diffusive degrees of freedom. In our simulations in paper I, we kept γ very small $\sim 10^{-2}$, hence we expect acoustic degrees of freedom to take the form of compression waves moving at speed c, with only weak dissipative effects.

Finally, we note that the speed of sound is affected by the confining potential, which we have ignored here. For wavelengths that are short compared to the variation of V, we can assume that the sound wave varies adiabatically with the Thomas–Fermi solution $\rho = \frac{\mu - V}{g}$, hence the speed of sound takes the form $c = \sqrt{\frac{\mu - V}{m}}$. Faster variations of the potential occur near the boundary, which presumably leads to scattering of the sound waves.

3.5 Vortices

We now turn our attention to quantized vortices, which are central to superfluids as they are the only carriers of rotation. Note first that since the superfluid velocity is a gradient $\mathbf{v} = \frac{\hbar}{m}\nabla\phi$, the vorticity $\omega = \nabla \times \nabla\phi$ vanishes unless ϕ is singular. Singularities in the phase ϕ are permissible at finite energy if the density ρ vanishes. A vanishing density, however, comes at the expense of an energy density $\mu^2/2g$ from the Hamiltonian in equation (3.5). We therefore expect the density to return to its equilibrium value quite rapidly, over a distance comparable to the coherence length ξ.

In addition to this compactness, the vortex must satisfy topological constraints for the wavefunction to be well defined: As we go around a loop C containing the singularity, the wavefunction must have the same value at the initial and final points of the loop. This constraint is satisfied if the phase changes by an integer

multiple of 2π, defining the *topological charge* s of the singularity by

$$\oint_C d\phi = \oint_C \nabla\phi \cdot \mathrm{d}\mathbf{r} = 2\pi s. \tag{3.23}$$

This quantity is an intrinsic property of the singularity, because continuous changes to the loop C results in continuous changes of the contour integral as long as ϕ is smooth; hence s can only change by discrete amounts when the loop crosses the singularity. Similarly, continuous changes in the phase ϕ cannot lead to discrete changes in the circulation integral. Hence, the singularity is topologically protected by the condition (3.23), which is why it is called a *topological defect*. If the loop encompasses more then one vortex, we can smoothly split the loop into smaller loops containing each vortex, hence the topological charge is additive,

$$\oint_C d\phi = 2\pi \sum_{\alpha \in C} s_\alpha, \tag{3.24}$$

with the sum running over each vortex of charge s_α contained in C.

Topological defects in 2D are point-like, because we can always shrink the loop down to a point. In 3D, we also have to consider perpendicular translations of the loop, without changing the topological charge. As a result, topological defects in 3D are line-like filaments going through the system, or closing in on themselves to form loops. In general, topological defects of the GPE are of codimension two, which means that they span $d-2$ dimensions where d is the dimension of the system. Mathematically, this is related to the fact that the minimizing order parameter $\psi = \sqrt{\frac{\mu - V}{g}} e^{i\phi}$ contains a $U(1)$ degree of freedom ϕ, hence the space of the minimizing order parameter has a nontrivial first homotopy group $\mathbb{Z}$, which gives rise to codimension two topological defects with charges in $\mathbb{Z}$ [41]. Similarly, higher homotopy groups are connected with topological defects of higher codimension (lower dimension), although we will not consider such defects in this thesis.

Recalling that the superfluid velocity is given by $\mathbf{v} = \frac{\hbar}{m}\nabla\phi$, we can restate the loop integral as a circulation integral of the velocity, $\oint_C \mathbf{v} \cdot \mathrm{d}\mathbf{r} = 2\pi\frac{\hbar}{m}s$. This circulation integral is reminiscent of the point vortices that we considered in chapter 2. However, while the charge s_α of classical vortices could vary continuously, in quantum fluids it is topologically constrained to take discrete values that are integer multiples of $\hbar/m$. This is the quantization of vorticity, and is the reason topological defects in this system are known as *quantized vortices*. We can represent the vorticity by a collection of point vortices by taking the circulation of $\mathbf{v}$

around the boundary of a surface S in 2D and using Stokes' theorem, giving

$$\oint_{\partial S} \mathbf{v} \cdot \mathrm{d}\mathbf{r} = \int_S (\nabla \times \mathbf{v}) \mathrm{d}^2\mathbf{r} = \frac{h}{m} \int_S S(\mathbf{r}) \mathrm{d}^2\mathbf{r}, \tag{3.25}$$

where we introduced the *vortex density* $S(\mathbf{r}) = \sum_\alpha s_\alpha \delta(\mathbf{r} - \mathbf{r}_\alpha)$. Since this equation must hold over all surfaces S, the vorticity of the fluid satisfies $\omega(\mathbf{r}) = \frac{h}{m}S(\mathbf{r})$.

We can gain more information about the typical structure of point vortices by considering a stationary, isolated vortex at the origin. Considering an infinite 2D system with no external potential for simplicity, an isotropic ansatz for a vortex with charge s is given by $\chi(r)e^{is\theta}$ where r, θ are polar coordinates. Setting $\partial_t\psi = 0$ in the dimensionless form of the GPE, we find after some computation that $\chi(\mathbf{r})$ must satisfy

$$r^2\partial_{rr}\chi + r\partial_r\chi - s^2\chi = 2r^2(\chi^2 - 1)\chi. \tag{3.26}$$

In addition we must have $\chi(0) = 0$ to ensure that the wavefunction is well-defined, and that χ must approach the equilibrium value of 1 as $r \to \infty$. Close to the origin we can ignore the right-hand side, giving an Euler–Cauchy equation with solutions $\chi \propto r^{\pm s}$, of which $r^{|s|}$ satisfies the boundary condition at $r = 0$. Thus, we have that $\psi = \Lambda r^{|s|}e^{is\theta}$ close to the vortex, where Λ is a slope that can only be determined by considering the full boundary value problem. In ref. [40], Λ was determined numerically for $|s| = 1$ to $\Lambda^2 \approx 0.6805$. As r increases, the right-hand side of equation (3.26) becomes more important and the solution will flatten out to the constant value of $\chi = 1$ after a distance roughly corresponding to the coherence length ξ.

The region close to the vortex where $\chi = \Lambda r^{|s|}$ is called the *vortex core*, and the region outside this core where $\chi \approx 1$ is called the *far field*. Note, however, that the nature of this vortex core differs from the core structure of a viscous classical vortex. While classical vortices have a continuous vorticity going smoothly to zero inside the vortex core, in quantized vortices the vorticity is strictly constrained to the delta function peak at the location of the defect, with the density going to zero in order to keep the kinetic energy finite. While the core of viscous classical vortices tend to grow diffusively with time, the core structure of quantized vortices have a well-defined size $\sim \xi$, independently of dissipative effects.

Denoting the core radius by $R_c \sim \xi$, we can compute the far-field energy of

the vortex as

$$E_{\text{far}} = \int_{r>R_c} \left[\frac{1}{2} |\nabla \psi|^2 + \frac{1}{2} (|\psi|^2 - 1)^2 \right] \mathrm{d}^2\mathbf{r} = \pi \int_{R_c}^{R} r \frac{s^2}{r^2} \mathrm{d}r = \pi s^2 \ln \frac{R}{R_c},$$
(3.27)

where R is the system size. Pismen [41] found that the full energy including the core structure takes the similar form $\pi s^2 \ln \frac{R\sqrt{e}}{a_0}$, where a_0 is a numerically determined constant related to the particular solution of equation (3.26), depending on $|s|$. In any case the vortex energy scales with s^2, suggesting that vortices with $|s| > 1$ are unstable, preferring to split into vortices of smaller charges which then repel each other. Indeed, in our simulations of the GPE of paper I, we see only singly charged vortices.

3.6 Vortex motion

The motion of vortices is controlled by deviations of ψ from the equilibrium vortex solution $\chi(r)e^{is\theta}$, of which phase perturbations $e^{i\phi(\mathbf{r})}$ are the most important. The coupling between vortices and phase perturbations has been studied rigorously by finding stationary vortex solutions in a comoving frame, and studying the energetic properties of such solutions by matched asymptotic expansion [41]. This gives rise to a rich phenomenology of the coupling between vortices and the acoustic field. However, the speed of a given vortex in a particular out-of-equilibrium state ψ can be obtained more simply by exploiting that the vortices coincide with the zeros of the wavefunction, which allows us to track those zeros. This method was originally proposed by Halperin [42] and further developed by Mazenko [43, 44]. We give an outline of this method here, because it serves as an introduction to the generalization of the method that we develop for dislocations in chapter 4 and paper IV.

Since $|\psi(r)| \sim r^{|s|}$ as $r \to 0$, the wavefunction ψ has a zero with multiplicity $|s|$ exactly where vortices of charge s are located. Assuming these are the only places where the wavefunction vanishes, the function $\delta(\psi)$ has singularities exactly at the vortex positions. By the transformation law of delta functions, this gives that

$$\sum_{\alpha} |s_\alpha| \delta(\mathbf{r} - \mathbf{r}_\alpha) = |D| \delta(\psi), \tag{3.28}$$

where D is the Jacobi determinant of the transformation of variables from $(\operatorname{Re}\psi, \operatorname{Im}\psi)$

to (x, y), given by

$$D = \begin{vmatrix} \partial_x \operatorname{Re} \psi & \partial_x \operatorname{Im} \psi \\ \partial_y \operatorname{Re} \psi & \partial_y \operatorname{Im} \psi \end{vmatrix} = \operatorname{Im}(\partial_x \psi^* \partial_y \psi) = \frac{1}{2i} \epsilon_{ij} \partial_i \psi^* \partial_j \psi. \tag{3.29}$$

In fact, using the local solution $\psi \propto r^{|s|} e^{is\theta}$ near the origin, we can show that D has the same sign as s, thus we can remove the absolute values and find an expression for the vortex density $S(\mathbf{r})$,

$$S(\mathbf{r}) = \sum_\alpha s_\alpha \delta(\mathbf{r} - \mathbf{r}_\alpha) = D\delta(\psi). \tag{3.30}$$

Since the topological charge is a conserved quantity, it should be possible to derive a conserved current for $S(\mathbf{r})$. Indeed, the Jacobi determinant D satisfies the conservation equation given by

$$\partial_t D + \nabla \cdot \mathbf{J}_D = 0, \quad J_i^D = \epsilon_{ij} \operatorname{Im}\left(\partial_j \psi^* \partial_t \psi\right), \tag{3.31}$$

as can be verified by substitution. We can also verify that

$$D\partial_t \delta(\psi) + \mathbf{J}_D \cdot \nabla \delta(\psi) = 0, \tag{3.32}$$

by differentiating through the delta function and inserting for D and $\mathbf{J}_D$. This allows us to derive a conservation equation for $S(\mathbf{r})$,

$$\begin{aligned}
\partial_t S = \partial_t \left[D\delta(\psi)\right] &= \partial_t D\delta(\psi) + D\partial_t \delta(\psi) \\
&= -\nabla \cdot \mathbf{J}_D \delta(\psi) - \mathbf{J}_D \cdot \nabla \delta(\psi) = -\nabla \cdot \left[\mathbf{J}_D \delta(\psi)\right],
\end{aligned} \tag{3.33}$$

so the conserved current of S is $\mathbf{J}_S = \mathbf{J}_D \delta(\psi)$. If vortices move with speed $\mathbf{v}_\alpha$, this current should also equal

$$\mathbf{J}_S = \sum_\alpha s_\alpha \mathbf{v}_\alpha \delta(\mathbf{r} - \mathbf{r}_\alpha) = \sum_\alpha \frac{\mathbf{J}_D}{D} s_\alpha \delta(\mathbf{r} - \mathbf{r}_\alpha), \tag{3.34}$$

where we also used equation (3.30) to rewrite $\delta(\psi)$. Setting the coefficients multiplying the delta functions equal to each other, we find that the velocity of vortex α is given by

$$\mathbf{v}_\alpha = \frac{\mathbf{J}(\mathbf{r}_\alpha)}{D(\mathbf{r}_\alpha)}. \tag{3.35}$$

In paper I, we used this expression to numerically measure the speed of individual vortices, by computing an average weighted by $|D|$ within a region where the wavefunction is close to zero. This allowed for robust velocity statistics of quantized vortices.

We can use the expression in equation (3.35) to heuristically compute how a vortex responds to phase perturbations. Consider a vortex at the origin given by $\psi_0 = \Lambda r^{|s|} e^{is\theta}$ for small r, which satisfies $\partial_t \psi_0(\mathbf{r} = 0) = 0$ and is therefore at rest. A phase disturbance is added by setting $\psi = \psi_0 e^{i\phi(\mathbf{r})}$, resulting in $\partial_t \psi \neq 0$, and the goal is to compute $\mathbf{v} = \frac{\mathbf{J}_D}{D}$ of the transformed wavefunction. Inserting ψ into the SPGPE and using $\psi_0(\mathbf{r} = 0) = 0$, we find

$$\partial_t \psi = (1 + i\gamma)\nabla \psi_0 \cdot \nabla \phi e^{i\phi}, \quad J_i^D = \epsilon_{ij} \operatorname{Im} \left[\partial_j \psi_0^*(1 + i\gamma)\partial_k \psi_0 \partial_k \phi \right]. \quad (3.36)$$

The particular solution for ψ_0 satisfies $i\partial_k \psi_0 = \frac{s}{|s|}\epsilon_{kl}\partial_l \psi_0$, which transforms the current to

$$J_i^D = \epsilon_{ij} \left[\operatorname{Im} \left(\partial_j \psi_0^* \partial_k \psi \right) + \gamma \frac{s}{|s|}\epsilon_{kl} \operatorname{Im} \left(\partial_j \psi_0^* \partial_l \psi \right) \right] \partial_k \phi. \quad (3.37)$$

To relate this to the Jacobi determinant D, note that it is invariant under the deformation at the origin because ψ_0 vanishes,

$$D = \frac{1}{2i}\epsilon_{il} \left(\partial_i \psi_0^* - i\psi_0^* \partial_i \phi \right) \left(\partial_l \psi_0 + i\psi_0 \partial_l \phi \right) = \frac{1}{2i}\epsilon_{il}\partial_i \psi_0 \partial_l \psi_0. \quad (3.38)$$

Applying ϵ_{jk} to this expression we find

$$\epsilon_{jk}D = \frac{1}{2i}(\delta_{ij}\delta_{kl} - \delta_{ik}\delta_{jl})\partial_i \psi_0^* \partial_l \psi_0 = \operatorname{Im} \left(\partial_j \psi_0^* \partial_k \psi_0 \right), \quad (3.39)$$

which we recognize from the current, allowing us to derive an expression for the vortex velocity,

$$J_i^D = \epsilon_{ij} \left(\epsilon_{jk}D + \gamma \frac{s}{|s|}\epsilon_{kl}\epsilon_{jl}D \right) \partial_k \phi, \quad \mathbf{v} = \frac{\mathbf{J}_D}{D} = -\nabla \phi + \gamma \frac{s}{|s|}\nabla^\perp \phi, \quad (3.40)$$

where we used that $\epsilon_{ij}\epsilon_{ik} = \delta_{jk}$ and $\nabla^\perp$ is the rotated gradient with components $(\partial_y, -\partial_x)$. Thus, conservative dynamics move the vortex along the ambient velocity field (ignoring the singular velocity induced by the vortex itself), while dissipative dynamics move the vortex perpendicularly to this field. Note, however, that in this derivation we have ignored effects such as the deformation of

the vortex core as it moves. This effect turns out to be somewhat important for the dissipative part of the vortex motion, leading to logarithmic corrections to the simple law specified here [41]. For the purpose of phenomenological modeling, however, such corrections are generally ignored [45].

Now assume that the only sources of velocity are the vortices themselves. If the vortices are well-separated so that their cores do not overlap, we can assume that the wavefunction is given by the product of stationary solutions with circulations s_α,

$$\psi = \prod_\alpha \psi_0(\mathbf{r} - \mathbf{r}_\alpha; s_\alpha), \qquad (3.41)$$

hence the dimensionless velocity field is given by the superposition of the velocity due to each vortex, $\mathbf{v}(\mathbf{r}) = \sum_\alpha s_\alpha \nabla \theta(\mathbf{r} - \mathbf{r}_\alpha)$, where $\theta(\mathbf{r} - \mathbf{r}_\alpha)$ is the polar angle relative to $\mathbf{r}_\alpha$. Evaluating the gradient, we find

$$v_i(\mathbf{r}) = -\epsilon_{ij} \sum_\alpha s_\alpha \frac{r_j - r_j^\alpha}{|\mathbf{r} - \mathbf{r}_\alpha|^2}, \qquad (3.42)$$

so the vortices themselves move with velocity

$$\mathbf{v}_\alpha = -\sum_{\beta \neq \alpha} s_\beta \frac{(\mathbf{r}_\alpha - \mathbf{r}_\beta)^\perp}{|\mathbf{r}_\alpha - \mathbf{r}_\beta|^2} + \gamma \sum_{\beta \neq \alpha} \frac{s_\alpha s_\beta}{|s_\alpha|} \frac{\mathbf{r}_\alpha - \mathbf{r}_\beta}{|\mathbf{r}_\alpha - \mathbf{r}_\beta|^2}. \qquad (3.43)$$

Hence, if we ignore compressible effects such as the vortex core structure and acoustic interactions, the Gross–Pitaevskii equation is reduced to a dynamical system of vortices similar to the point vortex model introduced in chapter 2, but with an additional dissipative vortex drift due to thermal dissipation, which has the effect of repelling like-signed vortices and attracting opposite-signed vortices. Using a more symmetric form of the Hamiltonian equations (2.37) that does not distinguish the conjugate variables, this dissipation can be included in extra dissipative terms, giving

$$\dot{x}_\alpha = \frac{1}{2\pi s_\alpha} \frac{\partial H}{\partial y_\alpha} - \frac{\gamma}{2\pi |s_\alpha|} \frac{\partial H}{\partial x_\alpha},$$
$$\dot{y}_\alpha = -\frac{1}{2\pi s_\alpha} \frac{\partial H}{\partial x_\alpha} - \frac{\gamma}{2\pi |s_\alpha|} \frac{\partial H}{\partial y_\alpha}, \qquad (3.44)$$

from which we can verify that the effect of γ is to dissipate energy from the point

vortex Hamiltonian,

$$\partial_t H = \sum_\alpha \left(\frac{\partial H}{\partial x_\alpha} \dot{x}_\alpha + \frac{\partial H}{\partial y_\alpha} \dot{y}_\alpha \right)$$

$$= -\gamma \sum_\alpha \frac{1}{2\pi |s_\alpha|} \left(\frac{\partial H}{\partial x_\alpha} \frac{\partial H}{\partial x_\alpha} + \frac{\partial H}{\partial y_\alpha} \frac{\partial H}{\partial y_\alpha} \right) < 0. \qquad (3.45)$$

This derivation ignores the acoustic degrees of freedom of the BEC, which are certainly present. For example, even isolated vortices emit acoustic radiation depending on their velocity, and acoustic waves themselves exert drag on a vortex. Pismen [41] showed that a corotating vortex pair at distance $2a$ emits acoustic energy at a rate $8\pi c^3 \xi^4 a^{-6}$; thus the distance increases as $\dot{a} = 4c\xi^4 a^{-5}$ to conserve energy. This effect by itself is subdominant compared to the $\gamma c/a$ decay due to thermal dissipation as long as $a > 4\xi\gamma^{-1/4}$, hence we can expect significant acoustic effects for vortices that are closely spaced compared with this distance.

The largest deviation from point-vortex behavior occurs when the vortex cores overlap. This is energetically disfavored for same-signed vortices, however dissipation will cause opposite-signed vortices to attract each other until their cores overlap. Such an event leads to complicated behavior that is not completely understood. Topologically, it is permissible for the two vortices to annihilate, as the circulation integral around both is zero. For this to happen, the energy associated with the core structure must dissipate, either to acoustic radiation or through the thermal friction coefficient. Recent experiments have suggested that instead of rapid annihilation, vortex–antivortex pairs tend to bind together into a state dubbed *vortexonium* [46], which then finally annihilates upon the collision with a third vortex. This collision could conceivably have important effects on the third vortex. However, such three-body annihilation processes were found to be suppressed as the dissipation parameter was increased, suggesting that a simple two-body process is sufficient to account for vortex pair annihilation in the presence of dissipation. In paper III, we account for annihilation by simply removing vortex–antivortex pairs that get closer than a given threshold distance.

We have also neglected the effect of the confining potential $V(\mathbf{r})$ in this analysis. Generally, a confining potential will cause a vortex to precess around the center of the condensate [47]. In the limit of an infinite cylindrical well with radius R, the confining potential is equivalent to a hard-wall boundary condition at $r = R$, which requires enforcing a no-flux boundary condition on the velocity field of point vortices. Such a boundary condition can be satisfied by adding im-

41

age vortices of opposite charge located at $\mathbf{r}_\alpha^v = \frac{R^2}{r_\alpha^2}\mathbf{r}_\alpha$, as well as image vortices of the same charge located at the origin. The positions of these images are not subject to additional dynamical equations, but are fully determined by the position of the physical vortex, however they do modify the velocity field. The effect is to modify the point-vortex Hamiltonian to

$$H = -\pi \sum_{\alpha \neq \beta} s_\alpha s_\beta \ln |\mathbf{r}_\alpha - \mathbf{r}_\beta| + \pi \sum_{\alpha,\beta} s_\alpha s_\beta \ln(|\mathbf{r}_\alpha - \mathbf{r}_\beta^v| r_\beta). \qquad (3.46)$$

Note that the coordinate expression in the second sum is symmetric under the interchange $\mathbf{r}_\alpha \leftrightarrow \mathbf{r}_\beta$, which is useful for computing the Hamiltonian equations of motion from this Hamiltonian. Indeed, taking the square and using $|\mathbf{v} - \mathbf{w}|^2 = v^2 + w^2 - 2\mathbf{v} \cdot \mathbf{w}$, we find the symmetric expression

$$|\mathbf{r}_\alpha - \mathbf{r}_\beta^v|^2 r_\beta^2 = \left(r_\alpha^2 r_\beta^2 + R^4 - 2R^2 \mathbf{r}_\alpha \cdot \mathbf{r}_\beta\right). \qquad (3.47)$$

3.7 Energy cascades in 2D BECs

Given the various effects of the acoustic degrees of freedom described above, one might expect the nature of turbulent states to be different from the analysis presented in chapter 2. For example, the annihilation of vortices breaks the conservation of enstrophy, because the quantity $\int \omega^2 \mathrm{d}^2\mathbf{r} = \sum_\alpha (s_\alpha)^2$ equals the total number of vortices. Consequently, forward energy cascades have been observed numerically in systems where compressible effects are important [48]. On the other hand, if the typical inter-vortex distance is large compared to the coherence length ξ, the compressible effects might be subdominant to the vortex gas [49]. Indeed, an inverse energy cascade has been observed in numerical experiments where the energy is dominated by the vortex gas [50, 51]. An important feature of these systems is that an initial period of vortex dipole annihilation tends to remove oppositely charged vortices from the vicinity of a given vortex, leading to small clusters of like-signed vortices that protect any given vortex from annihilation, thus restoring the approximate conservation of enstrophy.

A common way to study the interplay between compressible and incompressible effects is to account for density variations by introducing the density-weighted velocity $\mathbf{w} = \sqrt{\rho}\mathbf{v}$. This field, unlike $\mathbf{v}$, can have a rotational component $\nabla \times \mathbf{w} = (\nabla\sqrt{\rho}) \times \mathbf{v}$ if ρ varies perpendicularly to $\mathbf{v}$, for example near vortex cores. Performing a Helmholtz decomposition of $\mathbf{w}$ into incompressible and irrotational

parts,

$$\mathbf{w} = \mathbf{w}_I + \mathbf{w}_C, \quad \nabla \cdot \mathbf{w}_I = 0, \quad \nabla \times \mathbf{w}_C = 0, \quad \mathbf{w}_I \cdot \mathbf{w}_C = 0, \qquad (3.48)$$

we find a decomposition of the kinetic energy density $T = \frac{1}{2}w^2 = \frac{1}{2}w_I^2 + \frac{1}{2}w_C^2$ where the incompressible part is associated with the far field of vortices and the compressible part is associated with acoustic excitations and vortex cores [48, 52]. Proceeding as in chapter 2, we can study the energy spectra of each part separately,

$$E_C(k) = \frac{1}{2} \int_{|\mathbf{k}|=k} |\tilde{\mathbf{w}}_C(\mathbf{k})|^2 \mathrm{d}^d\mathbf{k}, \quad E_I(k) = \frac{1}{2} \int_{|\mathbf{k}|=k} |\tilde{\mathbf{w}}_I(\mathbf{k})|^2 \mathrm{d}^d\mathbf{k}. \qquad (3.49)$$

Numasato et al. [48] found a $k^{-5/3}$ incompressible energy spectrum associated with a *positive* energy flux, in a system where the compressible energy was of the same order of magnitude as the incompressible. By contrast, the inverse cascade was observed in systems where the incompressible energy accounted for a higher fraction of the total energy [50]. In the latter case, the cascade was associated with a clustering of vortices as suggested by Novikov's work on the point vortex model (see chapter 2).

In order to investigate such clustering effects, Bradley et al. [40] computed the energy spectrum of quasistatic vortex configurations of the kind leading to the point vortex model of the previous section. Their result reproduces the Novikov energy spectrum with a large-k modification due to the core structure,

$$E_I(k) = \frac{2\pi\mu^2\xi^3}{g} F_\Lambda(k\xi) \sum_{\alpha,\beta} s_\alpha s_\beta J_0(kr_{\alpha\beta}), \qquad (3.50)$$

where $F_\Lambda(k\xi)$ characterizes the energy spectrum of a single vortex with $\rho = (\Lambda r)^2$ near the vortex core, given by

$$F_\Lambda(k\xi) = \Lambda^{-1} f(k\xi\Lambda^{-1}), \quad f(z) = \frac{z}{4} \left[I_1\left(\frac{z}{2}\right) K_0\left(\frac{z}{2}\right) - I_0\left(\frac{z}{2}\right) K_1\left(\frac{z}{2}\right) \right]^2. \tag{3.51}$$

The single-vortex energy spectrum has the asymptotic behavior $f(z) \sim z^{-1}$ for $z \ll 1$ and $f(z) \sim z^{-3}$ for $z \gg 1$, which gives rise to a k^{-3} tail in the energy spectrum for length scales short compared to the vortex core size, while the Novikov energy spectrum is recovered for scales longer than the core size. Thus, arguing as in chapter 2, one expects that the inverse energy cascade in 2D quantum turbulence is associated with scale-free clustering of like-signed vortices.

The above discussion shows that 2D quantum turbulence features a complex interplay between compressible and vortex degrees of freedom, but the right conditions should allow numerical and experimental investigation into the clustering behavior of vortices in the inverse energy cascade. Papers I–III of this work were concerned with such an investigation.

3.8   Paper I

Given that the inverse energy cascade in quantum turbulence is associated with a particular self-similar structure of like-signed vortex clusters, we wanted to simulate a statistical steady-state turbulent regime using the Gross–Pitaevskii equation in order to look for statistical signatures of these clusters [1]. Following ref. [50], we used a BEC confined in a harmonic trap with a Gaussian stirring obstacle moving at speed $0.5c \leq v_{\text{ext}} \leq 0.8c$, which had been found to optimize the creation of small vortex clusters, preventing annihilation. Solving the Gross–Pitaevskii equation with a weak damping parameter $\gamma = 0.009$, we obtained a driven steady state determined by the energy balance of equation (3.11), featuring a large number of vortices with a tendency for clustering.

While we found a weak $k^{-5/3}$ scaling regime in the incompressible energy spectrum at certain times, this scaling did not survive statistical averaging, which suggests that compressible effects were still important. However, by using an algorithm for identifying like-signed vortex clusters, we could synthesize how the energy spectrum would look if only these vortex clusters were present, resulting in a clearer signal. This indicates that self-similar vortex clusters were indeed present, but isolated vortices and dipoles break this self-similarity.

We also found an $f^{-5/3}$ frequency scaling in the power spectrum of the vortex number fluctuations associated with the energy cascade. A similar frequency scaling has been observed for the vortex line density in numerical and experimental studies of 3D quantum turbulence in superfluid helium [53–55], where it was attributed to the advection of isolated vortex lines by the turbulent velocity field of the normal fluid component [56]. Similarly, we attributed the frequency scaling in the vortex number fluctuations to the advection of isolated vortices by the turbulent velocity field due to self-similar vortex clusters. In support of this argument, we found that the number fluctuations were dominated by the fluctuations of isolated vortices, while clusters of like-signed vortices did not follow the same scaling law.

Looking for other statistical signatures of these clusters, we found hints of a $v^{-5/3}$ probability tail in the distribution of clustered vortex velocities. A simple scaling argument shows why such a scaling law might be explained by self-similar clusters. A pair correlation function $g(\mathbf{r}) \sim r^{-\alpha}$ corresponds to a probability of seeing another vortex at a distance r of $p_r(r) = 2\pi r g(\mathbf{r}) \sim r^{1-\alpha}$. If the vortex velocity is due to one such other vortex, a simple transformation of variables gives a vortex velocity distribution (using $v(r) \sim r^{-1}$)

$$
P_v(v) \sim P_r(r)\frac{\mathrm{d}r}{\mathrm{d}v} \sim r^{1-\alpha}\frac{\mathrm{d}(v^{-1})}{\mathrm{d}v} \sim v^{\alpha-1}v^{-2} = v^{\alpha-3}, \tag{3.52}
$$

hence the self-similar structure of $\alpha = 4/3$ gives rise to a $v^{-5/3}$ tail in the vortex velocity distribution.

3.9 Paper II

To better understand the $v^{-5/3}$ tail in the velocity distribution, we performed a more detailed study of vortex velocity fluctuations inside a self-similar cluster in paper II [2], taking all the $N + 1$ vortices of the cluster into account. The computation is given in detail in the paper, so this section only summarizes the results.

Fixing a particular vortex at the origin, we assumed that the other N vortices are distributed around the vortex as $\tau(\mathbf{r}) = \frac{n'_\alpha}{N}r^{-\alpha'-1}$, where $\alpha' = \alpha - 1$ characterizes the distribution of distances from the origin $T(r) \sim r^{-\alpha'}$ due to the 2D measure $2\pi r\mathrm{d}r$. The fractal density $n_{\alpha'}$ is determined by the normalization of the distribution between the lower cutoff $a \sim \xi$ due to vortex core interactions and the upper cutoff due to the cluster size R, and is given by

$$
n_{\alpha'} = \frac{N(1-\alpha')}{2\pi(R^{1-\alpha'} - a^{1-\alpha'})}. \tag{3.53}
$$

Note that, in the paper, we use α' as the primary exponent and name this α, unlike the convention in this thesis. The self-similar distribution $\alpha = 4/3$ associated with the inverse energy cascade corresponds to $\alpha' = 1/3$ for the distance from the origin. Taking all the vortex charges $s_\alpha = 1$ in dimensionless units, this distribution of vortex positions then determines the velocity distribution $W(\mathbf{V})$

45

by superposition of the velocities $\phi(\mathbf{r}_\alpha)$ induced by each vortex,

$$W(\mathbf{V}) = \int \left[\prod_{\alpha=1}^{N} d\mathbf{r}_\alpha \tau(\mathbf{r}_\alpha) \right] \delta \left(\mathbf{V} - \sum_{\alpha=1}^{N} \phi(\mathbf{r}_\alpha) \right). \tag{3.54}$$

By manipulating this integral in spectral space, taking the thermodynamic limit $N \to \infty, R \to \infty$ while keeping $n_{\alpha'}$ fixed, and series expanding in $1/V$ to find the high-velocity tail, we found the series representation

$$W(\mathbf{V}) = \sum_{n=1}^{\infty} P_n n_{\alpha'}^n V^{n(\alpha'-1)-2}, \tag{3.55}$$

with a Gaussian cutoff for velocities larger than $1/a$ due to the low-distance cutoff $a \sim \xi$. The dimensionless prefactor P_n is computed by contour integrals in the complex plane, giving the values $P_1 = 1$ and

$$P_2 = -4^{1-\alpha'} \tan \frac{\pi\alpha'}{2} B \left(1 - \frac{\alpha'}{2}, \frac{1}{2} \right)^2, \tag{3.56}$$

where $B(x, y)$ is the Beta function. At high velocities below the cutoff $1/a$, the $n = 1$ term dominates, so the distribution for the velocity norm $V = |\mathbf{V}|$ is given by

$$P(V) = 2\pi V W(\mathbf{V}) = 2\pi n_{\alpha'} V^{\alpha'-2} = 2\pi n_{\alpha-1} V^{\alpha-3}, \tag{3.57}$$

so a fractal cluster with $\alpha = 4/3$ ($\alpha' = 1/3$) is indeed associated with $V^{-5/3}$ tail in the vortex velocity distribution. However, this power-law scaling breaks down for velocities low enough that the $n = 2$ term becomes important, namely when

$$n_{\alpha'} V^{\alpha'-3} = |P_2| n_{\alpha'}^2 V^{2\alpha'-4} \quad \Leftrightarrow \quad V = (|P_2| n_{\alpha'})^{1/(1-\alpha')}, \tag{3.58}$$

hence the scaling range in the vortex velocity distribution becomes smaller with increasing density $n_{\alpha'}$ of vortices. This explains the limited scaling range we observed in paper I, due to the relatively tightly spaced vortices in the BEC compared to the core radius $\sim \xi$.

3.10 Paper III

Given that the signals of self-similar vortex clusters in paper I were limited by compressible effects and a small system size, we decided to eliminate compressible effects and allow for larger systems by moving from the GPE to a driven and dissipative point vortex model in paper III [3]. We saw above that the dissipation parameter γ in the SPGPE (3.13) leads to a dissipative vortex drift in the motion of vortices, which is readily accounted for by modifying the Hamiltonian equations of motion to equation (3.46).

To model the driving force due to the stirring obstacle, we noticed that the main effect of the obstacle on the vortex gas is to create vortex dipoles with a characteristic distance $\sim d_s$ between the two created vortices, at a given rate. We therefore injected random dipoles into the system at a given rate, with a distance d_s between the two vortices. As the number of vortices increases and interact with each other, it is inevitable that a vortex–antivortex pair comes into contact with each other, at which point they are expected to annihilate due to compressible effects. We therefore removed such pairs that came closer than a distance $d_a < d_s$ from the system. If these processes occur at equal rates, the energy of the system changes approximately by $\pi \ln \frac{d_s}{d_a} > 0$ with each event, so this effect drives energy into the system at a length scale on the order of d_a and d_s.

The result was a turbulent steady state where we measured a negative spectral energy flux, as well as an average energy spectrum which showed a $k^{-5/3}$ scaling if we removed isolated vortices from the analysis as in paper I. Due to the larger system size and longer simulation times, we also obtained enough vortex statistics to probe the self-similar structure of vortex clusters directly. While previous work has focused on isolated vortex clusters of a single circulation charge [31, 40], we found this picture to be insufficient for analyzing the spatial structure of vortices in our system, which featured a diverse set of clusters of different sizes coupled to each other, often polluted with a few vortices of the opposite charge. We therefore generalized Novikov's statistical analysis to account for both vortex charges.

Recall that the energy spectrum of a system of vortices located at $\mathbf{r}_\alpha$ with charge s_α is given by equation (2.40), namely

$$E(k) = \frac{\pi}{k} \left(N + \sum_{\alpha \neq \beta} s_\alpha s_\beta J_0(k r_{\alpha\beta}) \right), \tag{3.59}$$

where we assume that $|s_\alpha| = 1$. Taking the average of this quantity and allowing

the number N of vortices to fluctuate, we find a dependence on the *weighted pair correlation* function, defined as

$$\rho g_w(\mathbf{r}) = \frac{1}{\langle N \rangle} \left\langle \sum_{\alpha \neq \beta} s_\alpha s_\beta \delta(\mathbf{r} - \mathbf{r}_{\alpha\beta}) \right\rangle, \tag{3.60}$$

where $\rho = \frac{\langle N \rangle}{A}$ is the number density of vortices. Note the weighting by the vortex charges s_α, leading to a different correlation function than those considered previously. This gives rise to an average energy spectrum given by

$$\left\langle \frac{E(k)}{N} \right\rangle = \frac{\pi}{k} \left(1 + \int J_0(kr) \rho g_w(\mathbf{r}) \mathrm{d}^2\mathbf{r} \right). \tag{3.61}$$

The $k^{-5/3}$ energy scaling would thus be associated with an $r^{-4/3}$ scaling in the weighted pair correlation function. Indeed, by numerically counting the number vortices near a given vortex weighted by the vortex charges, we found that the weighted pair correlation function satisfied such a power law, again after removing isolated vortices from the analysis. This result suggests that analyzing the self-similar structure of a single vortex cluster is not sufficient for understanding turbulent states in 2D quantum turbulence, due to strong interactions between vortex clusters of different signs.

As a final note, we remark that the weighted pair correlation function can be interpreted as a measure of the vorticity covariance. Using that the point vortices are related to vorticity by

$$\omega(\mathbf{r}) = 2\pi \sum_\alpha s_\alpha \delta(\mathbf{r} - \mathbf{r}_\alpha), \tag{3.62}$$

the vorticity covariance at separation $\mathbf{r}$ is given by

$$\langle \omega(\mathbf{r}' + \mathbf{r}) \omega(\mathbf{r}') \rangle = 4\pi^2 \left\langle \sum_{\alpha,\beta} s_\alpha s_\beta \delta(\mathbf{r}' + \mathbf{r} - \mathbf{r}_\alpha) \delta(\mathbf{r}' - \mathbf{r}_\beta) \right\rangle. \tag{3.63}$$

Assuming statistical homogeneity, this value is unchanged if we integrate over the

origin point $\mathbf{r}'$ and divide by the area A, giving

$$\langle \omega(\mathbf{r}' + \mathbf{r})\omega(\mathbf{r}')\rangle = \frac{4\pi^2}{A} \left\langle \sum_{\alpha,\beta} s_\alpha s_\beta \int \delta(\mathbf{r}' - \mathbf{r}_\alpha)\delta(\mathbf{r} + \mathbf{r}' - \mathbf{r}_\beta)\mathrm{d}^2\mathbf{r}' \right\rangle$$
$$= \frac{4\pi^2}{A} \left\langle \sum_{\alpha,\beta} s_\alpha s_\beta \delta(\mathbf{r} - \mathbf{r}_{\alpha\beta}) \right\rangle. \tag{3.64}$$

We split this sum into a part where $\alpha = \beta$, and a part where $\alpha \neq \beta$. In the first case, the charges simplify to $s_\alpha^2 = 1$, while the distance between vortices is 0, giving

$$\frac{4\pi^2}{A} \left\langle \sum_\alpha \delta(\mathbf{r}) \right\rangle = 4\pi^2 \frac{\langle N\rangle}{A}\delta(\mathbf{r}) = 4\pi^2\rho\delta(\mathbf{r}). \tag{3.65}$$

For the case of different vortices $\alpha \neq \beta$, can compare with the definition of the weighted pair correlation function in equation (3.60), giving

$$\frac{4\pi^2}{A} \left\langle \sum_{\alpha\neq\beta} s_\alpha s_\beta \delta(\mathbf{r} - \mathbf{r}_{\alpha\beta}) \right\rangle = \frac{4\pi^2}{A} \langle N\rangle \rho g_w(\mathbf{r}) = 4\pi^2\rho^2 g_w(\mathbf{r}), \tag{3.66}$$

so the vorticity covariance can be expressed using the weighted pair correlation function as

$$\langle \omega(\mathbf{r}' + \mathbf{r})\omega(\mathbf{r}')\rangle = 4\pi^2\rho\delta(\mathbf{r}) + 4\pi^2\rho^2 g_w(\mathbf{r}). \tag{3.67}$$

This shows that the self-similar structure of vortex clusters is the point-vortex equivalent of a similar $r^{-4/3}$ scaling in the vorticity correlation. Such a scaling is a well-known corollary of the $k^{-5/3}$ energy spectrum in classical turbulence, as can be shown for example by comparing the resulting enstrophy spectrum $Z(k) = k^2 E(k) \sim k^{1/3}$ with its definition in terms of vorticity correlations. Our expression of the energy spectrum in terms of the weighted pair correlation function can therefore be seen as an adaptation of these scaling arguments to the case of singular vortices.

Chapter 4

Elasticity and Plasticity

Solids undergoing deformation have two main modes of responding to the applied forces. Weak loads lead to smooth, slowly varying deformations resisted quickly by forces internal to the solid. These forces return the solid back to the equilibrium configuration almost instantaneously when the load is removed. Such deformations are called *elastic*, and the equilibrium behavior of solids under elastic loads is the study of *elasticity*. As the applied load is increased, the internal forces of the solid stabilize at a critical value known as the *yield stress* (see figure 4.1, left panel). Loads exceeding the yield stress will overcome the internal forces of the solid, causing it to start deforming irreversibly. This is called *plastic yielding*, and the study of the yielding transition is known as *plasticity*.

Macroscopic samples tend to have a consistent yield strength only depending on the particular material, except for effects depending on previous loading conditions such as work-hardening and material fatigue. For samples on the scale of micrometers, however, the yield strength starts varying wildly from sample to sample. At the same time, the smooth yielding transition breaks into a series of small-scale yielding events in between periods where the elastic stress builds up (see figure 4.1, right panel). The yield stress also shows a marked correlation with sample size, such that smaller crystals tend to be stronger [9, 57]. This complicated yielding behavior of single crystals has been attributed to the strong interaction of dislocations, which are topological defects in the crystal lattice similar to the quantized vortices of BECs. Experimental characterization of the small-scale yielding events by measuring acoustic emission shows that they are characterized by self-similar scaling laws consistent with a picture where large coherent structures of dislocations pinned to each other and to the lattice, suddenly undergo avalanche-like depinning events [58]. This shows that plasticity, similarly to 2D
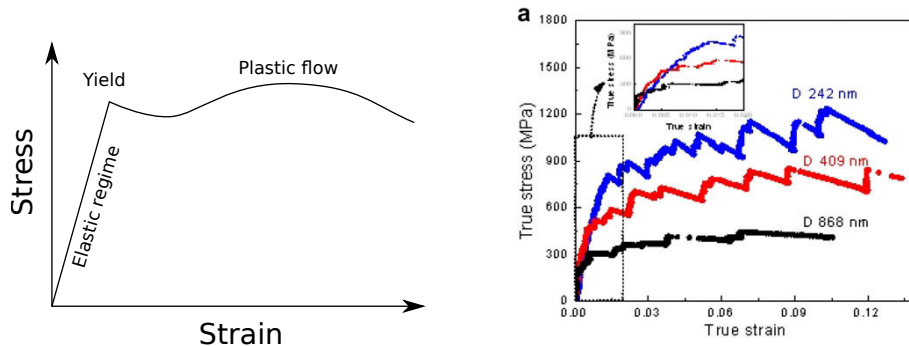
Figure 4.1: Left: conceptual illustration of plastic yielding in macroscopic solids. Stress and strain are linearly related for elastic deformations, until the yield point where plastic flow starts occurring. Right: Bursty yielding dynamics in a single-crystal nanopillar. Small-scale yielding events are interleaved with buildup of elastic stress. The characteristic yield stress increases with decreasing size. Reprinted from ref. [57], with permission from Elsevier.

turbulence, is characterized by the self-similar spatiotemporal statistics of singular structures moving through the medium.

Indeed, the most successful approach towards modeling the plastic yield transition is by considering the dislocations as the basic degrees of freedom [59], similar to how 2D quantum turbulence is reduced to a collection of point vortices. This approach, known as discrete dislocation dynamics (DDD), has gone a long way towards explaining the complex behavior of single-crystal plasticity [9]. However, it depends on phenomenological input such as how dislocations respond to applied forces, which are difficult to compute from first principles.

In the previous chapter, we saw how the *mesoscale* model of the Gross–Pitaevskii equation was very useful in deriving phenomenological higher-level models with controlled approximations. A similar mesoscopic model for crystal plasticity is known as the phase-field crystal (PFC). This model, however, fails to reproduce the strong separation of timescales between elastic and plastic motion common to all crystals. Our research therefore focused on gaining a sufficiently detailed understanding of elastic and plastic behavior in the PFC that we could propose a method of overcoming this issue.

We begin this chapter by introducing the basic concepts of linear elasticity and dislocation-mediated crystal plasticity, before introducing the PFC. We then summarize our contribution to understanding the elastic and plastic behavior of the PFC in paper IV, as well as our improved model in paper V.

4.1 Crystal lattices

A crystal structure is a periodic arrangement of atoms such that their equilibrium positions occur on a *crystal lattice*, $r_{\{n_i\}_i} = \sum_{i=1}^{d} n_i \mathbf{a}_i$, where $\{n_i\}$ are sets of d integers, d is the dimension of space, and $\mathbf{a}_i$ are the d primitive lattice vectors. For example, the 2D triangular lattice with lattice constant a can be constructed from the basis

$$\mathbf{a}_1 = \frac{a}{2}(\mathbf{e}_x + \sqrt{3}\mathbf{e}_y), \quad \mathbf{a}_2 = a\mathbf{e}_x, \tag{4.1}$$

where $\mathbf{e}_i$ is the unit vector in direction i. The spaces between the lattice points are called unit cells, and can be parameterized by $\sum_{i=1}^{d} t_i \mathbf{a}_i$ for $0 \leq t < 1$. The unit cells of the triangular lattice are equilateral triangles, hence the name of this lattice.

Crystal structures typically occur as symmetry-breaking phase transitions from a homogeneous and isotropic liquid phase, giving rise to the particular choice of crystal lattice. Given the periodicity of the crystal lattice, it is useful to study a given state in spectral space. Consider the density field $\rho(\mathbf{r})$, which is symmetric under the translation of a lattice vector. Any periodic function of $\mathbf{r}$ can be expanded as a Fourier series,

$$\rho(\mathbf{r}) = \sum_{\mathbf{g}} \rho_{\mathbf{g}} e^{i\mathbf{g}\cdot\mathbf{r}}, \tag{4.2}$$

where a real density field satisfies $\rho_{-\mathbf{g}} = \rho_{\mathbf{g}}^*$, and the sum runs over the vectors $\mathbf{g}$ such that the periodicity condition of the crystal lattice is satisfied. Translating the coordinate by a lattice vector gives the condition

$$\rho\left(\mathbf{r} + \sum_i n_i a_i\right) = \sum_{\mathbf{g}} \rho_{\mathbf{g}} e^{i\mathbf{g}\cdot\mathbf{r}} e^{i\sum_i n_i \mathbf{g}\cdot\mathbf{a}_i} = \sum_{\mathbf{g}} \rho_{\mathbf{g}} e^{i\mathbf{g}\cdot\mathbf{r}}, \tag{4.3}$$

which is satisfied whenever $\mathbf{g} \cdot \mathbf{a}_i$ is an integer multiple of 2π. The set of vectors satisfying this condition form another lattice called the *reciprocal lattice*, which has basis vectors $\mathbf{q}_i$ defined by

$$\mathbf{q}_i \cdot \mathbf{a}_j = 2\pi\delta_{ij}. \tag{4.4}$$

Indeed, writing $\mathbf{g} = \sum_j k_j \mathbf{q}_j$ for integral k_j, we find

$$\mathbf{g} \cdot \mathbf{a}_i = \sum_j k_j \mathbf{q}_j \cdot \mathbf{a}_i = 2\pi k_i, \tag{4.5}$$

which satisfies the periodicity requirement. For example, the basis vectors of a triangular lattice can be chosen as

$$\mathbf{q}_1 = q_T \mathbf{e}_y, \quad \mathbf{q}_2 = \frac{q_T}{2}\left(\sqrt{3}\mathbf{e}_x - \mathbf{e}_y\right), \quad q_T = \frac{4\pi}{\sqrt{3}a}. \tag{4.6}$$

4.2   Linear elasticity

It is crucial to have a good mathematical description of how solids respond to small reversible deformations before considering the larger, irreversible deformations of plasticity. The lowest-order such theory is called linear elasticity, and is essentially formulated as a linear response theory of how the free energy responds to small deformations.

Small deviations to a given crystal lattice are defined as an affine transformation $\mathbf{r} \mapsto \mathbf{r}' = \mathbf{r} + \mathbf{u}(\mathbf{r})$, where $\mathbf{u}(\mathbf{r})$ is the displacement vector, displacing the lattice from the equilibrium structure. Rigid body translations of the entire lattice clearly cost no energy, therefore the lowest-order possible term in free energy depending on displacement is quadratic in the *displacement gradients*,

$$\mathcal{F}_{\text{el}} = \frac{1}{2}\int d^d\mathbf{r}\, C_{ijkl}\partial_i u_j \partial_k u_l, \tag{4.7}$$

where the elastic tensor C_{ijkl} describes the stiffness of the material to various deformations. Since the integral is symmetric under the interchange $i, j \leftrightarrow k, l$, the elastic tensor must also have this symmetry. We can derive more conditions for the elastic tensor by requiring the elastic energy of a rigid rotation to be zero. Considering an infinitesimal rotation $\mathbf{r}' = \mathbf{r} + \boldsymbol{\omega} \times \mathbf{r}$, we see that the displacement vector has components $u_i = \epsilon_{ijk}\omega_j r_k$ which we can invert by taking the curl, giving

$$\epsilon_{ijk}\partial_j u_k = \epsilon_{ijk}\epsilon_{klr}\omega_l \delta_{jr} = \epsilon_{ijk}\epsilon_{ljk}\omega_l = 2\omega_i, \tag{4.8}$$

where we used that $\epsilon_{ijk}\epsilon_{ljk} = 2\delta_{il}$. For the elastic energy of this to be zero for all $\boldsymbol{\omega}$, it must be independent of $\epsilon_{ijk}\partial_j u_k$ for all $\mathbf{u}$; hence it must only depend on the

symmetric part of the displacement gradient, known as the infinitesimal strain:

$$e_{ij} = \frac{1}{2} \left(\partial_i u_j + \partial_j u_i \right).$$ (4.9)

This allows us to re-express the elastic energy as

$$\mathcal{F}_{\text{el}} = \frac{1}{2} \int \mathrm{d}^d \mathbf{r} \, C_{ijkl} e_{ij} e_{kl},$$ (4.10)

from which we can see that the elastic tensor must also be symmetric in $i \leftrightarrow j$ and $k \leftrightarrow l$.

The force density arising as a response to the deformation is then given by

$$f_j = -\frac{\delta \mathcal{F}_{\text{el}}}{\delta u_j} = \partial_i \left(C_{ijkl} \partial_k u_l \right) = \partial_i \sigma_{ij},$$ (4.11)

where the elastic stress is defined as $\sigma_{ij} = C_{ijkl} \partial_k u_l = C_{ijkl} e_{kl}$. This tensor can be interpreted as the Cauchy stress tensor denoting the force per area along the direction j, exerted on a surface element with normal vector n_i. By Gauss' law, such a definition leads to a force on a volume $\mathrm{d}V$ bounded by the surface Σ given by

$$F_j = \oint_\Sigma \sigma_{ij} n_i \mathrm{d}\Sigma = \int \partial_i \sigma_{ij} \mathrm{d}V,$$ (4.12)

in agreement with equation (4.11). By the symmetries of the elastic tensor, we see that the stress is also symmetric, $\sigma_{ij} = \sigma_{ji}$, which could also be derived by requiring the torque on infinitesimal volume elements to vanish [60].

In addition, the elastic tensor has to respect the symmetry of the underlying crystal lattice. For example, the elastic energy of the 2D triangular lattice must be invariant under rigid rotations of the displacement vector by $60°$. Similarly, if we look at large polycrystals consisting of many small crystal grains and only concern ourselves with scales larger than that of the individual grain, we can coarse-grain over the varying lattice orientations and obtain a continuously isotropic description. In that case the free energy must be invariant with respect to continuous rotations of the displacement vector. In the cases of isotropic elasticity and the 2D triangular lattice, it can be shown that the elastic tensor only depends on two independent parameters [8], namely

$$C_{ijkl} = \lambda \delta_{ij} \delta_{kl} + \mu \left(\delta_{ik} \delta_{jl} + \delta_{il} \delta_{jk} \right), \quad \sigma_{ij} = \lambda \delta_{ij} e_{kk} + 2\mu e_{ij},$$ (4.13)

where λ and μ are the Lamé parameters. In this case, the stress–strain relation can also be inverted easily. Noting first that the traces are related by $\sigma_{kk} = (d\lambda + 2\mu)e_{kk}$ where d is the number of dimensions, we find that

$$e_{ij} = \frac{1}{2\mu}\left(\sigma_{ij} - \lambda\delta_{ij}e_{kk}\right) = \frac{1}{2\mu}\left(\sigma_{ij} - \kappa\delta_{ij}\sigma_{kk}\right), \qquad (4.14)$$

where $\kappa = \frac{\lambda}{d\lambda+2\mu}$.

The formalism of linear elasticity allows us to compute the equilibrium response of a solid to applied forces. For example, assume a traction τ_i (that is, a force per area) is applied to the crystal boundary. The equilibrium deformation arising from these tractions is found by setting the internal forces to zero,

$$\partial_i\sigma_{ij} = C_{ijkl}\partial_i\left(\partial_k u_l + \partial_l u_k\right) = 0, \qquad (4.15)$$

with the boundary conditions that $n_j\sigma_{ij} = \tau_i$, and where n_j is the boundary normal vector. Solving the partial differential equation for $\mathbf{u}$, we find the crystal deformation response.

In two-dimensional simply connected spaces, there is a useful way of expressing all stress fields which solve the equilibrium condition $\partial_i\sigma_{ij} = 0$ through the *Airy stress function*. Given any smooth function χ, if we define a stress tensor by $\sigma_{ij} = \epsilon_{ik}\epsilon_{jl}\partial_{kl}\chi$, we have that

$$\partial_i\sigma_{ij} = \epsilon_{ik}\epsilon_{jl}\partial_{ikl}\chi = \epsilon_{jl}\partial_l\left(\epsilon_{ik}\partial_{ik}\right)\chi = 0, \qquad (4.16)$$

by commutation of partial derivatives. This shows that there is a continuous family of stress fields satisfying elastic equilibrium, so we need another condition to fully determine σ. Indeed, the symmetric tensor σ_{ij} has $\frac{d(d+1)}{2}$ independent quantities, so the d equations given by the equilibrium condition still leaves $\frac{d(d-1)}{2}$ independent quantities to be determined. In contrast, by expressing the stress as a function of the displacement gradient as in equation (4.15), the number of independent quantities goes back to d, giving a fully determined system of equations. The problem therefore occurs when moving from the displacement field $\mathbf{u}$ to the strain tensor e_{ij} as the free parameter, because this has more independent quantities. Indeed, not all symmetric tensors e_{ij} arise from gradients of vectors $\mathbf{u}$. It would therefore be useful to find a condition which assures that this is the case.

4.3 Compatibility of strain

A symmetric tensor e_{ij} which can be expressed as the symmetric gradient of a displacement field $\mathbf{u}$ is called a *compatible* strain tensor. We argued above that we need necessary and sufficient conditions for the compatibility of e_{ij}. A necessary condition is easily derived by noting that the curl of a gradient vanishes,

$$\epsilon_{ijk}\partial_j(\partial_k u_l) = 0. \tag{4.17}$$

Hence, by taking curls of the strain tensor, we see that

$$\epsilon_{ijk}\partial_j e_{kl} = \frac{1}{2}\left(\epsilon_{ijk}\partial_{jk}u_l + \epsilon_{ijk}\partial_{jl}u_k\right) = \frac{1}{2}\epsilon_{ijk}\partial_{jl}u_k,$$

$$\epsilon_{mnl}\epsilon_{ijk}\partial_{nj}e_{kl} = \frac{1}{2}\epsilon_{mnl}\epsilon_{ijk}\partial_j\partial_{nl}u_k = 0, \tag{4.18}$$

so a necessary condition for the strain to be compatible is that the double curl vanishes. St. Venant showed that this condition is also sufficient in a simply connected region [61], which proves that the condition of vanishing double curl,

$$\epsilon_{ijk}\epsilon_{mnl}\partial_{nj}e_{kl} = 0, \tag{4.19}$$

sufficiently determines the strain tensor along with the the condition of elastic equilibrium $\partial_i\sigma_{ij} = 0$.

For isotropic elasticity, this lets us derive an equation for determining the Airy function. The strain tensor determined by the Airy function is found by the inverse stress–strain relation,

$$e_{ij} = \frac{1}{2\mu}\left(\sigma_{ij} - \kappa\delta_{ij}\sigma_{kk}\right) = \frac{1}{2\mu}\left(\epsilon_{ik}\epsilon_{jl}\partial_{kl}\chi - \kappa\delta_{ij}\nabla^2\chi\right). \tag{4.20}$$

Hence, applying the 2D double curl, we find the equation

$$\epsilon_{ik}\epsilon_{jl}\partial_{ij}e_{kl} = \frac{1}{2\mu}\left(\epsilon_{ik}\epsilon_{jl}\epsilon_{km}\epsilon_{ln}\partial_{ijnm}\chi - \kappa\epsilon_{ik}\epsilon_{jk}\partial_{ij}\nabla^2\chi\right) = \frac{1-\kappa}{2\mu}\nabla^4\chi = 0, \tag{4.21}$$

where we used multiple instances of the identity $\epsilon_{ij}\epsilon_{ik} = \delta_{jk}$. This allows us to determine the stress function by solving a biharmonic equation, with second-order boundary conditions given by the tractions $n_i\epsilon_{ik}\epsilon_{jl}\partial_{kl}\chi = \tau_j$.

4.4 Dislocations

While linear elasticity describes smooth and reversible deformations of the lattice well, the irreversible, diffusive deformations of plasticity are associated with topological defects in the displacement field known as dislocations. The displacement field has a nontrivial topology because the reference lattice is symmetric under translations by a lattice vector, so the displacement of the crystal lattice by a lattice vector is equivalent to no displacement from an equivalent reference lattice. This means that the displacement vector is only defined up to equivalence between unit cells. Mathematically, we define displacements to be equivalent if they are translated by lattice vectors,

$$\mathbf{u} \sim \mathbf{u}' \Leftrightarrow \mathbf{u}' = \mathbf{u} + \sum_i n_i \mathbf{a}_i, \quad n_i \in \mathbb{Z}, \tag{4.22}$$

and consider displacements to take values in the quotient space $\mathbb{U} = \mathbb{R}^d / \sim$. It can be shown that this space is topologically equivalent to a d-torus, which has a fundamental group isomorphic to $\mathbb{Z}^d$. We should therefore expect the deformation field $\mathbf{u}$ to support topological defects of codimension two, with topological charges given by d integers.

Consider therefore a loop C in the crystal parameterized by $\mathbf{r}(t) : [0, 1] \to \mathbb{R}^d$ with $\mathbf{r}(0) = \mathbf{r}(1)$. This loop in real space induces a loop of displacement vectors $\mathbf{u}_c(t) = \mathbf{u}(\mathbf{r}(t)) : [0, 1] \to \mathbb{U}$, with the condition that the start and end points are equivalent, $\mathbf{u}_c(1) - \mathbf{u}_c(0) = \mathbf{b}$ for some lattice vector $\mathbf{b}$. In other words, taking the circulation of the displacement field around the loop, we find

$$\oint_C \mathrm{d}\mathbf{u} = \oint_C \nabla \mathbf{u} \cdot \mathrm{d}\mathbf{r} = \mathbf{u}_c(1) - \mathbf{u}_c(0) = \mathbf{b}. \tag{4.23}$$

This shows that the displacement field has topological defects known as dislocations, with the topological charge characterized by a lattice vector $\mathbf{b}$, known as the Burger's vector. The Burger's vector, as any lattice vector, can be expressed in terms of d integers as $\mathbf{b} = \sum_i n_i \mathbf{a}_i, n_i \in \mathbb{Z}$, and since the lattice vectors are linearly independent, addition of Burger's vectors is isomorphic to addition of the integers n_i. This shows that the dislocation charge $\mathbf{b}$ is isomorphic to the fundamental group $\mathbb{Z}^d$ of the d-torus, as expected.

In 3D, dislocations form lines permeating the crystal lattice. Of special interest is the relation between the line tangent vector $\mathbf{t}$ and the Burger's vector $\mathbf{b}$. If the Burger's vector is perpendicular to the line tangent, the dislocation can be
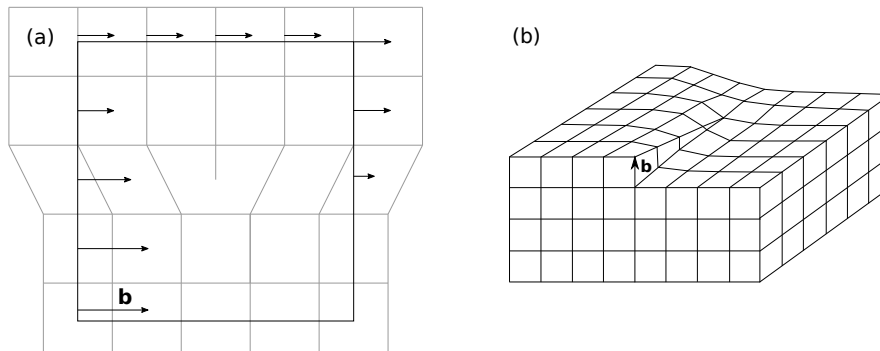
Figure 4.2: (a): Illustration of edge dislocation in the plane perpendicular to the dislocation line in a square lattice (gray lines). Following a loop (in this case a square) around the dislocation, we measure the lattice deformation by the displacement of the center of each unit cell. The deformation increases gradually, finally resolving to the Burger's vector **b** when we come back to the starting point. This is associated with a vertical crystal plane terminating at the position of the dislocation. (b): A screw dislocation in three dimensions, showing vertical displacement by the Burger's vector **b** around a horizontal loop.

visualized in the plane perpendicular to **t**. An example is given in figure 4.2, where we see the mismatch by **b** at the beginning and end of a square loop, as well as a crystal plane terminating at the dislocation.

In 2D, we can think of the point-like dislocation as the projection of a dislocation line going straight through the plane along the z axis. Thus, since the Burger's vector must lie in the plane, **b** is always perpendicular to **t**, so the edge dislocation is the only possible kind of dislocation in 2D. In 3D, however, we can have that **b** is parallel to **t**. This kind of dislocation is known as a screw dislocation, and is an essentially three-dimensional object, which is illustrated in figure 4.2 b. As we go around the loop, the crystal lattice is displaced in the direction perpendicular to the plane of the loop, causing a screw-like deformation of the lattice. As a third possibility, the Burger's vector can have components both along **t** and perpendicular to **t**, creating a *mixed* dislocation with features of both kinds. Indeed, as dislocation lines tend to curve around the crystal, these mixed dislocations will be common occurrences in three dimensions. Here, however, we focus on the plasticity of 2D systems, so we will not go further into the properties of such dislocations.

4.5 Plastic strain

We saw above that the displacement vector should really be thought of as an element of the space $\mathbb{U}$ which is a quotient space of the physical vector space $\mathbb{R}^d$. However, for physical interpretation it is still useful to think of the displacement vector as a physical vector in $\mathbb{R}^d$. In that case the displacement field will in general be multivalued, in a manner similar to the case of multivalued functions in complex analysis. We can recover a single-valued displacement field by adding the equivalent of a branch cut to the crystal, at the cost of a jump discontinuity across the branch cut. This branch cut takes the form of a surface Σ, called a slip plane, which terminates at the dislocation line and is tangent to the Burger's vector, such that the deformation field jumps by $\mathbf{b}$ as we cross the slip plane. For example, the slip plane is drawn as a dashed line in figure 4.3 a, with $\mathbf{u}^+$ above the line and $\mathbf{u}^-$ below the line, and $\mathbf{b} = \mathbf{u}^+ - \mathbf{u}^-$. The jump discontinuity is associated with a delta function peak in the strain given by [62]

$$e_{ij}^P = \frac{1}{2}(n_i b_j + n_j b_i)\delta(\zeta), \tag{4.24}$$

where $\mathbf{n}$ is the normal vector to the plane and ζ is the perpendicular distance from the plane. This discontinuity is however invisible to the microscopic physics of the crystal, as the slip plane is chosen arbitrarily. The stress can therefore only depend on the elastic part of the strain,

$$\sigma_{ij} = C_{ijkl}e_{kl}^{\text{el}} = C_{ijkl}(e_{kl} - e_{kl}^P). \tag{4.25}$$

Still, the plastic strain has a physical interpretation as an irreversible plastic deformation due to the lattice reorganization inherent in the creation of the dislocation. While the value of this strain carries the ambiguity of the choice of slip plane, changes in plastic strain under the motion of dislocations are not ambiguous. Consider moving an element $\mathrm{d}\mathbf{l}$ of a dislocation line by a small amount $\delta\mathbf{r}$. This causes the slip plane to grow or shrink by an amount $\delta\boldsymbol{\Sigma} = \mathbf{n}\delta\Sigma = \mathrm{d}\mathbf{l} \times \delta\mathbf{r}$, leading to a change in the plastic strain (see figure 4.3). A detailed study of the geometry of the problem leads to the expression [62]

$$\delta e_{ij}^P = \frac{1}{2}\left(b_i \epsilon_{jlm} + b_j \epsilon_{ilm}\right) t_m \delta(\xi)\delta x_l, \tag{4.26}$$
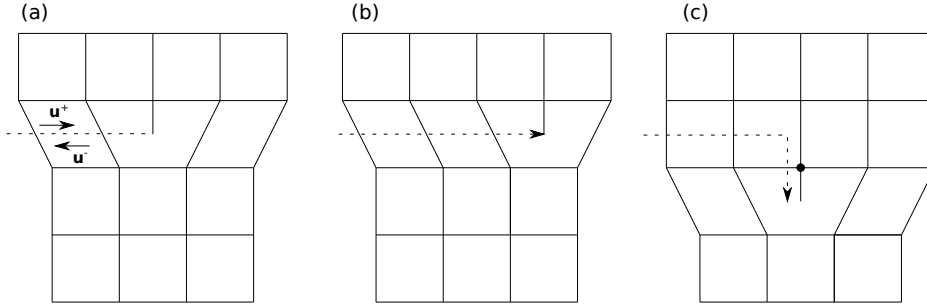
Figure 4.3: Illustration of dislocation motion in a square lattice. (a): The initial dislocation, with the slip plane indicated by the dashed line, and plastic slips $\mathbf{u}^+$ and $\mathbf{u}^-$ indicated by arrows. (b): Crystal lattice after the dislocation has moved along the slip plane, in the glide direction, accomplished purely through the re-organization of particle bonds. The increase in the slip plane is indicated by the arrow. (c): Crystal lattice after the dislocation has moved in the climb direction, normal to the slip plane. The new slip plane now has a component normal to the Burger's vector. A local increase in volume due to the addition of a lattice site (circle) is evident.

where $\mathbf{t}$ is the tangent vector to the dislocation line and ξ is the radius vector taken from the dislocation line. This shows that the change in plastic strain is independent of the choice of slip plane, only depending on quantities local to the dislocation.

If $\delta\mathbf{r}$ is parallel to $\mathbf{b}$, the new part $\delta\Sigma$ of the slip plane has a normal vector perpendicular to $\mathbf{b}$, hence the plane is tangent to $\mathbf{b}$. This type of motion is known as *glide*, and can be accomplished by a simple reorganization of the lattice (see figure 4.3). On the other hand, if $\delta\mathbf{r}$ is perpendicular to $\mathbf{b}$, known as *climb* motion, then the new part of the slip plane has normal vector along the slip direction $\mathbf{b}$. This leads to the appearance of a small void of size $\mathbf{b} \cdot \delta\Sigma$, which must be filled with material. Indeed, the plastic strain of equation (4.26) has a trace given by

$$\delta e_{ii}^P = \delta\mathbf{x} \cdot (\mathbf{t} \times \mathbf{b})\delta(\xi), \tag{4.27}$$

which is nonzero if $\delta\mathbf{x}$ has a component perpendicular to $\mathbf{t}$ and $\mathbf{b}$, that is, if the motion has a climb component. We see in figure 4.3 that climb motion is associated with adding or removing a lattice site from the crystal plane terminating at the dislocation in the square lattice. Climb motion is therefore coupled to mass transport processes such as vacancy diffusion, while glide motion can occur independently of mass transport. This is an important difference between the two

types of motion.

Differentiating the change in plastic strain with time, we can see that a moving dislocation is associated with a strain rate given by

$$\dot{e}_{ij}^{P} = \frac{1}{2} \left(b_i \epsilon_{jlm} + b_j \epsilon_{ilm} \right) t_m \delta(\xi) v_l, \tag{4.28}$$

where v_l is the velocity of the dislocation line element $\mathrm{d}\mathbf{l}$. Thus, if the crystal is continuously sheared with a steady-state differential strain rate $\dot{\gamma}$, one can assume that the strain rate is linked to the steady-state motion of straight dislocation lines in the appropriate direction by the Orowan relation [9]

$$\langle \dot{\gamma} \rangle = \langle \rho b v \rangle, \tag{4.29}$$

where ρ is the density of the moving dislocations and v is their speed. This general relation was proposed in very early experiments by Orowan and Becker. However, due to the strong interaction between dislocations and the crystal lattice, plastic motion tends to be more complex than this simple picture.

This is because dislocations interact with each other through the elastic stress field. By considering the work that the elastic field performs in displacing an element $\mathrm{d}\mathbf{l}$ by $\delta \mathbf{x}$, Peach and Koehler [63] derived the Peach–Koehler force,

$$F_i = \epsilon_{ijk} t_j \sigma_{kl} b_l, \tag{4.30}$$

although it was later shown that, because dislocation climb increases the volume locally, the stress must be replaced by the deviatoric stress $\sigma'_{ij} = \sigma_{ij} - \frac{1}{d} \delta_{ij} \sigma_{kk}$ [62].

4.6 Dislocation stresses

In addition to the plastic strain of equation (4.24), dislocations are also sources of elastic stresses and strains. This is because the elastic deformation $\mathbf{u}$ must contain a singularity at the position of the dislocation in order to satisfy the constraint of $\oint \mathrm{d}\mathbf{u} = \mathbf{b}$, requiring the particular solution of $\partial_i \sigma_{ij}$ to diverge at the dislocation position. Note that this singularity is physical, in contrast to the jump discontinuity in the plastic strain e_{ij}^{P}, which is due to a branch cut. For a point defect in 2D or a straight dislocation line in 3D, this singularity can be inserted by decomposing the displacement field into singular and nonsingular parts, $\mathbf{u} = \frac{1}{2\pi} \mathbf{b}\theta + \delta \mathbf{u}$, where

θ is the azimuthal angle relative to the dislocation and $\delta\mathbf{u}$ is smooth. $\delta\mathbf{u}$ is then determined by inserting the decomposition into the elastic equilibrium equation (4.15). For a single dislocation at the origin of an isotropic material with Burger's vector $\mathbf{b} = b\mathbf{e}_x$ along the x direction, one finds [8]

$$
\begin{aligned}
u_x &= \frac{b}{2\pi}\left(\theta + \frac{1}{2}\frac{\lambda+\mu}{\lambda+2\mu}\sin 2\theta\right), \\
u_y &= \frac{b}{2\pi}\left(\frac{\mu}{\lambda+2\mu}\ln r + \frac{1}{2}\frac{\lambda+\mu}{\lambda+2\mu}\cos 2\theta\right),
\end{aligned}
\tag{4.31}
$$

which gives rise to divergence-free stresses given by

$$
\begin{aligned}
\sigma_{xx} &= -D\frac{\sin\theta(2+\cos 2\theta)}{r}, \quad \sigma_{yy} = D\frac{\sin\theta\cos 2\theta}{r}, \\
\sigma_{xy} &= \sigma_{yx} = D\frac{\cos\theta\cos 2\theta}{r}, \quad D = \frac{b}{2\pi}\frac{2\mu(\lambda+\mu)}{\lambda+2\mu}.
\end{aligned}
\tag{4.32}
$$

This means, for example, that two dislocations in the plane with Burger's vectors $\pm b\mathbf{e}_x$, separated along x by a distance r, exert attractive forces on each other given by

$$
F_i = \epsilon_{ij}\sigma_{jk}b_k, \quad F_x = \sigma_{yx}b_x = \pm\frac{b^2}{2\pi}\frac{2\mu(\lambda+\mu)}{\lambda+2\mu}\frac{1}{r}, \quad F_y = -\sigma_{xx}b_x = 0, \tag{4.33}
$$

with the sign of F_x depending on which dislocation we are looking at, determining the sign of $\cos\theta$.

As an alternative to solving for the displacements, one can determine the stress directly by noting that the Burger's loop of equation (4.23) causes the strain tensor to be incompatible at the dislocation position. In two dimensions, one finds [8]

$$
\epsilon_{ik}\epsilon_{jl}\partial_{kl}e_{ij} = \epsilon_{ij}\partial_i B_j, \quad \text{where} \quad \mathbf{B}(\mathbf{r}) = \sum_\alpha \mathbf{b}_\alpha\delta(\mathbf{r}-\mathbf{r}_\alpha), \tag{4.34}
$$

which along with the equilibrium condition $\partial_i\sigma_{ij}$ determines the stress. Using this in equation (4.21) for the Airy stress function, we find

$$
\frac{1-\kappa}{2\mu}\nabla^4\chi = \epsilon_{ij}\partial_i B_j, \tag{4.35}
$$

showing explicitly how dislocations are singular sources for the elastic stress, similar to how point vortices serve as singular sources for the stream function in the

point vortex model (see chapter 2). This stress field will then act on other dislocations through the Peach–Koehler force. It remains, however, to determine how dislocations respond to such forces if we want to obtain a closed dynamical system similar to the point vortex model. One possibility is a simple over-damped model where the dislocation speed is proportional to the Peach–Koehler force, but with different mobilities in the glide and climb directions to account for the temperature-dependent coupling between climb motion and diffusive mass transport. However, in reality, the crystal lattice itself also exerts forces on the dislocation, known as Peierls stress barriers [62].

Ideally, one could study these processes from a mesoscale model of the crystal lattice, similar to how we studied vortex motion under controlled approximations in chapter 3. Here, however, a-priori modeling is more limited. The most obvious approach is to explicitly solve the equations of motion for each atom in the crystal structure, using appropriate two-body potentials to model the interaction between atoms. This approach is known as *molecular dynamics* (MD) and is very successful in modeling fast processes in crystals such as shock waves and lattice vibrations [64]. Dislocation motion, on the other hand, is a slow process coupled to the large-scale motion of the entire lattice (e.g. by Orowan's relation), and it is hard to access these slower timescales in MD, although some progress has been made using large, massively parallel computations [65]. It would therefore be useful to have a mesoscale model that resolves the crystal lattice to model lattice effects on dislocation motion, but ignores the fast timescales of lattice vibration in order to more easily access the long timescales of plasticity. The leading contender for such a model is the phase-field crystal, which we discuss next.

4.7 The phase-field crystal

The phase-field crystal was originally proposed as an extension of phase-field methods for tracking the interface between two coexisting phases in a first-order phase transition, to tracking the growth of the crystal phase in an isotropic liquid [66, 67]. For this to be feasible, the phase field must satisfy the same symmetry as the crystal lattice of the solid phase. As in other phase-field methods, the starting point is a Ginzburg–Landau type of free energy density containing a nonlocal term $g(\psi, \nabla^2 \psi)$,

$$\mathcal{F} = \int f(\psi, \nabla^2 \psi) = \mathrm{d}^2 \mathbf{r} \int \mathrm{d}^2 \mathbf{r} \left[\frac{r}{2} \psi^2 + \frac{1}{4} \psi^4 + g(\psi, \nabla^2 \psi) \right], \qquad (4.36)$$

where the phase field ψ is typically interpreted as a linear function of the atomic density, and the parameter r, known as the *quench depth*, represents the deviation of the temperature from the critical point. The nonlocal term $g(\psi, \nabla^2\psi)$ is chosen to be consistent with the symmetry of a given lattice, which for the triangular lattice leads to a gradient-expanded form given by $g(\psi, \nabla^2\psi) = \frac{1}{2}[(1+\nabla^2)\psi]^2$.

The equilibrium behavior of this system is given by minimizing the free energy at a fixed number of atoms $N = \int \psi \mathrm{d}^2\mathbf{r}$. This constraint is enforced by the method of Lagrange multipliers, which leads to the variational equation

$$\frac{\delta(\mathcal{F} - \mu_c N)}{\delta\psi} = \frac{\delta\mathcal{F}}{\delta\psi} - \mu_c = 0 \quad \Leftrightarrow \quad (1+\nabla^2)^2\psi + r\psi + \psi^3 = \mu_c. \quad (4.37)$$

The constant μ_c, interpreted as the chemical potential, is then chosen so that the solution of equation (4.37) has the required value for N.

Being a fourth-order nonlinear partial differential equation, this equation is difficult to analyze analytically without approximation. However, Elder and Grant [66] argued from general principles that the free energy should favor three kinds of solutions: constant solutions $\psi = \psi_0$, undulating stripes with a given wavenumber, and a solution with the symmetry of a triangular lattice. Such solutions can be expanded in the reciprocal lattice as in equation (4.2),

$$\psi = \sum_{\mathbf{g}} A_{\mathbf{g}} e^{i\mathbf{g}\cdot\mathbf{r}}, \quad (4.38)$$

where the sum runs over vectors in the reciprocal lattice consistent with the given symmetry. For stripes, this means that $\mathbf{g} = n\mathbf{q}_S$ for integral n and $\mathbf{q}_S$ the fundamental wave vector of the stripes, while for the triangular lattice, we use the reciprocal lattice basis vectors $\mathbf{q}_1, \mathbf{q}_2$ of equation (4.6). The operator $(1+\nabla^2)$ acting on one of these terms gives

$$(1+\nabla^2)\left(A_{\mathbf{g}} e^{i\mathbf{g}\cdot\mathbf{r}}\right) = (1-g^2)A_{\mathbf{g}} e^{i\mathbf{g}\cdot\mathbf{r}}, \quad (4.39)$$

hence we expect wave vectors of length $|\mathbf{g}| \approx 1$ to be energetically favored in this expansion, as well as the necessary $\mathbf{g} = 0$ term from the conservation of mass. This suggests that we should take $q_S \approx 1$ and $q_T \approx 1$, and the dominating terms in the amplitude expansion will be those corresponding to reciprocal lattice vectors of length q_T, namely $\pm\mathbf{q}_1, \pm\mathbf{q}_2$ and $\pm\mathbf{q}_3$ with $\mathbf{q}_3 = -\mathbf{q}_1 - \mathbf{q}_2$. We also expect the amplitudes of these vectors to be equal because of rotational symmetry. The

resulting ansatz is known as the one-mode approximation, and is given by

$$\psi_S = \psi_0 + A_S e^{i\mathbf{q}_S \cdot \mathbf{r}} + c.c., \quad \psi_T = \psi_0 + A_T \sum_{n=1}^{3} e^{i\mathbf{q}_n \cdot \mathbf{r}} + c.c. \qquad (4.40)$$

Inserting these ansatzes into the free energy and minimizing with respect to q_S, A_S and q_T, A_T, one finds $q_S = q_T = 1$ as expected, as well as equilibrium values for the amplitudes given by [66]

$$A_S = \sqrt{-\frac{r}{3} - \psi_0^2}, \quad A_T = \frac{1}{5}\left(|\psi_0| + \frac{1}{3}\sqrt{-15r - 36\psi_0^2}\right), \qquad (4.41)$$

which differs from the stripe value A and the triangular value A_t given in ref. [66] by numerical factors because of the different representation they use for the expansion. Requiring the amplitudes to be real and positive, we find that the stripe phase is only stable for $r < -3\psi_0^2$, and the triangular phase is only stable for $r < -\frac{12}{5}\psi_0^2$. More accurate stability bounds can be found by computing the free energy density of these equilibrium states, and compare them against each other and against the energy of the uniform state $\psi = \psi_0$. Since these are first-order symmetry-breaking phase transitions, one must also allow for coexistence between phases by performing a Maxwell construction. The resulting phase diagram is reprinted in figure 4.4.

Given that the triangular ground state satisfies the same symmetry as a triangular lattice, Elder and Grant [66] expected the equilibrium behavior of this state to satisfy the same linear elastic behavior as 2D triangular crystals. This means that a deformation $\mathbf{r}' = \mathbf{r} + \mathbf{u}(\mathbf{r})$ of the lattice results in a change in free energy which follows the linear stress–strain relation $\sigma_{ij} = C_{ijkl}\partial_k u_l$, with C_{ijkl} consistent with the symmetries of the lattice. The authors proved this by inserting the ground state ansatz (4.40) into the free energy integrated over a unit cell while deforming the coordinate system by bulk, shear and deviatoric deformations. Expanding the resulting free energy in the magnitude of these deformations and comparing the result to a similar expansion of the elastic energy (4.7), they found global elastic constants for the equilibrium crystalline phase consistent with the symmetry of the triangular lattice. Below, we will derive the same elastic constants via an expression for the stress tensor given *any* out of equilibrium state ψ.
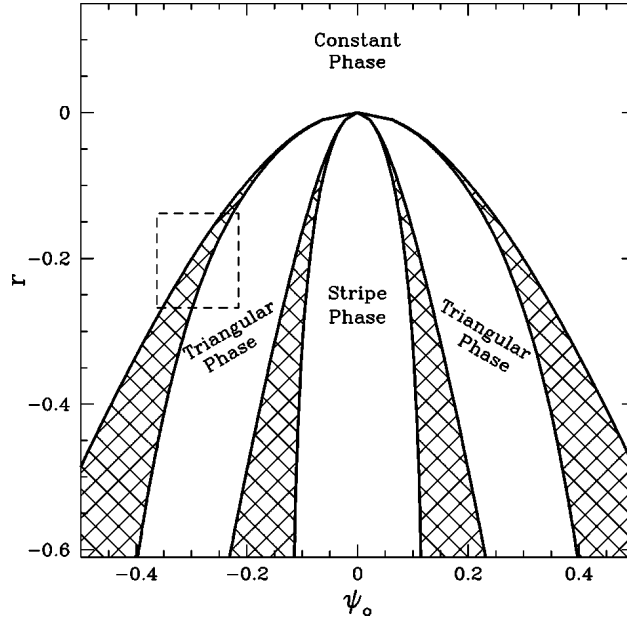
66

Figure 4.4: Phase diagram for the phase-field crystal in terms of the quench depth r and the conserved mean density ψ_0. Reprinted figure with permission from [66]. Copyright 2004 by the American Physical Society.

4.7.1 Nonequilibrium dynamics

While the free energy of equation (4.36) fully determines the equilibrium behavior of the phase field ψ, additional assumptions are needed to determine how states dynamically approach equilibrium. Because the phase field ψ is conserved, its dynamics must satisfy a conservation equation

$$\partial_t \psi + \nabla \cdot \mathbf{J} = 0, \tag{4.42}$$

however the behavior of $\mathbf{J}$ can be chosen arbitrarily. The most common assumption is that the system relaxes towards equilibrium in a purely dissipative way. We saw above that the free energy is minimized when the variation $\frac{\delta \mathcal{F}}{\delta \psi}$ is uniform, so we choose $\mathbf{J}$ to go in a direction which smooths out nonuniformities in this variation, $\mathbf{J} = -D\nabla \frac{\delta \mathcal{F}}{\delta \psi}$. Applying the divergence to this current, using the conservation equation, and rescaling the time coordinate with the diffusion constant D, we find

$$\partial_t \psi = \nabla^2 \frac{\delta \mathcal{F}}{\delta \psi} = \nabla^2 \left[(1 + \nabla^2)^2 \psi + r\psi + \psi^3 \right]. \tag{4.43}$$

This is the dynamical equation suggested originally in ref. [66, 67]. A similar dynamical equation has been derived from the classical density functional theory of a system of colloidal particles by a gradient expansion of the direct correlation function, given by [68, 69]

$$\partial_t \psi = \nabla \cdot \left(\psi \nabla \frac{\delta \mathcal{F}}{\delta \psi} \right),$$ (4.44)

which corresponds to a current equation given by $\mathbf{J} = -\psi \nabla \frac{\delta \mathcal{F}}{\delta \psi}$ due to the mobility of colloids depending on the colloidal density. This shows that the PFC corresponds to treating the mobility as constant, known as the constant mobility approximation. Such an approximation is not entirely controlled, but has the advantage of changing a fully nonlinear equation into one where the nonlinearity is contained in only one term. This has advantages for numerical work, as we will see in chapter 5.

In practice, we are only interested in states which are only slightly out of equilibrium, such as crystalline states that have been elastically and plastically deformed, or that are in coexistence with a surrounding liquid. We saw above that the amplitude expansion is useful for studying properties of equilibrium states, so it is natural to attempt to generalize this expansion to also capture deformed crystals. Given a deformation of the crystal by $\mathbf{r}' = \mathbf{r} + \mathbf{u}(\mathbf{r})$, we see that the opposite deformation $\mathbf{r} = \mathbf{r}' - \mathbf{u}$ will recover the reference lattice. Hence, the deformed crystal can be represented by

$$= \psi_0 + \sum_{\mathbf{g}>0} A_{\mathbf{g}} e^{i\mathbf{g} \cdot (\mathbf{r}-\mathbf{u})} = \psi_0 + \sum_{\mathbf{g}} \left(A_{\mathbf{g}} e^{-i\mathbf{g} \cdot \mathbf{u}} \right) e^{i\mathbf{g} \cdot \mathbf{r}},$$ (4.45)

which indicates that we could represent a more general state by allowing the complex phase of the amplitudes to vary slowly. Similarly, a liquid–solid boundary could be represented by the amplitudes going to zero across the boundary. A general state ψ which is slightly out of equilibrium could therefore be represented in the one-mode approximation by allowing the amplitudes to vary slowly in magnitude as well as phase,

$$\psi(\mathbf{r}) = \psi_0(\mathbf{r}) + \sum_n A_n(\mathbf{r}) e^{i\mathbf{q}_n \cdot \mathbf{r}} + c.c.,$$ (4.46)

where $A_n = A_{\mathbf{q}_n}$ is the amplitude corresponding to the oscillation along $\mathbf{q}_n$. Given that slowly varying amplitudes require less grid points to be represented

accurately, it would be preferable to consider the amplitudes as dynamical variables rather than the phase field ψ, which oscillates on the scale of the lattice. Assuming a constant mean density ψ_0, Goldenfeld et al. [70, 71] derived dynamical equations for the three independent amplitudes A_n using a renormalization group approach valid at $|r| \ll 1$, given by

$$\partial_t A_n = (\mathcal{L}_n - 1) \left[\mathcal{L}_n^2 A_n + (r + 3\psi_0^2)A_n \right]$$
$$- 6\psi_0 \prod_{m=1,m\neq n}^{3} A_m^* - 3A_n \left(2 \sum_{m=1}^{3} |A_m|^2 - |A_n|^2 \right), \qquad (4.47)$$

where $\mathcal{L}_n = \nabla^2 + 2i\mathbf{q}_n \cdot \nabla$. A more rigorous derivation using multiple scale theory leads to a similar equation where the $\mathcal{L}_n - 1$ operator is applied to all terms rather than just the first one [71, 72], reflecting the outer Laplacian operator in the original equation for ψ. In any case, Yeon et al. [72] argued that this outer operator can be approximated to $\mathcal{L}_n - 1 \approx -1$, which as an added benefit makes the equation less numerically stiff. Under a similar approximation they also found an appropriate equation for variations in the mean density ψ_0, which (ignoring their additional ψ^3 term in the free energy) is given by

$$\partial_t \psi_0 = \nabla^2 \left[(1+r)\psi_0 + \psi_0^3 + 6\psi_0 \sum_{n=1}^{3} |A_n|^2 + 6 \left(\prod_{n=1}^{3} A_n + \prod_{n=1}^{3} A_n^* \right) \right],$$
$$\partial_t A_n = - \left[\mathcal{L}_n^2 A_n + (r + 3\psi_0^2)A_n \right]$$
$$- 6\psi_0 \prod_{m=1,m\neq n}^{3} A_m^* - 3A_n \left(2 \sum_{m=1}^{3} |A_m|^2 - |A_n|^2 \right). \qquad (4.48)$$

The assumption of overdamped dynamics has the important consequence that all dynamical evolution is purely diffusive. Indeed, performing a linear stability analysis around the one-mode approximation for the equilibrium state, Elder and Grant found that local disturbances spread diffusively [66]. This is in marked contrast to the Gross–Pitaevskii equation for BECs, where we found acoustic degrees of freedom moving ballistically through the medium (see chapter 3). While plastic motion can be assumed to behave diffusively, elastic equilibrium is generally attained on a much faster timescale determined by the speed of sound in the crystal, which equation (4.43) cannot capture. This is problematic because it means that plastic motion will happen out of elastic equilibrium, in contrast to real crystals that can be assumed to be at elastic equilibrium at all times.

It is interesting to note that the difference between the GPE and equation (4.43) is that the GPE describes a complex field with two real degrees of freedom, so that additional momentum degrees of freedom can be represented in the complex phase, as we saw by deriving a hydrodynamic description. In contrast, the dynamical equation of the PFC has only one real degree of freedom. An early attempt to alleviate this problem was to add a momentum degree of freedom by letting the current have inertia while approaching equilibrium [73],

$$\partial_t \mathbf{J} + \beta \mathbf{J} = -\alpha^2 \nabla \frac{\delta \mathcal{F}}{\delta \psi} \quad \Rightarrow \quad \partial_t^2 \psi + \beta \partial_t \psi = \alpha^2 \nabla^2 \frac{\delta \mathcal{F}}{\delta \psi}. \tag{4.49}$$

Performing a linear stability analysis of this equation, the authors found short-wavelength ballistic degrees of freedom moving at a particular speed of sound. However, long wavelengths are still overdamped, causing a diffusive behavior which still fails to equilibrate the system properly [74, 75]. A variety of other methods have been proposed for the amplitude equations (4.47 and 4.48) for constraining the evolution to mechanical equilibrium [76] or coupling the phase field to a momentum-conserving mesoscopic velocity field [77]. However, by constraining themselves to amplitude-expanded equations, these approaches are only valid near the critical point $r = 0$ in the free energy. We will see below that the phenomenology of dislocation motion is very simple near criticality, with more interesting behavior at deeper quenches.

We therefore sought a phase-field crystal method using the original equation (4.43), which enforces mechanical equilibrium on the timescale of plastic deformation. We propose such a model in paper V, however arriving at this model required a better understanding of the local elastic and plastic behavior of the PFC. Such an understanding was the goal of paper IV [4], which we describe next.

4.8   Paper IV

A detailed understanding of the elastic properties of the PFC is helped by an expression for the elastic stress σ_{ij} at any given point. As described above, the elastic constants of the equilibrium triangular lattice were obtained in ref. [66] by computing the free energy of the deformed equilibrium state, but this does not provide an expression for the stress without knowing the elastic strain e_{ij}. We therefore developed different approach where stress is computed for any state ψ. The derivation is described in the paper, but we give it in more detail here.

Consider then a general state $\psi(\mathbf{r})$, and deform the coordinate system by a slowly varying displacement field $\mathbf{r}' = \mathbf{r} + \mathbf{u}(\mathbf{r})$ giving a new state $\psi'(\mathbf{r})$. We will assume that the density is unchanged under the deformation, so that evaluating the deformed state at the deformed position gives the same value as the original state at the original position, giving $\psi'(\mathbf{r}') = \psi(\mathbf{r})$. This assumption is only correct if the displacement has no volumetric component $\nabla \cdot \mathbf{u}$, because any change in local volume must be compensated by a change in ψ to conserve the particle number $N = \int \psi \mathrm{d}^2\mathbf{r}$. Our result for the λ Lamé coefficient, which is related to volumetric deformations, will therefore have corrections. Similar assumptions have been made in earlier work [66, 68, 76].

The energy of the deformed state can be computed in the deformed coordinate system as

$$\mathcal{F}[\psi'] = \int f\left[\psi'(\mathbf{r}'), \partial_i'\psi'(\mathbf{r}'), \partial_{ij}'\psi'(\mathbf{r}')\right] \mathrm{d}^2\mathbf{r}', \qquad (4.50)$$

where $f(\psi, \partial_i\psi, \partial_{ij}\psi)$ is a general free energy density depending on ψ and its derivatives, while ∂_i' denotes the derivative with respect to the $\mathbf{r}'$ coordinate. In order to compare this with the free energy of the original state, we change variables from $\mathbf{r}'$ to $\mathbf{r}$. The Jacobian of this transformation is given by

$$\begin{vmatrix} \partial_x(x + u_x) & \partial_x(y + u_y) \\ \partial_y(x + u_x) & \partial_y(y + u_y) \end{vmatrix} = 1 + \nabla \cdot \mathbf{u} + \mathcal{O}(\nabla\mathbf{u}^2), \qquad (4.51)$$

where we drop terms quadratic in the displacement gradient due to the slow variation of $\mathbf{u}$. Using that $\psi'(\mathbf{r}') = \psi(\mathbf{r})$, the integral transforms to

$$\mathcal{F}[\psi'] = \int f\left[\psi(\mathbf{r}), \partial_i'\psi(\mathbf{r}), \partial_{ij}'\psi(\mathbf{r})\right](1 + \nabla \cdot \mathbf{u})\mathrm{d}^2\mathbf{r}. \qquad (4.52)$$

The derivative operators on $\mathbf{r}'$ can be transformed to those acting on $\mathbf{r}$ by the chain rule,

$$\partial_i' = \frac{\partial}{\partial r_i'} = \frac{\partial r_k}{\partial r_i'}\frac{\partial}{\partial r_k} = \frac{\partial(r_k' - u_k)}{\partial r_i'}\partial_k = (\delta_{ik} - \partial_i'u_k)\partial_k. \qquad (4.53)$$

Applying this expression recursively, we see that $\partial_i'u_k = \partial_i u_k - \partial_i'u_l\partial_k u_l$. Neglecting the higher-order term, we see that

$$\partial_i' = (\delta_{ik} - \partial_i u_k)\partial_k + \mathcal{O}(\nabla\mathbf{u}^2), \qquad (4.54)$$

and by letting this operator act twice on a function ψ, we find the second-order derivative given by

$$\partial'_{ij}\psi = (\delta_{jl} - \partial_j u_l)\partial_l \left[(\delta_{ik} - \partial_i u_k)\partial_k \psi\right]$$
$$= \partial_{ij}\psi - \partial_j \left(\partial_i u_k \partial_k \psi\right) - \partial_j u_k \partial_{ik}\psi + \mathcal{O}(\nabla \mathbf{u}^2). \qquad (4.55)$$

From these expressions, we can see that see that the differences $\partial'_i - \partial_i$ and $\partial'_{ij} - \partial_{ij}$ are linear in the displacement gradient $\nabla \mathbf{u}$ and are therefore small parameters. We therefore linearize the free energy density of equation (4.52) in these differences. Writing $f' = f(\psi, \partial'_i \psi, \partial'_{ij}\psi)$ for brevity, we find

$$f' = f + \frac{\partial f}{\partial(\partial_i \psi)}(\partial'_i - \partial_i)\psi + \frac{\partial f}{\partial(\partial_{ij}\psi)}(\partial'_{ij} - \partial_{ij})\psi$$
$$= f - \frac{\partial f}{\partial(\partial_i \psi)}\partial_i u_k \partial_k \psi - \frac{\partial f}{\partial(\partial_{ij}\psi)}\left[\partial_j(\partial_i u_k \partial_k \psi) + \partial_j u_k \partial_{ik}\psi\right]. \qquad (4.56)$$

If the integrand were expressed as a linear function of the displacement gradient $\partial_i u_j$, the stress would follow from the definition $\mathcal{F}[\psi'] = \int \sigma_{ij}\partial_i u_j \mathrm{d}^2\mathbf{r}$. The first term inside the square brackets above is not on this form, however, so we perform an integration by parts on this term. Also relabeling the indices in order to factor the displacement gradient out of the integrand, we find

$$\mathcal{F}[\psi'] = \mathcal{F}[\psi] + \int (\nabla \cdot \mathbf{u})f\mathrm{d}^2\mathbf{r} - \int \frac{\partial f}{\partial(\partial_{ij}\psi)}\partial_i u_k \partial_k \psi \mathrm{d}\Sigma_j$$
$$- \int \left[\frac{\partial f}{\partial(\partial_i \psi)}\partial_j \psi - \partial_k \frac{\partial f}{\partial(\partial_{ik}\psi)}\partial_j \psi + \frac{\partial f}{\partial(\partial_{ik}\psi)}\partial_{jk}\psi\right]\partial_i u_j \mathrm{d}^2\mathbf{r}, \quad (4.57)$$

where $\mathrm{d}\Sigma_j = n_j \mathrm{d}\Sigma$ is the surface normal element of the system boundary. This results in an expression for the stress of an arbitrary state ψ, given by

$$\sigma_{ij} = -\frac{\partial f}{\partial(\partial_i \psi)}\partial_j \psi + \partial_k \frac{\partial f}{\partial(\partial_{ik}\psi)}\partial_j \psi - \frac{\partial f}{\partial(\partial_{ik}\psi)}\partial_{jk}\psi + \delta_{ij}f. \qquad (4.58)$$

For the particular free energy density $f(\psi, \nabla^2\psi) = \frac{1}{2}(\mathcal{L}\psi)^2 + \frac{r}{2}\psi^2 + \frac{1}{4}\psi^4$ with $\mathcal{L} = 1 + \nabla^2$, we find that the stress is given by

$$\sigma_{ij} = \partial_i \mathcal{L}\psi \partial_j \psi - \mathcal{L}\psi \partial_{ij}\psi + \delta_{ij}f. \qquad (4.59)$$

Since ψ will typically have oscillations with wavenumber ~ 1, the resulting ex-

pression for the stress will also have such oscillations. This is because the stress we have computed resolves the forces on each individual lattice site. Since we are more interested in the bulk force on a mesoscopic volume element, we average this stress field over a region roughly corresponding to a unit cell to find the mesoscopic stress field,

$$\overline{\sigma}_{ij}(\mathbf{r}) = \langle \sigma_{ij}(\mathbf{r}') \rangle_{UC} = \int \sigma_{ij}(\mathbf{r}')C(\mathbf{r}' - \mathbf{r})\mathrm{d}^2\mathbf{r}', \qquad (4.60)$$

where $C(\mathbf{r})$ is an appropriately chosen filter function. In practice, we choose $C(\mathbf{r})$ to be a Gaussian of width a, and compute the convolution as a multiplication in Fourier space.

The elastic constants near equilibrium can then be derived by inserting the deformed amplitude expansion of equation (4.45), ignoring modes $|\mathbf{g}| > 1$, into the mesoscopic stress. We also ignore the isotropic term $\delta_{ij}f$, which is second-order in the displacement. The resulting computations are tedious but straightforward, and are outlined in the paper. For the microscopic stress σ_{ij}, one obtains terms of the form

$$\partial_i u_j \sum_{\mathbf{g},\mathbf{g}'} A_{\mathbf{g}} A_{\mathbf{g}'} e^{i(\mathbf{g}+\mathbf{g}')\cdot(\mathbf{r}-\mathbf{u})}. \qquad (4.61)$$

Taking the average of this over a unit cell of the triangular lattice, we can use that the deformation field varies slowly to take the factors related to $\mathbf{u}$ outside the integral and use that

$$\left\langle e^{i(\mathbf{g}+\mathbf{g}')\cdot\mathbf{r}} \right\rangle_{UC} = \delta_{\mathbf{g},-\mathbf{g}'}, \qquad (4.62)$$

which simplifies the double sum into a single sum. The end result is

$$\overline{\sigma}_{ij} = 8A_T^2 \partial_k u_l \sum_{n=1}^{\infty} q_i^n q_j^n q_k^n q_l^n, \qquad (4.63)$$

which upon inserting the reciprocal lattice basis vectors yields Lamé parameters $\lambda = \mu = 3A_T^2$, consistent with earlier results [68, 76]. Numerical tests confirmed this result.

4.8.1 Dislocations in the PFC

To see how dislocations are represented in the phase-field crystal, consider an amplitude $A_{\mathbf{g}}$ in the deformed amplitude expansion of equation (4.45), where the displacement $\mathbf{u}$ leads to a factor $e^{-i\mathbf{g}\cdot\mathbf{u}}$ in the phase. Using the loop integral in

equation (4.23), the phase of the amplitude carries a circulation given by

$$\oint_C \mathrm{d}(\arg A_{\mathbf{g}}) = \oint_C \mathrm{d}\left(-\mathbf{g} \cdot \mathbf{u}\right) = -\mathbf{g} \cdot \oint_C \mathrm{d}\mathbf{u} = -\mathbf{g} \cdot \mathbf{b}, \qquad (4.64)$$

showing that any dislocation with Burger's vector $\mathbf{b}$ is associated with a quantized vortex of circulation $-\mathbf{g} \cdot \mathbf{b}$, which is an integer multiple of 2π as long as $\mathbf{b}$ is a lattice vector. This fact allows us to adapt the method of Halperin and Mazenko for studying the motion of quantized vortices which we outlined in chapter 3, to the motion of dislocations in the PFC. Considering the three amplitudes A_n, we define for each dislocation the three corresponding vortex charges $s_n^\alpha = \frac{1}{2\pi}\mathbf{q}_n \cdot \mathbf{b}_\alpha$. The quantized vortex in the phase of A_n must correspond to a zero in the magnitude with multiplicity $|s_n^\alpha|$ if this charge is nonzero. Hence, arguing as we did for vortices in the BEC, we find

$$\frac{1}{2\pi}\mathbf{q}_n \cdot \mathbf{B}(\mathbf{r}) = \sum_\alpha s_n^\alpha \delta(\mathbf{r} - \mathbf{r}_\alpha) = -D_n\delta(A_n), \quad D_n = \mathrm{Im}(\partial_x A_n^* \partial_y A_n), \quad (4.65)$$

where the minus sign is due to the vortex having charge $-s_n^\alpha$. The three reciprocal lattice basis vectors satisfy the identity [78]

$$\sum_{n=1}^{3} q_i^n q_j^n = \frac{3}{2}\delta_{ij}, \qquad (4.66)$$

as can be seen by checking all cases. This identity lets us invert the above relation by multiplying with $\frac{4\pi}{3}\sum_n \mathbf{q}_n$, giving an expression for the dislocation density which depends only on the amplitudes A_n,

$$B_i(\mathbf{r}) = \frac{2}{3}\sum_{n=1}^{3} q_i^n q_j^n B_j(\mathbf{r}) = -\frac{4\pi}{3}\sum_{n=1}^{3} q_i^n D_n\delta(A_n). \qquad (4.67)$$

This expression lets us compute the motion of dislocations by following the motion of the amplitudes. The field $D_n\delta(A_n)$ has conserved current given by $\mathbf{J}_n\delta(A_n)$, where $\mathbf{J}_n$ has components

$$J_i^{(n)} = \epsilon_{ij}\,\mathrm{Im}\left(\partial_t A_n \partial_j A_n^*\right), \qquad (4.68)$$

74

which gives a corresponding conservation equation for $\mathbf{B}(\mathbf{r})$,

$$\partial_t B_i = -\frac{4\pi}{3} \sum_{n=1}^{3} q_i^n \partial_t \left[D_n \delta(A_n) \right] = \partial_j \left(\frac{4\pi}{3} \sum_{n=1}^{3} q_i^n J_j^{(n)} \delta(A_n) \right). \qquad (4.69)$$

This equation shows that current of the i'th component of $\mathbf{B}$ along the r_j direction is defined as

$$\mathcal{J}_{ij} = -\frac{4\pi}{3} \sum_{n=1}^{3} q_i^n J_j^{(n)} \delta(A_n). \qquad (4.70)$$

Comparing with the current corresponding to each dislocation having velocity $\mathbf{v}_\alpha$, $\mathcal{J}_{ij} = \sum_\alpha b_i^\alpha v_j^\alpha \delta(\mathbf{r} - \mathbf{r}_\alpha)$ gives the expression for the velocity,

$$v_j^\alpha = \frac{2}{3} \sum_{n=1}^{3} \frac{(\mathbf{q}_n \cdot \mathbf{b}_\alpha)^2}{|\mathbf{b}_\alpha|^2} \frac{J_j^{(n)}(\mathbf{r}_\alpha)}{D_n(\mathbf{r}_\alpha)} = \frac{1}{S_\alpha^2} \sum_{n=1}^{3} (s_\alpha)^2 \frac{J_j^{(n)}(\mathbf{r}_\alpha)}{D_n(\mathbf{r}_\alpha)}, \qquad (4.71)$$

where we defined $S_\alpha^2 = \sum_{n=1}^{3} (s_\alpha)^2$. Numerically, we computed this velocity by taking the average of the numerator and the denominator within a thresholded region, weighted by a Gaussian approximation of $\delta(A_n)$, then dividing. When computing the current $\mathbf{J}_n$, we used a value for $\partial_t A_n$ found by a numerical amplitude expansion of $\partial_t \psi$ (see chapter 5), thus the result did not depend on the validity of equation (4.48) for the amplitude evolution. The resulting velocity was compared with a finite time difference of vortex positions, giving excellent agreement.

Finally, we computed the response of a dislocation to external deformations in the same way as we computed the motion of vortices in BECs in chapter 3. Considering a stationary dislocation at the origin with Burger's vector $\mathbf{b}$, we assumed that the amplitude takes the form of an isotropic solution near the origin. This is a stationary solution of equation (4.48) near the origin as long as $|s_n| \leq 1$, but it is not necessarily the true form that the amplitude would take. Indeed, given the anisotropic nature of the $\mathcal{L}_n = \nabla^2 + 2i\mathbf{q}_n \cdot \nabla$ operator, we might expect an anisotropic vortex solution, but general solutions of $\mathcal{L}_n^2 A_n = 0$ are difficult to find. Applying a smoothly varying displacement field $\tilde{A}_n = A_n e^{-i\mathbf{q}_n \cdot \tilde{\mathbf{u}}}$, we computed $\partial_t \tilde{A}_n$ and the resulting dislocation velocity, giving

$$v_i = \frac{4b_m}{\pi S^2} \epsilon_{ij} \partial_k \tilde{u}_l \sum_{n=1}^{3} q_m^n q_j^n q_k^n q_l^n = \frac{1}{4\pi A_0^2} \epsilon_{ij} \tilde{\sigma}_{jk} b_k, \qquad (4.72)$$

where $\tilde{\sigma}_{jk}$ is the mesoscopic stress corresponding to the displacement field $\tilde{\mathbf{u}}$,

that is, ignoring the singular stress associated with the dislocation at the origin. This is proportional to the Peach–Koehler force of equation (4.30), showing that dislocations in this case move as overdamped particles. Notably, the mobility is equal for both glide and climb. This might be correct in the near-critical $|r| \ll 1$ regime where equation (4.48) is valid, though numerical measurements suggest that this is not the case. Possibly the isotropic vortex solution we chose for A_n gives rise to this discrepancy, or the fact that we ignored the density variation due to volumetric deformations.

Numerical verification of this result was difficult because of the need to compute the stress $\tilde{\sigma}_{ij}$ with the dislocation itself subtracted. We made a rough comparison by computing the stress induced from the other dislocations assuming elastic equilibrium, using equation (4.32). This gave comparable velocities in the glide case, however climb motion deviated significantly. In any case, the assumption of elastic equilibrium is dubious because of the purely diffusive dynamics of the PFC, as discussed above.

At deeper quenches, the amplitude equation (4.48) is not valid, so the overdamped motion of equation (4.72) gives way to more complicated behavior. Numerically, we saw that the glide velocity oscillates on the scale of the lattice in this case. We attribute this to the lattice itself exerting forces on the dislocation depending on the quench depth, similar to Peierls forces.

4.9 Paper V

Having obtained a good understanding of the elastic and plastic behavior of the PFC, we now aimed to use this understanding for enforcing elastic equilibrium during diffusive time evolution in paper V [5].

The idea was to apply a smooth deformation $\mathbf{r}' = \mathbf{r} + \mathbf{u}^\delta$ to ψ such that $\psi^{\mathrm{eq}}(\mathbf{r}') = \psi(\mathbf{r})$, where $\mathbf{u}^\delta$ was chosen so that $\psi^{\mathrm{eq}}(\mathbf{r})$ is in elastic equilibrium. The PFC satisfies linear elasticity far away from dislocations, hence the stress field of ψ^{eq} is related to $\mathbf{u}^\delta$ through the *residual stress* σ_{ij}^δ,

$$\sigma_{ij}^{\mathrm{eq}} = \sigma_{ij}^\psi + \sigma_{ij}^\delta, \quad \sigma_{ij}^\delta = \lambda \delta_{ij} e_{kk}^\delta + 2\mu e_{ij}^\delta, \quad e_{ij}^\delta = \frac{1}{2} \left(\partial_i u_j^\delta + \partial_j u_i^\delta \right). \quad (4.73)$$

This allowed us to determine $\mathbf{u}^\delta$ by requiring $\partial_i \sigma_{ij}^{\mathrm{eq}} = \partial_i \left(\sigma_{ij}^\psi + \sigma_{ij}^\delta \right) = 0$. We solved this equation using the Airy stress function χ, setting $\sigma_{ij}^{\mathrm{eq}} = \epsilon_{ik}\epsilon_{jl}\partial_{kl}\chi$. Recall that the stress function must be determined by the incompatibility equation

76

(4.21). We can simplify this equation further by noting that, since the applied deformation $\mathbf{u}^\delta$ is smooth, its corresponding strain tensor e_{ij}^δ is compatible. Hence, determining e_{ij}^{eq} from σ_{ij}^{eq} and applying the double curl, we find

$$
\begin{aligned}
\frac{1-\kappa}{2\mu}\nabla^4\chi &= \frac{1}{2\mu}\epsilon_{ik}\epsilon_{jl}\partial_{kl}\left(\sigma_{ij}^\psi - \kappa\delta_{ij}\sigma_{mm}^\psi\right) + \frac{1}{2\mu}\epsilon_{ik}\epsilon_{jl}\left(\sigma_{ij}^\delta - \kappa\delta_{ij}\sigma_{kk}^\delta\right) \\
&= \frac{1}{2\mu}\left(\epsilon_{ik}\epsilon_{jl}\partial_{kl}\sigma_{ij}^\psi - \kappa\nabla^2\sigma_{kk}^\psi\right).
\end{aligned}
\tag{4.74}
$$

Solving this equation using spectral methods, we could obtain σ_{ij}^{eq}, which again determines the residual strain e_{ij}^δ by subtracting the original stress σ_{ij}^ψ and inverting the stress–strain relation. The residual strain field was then integrated to determine the deformation field $\mathbf{u}^\delta$.

In this way we could, at each point in time, determine the deformation that would bring the state ψ into elastic equilibrium. We applied this deformation between each timestep using a Taylor expansion of the relation $\psi'(\mathbf{r}) = \psi(\mathbf{r} - \mathbf{u})$. Numerically, we observed that the motion of dislocations deviate significantly from the speed obtained by inserting equation (4.32) into (4.72) in the standard PFC. Applying the deformation, the two agreed well up to oscillations in the dislocation speed at deep quenches, which as mentioned above we attribute to Peierls forces from the lattice.

This shows that we have obtained a version of the PFC model where elastic deformations are relaxed to elastic equilibrium at each point in time, which is a significant step towards modeling realistic crystal systems. We hope to apply this model in the future towards modeling the large-scale temporal evolution of an ensemble of dislocations, in order to better understand the plastic yielding transition.

Chapter 5

Numerical methods

In this chapter, we describe the numerical methods that we employ throughout the thesis project. The Gross–Pitaevskii equation for quantum turbulence and the equation governing the phase-field crystal are very similar in structure, being weakly nonlinear. We describe the exponential time differencing method for solving such equations, as well as a symplectic time integration method that we employed for the point-vortex simulations of paper III. Finally, we describe a useful method of numerically obtaining the slowly varying amplitudes of a phase field ψ in the amplitude decomposition of equation (4.46).

5.1 Exponential time differencing

Fourier transformation is a very powerful technique for computing numerical properties of fields defined on a uniform grid with periodic boundaries. A good example of this power is through the technique of spectral differentiation, which allows the solution of linear time-independent partial differential equations (PDEs) by solving algebraic equations in reciprocal space. For example, the biharmonic equation (4.35) for the Airy stress function χ is expressed in spectral space by

$$\frac{1 - \kappa}{2\mu} k^4 \tilde{\chi}(\mathbf{k}) = i\epsilon_{ij} k_i \tilde{B}_j, \tag{5.1}$$

which can be solved for $k > 0$ by simply dividing with k^4 as well as the constant coefficients. The choice for $k = 0$ corresponds to a constant term in the solution of χ, which is immaterial because the stress is given by derivatives of χ; hence we simply choose $\tilde{\chi}(0) = 0$. A similar example of using spectral methods for solving

PDEs is used in paper V for integrating the residual strain e_{ij}^δ to a deformation field $\mathbf{u}^\delta$.

Similarly, linear time-dependent PDEs decouple in spectral space into a collection of time-dependent ordinary differential equations, one for each wavenumber $\mathbf{k}$. Each of these equations can be solved exactly, giving a large advantage over numerical time difference schemes. This can also be exploited to derive better time difference schemes for the weakly nonlinear PDEs we use in this thesis, by the method of exponential time differencing [79].

Because we will use this method for both the Gross–Pitaevskii equation (3.13) and the PFC evolution equation (4.43), we write the two PDEs in a common form given by

$$\partial_t \psi(\mathbf{r}, t) = \omega(\nabla)\psi(\mathbf{r}, t) + N(\mathbf{r}, t), \tag{5.2}$$

where $\omega(\nabla)$ is a linear differential operator and $N(\mathbf{r}, t)$ is a general function of time and space denoting the nonlinear part of the PDE. Taking the Fourier transform, we find

$$\partial_t \tilde{\psi}(\mathbf{k}, t) = \tilde{\omega}(\mathbf{k})\tilde{\psi}(\mathbf{k}, t) + \tilde{N}(\mathbf{k}, t), \tag{5.3}$$

where $\tilde{N}(\mathbf{k}, t) = F[N(\mathbf{r}, t)]$, and $\tilde{\omega}(\mathbf{k})$ is computed by replacing ∇ by $i\mathbf{k}$ in $\omega(\nabla)$. We can solve the linear part of this equation by multiplying by the integrating factor $e^{-\tilde{\omega}(\mathbf{k})t}$, giving

$$\partial_t \left(\tilde{\psi}(\mathbf{k}, t)e^{-\tilde{\omega}(\mathbf{k})t} \right) = e^{-\tilde{\omega}(\mathbf{k})t}\tilde{N}(\mathbf{k}, t). \tag{5.4}$$

Integrating this equation from t to $t + \Delta t$, we find the formal solution

$$\tilde{\psi}(\mathbf{k}, t + \Delta t) = e^{\tilde{\omega}(\mathbf{k})\Delta t}\tilde{\psi}(\mathbf{k}, t) + e^{\tilde{\omega}(\mathbf{k})(t+\Delta t)} \int_t^{t+\Delta t} e^{-\tilde{\omega}(\mathbf{k})t'}\tilde{N}(\mathbf{k}, t')\mathrm{d}t'$$

$$= e^{\tilde{\omega}(\mathbf{k})\Delta t}\tilde{\psi}(\mathbf{k}, t) + e^{\tilde{\omega}(\mathbf{k})\Delta t} \int_0^{\Delta t} e^{-\tilde{\omega}(\mathbf{k})\tau}\tilde{N}(\mathbf{k}, t + \tau)\mathrm{d}\tau, \tag{5.5}$$

where we made the substitution $\tau = t' - t$. We now approximate $\tilde{N}(\mathbf{k}, t')$ as linearly time-dependent in the interval $(t, t + \Delta t)$, given by

$$\tilde{N}(\mathbf{k}, t + \tau) = N_0 + \frac{N_1}{\Delta t}\tau, \tag{5.6}$$

where $N_0 = \tilde{N}(t)$ and $N_1 = \tilde{N}(t + \Delta t) - N_0$. Evaluating the integral in equation

(5.5), we find the solution

$$\tilde{\psi}(\mathbf{k}, t + \Delta t) = e^{\tilde{\omega}(\mathbf{k})\Delta t}\tilde{\psi}(\mathbf{k}, t) + \frac{N_0}{\tilde{\omega}(\mathbf{k})}\left(e^{\tilde{\omega}(\mathbf{k})\Delta t} - 1\right)$$

$$+ \frac{N_1}{\tilde{\omega}(\mathbf{k})}\left[\frac{1}{\tilde{\omega}(\mathbf{k})\Delta t}(e^{\tilde{\omega}(\mathbf{k})\Delta t} - 1) - 1\right]. \qquad (5.7)$$

Computing the value for N_1 requires knowledge of the state at $t + \Delta t$ before we compute it. A predictor–corrector scheme is therefore employed, where we first evaluate equation (5.7) setting $N_1 = 0$, which corresponds to assuming that $\tilde{N}(t')$ is constant in the interval $(t, t + \Delta t)$. This gives an estimate for the state at $t + \Delta t$, providing a value N_1 which we can use to add the last term of the equation and correct for the error we made in setting $N_1 = 0$. In principle, this procedure can be iterated over more steps, however we use only one such correction step in our work.

In order to apply this method to the GPE (3.13) for quantum turbulence, we choose

$$\tilde{\omega}(\mathbf{k}) = (i + \gamma)\left(1 - \frac{1}{2}k^2\right), \quad N(\mathbf{r}, t) = -(i + \gamma)\left[V\psi + |\psi|^2\psi\right]. \qquad (5.8)$$

When solving this equation, we use the Thomas–Fermi ground state $\psi = \sqrt{1 - V}$ for the initial condition, which is only an approximately stationary state. We therefore apply a short period of dissipative relaxation before starting the simulation. This is achieved by replacing the $i + \gamma$ prefactor with 1 while keeping the external potential constantly equal to $V(t = 0)$, which corresponds to evolving the conservative GPE (3.4) in imaginary time, as is common practice for computing quantum-mechanical ground states numerically. For the PFC equation, we choose

$$\tilde{\omega}(\mathbf{k}) = -k^2\left[(1 - k^2)^2 + r\right], \quad N(\mathbf{r}, t) = \nabla^2\psi^3. \qquad (5.9)$$

Because this equation is purely dissipative, the accurate choice of initial condition is less important in this case.

5.2 Symplectic method for the point vortex model

In paper III, we studied quantum turbulence by treating point vortices as the only dynamical degrees of freedom. Since the dynamical equations 3.44 of the point

vortex model have the structure of a Hamiltonian system apart from the small dissipation constant, a time integration scheme which is compatible with this structure, known as a *symplectic* method, is preferable in order to accurately conserve the energy of the vortex gas. Explicit time difference schemes which are symplectic exist for separable Hamiltonians, that is, if the Hamiltonian can be decomposed into terms depending on the two sets of conjugate variables independently, $H = V(\{x_\alpha\}) + T(\{y_\alpha\})$ [80]. Unfortunately, the $\ln r_{\alpha\beta}$ terms of the point vortex Hamiltonian show that this system is not separable. We therefore use an implicit time difference scheme for integrating the conservative part of this system, namely the fully implicit Gauss–Legendre method of fourth order. Denoting the conservative velocity of vortex α depending on the N vortex positions $\mathbf{r}_\beta$ by $\mathbf{v}_\alpha^c(\mathbf{r}_\beta)$, a time step is performed by finding a set of $2N$ velocities $\mathbf{w}_{\alpha,i}$ that solve the system of equations

$$\mathbf{w}_{\alpha,j} = \mathbf{v}_\alpha^c \left(\mathbf{x}_\beta + \Delta t a_{ij} \mathbf{w}_{\beta,i} \right), \tag{5.10}$$

where

$$a_{11} = a_{22} = \frac{1}{4}, \quad a_{12} = \frac{1}{4} - \frac{\sqrt{3}}{6}, \quad a_{21} = \frac{1}{4} + \frac{\sqrt{3}}{6}. \tag{5.11}$$

The new set of vortex positions $\mathbf{r}_\alpha'$ is then computed by

$$\mathbf{r}_\alpha' = \mathbf{r}_\alpha + \frac{\Delta t}{2} \left(\mathbf{w}_{\alpha,1} + \mathbf{w}_{\alpha,2} \right). \tag{5.12}$$

We solve the nonlinear set of equations (5.10) by fixed-point iteration. Setting $\mathbf{w}_{\alpha,i}^{(0)} = \mathbf{v}_\alpha(\mathbf{r}_\beta)$, we iterate the equation

$$\mathbf{w}_{\alpha,j}^{(n+1)} = \mathbf{v}_\alpha^c \left(\mathbf{x}_\beta + \Delta t a_{ij} \mathbf{w}_{\beta,i}^{(n)} \right) \tag{5.13}$$

until the distance between successive values is below a threshold. This simple iteration can be improved by extrapolating from previous values of $\mathbf{w}$, but we did not implement such optimizations.

Finally, the dissipative part of the evolution is computed by a simple explicit Euler scheme,

$$\mathbf{r}_\alpha(t + \delta t) = \mathbf{r}_\alpha' + \Delta t \mathbf{v}_\alpha^d(\mathbf{r}_\beta). \tag{5.14}$$

This scheme is sufficient because $|\mathbf{v}_\alpha^d| \ll \mathbf{v}_\alpha^c$ due to the dissipation parameter γ being small. In addition, phenomenological vortex creation and annihilation rules are applied; these are described in the paper.

5.3 Numerical amplitude decomposition

In papers IV–V, we evolved the PFC equation (4.43) numerically in order to test the nonequilibrium behavior of the PFC. In the analysis of these numerical results, it is very useful to compute the slowly varying amplitudes $A_n(\mathbf{r}) = |A_n(\mathbf{r})|e^{-i\mathbf{q}_n \cdot \mathbf{u}(\mathbf{r})}$ numerically, because they contain information about the displacement field as well as the position of dislocations.

If the states were in equilibrium, the constant amplitudes could be recovered simply by Fourier transforming the phase field ψ. This suggests that slowly varying amplitudes could be recovered by taking the Fourier transform over a region that is small compared to the variation, but still large enough that the $e^{i\mathbf{q}_n \cdot \mathbf{r}}$ oscillation of ψ is visible. Hence, we might guess that the amplitude can be estimated by taking a spatial average given by

$$A_n(\mathbf{r}) = \left\langle \psi e^{-i\mathbf{g}\cdot\mathbf{r}'} \right\rangle_{\mathbf{r}'\text{ close to }\mathbf{r}}. \tag{5.15}$$

Here we will provide a more careful argument for such a procedure, following a similar technique developed for the analysis of transmission electron micrographs [81].

Consider therefore a state ψ in the amplitude expansion with slowly varying amplitudes, given by

$$\psi(\mathbf{r}) = \sum_{\mathbf{g}} A_{\mathbf{g}}(\mathbf{r})e^{i\mathbf{g}\cdot\mathbf{r}}, \tag{5.16}$$

such that $\psi_0 = A_{\mathbf{g}=0}$ and $A_{\mathbf{g}}^* = A_{-\mathbf{g}}$. Taking the Fourier transform and using the convolution theorem, we obtain

$$\tilde{\psi}(\mathbf{k}) = \frac{1}{(2\pi)^2}\sum_{\mathbf{g}}\int \tilde{A}_{\mathbf{g}}(\mathbf{k}-\mathbf{k}')F\left[e^{i\mathbf{g}\cdot\mathbf{r}}\right](\mathbf{k}')\mathrm{d}^2k' = \sum_{\mathbf{g}}\tilde{A}_{\mathbf{g}}(\mathbf{k}-\mathbf{g}), \quad (5.17)$$

where we also used that $F\left[e^{i\mathbf{g}\cdot\mathbf{r}}\right](\mathbf{k}') = (2\pi)^2\delta(\mathbf{k}'-\mathbf{g})$. The assumption that the amplitudes $A_{\mathbf{g}}$ vary slowly compared to the lattice constant $a = 4\pi/\sqrt{3}$ corresponds to their Fourier-transformed versions being strongly peaked near 0 with width $\sim 1/a = \sqrt{3}/4\pi$. This allows us to isolate an amplitude $A_{\mathbf{g}}$ by multiplying with a similarly peaked function, for example a Gaussian of width $1/a$,

$$e^{-a^2(\mathbf{k}-\mathbf{g})^2/2}\tilde{\psi}(\mathbf{k}) \approx e^{-a^2(\mathbf{k}-\mathbf{g})^2/2}\tilde{A}_{\mathbf{g}}(\mathbf{k}-\mathbf{g}). \tag{5.18}$$

Transforming the right-hand side of this equation back to real space using the shift

property and the convolution theorem, we find a locally averaged version $\overline{A}_{\mathbf{g}}$ of the amplitude,

$$e^{i\mathbf{g}\cdot\mathbf{r}}\overline{A}_{\mathbf{g}}(\mathbf{r}) = e^{i\mathbf{g}\cdot\mathbf{r}}\int A_{\mathbf{g}}(\mathbf{r}')C(\mathbf{r}-\mathbf{r}')\mathrm{d}^2\mathbf{r}' \approx F^{-1}\left[e^{-a^2(\mathbf{k}-\mathbf{g})^2/2}\tilde{\psi}(\mathbf{k})\right] \quad (5.19)$$

where $C(\mathbf{r})$ is a real-space normalized Gaussian of width $a = 4\pi/\sqrt{3}$, given by

$$C(\mathbf{r}) = \frac{1}{2\pi a^2}e^{-r^2/2a^2}. \tag{5.20}$$

This shows that $\overline{A}_{\mathbf{g}}$ can be computed numerically by the expression

$$\overline{A}_{\mathbf{g}}(\mathbf{r}) \approx e^{-i\mathbf{g}\cdot\mathbf{r}}F^{-1}\left[e^{-8\pi^2(\mathbf{k}-\mathbf{g})^2/3}\tilde{\psi}(\mathbf{k})\right] = \int e^{-i\mathbf{g}\cdot\mathbf{r}'}\psi(\mathbf{r}')C(\mathbf{r}-\mathbf{r}')\mathrm{d}^2\mathbf{r}', \tag{5.21}$$

where we substituted the value for $a = 4\pi/\sqrt{3}$. The first expression in terms of Fourier transforms is the most useful for numerical computation, while the second expression in terms of a convolution shows that our initial guess in equation (5.15) is correct, except for the local averaging of the resulting amplitude.

Chapter 6

Summary and outlook

We have studied the two fields of quantum turbulence and plasticity, focusing on topological defects as a common feature of both systems. Two-dimensional quantum turbulence is well described by the interaction of nondiffusive point vortices with an additional thermal drift, while point-like or line-like dislocations are essential in understanding the complex yielding behavior of microscopic crystals. In both cases, the complex macroscopic behavior is associated with the emergence of particular spatial structures of vortices or dislocations.

In chapter 3 and papers I–III, we demonstrated how the inverse energy cascade in two-dimensional quantum turbulence is associated with a diverse set of vortex clusters with different sizes and circulation signs, collectively expressing a self-similar structure. We introduced the weighted pair correlation function $g_w(\mathbf{r})$ as a novel statistical measure to express this collective structure. The self-similar structure of vortices leads to the $k^{-5/3}$ Kolmogorov scaling law in the energy spectrum, as well as self-similar scaling laws in other statistical quantities such as vortex number fluctuations and the distribution of vortex velocities. Taken together, these facts clarify how the inverse energy cascade is expressed on the scale of the quantized vortex.

By connecting the weighted pair correlation function with two-point correlations in the vorticity, we have found a new relationship between the scaling arguments of classical turbulence and the statistics of singular point vortices in quantum turbulence. Further exploration of the correspondence between classical and quantum turbulence would be interesting. For example, the self-similar scaling of the vorticity pair correlation has been related to the conformal invariance of constant vorticity lines in 2D classical turbulence, which again corresponds to these lines being equivalent to a particular form of Brownian motion [82]. A

similar property cannot hold for point vortices without coarse-graining out the delta functions in the vorticity field. On the other hand, the stream function takes continuous values between the vortices and shows complicated streamlines which might be related to the self-similar statistics of vortex positions.

The particular microscopic processes leading to the emergence of self-similar vortex clusters are still not understood. Vortex clusters are the natural result of an evaporative heating process due to dipole annihilation [27], but the self-similar structure of these clusters cannot be explained by equilibrium thermodynamical considerations. A detailed understanding of the nonequilibrium behavior of the vortex gas is an important step towards understanding this self-similarity. The diffusive behavior of a collection of vortices has been studied theoretically using the point vortex model [83], as well as numerically using both the point vortex model and the Gross–Pitaevskii equation [84]. A hydrodynamical theory for the flow of conservative point vortices was developed in ref. [85], which shows that the coarse-grained vortex gas does not exactly follow the fluid velocity, because of anomalous stresses in the hydrodynamical equations for the vortex flow. A study of such coarse-grained descriptions of the vortex gas in the presence of small-scale driving forces and large-scale dissipation might lead to progress on this front.

In chapter 4, we described how the complicated response of microscopic crystals under heavy loads is associated with the depinning of complicated dislocation patterns. Dislocations, being topological defects of codimension two, are very similar to the quantized vortices of quantum turbulence. In particular, two-dimensional dislocations are point-like singularities in the deformation field with logarithmic interaction potentials, just like quantized vortices in 2D quantum turbulence. One important difference is that dislocations behave purely dissipatively, instead of the mostly conservative motion of vortices. However, given a nonequilibrium steady-state where the dissipated energy is balanced by a driving force, comparisons could possibly be made between the two systems. We might therefore expect the origins of vortex structures of quantum turbulence to be related to the origins of dislocation structures in crystal plasticity.

Unfortunately, the response of dislocations to driving forces is more complicated than the simple advection of well-separated point vortices, because of effects like the pinning of dislocations to the crystal lattice. Such effects could be studied rigorously through a proper mesoscale model of the crystal lattice. The phase-field crystal is a good candidate for such a model, but suffers from the missing separation of timescales between elastic and plastic deformations. In papers IV–V we developed a better understanding of the elastic and plastic behavior of the PFC,

which we used to propose a more realistic mesoscale model for crystal plasticity. We hope that this model is useful in studying the behavior of dislocations in the presence of applied forces, leading to a better understanding of how dislocations form spatial patterns, and the avalanche-like depinning of these patterns.

Bibliography

[1] A. Skaugen and L. Angheluta, "Vortex clustering and universal scaling laws in two-dimensional quantum turbulence," Physical Review E **93**, 032106 (2016).

[2] A. Skaugen and L. Angheluta, "Velocity statistics for nonuniform configurations of point vortices," Physical Review E **93**, 042137 (2016).

[3] A. Skaugen and L. Angheluta, "Origin of the inverse energy cascade in two-dimensional quantum turbulence," Physical Review E **95**, 052144 (2017).

[4] A. Skaugen, L. Angheluta, and J. Viñals, "Dislocation dynamics and crystal plasticity in the phase-field crystal model," Physical Review B **97**, 054113 (2018).

[5] A. Skaugen, L. Angheluta, and J. Viñals, "Mesoscale model of dislocation motion and crystal plasticity," arXiv preprint arXiv:1807.10245 (2018).

[6] S. P. Sutera and R. Skalak, "The history of Poiseuille's law," Annual Review of Fluid Mechanics **25**, 1–20 (1993).

[7] O. Reynolds, "An experimental investigation of the circumstances which determine whether the motion of water shall be direct or sinuous, and of the law of resistance in parallel channels," Philosophical Transactions of the Royal Society of London **174**, 935–982 (1883).

[8] P. M. Chaikin and T. C. Lubensky, *Principles of condensed matter physics* (Cambridge university press, 2000).

[9] S. Papanikolaou, Y. Cui, and N. Ghoniem, "Avalanches and plastic flow in crystal plasticity: an overview," Modelling and Simulation in Materials Science and Engineering **26**, 013001 (2017).

[10] M. Lesieur, *Turbulence in fluids: fourth revised and enlarged edition*, eng, Vol. 84, Fluid Mechanics and its Applications (Springer Netherlands, Dordrecht, 2008).

[11] H.-Y. Shih, T.-L. Hsieh, and N. Goldenfeld, "Ecological collapse and the emergence of travelling waves at the onset of shear turbulence," Nature Physics **12**, 245 (2016).

[12] G. Lemoult, L. Shi, K. Avila, S. V. Jalikop, M. Avila, and B. Hof, "Directed percolation phase transition to sustained turbulence in couette flow," Nature Physics **12**, 254–258 (2016).

[13] A. N. Kolmogorov, "The local structure of turbulence in incompressible viscous fluid for very large reynolds numbers," Doklady Akademii Nauk SSSR **30**, 299–303 (1941), [Reprinted in Proceedings of the Royal Society of London A, Vol. 434, 9–13 (1991)].

[14] U. Frisch, P.-L. Sulem, and M. Nelkin, "A simple dynamical model of intermittent fully developed turbulence," Journal of Fluid Mechanics **87**, 719–736 (1978).

[15] A. N. Kolmogorov, "A refinement of previous hypotheses concerning the local structure of turbulence in a viscous incompressible fluid at high reynolds number," Journal of Fluid Mechanics **13**, 82–85 (1962).

[16] Y. Couder, "Two-dimensional grid turbulence in a thin liquid film," Journal de Physique Lettres **45**, 353–360 (1984).

[17] M. Gharib and P. Derango, "A liquid film (soap film) tunnel to study two-dimensional laminar and turbulent shear flows," Physica D: Nonlinear Phenomena **37**, 406–416 (1989).

[18] *The Bruce Murray Space Image Library*, `http://www.planetary.org/multimedia/space-images/`, accessed online July 28, 2018.

[19] G. K. Batchelor, "Computation of the energy spectrum in homogeneous two-dimensional turbulence," The Physics of Fluids **12**, II–233 (1969).

[20] R. H. Kraichnan, "Inertial-range transfer in two-and three-dimensional turbulence," Journal of Fluid Mechanics **47**, 525–535 (1971).

[21] R. H. Kraichnan, "Inertial ranges in two-dimensional turbulence," Physics of Fluids **10**, 1417–1423 (1967).

[22] S. Chen, R. E. Ecke, G. L. Eyink, M. Rivera, M. Wan, and Z. Xiao, "Physical mechanism of the two-dimensional inverse energy cascade," Physical Review Letters **96**, 084502 (2006).

[23] H. Xia, H. Punzmann, G. Falkovich, and M. G. Shats, "Turbulence-condensate interaction in two dimensions," Physical Review Letters **101**, 194504 (2008).

[24] R. H. Kraichnan, "Eddy viscosity in two and three dimensions," Journal of the atmospheric sciences **33**, 1521–1536 (1976).

[25] L. Onsager, "Statistical hydrodynamics," Il Nuovo Cimento **6**, 279–287 (1949).

[26] P. K. Newton, *The n-vortex problem: analytical techniques*, Vol. 145 (Springer Science & Business Media, 2013).

[27] T. Simula, M. J. Davis, and K. Helmerson, "Emergence of order from turbulence in an isolated planar superfluid," Physical Review Letters **113**, 165302 (2014).

[28] P. Meunier, S. Le Dizès, and T. Leweke, "Physics of vortex merging," Comptes Rendus Physique **6**, 431–450 (2005).

[29] R. Benzi, M. Colella, M. Briscolini, and P. Santangelo, "A simple point vortex model for two-dimensional decaying turbulence," Physics of Fluids A: Fluid Dynamics **4**, 1036–1039 (1992).

[30] E. D. Siggia and H. Aref, "Point-vortex simulation of the inverse energy cascade in two-dimensional turbulence," Physics of Fluids **24**, 171–173 (1981).

[31] E. Novikov, "Dynamics and statistics of a system of vortices," Journal of Experimental and Theoretical Physics **41**, 937 (1975).

[32] M. S. Paoletti and D. P. Lathrop, "Quantum turbulence," Annual Review of Condensed Matter Physics **2**, 213–234 (2011).

[33] M. Tsubota, "Quantum turbulence: from superfluid helium to atomic Bose–Einstein condensates," Contemporary Physics **50**, 463–475 (2009).

[34] M. S. Paoletti, M. E. Fisher, K. R. Sreenivasan, and D. P. Lathrop, "Velocity statistics distinguish quantum turbulence from classical turbulence," Physical Review Letters **101**, 154501 (2008).

[35] R. P. Feynman, "Application of quantum mechanics to liquid helium," in *Progress in low temperature physics*, Vol. 1 (Elsevier, 1955), pp. 17–53.

[36] D. Poole, H. Scoffield, C. Barenghi, and D. Samuels, "Geometry and topology of superfluid turbulence," Journal of Low Temperature Physics **132**, 97–117 (2003).

[37] K. Schwarz, "Three-dimensional vortex dynamics in superfluid He 4: Homogeneous superfluid turbulence," Physical Review B **38**, 2398 (1988).

91

[38] A. C. White, B. P. Anderson, and V. S. Bagnato, "Vortices and turbulence in trapped atomic condensates," Proceedings of the National Academy of Sciences, 201312737 (2014).

[39] F. Dalfovo, S. Giorgini, L. P. Pitaevskii, and S. Stringari, "Theory of Bose–Einstein condensation in trapped gases," Rev. Mod. Phys. **71**, 463–512 (1999).

[40] A. S. Bradley and B. P. Anderson, "Energy spectra of vortex distributions in two-dimensional quantum turbulence," Physical Review X **2**, 041001 (2012).

[41] L. M. Pismen, *Vortices in nonlinear fields: from liquid crystals to super-fluids, from non-equilibrium patterns to cosmic strings*, Vol. 100 (Oxford University Press, 1999).

[42] B. Halperin, "Statistical mechanics of topological defects," in *Physics of defects*, edited by R. Balian et al. (North Holland, Amsterdam, 1981).

[43] G. F. Mazenko, "Vortex Velocities in the $O(n)$ Symmetric Time-Dependent Ginzburg–Landau Model," Physical Review Letters **78**, 401–404 (1997).

[44] G. F. Mazenko, "Defect statistics in the two-dimensional complex Ginzburg–Landau model," Physical Review E **64**, 016110 (2001).

[45] J. H. Kim, W. J. Kwon, and Y. Shin, "Role of thermal friction in relaxation of turbulent Bose–Einstein condensates," Physical Review A **94**, 033612 (2016).

[46] A. J. Groszek, T. P. Simula, D. M. Paganin, and K. Helmerson, "Onsager vortex formation in Bose–Einstein condensates in two-dimensional power-law traps," Physical Review A **93**, 043614 (2016).

[47] A. L. Fetter and A. A. Svidzinsky, "Vortices in a trapped dilute Bose–Einstein condensate," Journal of Physics: Condensed Matter **13**, R135 (2001).

[48] R. Numasato, M. Tsubota, and V. S. L'vov, "Direct energy cascade in two-dimensional compressible quantum turbulence," Physical Review A **81**, 063630 (2010).

[49] R. Numasato and M. Tsubota, "Possibility of inverse energy cascade in two-dimensional quantum turbulence," Journal of Low Temperature Physics **158**, 415 (2010).

[50] M. T. Reeves, B. P. Anderson, and A. S. Bradley, "Classical and quantum regimes of two-dimensional turbulence in trapped Bose–Einstein condensates," Physical Review A **86**, 053621 (2012).

[51] M. T. Reeves, T. P. Billam, B. P. Anderson, and A. S. Bradley, "Inverse energy cascade in forced two-dimensional quantum turbulence," Physical Review Letters **110**, 104501 (2013).

[52] C. Nore, M. Abid, and M. Brachet, "Kolmogorov turbulence in low-temperature superflows," Physical Review Letters **78**, 3896 (1997).

[53] A. W. Baggaley and C. F. Barenghi, "Vortex-density fluctuations in quantum turbulence," Physical Review B **84**, 020504 (2011).

[54] A. W. Baggaley, J. Laurie, and C. F. Barenghi, "Vortex-density fluctuations, energy spectra, and vortical regions in superfluid turbulence," Physical Review Letters **109**, 205304 (2012).

[55] P.-E. Roche, P. Diribarne, T. Didelot, O. Français, L. Rousseau, and H. Willaime, "Vortex density spectrum of quantum turbulence," EPL (Europhysics Letters) **77**, 66002 (2007).

[56] P.-E. Roche and C. F. Barenghi, "Vortex spectrum in superfluid turbulence: interpretation of a recent experiment," EPL (Europhysics Letters) **81**, 36002 (2008).

[57] Y. Kim, D. Jang, and J. Greer, "Insights into deformation behavior and microstructure evolution in nb single crystalline nano-pillars under uniaxial tension and compression," Scripta Materiala **61**, 300–3 (2009).

[58] J. Weiss, W. B. Rhouma, T. Richeton, S. Dechanel, F. Louchet, and L. Truskinovsky, "From mild to wild fluctuations in crystal plasticity," Physical Review Letters **114**, 105504 (2015).

[59] R. LeSar, "Simulations of dislocation structure and response," Annual Review of Condensed Matter Physics **5**, 375–407 (2014).

[60] A. Spencer, *Continuum mechanics* (Dover Publications, 2004).

[61] C. Amrouche, P. G. Ciarlet, L. Gratie, and S. Kesavan, "On Saint Venant's compatibility conditions and Poincaré's lemma," Comptes Rendus Mathematique **342**, 887–891 (2006).

[62] A. M. Kosevich, "Crystal dislocations and the theory of elasticity," in *Dislocations in solids*, Vol. 1, edited by F. R. N. Nabarro (North-Holland, New York, 1979), p. 33.

[63] M. Peach and J. Koehler, "The forces exerted on dislocations and the stress fields produced by them," Physical Review **80**, 436 (1950).

93

[64] B. L. Holian and P. S. Lomdahl, "Plasticity induced by shock waves in nonequilibrium molecular-dynamics simulations," Science **280**, 2085–2088 (1998).

[65] V. Yamakov, D. Wolf, S. R. Phillpot, A. K. Mukherjee, and H. Gleiter, "Dislocation processes in the deformation of nanocrystalline aluminium by molecular-dynamics simulation," Nature materials **1**, 45 (2002).

[66] K. R. Elder and M. Grant, "Modeling elastic and plastic deformations in nonequilibrium processing using phase field crystals," Physical Review E **70**, 051605 (2004).

[67] K. R. Elder, M. Katakowski, M. Haataja, and M. Grant, "Modeling elasticity in crystal growth," Physical Review Letters **88**, 245701 (2002).

[68] K. R. Elder, N. Provatas, J. Berry, P. Stefanovic, and M. Grant, "Phase-field crystal modeling and classical density functional theory of freezing," Physical Review B **75**, 064107 (2007).

[69] S. van Teeffelen, R. Backofen, A. Voigt, and H. Löwen, "Derivation of the phase-field-crystal model for colloidal solidification," Physical Review E **79**, 051404 (2009).

[70] B. P. Athreya, N. Goldenfeld, and J. A. Dantzig, "Renormalization-group theory for the phase-field crystal equation," Physical Review E **74**, 011601 (2006).

[71] N. Goldenfeld, B. P. Athreya, and J. A. Dantzig, "Renormalization group approach to multiscale simulation of polycrystalline materials using the phase field crystal model," Physical Review E **72**, 020601 (2005).

[72] D.-H. Yeon, Z.-F. Huang, K. R. Elder, and K. Thornton, "Density-amplitude formulation of the phase-field crystal model for two-phase coexistence in two and three dimensions," Philosophical Magazine **90**, 237–263 (2010).

[73] P. Stefanovic, M. Haataja, and N. Provatas, "Phase-field crystals with elastic interactions," Physical Review Letters **96**, 225504 (2006).

[74] S. Majaniemi, M. Nonomura, and M. Grant, "First-principles and phenomenological theories of hydrodynamics of solids," The European Physical Journal B **66**, 329–335 (2008).

[75] V. Heinonen, C. Achim, and T. Ala-Nissila, "Long-wavelength properties of phase-field-crystal models with second-order dynamics," Physical Review E **93**, 053003 (2016).

[76] V. Heinonen, C. V. Achim, K. R. Elder, S. Buyukdagli, and T. Ala-Nissila, "Phase-field-crystal models and mechanical equilibrium," Physical Review E **89**, 032411 (2014).

[77] V. Heinonen, C. Achim, J. Kosterlitz, S.-C. Ying, J. Lowengrub, and T. Ala-Nissila, "Consistent hydrodynamics for phase field crystals," Physical review letters **116**, 024303 (2016).

[78] V. Heinonen et al., "Phase field crystal models and fast dynamics," (2016).

[79] S. M. Cox and P. C. Matthews, "Exponential time differencing for stiff systems," Journal of Computational Physics **176**, 430–455 (2002).

[80] R. I. McLachlan and P. Atela, "The accuracy of symplectic integrators," Nonlinearity **5**, 541 (1992).

[81] M. Hÿtch, E. Snoeck, and R. Kilaas, "Quantitative measurement of displacement and strain fields from HREM micrographs," Ultramicroscopy **74**, 131–146 (1998).

[82] G. Boffetta, D. Bernard, A. Celani, and G. Falkovich, "Conformal invariance in two-dimensional turbulence," in *Advances in turbulence xi* (Springer, 2007), pp. 164–166.

[83] P.-H. Chavanis, "Kinetic theory of point vortices: diffusion coefficient and systematic drift," Physical Review E **64**, 026309 (2001).

[84] E. Rickinson, N. G. Parker, A. W. Baggaley, and C. F. Barenghi, "Diffusion of quantum vortices," Phys. Rev. A **98**, 023608 (2018).

[85] P. Wiegmann and A. G. Abanov, "Anomalous hydrodynamics of two-dimensional vortex fluids," Physical Review Letters **113**, 034501 (2014).

Part II

Papers

Paper I

Vortex clustering and universal scaling laws in two-dimensional quantum turbulence
Audun Skaugen and Luiza Angheluta
Physical Review E **93**, 032106 (2016)
Reference: [1]

Vortex clustering and universal scaling laws in two-dimensional quantum turbulence

Audun Skaugen[*] and Luiza Angheluta

Department of Physics, University of Oslo, P.O. 1048 Blindern, 0316 Oslo, Norway

(Received 27 November 2015; published 7 March 2016)

We investigate numerically the statistics of quantized vortices in two-dimensional quantum turbulence using the Gross-Pitaevskii equation. We find that a universal $-5/3$ scaling law in the turbulent energy spectrum is intimately connected with the vortex statistics, such as number fluctuations and vortex velocity, which is also characterized by a similar scaling behavior. The $-5/3$ scaling law appearing in the power spectrum of vortex number fluctuations is consistent with the scenario of passive advection of isolated vortices by a turbulent superfluid velocity generated by like-signed vortex clusters. The velocity probability distribution of clustered vortices is also sensitive to spatial configurations, and exhibits a power-law tail distribution with a $-5/3$ exponent.

I. INTRODUCTION

Richardson's cascade picture of turbulence captures, in essence, the transport of energy across scales in *three-dimensional* (3D) classical fluids: Energy is injected at large scale, and a self-similar breakdown of vortices transports energy down to the dissipative, small scales. This *direct* energy cascade develops because the kinetic energy in 3D turbulence is the dominant statistically invariant quantity, and is associated with Kolmogorov's law for the energy spectrum $E(k) \sim k^{-5/3}$ for wave numbers k in the inertial range, i.e., between the injection and dissipation scales.

By contrast, *two-dimensional* (2D) classical turbulence manifests itself in a spectacularly different way due to the absence of vortex stretching and twisting. Apart from the kinetic energy, the total vorticity is also a statistical invariant which leads to two inertial cascades, namely, an *inverse* energy cascade from small to large scales with the emergence of coherent rotating structures at large scales, and a direct cascade of enstrophy associated with the conservation of vorticity [1]. Even though the energy flows in the opposite direction, the turbulent energy spectrum still follows the Kolmogorov $k^{-5/3}$ law in the inverse cascade regime, up to the injection scale below which it crosses over to a k^{-3} scaling associated with the forward enstrophy cascade [1]. There is no full consent on the physical mechanism behind the inverse energy cascade. In fact, several physical processes have been proposed, such as Kraichnan's picture of "thinning" of small-scale vorticity by strain at large scale [2,3], and the Onsager's picture of *clustering* of same-signed vortices [4].

Albeit the turbulence phenomenon and its spectral energy transport emerge from the formation and interaction of vortices, the relationship between the statistical properties of turbulence and vortex dynamics is still an open and challenging problem. The role of vortices as the primary structures in turbulence has been long recognized since the pioneering work of Onsager on the statistical description of 2D turbulence in terms of an ensemble of interacting point vortices [4]. This reduction of turbulence to a complex bundle of vortices has become an effective way of studying turbulence since the realization of turbulent states in quantum fluids [5,6], and the

remarkable discovery that quantum turbulence shares similar large-scale statistical properties as classical turbulence [5,7].

Unlike classical vortices which have a diffusive, continuous size and vorticity, quantum vortices are defined by a quantized circulation, i.e., $\Gamma = \oint_C \vec{v} \cdot d\vec{l} = n\kappa$, where n is an integer and $\kappa = h/m$ is the quantum circulation, which leads to vortex filaments (in three dimensions) and pointlike vortices (in two dimensions) with well-defined vortex cores. Quantum turbulence is generally referred to as a complex tangle of these quantized vortices. Despite their quantum nature, the turbulent energy spectrum generated by the interaction of these vortices is characterized by Kolmogorov's classical $k^{-5/3}$ scaling law on scales larger than the mean separation between vortices in superfluids [5] and Bose Einstein condensates [6]. The similarity between classical and quantum turbulence underscores the universality of turbulence, and the approach to turbulence from vortex dynamics.

In 3D quantum turbulence, the energy spectrum is associated with a *direct* energy cascade [5,8]. The vortex statistics in the turbulent regime has a particular signature. For instance, vortex line density L is a fluctuating quantity due to vortex interactions. Its frequency power spectrum density decreases as $f^{-5/3}$, which is at odds with the classical interpretation of L as a measure of superfluid vorticity, $\omega = \kappa L$ [9]. However, this puzzle was cleared out by a phenomenological model in which the vortex line density L is decomposed into polarized and unpolarized filaments, and the analogy to a passive field advection by turbulence is used to explain the $f^{-5/3}$ spectrum [9–11]. This scaling law of the power spectrum of vortex line fluctuations was observed experimentally in both ^{4}He [12] and ^{3}He-B [13], as well as in numerical simulations of vortex filament model [10,11]. In addition to the vortex line statistics, the fluctuations in the superfluid turbulent velocity are also broadly distributed and characterized by a universal v^{-3} power-law tail which has been reported experimentally in superfluids [14] and in numerical simulations of 3D trapped Bose-Einstein condensates using the Gross-Pitaevskii equation and the vortex model [15].

While a Kolmogorov $-5/3$ scaling regime in the incompressible kinetic energy spectrum has also been observed in 2D quantum turbulence, the direction of the energy cascade here is more controversial because the compressibility of quantum fluids introduces additional small-scale dissipation by pair-vortex annihilations with phonon emission [16–19]. Since

_____
[*]audun.skaugen@fys.uio.no

it is more tricky to determine the energy flux across scales due to vortex-phonon interactions, the cascade is typically inferred by indirect methods. In systems where energy is injected at long wavelengths and dissipation is most effective at small scales due to compressibility effects and vortex annihilations, a *direct* energy cascade is proposed to dominate the inertial scaling. This was inferred either from the temporal evolution of the energy spectrum [16,20], or the energy flux across a black-hole event horizon in a holographic gravity dual model of superfluid turbulence [20]. On the contrary, an *inverse* energy cascade is attributed to the dynamical regime dominated by vortex clustering and energy injection on scales comparable to the vortex-core size [17,18,21]. Vortex clustering serves to suppress annihilation events, restoring the conservation of enstrophy in a statistical sense. Several numerical studies of the 2D Gross-Pitaevskii equation and point vortex model [17–19,21] have been focusing on the effect of vortex clustering on the inverse cascade of the incompressible kinetic energy.

The aim of this paper is to study the particular signature of an inverse energy cascade on the statistical properties of vortices. We use the damped Gross-Pitaevskii equation with a stirring potential as proposed in Ref. [17], which can simulate a statistically steady state turbulent regime of a 2D trapped BEC undergoing stirring, where vortices are emitted in clusters in the wake of the stirring obstacle. As shown previously [17], the incompressible energy spectrum develops a $k^{-5/3}$ power law in the clustering regime. By investigating the effect of vortex clustering on the vortex statistics, we find that both the power spectrum of vortex number fluctuations and the distribution of clustered vortex velocities are characterized by a universal power-law behavior with a $-5/3$ exponent, similar to the scaling law for the energy spectrum.

The structure of the paper is as follows. In Sec. II, we present the damped Gross-Pitaevskii model with a Gaussian stirring potential for simulating 2D turbulence in trapped Bose-Einstein condensates (BECs). The numerical method of tracking vortices and the clustering algorithm for finding clusters of like-signed vortices are detailed in Sec. III. The incompressible energy spectrum is discussed in Sec. IV, while the statistics of vortex number fluctuations and vortex velocity fluctuations are presented in Secs. V and VI. Finally, Sec. VII contains a brief summary and concluding remarks.

II. GROSS-PITAEVSKII EQUATION

We consider a 2D Bose-Einstein condensate described by the wave function $\psi(\vec{r},t)$, with $|\psi|^2$ related to the particle density of the condensate. The evolution of the wave function $\psi(\vec{r})$ is described in the mean-field approximation by the damped Gross-Pitaevski equation (dGPE). We use an augmented GPE with a time-dependent external potential for generating statistically steady state quantum turbulence as proposed in Ref. [17]. In two dimensions, the dynamics is described by

$$\frac{\partial \psi}{\partial t} = (i + \gamma)\left(\frac{1}{2}\nabla^2 + 1 - V(\vec{r},t) - g|\psi|^2\right)\psi, \quad (1)$$

with the damping rate γ which models phenomenologically the energy dissipation by interaction with a thermal bath. Equation (1) is written in dimensionless units by appropriate rescaling of space and time in characteristic units of the coherence length ξ and typical time $\xi/c = \hbar/\mu$, where $c = \sqrt{\mu/m}$ is the speed of sound determined by the chemical potential μ and the particle's mass m. The parameter g describes the nonlinear self-interaction of the condensate, and can be eliminated from the equation by a rescaling of the wave function $\psi \to \sqrt{g}\psi$, thus

$$\frac{\partial \psi}{\partial t} = (i + \gamma)\left(\frac{1}{2}\nabla^2 + 1 - V(\vec{r},t) - |\psi|^2\right)\psi. \quad (2)$$

The time-dependent external potential $V(\vec{r},t)$ is measured in units of chemical potential μ, and consists of a trapping potential $V_t(\vec{r})$ and a time-dependent stirring potential $V_{\text{ext}}(\vec{r},t)$ used to generate quantum turbulence as proposed in Ref. [17]. The trap is given by the harmonic potential as

$$V_t(\vec{r}) = \frac{1}{2}\omega_t^2 r^2, \quad (3)$$

such that it causes the Thomas-Fermi solution of ψ to vanish when the harmonic potential exceeds the chemical potential, thus for radii larger than the Thomas-Fermi length $R_{TF} = \sqrt{2}/\omega_t$. Given a desired size of R_{TF} of the condensate, we can therefore choose the parameter as $\omega_t = \sqrt{2}/R_{TF}$.

The time-dependent stirring potential $V_{\text{ext}}(\vec{r},t)$ is given by a Gaussian obstacle centered at $\vec{r}_{\text{ext}}(t)$,

$$V_{\text{ext}}(\vec{r},t) = V_0 \exp\left\{-\frac{|\vec{r} - \vec{r}_{\text{ext}}(t)|^2}{w^2}\right\}, \quad (4)$$

where $V_0 > 1$ is the height of the obstacle, and the width is set to $w = 4\xi$. The center of the obstacle moves in a circle of radius $R_{\text{ext}} = 0.4R_{TF}$ with a speed v_{ext}, so that

$$\vec{r}_{\text{ext}}(t) = R_{\text{ext}}\left[\cos\left(\frac{v_{\text{ext}}}{R_{\text{ext}}}t\right)\vec{i} + \sin\left(\frac{v_{\text{ext}}}{R_{\text{ext}}}t\right)\vec{j}\right], \quad (5)$$

where $\vec{i}$ and $\vec{j}$ are unit vectors in the x-y plane.

We set the values of the model parameters in the parameter space associated with the turbulent regime [17]. We consider the particular values $V_0 = 1.4\mu$, $R_{TF} = 0.8 \times 256\xi$, and $\gamma = 0.009$, and vary the stirring speed v_{ext} of the Gaussian obstacle so that we obtain a more robust clustering of vortices in the wake of the obstacle.

We solve the dGPE from Eq. (2) numerically by using spectral methods with exponential time differencing, and study different dynamical regimes depending on the different values of the stirring speed v_{ext}.

III. TRACKING AND CLUSTERING OF VORTICES

We locate the position and velocity of quantized vortices directly from the wave funtion ψ using the field formulation of Halperin [22] and Mazenko [23]. A similar numerical implementation of this method was studied numerically for Ginzburg-Landau and Swift-Hohenberg dynamics in Ref. [24]. The key insight behind this method is that vortices occur exactly where the wave function vanishes inside the Thomas-Fermi radius, i.e., for $V < \mu$. The zeros of the $\psi(\vec{r},t)$ field can be related to the density of vortices $\rho(\vec{r},t)$ by the transformation
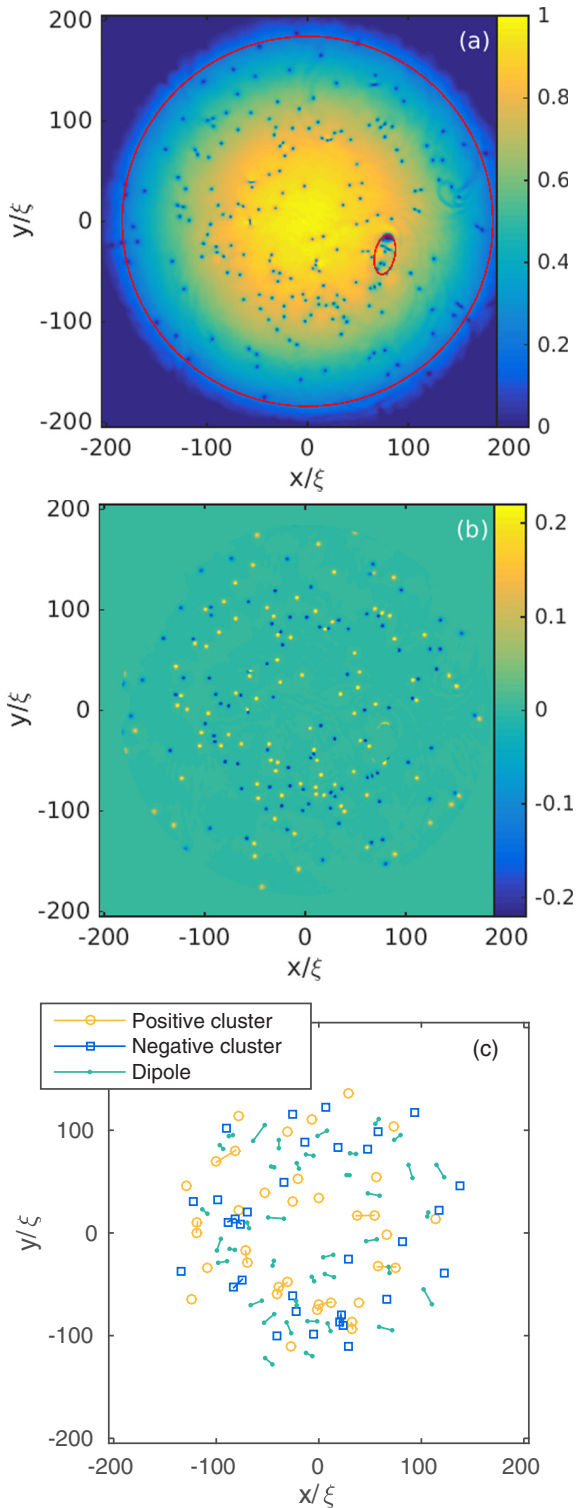
FIG. 1. Time snapshot of (a) the density field $|\psi|$, (b) the measure of the quantized vorticity, and (c) clustering of the like-signed vortices.

$\rho(\vec{r},t) = \delta(\psi)\mathcal{D}(\vec{r},t)$, with the Jacobian determinant given by [23,24]

$$\mathcal{D} = \begin{vmatrix} \partial_x \operatorname{Re} \psi & \partial_y \operatorname{Re} \psi \\ \partial_x \operatorname{Im} \psi & \partial_y \operatorname{Im} \psi \end{vmatrix} = \operatorname{Im}(\partial_x \psi^* \partial_y \psi). \quad (6)$$

This Jacobian field is zero everywhere except within a vortex core, and its sign indicates the rotational direction of the vortex. We can therefore apply a threshold to the determinant in order to locate these vortex cores. However, due to the presence of the external potential V, the maximum value of $\mathcal{D}$ will vary roughly as $|\psi_{TF}|^2 = 1 - V$. We therefore normalize the field $\mathcal{D}$ by this factor, and search for regions where $\mathcal{D}/(1 - V)$ exceeds a given threshold. There are two spatial regions where this method becomes inapplicable. One is the boundary region close to R_{TF}, where the wave function vanishes quickly. The other one is the stirring obstacle and its wake where a dense collection of vortices are frequently nucleated and vortex cores might not be isolated from each other. To remove these boundary effects, we apply two masks to the normalized $\mathcal{D}$ field before applying the threshold. The boundaries of these masks are drawn on the absolute value of the wave function in Fig. 1(a), and correspond to setting to zero the value of $\mathcal{D}$ outside a circle of radius $0.9R_{TF}$ and inside an ellipse with the stirrer at one focus. The resulting normalized $\mathcal{D}$ field with these boundary masks applied is shown in Fig. 1(b).

Vortex positions can now be located by calculating the center of mass of each connected region found. As discussed in the Introduction, an inverse energy cascade is associated with clustering of vortices of the same circulation. We therefore implement a clustering algorithm using the method outlined in Ref. [18]. In this algorithm, a pair of oppositely charged vortices are considered a dipole if they are closer to each other than either is to any other vortex. Two like-charged vortices are considered part of the same cluster if they are closer to each other than either is to any oppositely charged nondipole vortex. The resulting vortex positions and the clusters of like-signed vortices are shown in Fig. 1(c).

The clustering analysis allows us to measure the *clustered fraction*, defined as the number of *clustered* vortices relative to the total number of vortices. The fluctuations in the clustered fraction is compared with those in the number of vortices as shown in Fig. 2 for different values of the stirring velocity. We notice that the vortex count is increasing from zero and then is fluctuating around a steady-state value after a few rounds of the stirring obstacle. There is an initial spike in clustering, as the stirring obstacle readily creates clusters. This high amount of clustering is however not sustainable, and the clustered fraction settles at a lower level. The vortex counts fluctuate very little in the initial stages, when the amount of clustering is large. This makes sense because clustered vortices seldom interact with opposite-signed vortices to annihilate with. As the amount of clustering settles down, the fluctuations increase in strength. We also observe that there is a tendency for the clustered fraction to fluctuate towards larger values when the stirring obstacle moves slower.

IV. ENERGY SPECTRUM

Quantum turbulence in BECs is characterized by a cascade of energy across inertial scales analogous to that of a turbulent flow in classical fluids. An energy cascade is associated with a kinetic energy spectrum which exhibits a $-5/3$ power law over the inertial wave numbers. The classical energy spectrum is obtained by a spectral decomposition of the kinetic energy
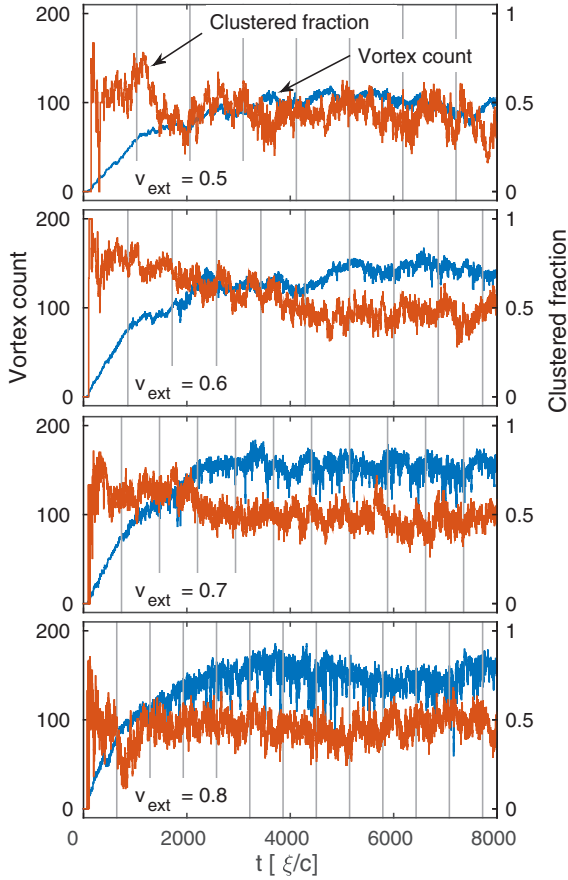
FIG. 2. Time windows of the vortex density fluctuations versus fraction of vortex clusters for different values of the stirring velocity v_{ext}. Vertical lines mark times where the stirrer has moved in a complete circle around the condensate.

of an incompressible fluid,

$$E_{kinetic} = \frac{1}{2} \int d^2\vec{r}\, \rho v^2 = \int dk\, E(k), \qquad (7)$$

where the classical fluid density ρ is constant, and the energy spectrum is the accumulated energy in a shell in the $\vec{k}$ space,

$$E(k) = \int_{|\vec{k}|=k} d^2\vec{k}\, \mathcal{E}(\vec{k}). \qquad (8)$$

Using homogeneity and the convolution theorem, this spectral density can be calculated from the Fourier-transformed velocities as

$$\mathcal{E}(\vec{k}) = \frac{1}{2}\rho \vec{v}(\vec{k}) \cdot \vec{v}(-\vec{k}). \qquad (9)$$

By analogy, the same definition of the energy spectrum for the BEC holds, but with two modifications due to the compressibility of a quantum fluid [25]. First, as the density of the superfluid is not constant, the superfluid velocity field obtained by the Madelung transformation must be weighted by the square root of the density as

$$\vec{u}(\vec{r}) = \sqrt{\rho(\vec{r})}\nabla \theta(\vec{r}), \qquad (10)$$

where $\theta(\vec{r})$ is the phase of the wave function ψ. Second, this weighted velocity field is decomposed into compressible and
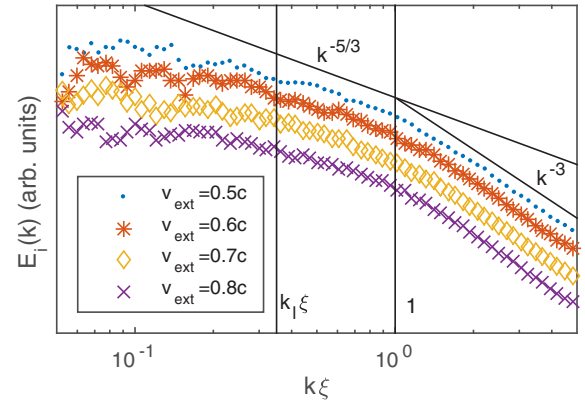
FIG. 3. Log-log plot of the incompressible energy spectra at $t = 5060\xi/c$ for the various stirring velocities. The two vertical lines mark $k\xi = 1$, where the core structure becomes important, and the approximate wave number $k_l = 2\pi/l$ corresponding to the mean intervortex distance l. The different spectra are shifted vertically for comparison.

incompressible parts, as follows:

$$\vec{u} = \vec{u}_c + \vec{u}_i, \text{ where } \nabla \cdot \vec{u}_i = 0 \text{ and } \nabla \times \vec{u}_c = 0. \qquad (11)$$

The incompressible energy spectrum is then calculated as

$$E_i(k) = \int_{|\vec{k}|=k} d^2\vec{k}[\vec{u}_i(\vec{k}) \cdot \vec{u}_i(-\vec{k})]. \qquad (12)$$

We calculate the incompressible energy spectrum from Eq. (12) for different speeds of the stirring obstacle and the result is shown in Fig. 3. We notice that at wave numbers larger than $1/\xi$ (corresponding to scales smaller than $2\pi\xi$), the energy spectrum follows a universal k^{-3} power-law tail independent of the stirring velocity and the model parameters. Although the -3 exponent is the same as that for the enstrophy cascade in two-dimensional classical turbulence, in the case of quantum turbulence this regime is determined by the quantum vortex core structure [21]. The energy injection scale falls in the intermediate scales between the vortex core size and the mean vortex separation l, where the k^{-3} scaling also crosses over to a different regime. On length scales larger than l but smaller than the Thomas-Fermi radius, equivalently for $2\pi/R_{FT} < k < 2\pi/l$, a $k^{-5/3}$ starts to develop in association to vortex clustering. Admittedly, this wave-number range is too narrow to confidently claim the existence of an inertial scaling regime, although it was assumed in previous similar studies [17,18]. In fact, it was recently shown in Ref. [19] that an accidental $k^{-5/3}$ may occur as a crossover regime between the two asymptotic scaling regimes of the energy spectrum of isolated vortices, i.e., k^{-1} at large k's and k^{-3} at small k's, and that it disappears when the effect of vortex-core size is removed. To test that the $k^{-5/3}$ is indeed a true scaling regime, but very limited by finite size effects and an insufficient separation of scales, we seek to control these effects by separating out the contribution due to vortex clusters.

Energy spectrum of clustered vortices

One possible reason for the poor Kolmogorov scaling signal in Fig. 3 is the fact that there are many more isolated vortices

and dipoles compared to vortex clusters, as we can see in Fig. 2. Another important effect that we believe may dominate the statistics is the limited separation of scales between the Thomas-Fermi radius and the mean vortex separation.

As discussed in previous works, e.g., [17–19,21], the inverse energy cascade in two-dimensional quantum turbulence is attributed to clustering of like-signed vortices. In order to isolate the contributions of clustered vortices to the energy spectra, we use the analytical approach from Ref. [21] to calculate the energy spectrum resulting from a given configuration of vortices taken from our numerical simulations of the dGPE.

Based on the superposition principle of the velocity induced by N well-separated vortices, the incompressible energy spectrum can be determined by the energy spectrum of a single vortex and the configurational distribution function of vortices as [21]

$$E_i^N(k) \propto F_\Lambda(k\xi) G_N(k), \tag{13}$$

where $F_\Lambda(k\xi)$ is the single-vortex energy spectrum calculated as

$$F_\Lambda(k\xi) = \Lambda^{-1} f(k\xi \Lambda^{-1}), \tag{14}$$

with Λ being the slope of the wave function of the center of the vortex core and

$$f(z) = \frac{z}{4}\left[I_1\left(\frac{z}{2}\right)K_0\left(\frac{z}{2}\right) - I_0\left(\frac{z}{2}\right)K_1\left(\frac{z}{2}\right)\right]^2. \tag{15}$$

The configurational function $G_N(k)$ for N vortices with positions $\vec{r}_p$ and circulation signs $\kappa_p = \pm 1$ is calculated as [21]

$$G(k) = 1 + \frac{2}{N}\sum_{p=1}^{N-1}\sum_{q=p+1}^{N}\kappa_p\kappa_q J_0(k|\vec{r}_p - \vec{r}_q|). \tag{16}$$

We use the clustering analysis described in the previous section to extract the position of clustered vortices from vortex configurations obtained numerically. We then calculate the separate contribution to the energy spectrum of various subsets of vortices using Eq. (13). The result is illustrated in Fig. 4.
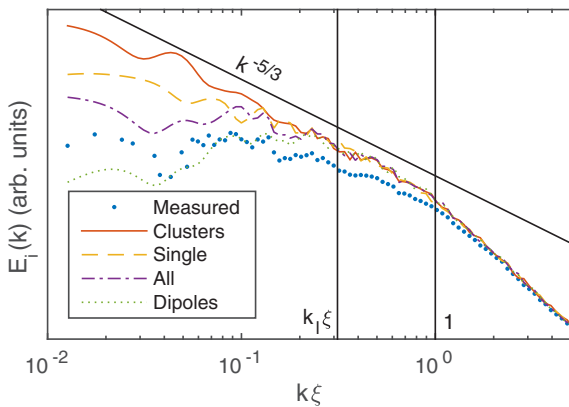
The energy spectrum due to all vortices follows the measured energy spectrum closely, apart from lower measured energies at low wave numbers. This is because the analytical solution does not take into account the density profile of the superfluid, which drops off to lower values at larger scales. If we isolate the contribution of vortex clusters, the Kolmogorov $k^{-5/3}$ scaling laws extend to much smaller wave numbers, and approaches a decade of scaling. Also, we have checked that this scaling law persists for $k < 2\pi/l$ even when we remove the effect of the core size.

V. VORTEX NUMBER FLUCTUATIONS

To understand the connection between the statistical properties of turbulence, e.g., energy spectrum and vortex dynamics, we study the statistics of vortex number fluctuations and vortex velocity.

We investigate the effect of the vortex clustering on vortex number fluctuations, in terms of their power spectrum. Temporal fluctuations of vortex counts are marked by a transient period due to the nucleation of vortices in the wake of the stirring obstacle. This transient time is excluded from the statistics, therefore we look at fluctuations in the steady-state regime, i.e., $t > 4000\xi/c$. The resulting power spectra are shown in Fig. 5. We see a power-law decay with an exponent close to $-5/3$, at least for the lower values of the stirring velocities.

The same power-law exponent for the power spectra of the vortex line density was reported experimentally and numerically for 3D counterflow turbulence in the superfluid helium [10–12]. A phenomenological explanation of this scaling behavior based on the passive advection by turbulence was proposed in Ref. [9]. The argument is that the vortex line density L can be decomposed into two parts, $L_{||} + L_\times$, which behave differently. The *polarized* vortex line density $L_{||}$ consists of vortex lines arranged in parallel, so as to set up a large-scale rotational flow which follows the $k^{-5/3}$ spectrum of the turbulent normal fluid. The *unpolarized* part, $L_\times$, is a complex tangle of vortices, so that the resulting velocity field tends to cancel out. Because of this cancellation, the unpolarized vortex lines do not actively affect the velocity field and can be considered as a *passive vector*, which is simply advected by the normal fluid. Hence, the spatial fluctuations

FIG. 4. Analytical incompressible energy spectra calculated from the vortex configuration found at $t = 5060\xi/c$ with $v_{ext} = 0.5c$. This is compared to the numerical energy spectrum directly calculated from the velocity field, as described in Sec. IV.
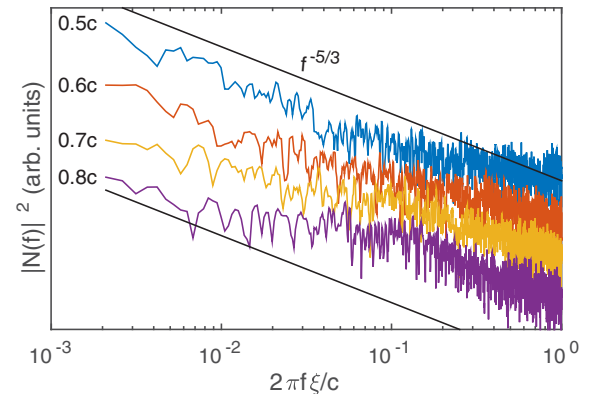

FIG. 5. Log-log plots of the power spectra of vortex number fluctuations, at different stirring velocities. The spectra are shifted vertically to keep them from overlapping.
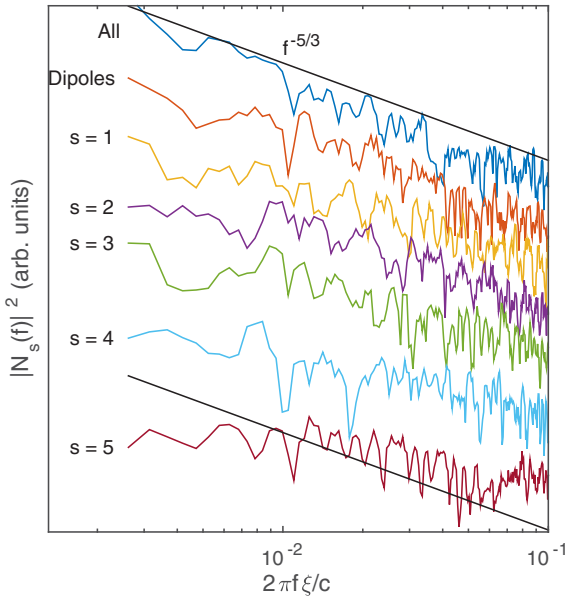
FIG. 6. Power spectra for the number of vortices contained in clusters of a given size s, with $v_{ext} = 0.5c$. The larger the cluster size, the more the power spectrum falls off from the $f^{-5/3}$ power law at low frequencies.

of the $L_\times$ field follows the same $k^{-5/3}$ scaling as that of a passive scalar advected by the turbulence in the Obukhov-Corrsin theory [26–28]. By Taylor's frozen hypothesis, the frequency power spectrum has the same scaling form as the wave-number power spectrum, hence $f^{-5/3}$. The fluctuations in the total line density is dominated by the $L_\times$ fluctuations, because the polarized vortices tend not to interact by reconnections.

We propose that a similar scenario also holds in two dimensions and can account for the $f^{-5/3}$ power spectrum of vortex counts. The vortex density n can be decomposed into the density of *clustered* vortices n_c and the density of unclustered vortices n_u. The clustered vortices set up a velocity field $\vec{v}_c$ which follows the $k^{-5/3}$ scaling, as discussed in the previous section. Their density does not fluctuate as rapidly as that of the isolated vortices, i.e., clustered vortices can be envisaged as the persistent structures. The unclustered vortices do not contribute to the energy scaling, but are passively advected by the $\vec{v}_c$ field. Hence the temporal fluctuations in the vortex counts is dominated by those of the isolated vortices and, using the passive scalar analogy, the power spectrum is described by a $f^{-5/3}$ on time scales corresponding to the inertial-convective regime.

In Fig. 6, we show that indeed the power spectrum of isolated vortices follows a $f^{-5/3}$ scaling consistent with the passive advection model, whereas the scaling regime tends to disappear as we look at vortex clusters of increasing size.

VI. VORTEX VELOCITY STATISTICS

As discussed in Sec. IV, the kinetic energy spectrum is calculated from the superfluid velocity field given by Madelung transform as $\vec{v}_s = \nabla\phi$, where ϕ is the phase of the wave function ψ. The statistics of large turbulent velocity

fluctuations is however dominated by the single-vortex effects. It is known that the probability distribution of the velocity induced by a single point vortex has a power-law tail given by $p(v_s) \sim v_s^{-3}$, which can also be predicted from a simple scaling argument. Given that the velocity induced by an isolated vortex decays as $1/r$ at the distance r from the vortex, then from the transformation of variables in the probabilities, $p(v_s)dv_s = q(r)dr$, it follows that $p(v_s) = q[r(v_s)]|\frac{\partial r}{\partial v_s}|$ where $q(r)dr$ is the probability of finding a vortex between r and $r + dr$. Thus, for a uniform distribution of isolated vortices in the plane, $q(r) \propto r$, it follows that $p(v_s) \sim v_s^{-3}$. This can also be derived from the point vortex model for configurations of N uniformly distributed vortices [29].

Because high velocity fluctuations are induced in the proximity of a vortex, and the distance between vortices is bounded below by the vortex size $\sim\xi$, the single-vortex velocity distribution dominates the high-velocity tail, at least for $v_s > c$. This is one reason that it has also been observed experimentally in quantum turbulence in superfluids [14] and reproduced numerically in BEC [15]. However, because the tail distribution of the superfluid velocity is dominated by contribution of single vortices, it cannot be used as a measure which can signal a turbulent cascade.

On the other hand, the statistics of vortex velocities is an indicator of vortex clustering hence can be used as an indirect way to determine if the quantum turbulence exhibits an inverse energy cascade. As shown in Refs. [21,30], the $k^{-5/3}$ energy spectrum is associated with vortex clusters, where vortices follow a fractal spatial distribution inside a cluster with the probability distribution $q(r) \sim r^{-1/3}$. The simple scaling argument predicts that such clustering gives rise instead to a $v^{-5/3}$ power-law tail. In a separate study [31], we show that the $v^{-5/3}$ also follows from the point-vortex model with a nonuniform distribution of vortices. In principle, this scaling appears in the superfluid velocity distribution at intermediate velocities $v_s < c$, but it may be difficult to observe it in practice if there are not sufficiently many vortex clusters compared to isolated vortices.

In order to sample cluster velocities more efficiently we turn to the vortex velocities. The method of locating vortices from the zeros of the wave function ψ also provides a way of calculating the velocity of a vortex from the time derivative and gradients of ψ [24]. Namely, the velocity of a vortex located at position $\vec{r}$ is determined by the current of vortex charge, and given as

$$v_x = \frac{1}{\mathcal{D}} \text{Im}(\dot{\psi}\partial_y\psi^*), \quad v_y = -\frac{1}{\mathcal{D}} \text{Im}(\dot{\psi}\partial_x\psi^*). \quad (17)$$

Numerically, we calculate the weighted average of this value across the region where $\mathcal{D}$ exceeds a threshold.

As there are only a few hundred vortices present at a given time step, we have to gather velocity values over time in order to collect sufficient statistics for a vortex velocity histogram. The advantage, however, is that we can pick out only those vortices which belong to a cluster of a given size. This allows us to specifically sample the velocity statistics of vortices inside a cluster, and compare this to other vortices.

Such a comparison is shown in Fig. 7, where we have three different velocity distributions: (i) for all vortices, (ii) for isolated vortices, and (iii) for vortices belonging to clusters
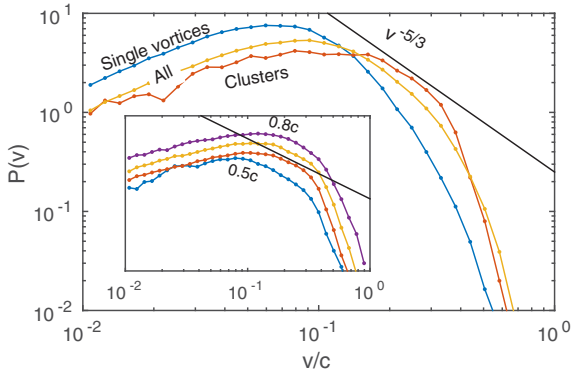
FIG. 7. Vortex velocity distributions using three different sets of vortices: All vortices, single vortices, and vortices belonging to clusters of size 4. Inset: Vortex velocity distributions for clusters of size 3 for different stirring velocities, shifted vertically for comparison. Solid lines indicate the slope corresponding to a $v^{-5/3}$ scaling law.

of size equal to four vortices. We see that the distribution of velocities corresponding to clustered vortices seems to follow a $v^{-5/3}$ scaling regime up to an ultraviolet cutoff at $v \gtrsim 0.5c$. Like for the energy spectrum, an insufficient separation of scales limits the extent of the scaling range for $P(v)$, and additional insights are needed in order to identify the power law. In Ref. [31], we showed that the scaling range for the tail distribution is controlled by the mean density of clustered vortices, and that a sufficiently low density is necessary for the onset of a scaling range. Thus, we attribute the narrow power-law tail in the numerical simulations to a high density of vortices inside clusters, which in turn is related to the fact that the vortex core size and Thomas-Fermi radius are not sufficiently far apart.

In addition, we notice that the probability distribution of velocities sampled on isolated vortices lacks a scaling regime. This we attribute to the fact that clustered vortices and dipoles act like "obstacles" that prevent a uniform spread of the isolated vortices within the disk. We have checked that the v^{-3} scaling appears when we redistribute the isolated vortices uniformly in the plane disregarding the presence of these obstacles.

The inset plot in Figure 7 shows the distribution of velocities of clustered vortices of size 3 for different stirring velocities. We notice that the $-5/3$ power-law tail seems to be more strongly expressed at lower stirring velocities where the contribution from clustered vortices becomes important. At higher stirring velocities, the lifespan of clustered vortices is reduced and the statistics is dominated by the isolated vortices, which do not exhibit a scaling range.

VII. SUMMARY AND CONCLUSIONS

In summary, we have shown that the spectral energy transport in 2D quantum turbulence can be signaled from the statistics of vortex number and velocity fluctuations. This connection depends on the spatial clustering of like-signed vortices. To show that the inertial $k^{-5/3}$ regime of the spectral energy is due to the vortex clustering, we have studied separately the contribution of clusters and isolated vortices to the energy spectrum.

Moreover, vortex clustering is also central to explaining the $f^{-5/3}$ scaling which we observe in the power spectrum of the vortex number fluctuations. The explanation relies on decomposing the vortex density field into clusters, which set up a prevailing velocity field, and single vortices which are passively advected by this field. Of the various signals of the inverse energy cascade, the power spectrum scaling is the most striking, as it covers a larger range of frequencies than the energy spectrum. One possible reason for this is that finite-size effects are less strongly expressed in the temporal domain. The inverse energy cascade due to vortex clustering corresponds to a particular statistical signature on the vortex velocity. We find that the clustered vortex velocity probability distribution develops a $v^{-5/3}$ power-law tail which we observed in our dGPE numerical simulations and can predict from a fractal distribution of vortices inside a vortex cluster [31].

We believe that the power spectrum of vortex number fluctuations is an experimentally accessible quantity like in 3D experiments, so the predicted scaling law corresponding to the 2D inverse energy cascade can also be tested in highly oblate BECs.

A connection between the superfluid velocity distribution and the quantum energy spectrum was also established in the hydrodynamic approximation in Ref. [32], and used to study the emergence of coherent rotating structures in decaying 2D turbulence.

We have focused on the lowest order turbulence statistics in the regime dominated by vortex dynamics. It would be interesting for the classical-quantum analogy to however go beyond the energy spectrum and study the intermittency effects. While intermittency corrections to scaling of higher order structure functions have been observed in 3D quantum superfluids [7,33,34], this has not yet been investigated in the 2D quantum turbulence. The obvious question would be whether the direct cascade is intermittent, while the inverse cascade is nonintermittent.

[1] R. H. Kraichnan and D. Montgomery, Rep. Prog. Phys. **43**, 547 (1980).

[2] R. H. Kraichnan, J. Atmos. Sci. **33**, 1521 (1976).

[3] S. Chen, R. E. Ecke, G. L. Eyink, M. Rivera, M. Wan, and Z. Xiao, Phys. Rev. Lett. **96**, 084502 (2006).

[4] L. Onsager, Nuovo Cimento **6**, 279 (1949).

[5] M. S. Paoletti and D. P. Lathrop, Annu. Rev. Condens. Matter Phys. **2**, 213 (2011).

[6] T. W. Neely, A. S. Bradley, E. C. Samson, S. J. Rooney, E. M. Wright, K. J. H. Law, R. Carretero-González, P. G. Kevrekidis, M. J. Davis, and B. P. Anderson, Phys. Rev. Lett. **111**, 235301 (2013).

[7] C. F. Barenghi, V. S. Lvov, and P.-E. Roche, Proc. Natl. Acad. Sci. USA **111**, 4683 (2014).

[8] M. Kobayashi and M. Tsubota, Phys. Rev. A **76**, 045603 (2007).

[9] P.-E. Roche and C. F. Barenghi, Europhys. Lett. **81**, 36002 (2008).

[10] A. W. Baggaley and C. F. Barenghi, Phys. Rev. B **84**, 020504 (2011).

[11] A. W. Baggaley, J. Laurie, and C. F. Barenghi, Phys. Rev. Lett. **109**, 205304 (2012).

[12] P.-E. Roche, P. Diribarne, T. Didelot, O. Français, L. Rousseau, and H. Willaime, Europhys. Lett. **77**, 66002 (2007).

[13] D. I. Bradley, S. N. Fisher, A. M. Guénault, R. P. Haley, S. OSullivan, G. R. Pickett, and V. Tsepelin, Phys. Rev. Lett. **101**, 065302 (2008).

[14] M. S. Paoletti, M. E. Fisher, K. R. Sreenivasan, and D. P. Lathrop, Phys. Rev. Lett. **101**, 154501 (2008).

[15] A. C. White, C. F. Barenghi, N. P. Proukakis, A. J. Youd, and D. H. Wacks, Phys. Rev. Lett. **104**, 075301 (2010).

[16] R. Numasato, M. Tsubota, and V. S. Lvov, Phys. Rev. A **81**, 063630 (2010).

[17] M. T. Reeves, B. P. Anderson, and A. S. Bradley, Phys. Rev. A **86**, 053621 (2012).

[18] M. T. Reeves, T. P. Billam, B. P. Anderson, and A. S. Bradley, Phys. Rev. Lett. **110**, 104501 (2013).

[19] T. P. Billam, M. T. Reeves, and A. S. Bradley, Phys. Rev. A **91**, 023615 (2015).

[20] P. M. Chesler, H. Liu, and A. Adams, Science **341**, 368 (2013).

[21] A. S. Bradley and B. P. Anderson, Phys. Rev. X **2**, 041001 (2012).

[22] B. I. Halperin, in *Physics of Defects*, Proceedings of the Les Houches Summer School, Session XXXV, edited by R. Balian, M. Kléman, and J. P. Poirier (North-Holland Press, Amsterdam, 1981), p. 816.

[23] G. F. Mazenko, Phys. Rev. E **64**, 016110 (2001).

[24] L. Angheluta, P. Jeraldo, and N. Goldenfeld, Phys. Rev. E **85**, 011153 (2012).

[25] C. Nore, M. Abid, and M. E. Brachet, Phys. Rev. Lett. **78**, 3896 (1997).

[26] S. Corrsin, J. Appl. Phys. **22**, 469 (1951).

[27] A. Obukhov, Structure of the Temperature Field in Turbulent Flow, Technical Report, DTIC Document AD0683016, 1968 (unpublished).

[28] R. H. Kraichnan, Phys. Fluids **11**, 945 (1968).

[29] P.-H. Chavanis and C. Sire, Phys. Rev. E **62**, 490 (2000).

[30] E. A. Novikov, Zh. Eksp. Teor. Fiz. **68**, 1868 (1976).

[31] A. Skaugen and L. Angheluta, arXiv:1601.06563.

[32] M. T. Reeves, T. P. Billam, B. P. Anderson, and A. S. Bradley, Phys. Rev. A **89**, 053631 (2014).

[33] J. Maurer and P. Tabeling, Europhys. Lett. **43**, 29 (1998).

[34] L. Boué, V. Lvov, A. Pomyalov, and I. Procaccia, Phys. Rev. Lett. **110**, 014502 (2013).

II

Paper II

Velocity statistics for nonuniform configurations of point vortices
Audun Skaugen and Luiza Angheluta
Physical Review E **93**, 042137 (2016)
Reference: [2]

Velocity statistics for nonuniform configurations of point vortices

Audun Skaugen[*] and Luiza Angheluta

Department of Physics, University of Oslo, P.O. 1048 Blindern, 0316 Oslo, Norway

Within the point-vortex model, we compute the probability distribution function of the velocity fluctuations induced by same-sign vortices scattered within a disk according to a fractal distribution of distances to the origin $\sim r^{-\alpha}$. We show that the different random configurations of vortices induce velocity fluctuations that are broadly distributed and follow a power-law tail distribution $P(V) \sim V^{\alpha-2}$ with a scaling exponent determined by the α exponent of the spatial distribution. We also show that the range of the power-law scaling regime in the velocity distribution is set by the mean density of vortices and the exponent α of the vortex density distribution.

I. INTRODUCTION

Two-dimensional (2D) turbulent flows are known to exhibit an inverse energy cascade, where the kinetic energy is transferred from smaller to larger scales, which can lead to a condensation of energy at low wave numbers [1]. This results in the formation of transient, large-scale rotating structures by an aggregation process or clustering of same-sign vortices by analogy to the Richarsdon's cascade of energy through a breakdown of vortices in three-dimensional turbulence [2]. For this reason, the vorticity dynamics is crucial in 2D turbulence. Onsager's point-vortex model [3] provides an approximate statistical description of turbulence, where vorticity is represented as a set of localized point vortices described by a Hamiltonian dynamics that generates dynamical regimes of clustering of same-sign vortices. Since the experimental realization of quantum turbulence in 2D Bose-Einstein condensates [4], the point-vortex model has become a particularly powerful way to study both the statistical properties of interacting quantized vortices and the analogy between the classical and quantum turbulent cascades [5–8].

Several studies on the clustering regime of same-sign vortices show that an inverse energy cascade develops for a self-similar spatial distribution of clustered vortices where the distance between vortices inside a cluster follows a power-law distribution $\sim r^{-\alpha}$, where $\alpha = 1/3$ corresponds to the Kolmogorov scaling of the incompressible energy spectrum in the wave number space $E(k) \sim k^{-5/3}$ [5,9]. In a recent numerical study of 2D quantum turbulence [8], we investigated the relationship between statistical properties of vortices and the inverse energy cascade, using the damped Gross-Pitaevskii equation. In particular, we showed that the vortex clustering regime, contributing to the formation of $k^{-5/3}$ scaling in the incompressible energy spectrum at length scales above the mean vortex distance, is also signaled by a power-law tail in the probability distribution of vortex velocity fluctuations $P(V) \sim V^{-5/3}$. However, in these kinds of numerical studies, the scaling range in both the energy spectrum and velocity probability distribution is limited by finite-size effects and mean vortex density and it is numerically challenging to reduce these effects. Therefore, the aim of this paper is to provide an analytical calculation of the $P(V)$ for clustered vortices where

we can vary the mean vortex distance and the system size. This way, we are able to show that the range of the power-law tail increases with decreasing mean density of clustered vortices, while it is relatively robust to finite-size effects related to a low number of cluster vortices within a small radius as long as the mean density is kept fixed. Moreover, the power-law exponent for $P(V)$ is directly related to the fractal distribution of clustered vortices as $P(V) \sim V^{\alpha-2}$.

The statistical distribution of velocity fluctuations induced by uniformly distributed random vortex configurations is known to follow $P(V) \sim V^{-3}$ that can be predicted from the point-vortex model [10]. Similar analytical techniques have been applied to studying fluctuations in the force of gravity in stellar systems. The statistics of the gravitational force induced by a fractal distribution of stars in d dimensions was shown to give rise to a power-law tail distribution $W(F) \sim F^{-\gamma}$ [11]. In particular, in two dimensions the force of gravity has a $1/r$ dependence, so these results are applicable to the point-vortex model. Here $W(F) \sim F^{\alpha-2}$ was found, consistent with our results.

In this paper we calculate the general velocity distribution induced by nonuniform random vortex configurations that have a fractal distribution $r^{-\alpha}$ with a particular focus on the range of the universal velocity scaling regime. We start by describing our point-vortex model for the inertial cluster in Sec. II and derive a formal expression for the velocity distribution $W(\vec{V})$ in Sec. III. The high-velocity cutoff due to finite core size is studied in Sec. IV, while the power-law scaling regime is derived in Sec. V. We study the range of this scaling regime in Sec. VI and verify our results using numerical sampling in Sec. VII. We summarize in Sec. VIII. Some detailed calculations are presented in the Appendixes.

II. POINT VORTEX MODEL FOR A CLUSTER

We consider an ensemble of N identical point vortices distributed within a disk of radius R such that the probability of having a vortex at position $\vec{r}$ follows a power law with the distance $\tau(\vec{r})d\vec{r} \propto |\vec{r}|^{-\alpha-1}d\vec{r}$ [9]. Hence, the probability distribution $T(r)$ of the distance from the origin $r = |\vec{r}|$ will pick up a factor $2\pi r$ from the 2D measure, so

$$T(r) \propto 2\pi r r^{-\alpha-1} \propto r^{-\alpha}, \qquad (1)$$

---
[*]audun.skaugen@fys.uio.no

with $\alpha = 1/3$ corresponding to the distribution of clustered vortices associated with the inverse energy cascade in two-dimensional quantum turbulence [5,9].

Because vortices of opposite sign annihilate when they get within a distance a related to the coherence length ξ, we modify the distribution $\tau(\vec{r})$ by introducing a lower cutoff $a \sim \xi$ coming from finite vortex cores. Using the normalization condition

$$\int_{|\vec{r}|=a}^{R} |\vec{r}|^{-\alpha-1} d\vec{r} = \frac{2\pi}{1-\alpha}(R^{1-\alpha} - a^{1-\alpha}), \qquad (2)$$

we derive the normalized probability distribution of a vortex position inside a cluster as

$$\tau(\vec{r}) = \frac{1-\alpha}{2\pi(R^{1-\alpha} - a^{1-\alpha})}|\vec{r}|^{-\alpha-1} = \frac{n_\alpha}{N}r^{-\alpha-1}. \qquad (3)$$

Here we have introduced the fractal mean density

$$n_\alpha = \frac{N(1-\alpha)}{2\pi(R^{1-\alpha} - a^{1-\alpha})}, \qquad (4)$$

where fractal alludes to the fact that this cluster is self-similar with fractal dimension $1 - \alpha$. This n_α is the mean density that is kept fixed when we later take the thermodynamic limit of $N, R \to \infty$.

A vortex at position $\vec{r}$ induces a velocity at the origin given by [3,10,12]

$$\vec{\phi}(\vec{r}) = -\frac{\gamma}{2\pi}\frac{\vec{r}_\perp}{r^2}, \qquad (5)$$

where $\gamma = 2\pi\xi c$ is the quantized circulation. The $\perp$ subscript denotes the counterclockwise rotation of a vector with an angle $\pi/2$. Hence, for a configuration of N vortices at positions $\vec{r}_i$, the velocity induced at the origin is a superposition of the velocity generated by each vortex from Eq. (5), i.e., $\sum_{i=1}^{N} \vec{\phi}(\vec{r}_i)$.

The velocity at the origin will fluctuate from one cluster configuration to another and the probability of observing a velocity $\vec{V}$ can be calculated by averaging over all possible configurations of clustered vortices that yield a velocity $\vec{V}$ at origin, namely,

$$W(\vec{V}) = \int \left[\prod_{i=1}^{N} d\vec{r}_i \tau(\vec{r}_i) \right] \delta\left(V - \sum_{i=1}^{N} \vec{\phi}(\vec{r}_i) \right). \qquad (6)$$

We have assumed that the positions of vortices inside the cluster are uncorrelated such that the N-point configurational distribution factorizes into the N product of the probability τ of finding a vortex.

III. FORMAL SOLUTION

In order to decouple the N-dimensional integral from Eq. (6), we Fourier expand the Dirac delta function as $\delta(\vec{x}) = \frac{1}{(2\pi)^2} \int e^{-i\vec{\rho}\cdot\vec{x}} d\vec{\rho}$ and insert it into Eq. (6), giving

$$W(\vec{V}) = \frac{1}{(2\pi)^2} \int d\vec{\rho}\, e^{-i\vec{\rho}\cdot\vec{V}} \prod_{i=1}^{N} \int d\vec{r}_i \tau(\vec{r}_i) e^{i\vec{\rho}\cdot\vec{\phi}(\vec{r}_i)}. \qquad (7)$$

Upon noticing that the N inner integrals are identical, this can be simplified to

$$\begin{aligned} W(\vec{V}) &= \frac{1}{(2\pi)^2} \int d\vec{\rho}\left(\int d\vec{r}\, \tau(\vec{r}) e^{i\vec{\rho}\cdot\vec{\phi}(\vec{r})} \right)^N e^{-i\vec{\rho}\cdot\vec{V}} \\ &= \frac{1}{(2\pi)^2} \int d\vec{\rho}\, A(\vec{\rho}) e^{-i\vec{\rho}\cdot\vec{V}}, \end{aligned} \qquad (8)$$

where $A(\vec{\rho})$ is the Fourier transform of $W(\vec{V})$ in the velocity's conjugate space $\vec{\rho}$ and is given by

$$\begin{aligned} A(\vec{\rho}) &= \left(\frac{n_\alpha}{N} \int_{|\vec{r}|=a}^{R} r^{-\alpha-1} e^{i\vec{\rho}\cdot\vec{\phi}(\vec{r})} d\vec{r} \right)^N \\ &= \left[1 - \frac{n_\alpha}{N} \int_{|\vec{r}|=a}^{R} r^{-\alpha-1}(1 - e^{i\vec{\rho}\cdot\vec{\phi}(\vec{r})}) d\vec{r} \right]^N. \end{aligned} \qquad (9)$$

Here we made use of the identity $\frac{n_\alpha}{N} \int r^{-\alpha-1} d\vec{r} = 1$ in order to write the integral in a form that converges to the exponential function in the large-N limit, i.e.,

$$\lim_{N\to\infty} \left(1 - \frac{x}{N} \right)^N = e^{-x}. \qquad (10)$$

This identity is valid as long as x increases less rapidly than N. Thus, in the thermodynamic limit of large R and N, we can write $A(\vec{\rho}) = e^{-n_\alpha C(\vec{\rho})}$, where

$$C(\vec{\rho}) = \int_{|\vec{r}|=a}^{R} r^{-\alpha-1}(1 - e^{i\vec{\rho}\cdot\vec{\phi}(\vec{r})}) d\vec{r}, \qquad (11)$$

as long as $C(\vec{\rho})$ increases less rapidly than N.

We now change variables from $\vec{r}$ to $\vec{\phi}$, giving a Jacobi determinant

$$\left\| \frac{\partial(\vec{r})}{\partial(\vec{\phi})} \right\| = -\left(\frac{\gamma}{2\pi} \right)^2 \phi^{-4}. \qquad (12)$$

Since $|\vec{\phi}| = \gamma/2\pi r$, we have $r = \gamma/2\pi\phi$, so

$$C(\vec{\rho}) = \left(\frac{\gamma}{2\pi} \right)^{1-\alpha} \int_{|\vec{\phi}|=\gamma/2\pi R}^{\gamma/2\pi a} \phi^{\alpha-3}(1 - e^{i\vec{\rho}\cdot\vec{\phi}}) d\vec{\phi}, \qquad (13)$$

where the negative sign from the Jacobian is canceled by interchanging the limits of integration. Switching to polar coordinates measured relative to the direction of $\vec{\rho}$ and rewriting the limits using $\gamma = 2\pi\xi c$,

$$\begin{aligned} C(\vec{\rho}) &= \left(\frac{\gamma}{2\pi} \right)^{1-\alpha} \int_{c\xi/R}^{c\xi/a} \phi^{\alpha-2} \int_0^{2\pi} d\theta(1 - e^{i\rho\phi\cos\theta}) d\phi \\ &= \times 2\pi\left(\frac{\gamma}{2\pi} \right)^{1-\alpha} \int_{sc}^{s'c} \phi^{\alpha-2}[1 - J_0(\rho\phi)] d\phi, \end{aligned} \qquad (14)$$

where $s = \xi/R$ gives the separation of scales between the coherence length ξ and the system size R and $s' = \xi/a \lesssim 1$ relates the lower cutoff a to the coherence length. Finally, substituting $x = \rho\phi$, we find

$$\begin{aligned} C(\vec{\rho}) &= 2\pi\left(\frac{\gamma\rho}{2\pi} \right)^{1-\alpha} \int_{s\rho c}^{s'\rho c} [1 - J_0(x)] x^{\alpha-2} dx \\ &= 2\pi\kappa(\rho; s, s')\left(\frac{\gamma\rho}{2\pi} \right)^{1-\alpha}, \end{aligned} \qquad (15)$$

where $\kappa(\rho; s, s')$ is the dimensionless number given by the integral. The behavior of this κ function in different regimes is the key to investigating the various regimes of $W(\vec{V})$, as we will see in the following sections. Summarizing, we have the formal solution

$$
W(\vec{V}) = \frac{1}{(2\pi)^2} \int A(\vec{\rho}) e^{i\vec{\rho}\cdot\vec{V}} d\vec{\rho}
$$
$$
= \frac{1}{(2\pi)^2} \int_0^{2\pi} d\theta \int_0^\infty \rho e^{-n_\alpha C(\rho)} e^{i\rho V \cos\theta} d\rho, \quad (16)
$$

where we introduced polar coordinates with the angle measured relative to the direction of $\vec{V}$.

IV. HIGH-VELOCITY CUTOFF

As we have noted, we have introduced a lower limit a to how close a vortex can get to the origin. This limits the velocity that a single vortex can induce to $V_a = \gamma/2\pi a = s'c$, so we should expect a cutoff in the velocity distribution around this value. For velocities larger than $s'c$, values of ρ larger than $1/s'c$ will tend to cancel out by the oscillating factor $e^{i\rho V}$. It therefore suffices to consider $\rho < 1/s'c$. In this case, the $\kappa(\rho; s, s')$ integral has limits $s'\rho c < 1$ and $s\rho c \ll 1$. The lower limit can be taken to be zero, while the small upper limit means that we can expand the Bessel function as $J_0(x) = 1 - x^2/4$, so

$$
\kappa(\rho; s, s') = \int_0^{s'\rho c} x^\alpha dx = \frac{1}{1+\alpha}(s'\rho c)^{1+\alpha}. \quad (17)
$$

Using $s'\rho c = \gamma\rho/2\pi a$, we therefore see that

$$
C(\vec{\rho}) = \frac{2\pi}{(1+\alpha)a^{1+\alpha}}\left(\frac{\gamma\rho}{2\pi}\right)^2. \quad (18)
$$

Thus the $A(\vec{\rho})$ is a Gaussian function, which is invariant upon Fourier transformation. We therefore obtain a Gaussian distribution for the cutoff tail of $W(\vec{V})$,

$$
W(\vec{V})_{V \gg c} = (1+\alpha)\frac{a^{1+\alpha}}{2n_\alpha\gamma^2}\exp\left(-(1+\alpha)\frac{\pi a^{1+\alpha}}{2n_\alpha\gamma^2}V^2\right). \quad (19)
$$

V. POWER-LAW TAIL DISTRIBUTION

We now explore the intermediate scaling regime, where a power-law tail distribution can develop when $sc \ll V < s'c$. For these velocities, the main contribution to the Fourier transform is when $1/s'c < \rho \ll 1/sc$. In the $\kappa(\rho; s, s')$ integral, this means that the lower limit $s\rho c \ll 1$ and can be taken to be zero. The upper limit is larger than 1 and since the integrand falls off rapidly for $x > 1$ we can extend this limit to infinity. Thus we find that in this regime, $\kappa(\rho; s, s') = \kappa$ is a constant and is equal to (see Appendix B)

$$
\kappa = \int_0^\infty [1 - J_0(x)]x^{\alpha-2}dx
$$
$$
= -\frac{1}{\pi}\sin\frac{\pi\alpha}{2}\Gamma(\alpha-1)B\left(1-\frac{\alpha}{2}, \frac{1}{2}\right), \quad (20)
$$

where $B(a,b)$ is the Beta function. This is a positive number in the range $-1 < \alpha < 1$. Since κ is constant $C(\rho) \sim \rho^{1-\alpha}$,

so $A(\vec{\rho})$ does not have Gaussian behavior. We explore the consequences of this by studying the Fourier transform integral from Eq. (16).

Using the symmetry of the cosine function, we can restrict the polar integration from 0 to π in exchange for a factor of 2. Changing variables to $t = \cos\theta$ and $z = \rho V$, we find that Eq. (16) is equivalent to

$$
W(\vec{V}) = \frac{1}{2\pi^2 V^2}\int_{-1}^1 \frac{dt}{\sqrt{1-t^2}}\int_0^\infty z e^{izt} e^{-n_\alpha C(z/V)}dz. \quad (21)
$$

In order to analyze the high-velocity behavior of this distribution, we would like to expand $e^{-n_\alpha C(z/V)}$ in powers of z/V and integrate term by term. However, this interchange of limits requires the inner integral to be an analytical function of t. However, as any neighborhood of real numbers contains numbers with an imaginary part of either sign, the e^{izt} factor will cause the integral to blow up on any neighborhood of t.

We can however deform the integration contours in order to ensure that the real part of izt is always strictly negative. The trick is to rotate the ray of the z integration by an angle $\omega(t)$ that depends on the argument of t. In order to avoid a discontinuous change of $\arg t$ from π to 0, we first deform the t integral to the unit semicircle S in the positive imaginary half plane, as illustrated in Fig. 1. Thus $\arg t$ will go continuously from π to 0.

The exponent izt now has the argument $\arg(izt) = \pi/2 + \omega(t) + \arg t$ and $\omega(t)$ should be chosen so that this is kept between $\pi/2$ and $3\pi/2$ for the real part to be negative. We also need to keep the real part of $C(z/V) \propto z^{1-\alpha}$ positive, which means that $\arg z^{1-\alpha} = (1-\alpha)\omega(t)$ must be kept between $-\pi/2$ and $\pi/2$. These constrains are satisfied by the choice [10]

$$
\omega(t) = \frac{1}{8}\left(\frac{\pi}{2} - \arg t\right). \quad (22)
$$

We can now expand $e^{-n_\alpha C(z/V)}$ in powers of $1/V$ and integrate term by term

$$
W(\vec{V}) = \frac{1}{2\pi^2 V^2}\sum_{n=0}^\infty \frac{1}{n!}(-2\pi n_\alpha \kappa)^n\left(\frac{\gamma}{2\pi V}\right)^{n(1-\alpha)}
$$
$$
\times \int_\tau \frac{dt}{\sqrt{1-t^2}}\int_{\omega_t} z e^{izt} z^{n(1-\alpha)}dz. \quad (23)
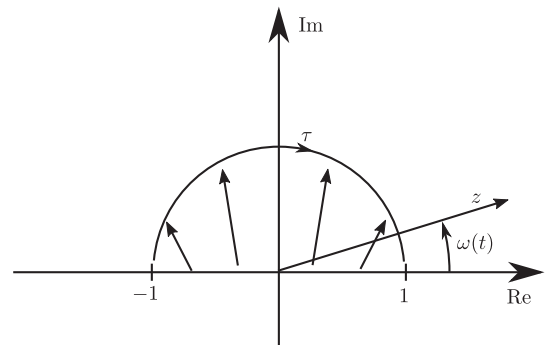$$

FIG. 1. Deforming the contours of integration.

After this interchange of limits, we can again rotate the ray of integration so that izt is negative real by choosing $\omega(t) = \frac{\pi}{2} - \arg t$. We then substitute $y = -izt$, making this integral a real integral on the positive real axis:

$$W(\vec{V}) = -\frac{1}{2\pi^2 V^2} \sum_{n=0}^{\infty} \frac{1}{n!} (-2\pi n_\alpha \kappa)^n \left(\frac{i\gamma}{2\pi V}\right)^{n(1-\alpha)}$$
$$\times \int_\tau \frac{dt}{t^{2+n(1-\alpha)}\sqrt{1-t^2}} \int_0^\infty e^{-y} y^{1+n(1-\alpha)} dy. \quad (24)$$

In Appendix A we show that the t integral from the $n = 0$ term vanishes,

$$\int_\tau \frac{dt}{t^2\sqrt{1-t^2}} = 0, \quad (25)$$

while the $n = 1$ integral does not,

$$\lambda = \int_\tau \frac{dt}{t^{3-\alpha}\sqrt{1-t^2}}$$
$$= -\frac{i}{2}(1 + e^{i\pi\alpha}) B\left(\frac{3-\alpha}{2}, \frac{1}{2}\right). \quad (26)$$

Thus, recognizing the Gamma function for the y integral, the velocity distribution is, to leading order in $1/V$, given by

$$W(\vec{V}) = \frac{2\pi n_\alpha \kappa}{2\pi^2 V^2} \left(\frac{i\gamma}{2\pi V}\right)^{1-\alpha} \lambda \Gamma(3-\alpha)$$
$$= \frac{\kappa\lambda}{\pi} \Gamma(3-\alpha) e^{i\pi(1-\alpha)/2} n_\alpha \left(\frac{\gamma}{2\pi}\right)^{1-\alpha} V^{\alpha-3}. \quad (27)$$

In Appendix C we show that the dimensionless prefactors combine to unity,

$$\frac{\kappa\lambda}{\pi} \Gamma(3-\alpha) e^{i\pi(1-\alpha)/2} = 1, \quad (28)$$

so that we are left with the simple expression for the tail,

$$W(\vec{V}) = n_\alpha \left(\frac{\gamma}{2\pi}\right)^{1-\alpha} V^{\alpha-3}. \quad (29)$$

The distribution for the velocity norm picks up a factor $2\pi V$ from the 2D measure

$$P(|\vec{V}| = V) = 2\pi n_\alpha \left(\frac{\gamma}{2\pi}\right)^{1-\alpha} V^{\alpha-2}. \quad (30)$$

Taking the limit $\alpha \to -1$ recovers the familiar V^{-3} velocity tail associated with a uniformly random distribution of point vortices. On the other hand, by substituting $\alpha = 1/3$ as in the vortex clustering associated with the inverse energy cascade, we obtain that the tail distribution develops a $V^{-5/3}$ scaling regime.

VI. RANGE OF THE POWER-LAW SCALING

The series expansion for $W(\vec{V})$ in Eq. (24) contains terms of higher order in $1/V$, which will become increasingly important for lower velocities V. When these terms are included we no longer have a simple power-law scaling, so studying these terms will tell us the expected scaling range for the high-velocity tail.

The $n = 2$ term in Eq. (24) is

$$W_2(\vec{V}) = P_2 n_\alpha^2 \left(\frac{\gamma}{2\pi}\right)^{2-2\alpha} V^{2\alpha-4}, \quad (31)$$

where the dimensionless prefactor can be shown to equal

$$P_2 = -4^{1-\alpha} \tan\frac{\pi\alpha}{2} B\left(1 - \frac{\alpha}{2}, \frac{1}{2}\right)^2. \quad (32)$$

Note that this prefactor is positive when $\alpha < 0$. This means that for negative α the distribution will initially increase above the expected power law, before higher-order terms cause the distribution to fall off. Thus the deviation from the power-law tail distribution will manifest itself as a bulge below the scaling regime. For $\alpha > 0$ the prefactor is negative, so no such bulge appears.

For $\alpha = 0$ the second-order contribution vanishes, so we will need to use the third-order contribution in order to analyze the range of the power-law scaling. The relevant prefactor is

$$P_3(\alpha = 0) = -6\pi^2. \quad (33)$$

The velocity where the $n = 2$ contribution is as important as the $n = 1$ term can now be found by solving the equation

$$|P_2| n_\alpha^2 \left(\frac{\gamma}{2\pi}\right)^{2-2\alpha} V^{2\alpha-4} = n_\alpha \left(\frac{\gamma}{2\pi}\right)^{1-\alpha} V^{\alpha-3}, \quad (34)$$

which gives us a cutoff velocity

$$V_{\text{cut}} = \frac{\gamma}{2\pi} (|P_2| n_\alpha)^{1/(1-\alpha)}. \quad (35)$$

Solving a similar equation for the third-order term gives the $\alpha = 0$ case

$$V_{\text{cut}}(\alpha = 0) = \frac{\gamma}{2\pi} \sqrt{6\pi n_0}. \quad (36)$$

This means that the $V^{\alpha-3}$ scaling can only develop between the lower cutoff velocity V_{cut} and the upper cutoff $s'c$. Notice that the lower cutoff value for a given α is entirely controlled by the mean density: The larger the gap between the vortex core size and the mean vortex separation, the wider the range of velocity scaling. When $n_\alpha = a^{\alpha-1}/|P_2|$ we find that $V_{\text{cut}} = s'c$, so there is no room for a power-law scaling to develop at densities of this order. Similarly, in order to get a full decade of power-law scaling we need the density to satisfy $n_\alpha < (10a)^{\alpha-1}/|P_2|$.

VII. NUMERICAL SAMPLING OF CLUSTERED VORTICES

We check the analytical predictions of the velocity distribution arising from a fractal configuration of N-point vortices $\{\vec{r}_i\}_{n=1}^N$, by using the same kind of numerical sampling method as described in Ref. [5]. The spatial sampling method generates a localized finite configuration of power-law-distributed vortices with respect to their distances from the origin r_i by taking into account the finite vortex core size $a \sim \xi$ and system size $\sim R$. In this case we fix $a = \xi$, so the sampled fractal distribution normalized in the interval bounded by these cutoffs $[\xi, R]$ is

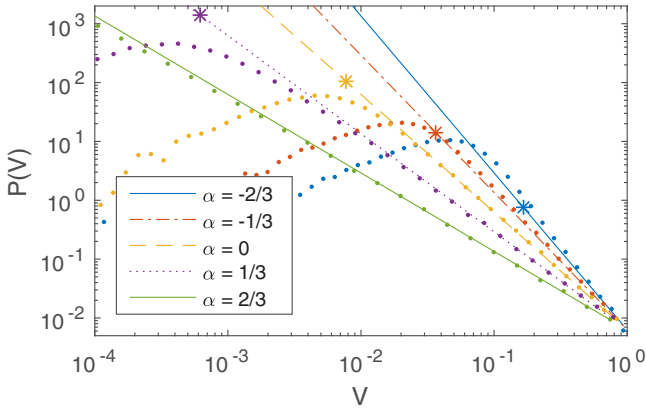$$T_\alpha(r) = \frac{1-\alpha}{R^{1-\alpha} - \xi^{1-\alpha}} r^{-\alpha}. \quad (37)$$

FIG. 2. Velocity probability distribution $P(V)$ of a spatially sampled fractal configuration of point vortices with power-law exponents α ranging from $-2/3$ (steepest power law) to $2/3$ (shallowest power law). The mean density is fixed to $n_\alpha = 10^{-3}$. Straight lines show the corresponding power law $2\pi n_\alpha V^{\alpha-2}$, while the asterisks show the points where the next-order contribution from the power-law expansion is as large as the first-order contribution. Notice that the range of power-law scaling increases with α and the positive second-order contribution at negative α, as predicted in Sec. VI.

We choose ξ as the unit of space and c as the unit of velocity, so $\xi = c = 1$. To sample vortex distances r_i from this distribution, we first generate N random numbers u_i in the unit interval $[0,1]$. The uniformly distributed random numbers are then mapped onto the set of distances $\{r_i\}$ that follow a fractal distribution given by Eq. (37) upon the transformation

$$r_i = [u_i R^{1-\alpha} + (1 - u_i)\xi^{1-\alpha}]^{1/(1-\alpha)}. \quad (38)$$

The vortex angles θ_i are assumed to be uniformly distributed within $[0,2\pi]$. Therefore, the position vector of vortex i is $\vec{r}_i = r_i(\cos\theta_i \vec{e}_x + \sin\theta_i \vec{e}_y)$.

From the configuration of vortex positions $\{\vec{r}_i\}_{i=1}^N$, we then compute the velocity induced at the cluster's origin using the superposition principle and Eq. (5), i.e., $\vec{v} = \sum_{i=1}^N \vec{\phi}(\vec{r}_i)$. In Figs. 2–4 we show how the range of power-law scaling of $P(V)$ depends on parameters such as the exponent α, the mean vortex density n_α, and number of clustered vortices N at a fixed density n_α. For a fixed mean density, we notice that the range of the power-law scaling increases with α (see Fig. 2), whereas it remains relatively robust to the number of clustered vortices as shown in Fig. 4. On the other hand, the scaling range extends over more decades in velocity fluctuations as the mean vortex density decreases, as shown in Fig. 3, also consistent with the theoretical prediction of lower velocity cutoff V_{cut} from Eq. (35), which only depends on the mean density. We can scale out this dependence on n_α as defining $\tilde{V} = V/n_\alpha^{1/(1-\alpha)}$, which means that the probability distribution of V can be written as $P(V) = n_\alpha^{-1/(1-\alpha)}\mathcal{P}(V/n_\alpha^{1/(1-\alpha)})$. In the scaling regime of $P(V)$, the rescaled distribution follows $\mathcal{P}(\tilde{V}) \sim \tilde{V}^{\alpha-2}$ independently of n_α. This data collapse is shown in Fig. 3(b).

We can understand the weak dependence on N for fixed n_α by noting that the thermodynamic limit $N \to \infty$ was used only once during our derivation, namely, by making use of the exponential identity in Eq. (10). The accuracy of this identity
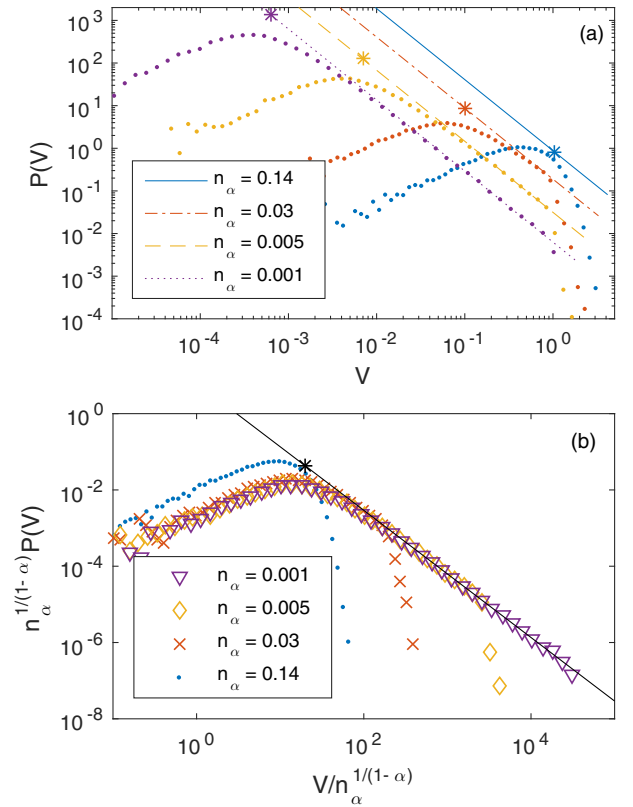

FIG. 3. (a) Plot of $P(V)$ of a spatially sampled fractal configuration of point vortices with $\alpha = 1/3$ and the mean density n_α varying from 10^{-3} to the critical value 0.14 where the scaling vanishes. Straight lines and asterisks are as in Fig. 2. (b) Data collapse in the scaling regime of $P(V)$ when the dependence on n_α is scaled out, i.e., $P(V) = n_\alpha^{-1/(1-\alpha)}\mathcal{P}(V/n_\alpha^{1/(1-\alpha)})$.

is controlled by the ratio $\frac{x}{N} = \frac{n_\alpha}{N}C(\rho)$. In the scaling regime we have $\rho \ll 1/sc$, which implies

$$\frac{n_\alpha}{N}C(\rho) = \frac{n_\alpha}{N}\left(\frac{\gamma\rho}{2\pi}\right)^{1-\alpha} 2\pi\kappa \ll \frac{1-\alpha}{R^{1-\alpha} - a^{1-\alpha}}R^{1-\alpha}\kappa, \quad (39)$$

and therefore, since $a \ll R$,

$$\frac{x}{N} \ll (1-\alpha)\kappa. \quad (40)$$

We notice that $(1 - \alpha)\kappa$ is independent of N and R and is of the order of unity, except for the limit case of a uniform distribution of vortices $\alpha \to -1$, where it diverges. Thus $\frac{x}{N} \ll 1$, so the exponential identity is a good approximation. This means that finite-size effects due to small system size and number of clustered vortices have small corrections to the scaling range compared to the dominant effect, which is given by the mean density n_α of clustered vortices. We have checked that the dependence of the sampled distribution on N and R for fixed n_α remains weak for a wide range of mean densities n_α and scaling exponents $\alpha > 0$.

VIII. CONCLUSION

We have determined the probability distribution of velocity fluctuations arising from fractal configuration of clustered
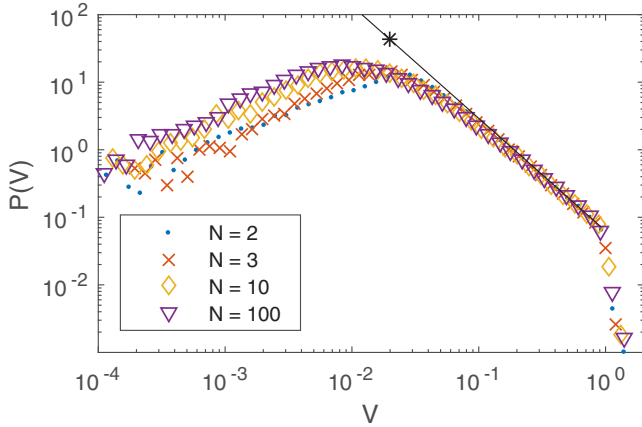
FIG. 4. Sampled velocity distributions at different cluster sizes N, but at the same density $n_\alpha = 0.01$ and power-law exponent $\alpha = 1/3$. We notice that the size of the cluster has a minimal effect on the scaling regime, even quite far away from the thermodynamic limit $N, R \to \infty$ at fixed n_α.

vortices. We recovered two limit cases that are particularly relevant for turbulent flows. The uniform distribution of vortices that corresponds to $\alpha = -1$ is the stationary configurational probability of a free system of uncorrelated vortices and is used as a proxy to describe 2D turbulent flows with no transfer of energy across scales [9,10]. In this case, the induced velocity fluctuations follow the known V^{-3} tail distribution. A similar tail distribution has been observed in 3D superfluid turbulence and attributed to vortex reconnections [13] and also reproduced in 3D simulations of quantum turbulence in Bose-Einstein condensates [14,15]. While it is plausible that a forward energy cascade in three dimensions can be described through a uniform tangle of quantized vortices, the inverse energy cascade in 2D turbulence is built on a self-similar distribution of clustered vortices, such that the Kolmogorov spectrum $E(k) \sim k^{-5/3}$ is attributed to $\alpha = 1/3$. This spatial self-similarity of vortices induces a different power law in the tail distribution of the velocity fluctuations, namely, as $\sim V^{-5/3}$.

ACKNOWLEDGMENTS

APPENDIX A: DERIVATION OF THE λ INTEGRAL

We are considering integrals of the type

$$I_m = \int_\tau \frac{dt}{t^m \sqrt{1 - t^2}}, \tag{A1}$$

where m is a possibly fractional power. Of particular interest are the cases $m = 2$ and $m = 3 - \alpha$, which appear as Eqs. (25) and (26), respectively.

Our strategy will be to deform the integration contour back to the real axis. However, the pole of order m at the origin is likely to cause problems, which is exactly the reason why
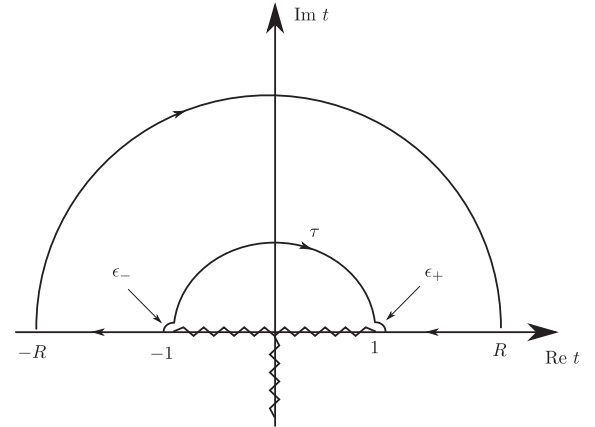

FIG. 5. Branch cuts and contours of integration.

we lifted the contour to the complex plane in the first place. We therefore avoid the origin by enlarging the contour to the intervals $[-1, -\infty]$ and $[1, \infty]$ (see Fig. 5).

When doing this, we will need to keep any branch cuts out of the way. The fractional power t^m has a branch cut along the negative real axis, which we can simply rotate away to the negative imaginary axis by the standard transformation $t^m \to e^{-i\chi}(e^{i\chi/m} t)^m$, with an appropriate choice for χ. This transformation leaves the integral invariant and can thus be left implicit.

For the square root we apply the transformation $\sqrt{1 - t^2} = \pm i \sqrt{t^2 - 1}$ in order to keep the branch cuts out of the way on the $[-1, 1]$ interval. However, we do need to be careful in choosing the sign of the imaginary unit. As $\arg t$ descends from π to 0, the argument of $1 - t^2$ stays in the interval $[-\pi/2, \pi/2]$, not crossing the branch cut of the square root. On the other hand, the argument of $t^2 - 1$ crosses the negative real axis at $\arg t = \pi/2$.

In order to work out the correct sign of the imaginary unit, we calculate the argument of $t^2 - 1$ using the polar form $t = e^{i\theta}$:

$$\arg(t^2 - 1) = \arg(e^{2i\theta} - 1) = \arg[e^{i\theta}(e^{i\theta} - e^{-i\theta})]$$
$$= \arg(2i \sin\theta \, e^{i\theta}) = \arg e^{i(\theta + \pi/2)}$$
$$= \mathcal{P}(\theta + \pi/2), \tag{A2}$$

where $\mathcal{P}(\theta)$ normalizes the angle to lie in the principal branch interval $(-\pi, \pi]$. Similarly, the argument of $1 - t^2$ is $\mathcal{P}(\theta - \pi/2)$. The principal branch of the square root halves these angles, so

$$\arg \frac{\sqrt{1 - t^2}}{\sqrt{t^2 - 1}} = \frac{1}{2}\mathcal{P}(\theta - \pi/2) - \frac{1}{2}\mathcal{P}(\theta + \pi/2). \tag{A3}$$

By checking cases in this expression, we can now verify that

$$\frac{\sqrt{1 - t^2}}{\sqrt{t^2 - 1}} = \begin{cases} i & \text{for } \pi \leqslant \theta < \pi/2 \\ -i & \text{for } \pi/2 \leqslant \theta \leqslant 0. \end{cases} \tag{A4}$$

Thus the sign of the imaginary unit changes when the contour crosses the imaginary axis.

The integral can now be written

$$I_m = \left(\int_{\epsilon^-} + \int_{-1-\epsilon}^{-R} + \int_{|t|=R} + \int_{R}^{1+\epsilon} + \int_{\epsilon^+} \right) \frac{dt}{\pm i t^m \sqrt{t^2-1}}$$
$$= I_{\epsilon^-} + I_- + I_R + I_+ + I_{\epsilon^+}. \quad (A5)$$

For the radius R semicircle, we substitute $t = Re^{i\theta}$ and find

$$|I_R| \leqslant R \int_0^\pi \frac{d\theta}{R^m |\sqrt{1-R^2 e^{2i\theta}}|}$$
$$\rightarrow \frac{R}{R^{m+1}} \pi \rightarrow 0, \quad (A6)$$

as long as $m > 0$, which is true for both our cases. Similarly, we find that the ϵ quarter-circle integrals go like $\sqrt{\epsilon}$ and thus vanish when $\epsilon \rightarrow 0$. Taking $R \rightarrow \infty$ and $\epsilon \rightarrow 0$ and flipping the limits on the positive integral, we are left with

$$I_m = I_- + I_+ = \left(\int_{-1}^{-\infty} - \int_1^\infty \right) \frac{dt}{\pm i t^m \sqrt{t^2-1}}. \quad (A7)$$

For the negative part we substitute $t \rightarrow -t$, which transforms dt/t^m to $-(-1)^{-m} dt/t^m$. Inserting the proper signs for the imaginary unit in each part of the integral, this gives us

$$I_m = -i(1 - e^{-i\pi m}) \int_1^\infty \frac{dt}{t^m \sqrt{t^2-1}}. \quad (A8)$$

We now recall the definition of the Beta function

$$B(a,b) = \int_0^1 x^{a-1}(1-x)^{b-1} dx. \quad (A9)$$

Our integral can be transformed into this form with a substitution $x = 1/t^2$, which leads to $dt = -\frac{1}{2} x^{-3/2} dx$. Thus,

$$I_m = -\frac{i}{2}(1 - e^{-i\pi m}) \int_0^1 \frac{dx}{x^{-m/2} x^{3/2} \sqrt{1/x - 1}}$$
$$= -\frac{i}{2}(1 - e^{-i\pi m}) \int_0^1 x^{m/2-1}(1-x)^{-1/2}$$
$$= -\frac{i}{2}(1 - e^{-i\pi m}) B\left(\frac{m}{2}, \frac{1}{2} \right). \quad (A10)$$

With $m = 2$, or indeed m any even number, this integral vanishes due to $1 - e^{-2i\pi} = 0$, which proves Eq. (25). For the other case, we substitute $m = 3 - \alpha$ and find

$$\lambda = I_{3-\alpha} = -\frac{i}{2}(1 + e^{i\pi\alpha}) B\left(\frac{3-\alpha}{2}, \frac{1}{2} \right). \quad (A11)$$

APPENDIX B: DERIVATION OF THE κ INTEGRAL

We are considering the integral

$$\kappa = \int_\epsilon^\infty [1 - J_0(x)] x^{\alpha-2} dx = I_D - I_J, \quad (B1)$$

with the understanding that ϵ should be taken to zero. We would like our results to be valid for $\alpha \in (-1,1)$, which includes the interesting case $\alpha = 1/3$ and allows us to take the limit $\alpha \rightarrow -1$. The first term yields a divergence in ϵ,

$$I_D = \int_\epsilon^\infty x^{\alpha-2} dx = \frac{1}{1-\alpha} \epsilon^{\alpha-1}, \quad (B2)$$

but by series expanding the Bessel function we know that the full integral contains no such divergence. Thus the second term

must contain a divergence that cancels the first one. Studying this term, we use the integral representation of the Bessel function to write

$$I_J = \frac{1}{\pi} \int_\epsilon^\infty \int_0^\pi \cos(x \cos\theta) x^{\alpha-2} d\theta \, dx$$
$$= \frac{1}{\pi} \int_0^1 \int_\epsilon^\infty 2\cos(xt) x^{\alpha-2} dx \frac{dt}{\sqrt{1-t^2}}, \quad (B3)$$

where we substituted $t = \cos\theta$ and made use of the symmetry of the cosine to halve the integration limits in exchange for a factor of 2. We now study the the integral over x, which can be written as

$$\int_\epsilon^\infty x^{\alpha-2} e^{ixt} dx + \int_\epsilon^\infty x^{\alpha-2} e^{-ixt} dx = I_x + I_x^*. \quad (B4)$$

These integrals are suggestive of Gamma function integrals. However, substituting $y = -ixt$ takes the integration contour to the negative imaginary axis. To avoid this, we first rotate the contour of integration to the positive imaginary axis:

$$I_x = \left(\int_{C(\epsilon)} + \int_{i\epsilon}^{iR} - \int_{C(R)} \right) x^{\alpha-2} e^{ixt} dx, \quad (B5)$$

where $C(r)$ is the quarter circle of radius r going from the real to the positive imaginary axis and R is to be taken to infinity. The outer quarter-circle integral vanishes,

$$\lim_{R\to\infty} \int_{C(R)} x^{\alpha-2} e^{ixt} dx = 0, \quad (B6)$$

but on the inner contour we pick up a divergence in ϵ. Substituting $x = \epsilon e^{i\theta}$,

$$I_\epsilon = \int_{C(\epsilon)} x^{\alpha-2} e^{ixt} dx$$
$$= i\epsilon^{\alpha-1} \int_0^{\pi/2} e^{i(\alpha-1)\theta} e^{it\epsilon e^{i\theta}} d\theta. \quad (B7)$$

For small ϵ we can expand the second exponential. In order to keep track of all divergences when $\alpha < 0$ we need to expand to first order,

$$I_\epsilon = i\epsilon^{\alpha-1} \int_0^{\pi/2} e^{i(\alpha-1)\theta}(1 + it\epsilon e^{i\theta}) d\theta$$
$$= \frac{\epsilon^{\alpha-1}}{\alpha-1}(-ie^{i\alpha\pi/2} - 1) + i\frac{t\epsilon^\alpha}{\alpha}(e^{i\alpha\pi/2} - 1). \quad (B8)$$

Here we assumed $\alpha \neq 0$; the $\alpha = 0$ case is handled below. In the integral along the imaginary axis we can substitute $y = -ixt$, bringing it to the Gamma function form

$$\int_{i\epsilon}^{i\infty} x^{\alpha-2} e^{ixt} dx = \left(\frac{i}{t} \right)^{\alpha-1} \int_{\epsilon t}^\infty y^{\alpha-2} e^{-y} dy$$
$$= -\frac{ie^{i\pi\alpha/2}}{t^{\alpha-1}} \Gamma(\alpha-1, \epsilon t), \quad (B9)$$

where $\Gamma(\alpha - 1, \epsilon t)$ is the upper incomplete Gamma function. Because $\alpha - 1 < 0$, this does not actually converge to $\Gamma(\alpha - 1)$ when $\epsilon \rightarrow 0$. However, the incomplete Gamma function satisfies

$$\Gamma(s,x) = \frac{\Gamma(s+1,x)}{s} - \frac{x^s}{s} e^{-x}, \quad (B10)$$

as can be verified from an integration by parts. We can make use of this in order to separate out all the diverging terms,

$$
\begin{aligned}
\Gamma(\alpha-1,\epsilon t) &= \frac{\Gamma(\alpha,\epsilon t)}{\alpha-1} - \frac{(\epsilon t)^{\alpha-1}}{\alpha-1} e^{-\epsilon t} \\
&= \frac{\Gamma(\alpha+1,\epsilon t)}{\alpha(\alpha-1)} - \frac{(\epsilon t)^{\alpha}}{\alpha(\alpha-1)} e^{-\epsilon t} - \frac{(\epsilon t)^{\alpha-1}}{\alpha-1} e^{-\epsilon t}.
\end{aligned}
\tag{B11}
$$

The first term converges to $\Gamma(\alpha-1)$. To order ϵ^{α}, we obtain

$$
\Gamma(\alpha-1,\epsilon t) = \Gamma(\alpha-1) - \frac{(\epsilon t)^{\alpha-1}}{\alpha-1} + \frac{(\epsilon t)^{\alpha}}{\alpha}.
\tag{B12}
$$

Thus we can see that I_x combines to

$$
I_x = -\frac{\epsilon^{\alpha-1}}{\alpha-1} - it\frac{\epsilon^{\alpha}}{\alpha} - i\frac{e^{i\pi\alpha/2}}{t^{\alpha-1}}\Gamma(\alpha-1),
\tag{B13}
$$

which combines with the complex conjugate to

$$
I_x + I_x^* = 2\frac{\epsilon^{\alpha-1}}{1-\alpha} + \frac{2}{t^{\alpha-1}}\sin\frac{\pi\alpha}{2}\Gamma(\alpha-1).
\tag{B14}
$$

Inserting this result back into the Bessel function integral in Eq. (B3), we find

$$
\begin{aligned}
I_J &= \frac{2}{\pi}\int_0^1 \left(\frac{\epsilon^{\alpha-1}}{1-\alpha} + \sin\frac{\pi\alpha}{2}\Gamma(\alpha-1)t^{1-\alpha}\right)\frac{dt}{\sqrt{1-t^2}} \\
&= \frac{\epsilon^{\alpha-1}}{1-\alpha} + \frac{2}{\pi}\sin\frac{\pi\alpha}{2}\Gamma(\alpha-1)\int_0^1 \frac{t^{1-\alpha}\,dt}{\sqrt{1-t^2}}.
\end{aligned}
\tag{B15}
$$

Notice the first diverging term here, which will cancel the divergence in Eq. (B2) exactly. We can reduce the final integral to a Beta function using a substitution $u = t^2$,

$$
\begin{aligned}
\int_0^1 \frac{t^{1-\alpha}\,dt}{\sqrt{1-t^2}} &= \frac{1}{2}\int_0^1 u^{-\alpha/2}(1-u)^{-1/2}du \\
&= \frac{1}{2}B\left(1-\frac{\alpha}{2},\frac{1}{2}\right),
\end{aligned}
\tag{B16}
$$

so the final result of the κ integral is

$$
\kappa = I_D - I_J = -\frac{1}{\pi}\sin\frac{\pi\alpha}{2}\Gamma(\alpha-1)B\left(1-\frac{\alpha}{2},\frac{1}{2}\right).
\tag{B17}
$$

Returning to the $\alpha = 0$ case, Eq. (B8) can be written

$$
\begin{aligned}
I_\epsilon &= i\epsilon^{-1}\int_0^{\pi/2} e^{-i\theta}(1+it\epsilon e^{i\theta})d\theta \\
&= i\epsilon^{-1}(-i-1) - t\frac{\pi}{2}.
\end{aligned}
\tag{B18}
$$

The integral along the imaginary axis in Eq. (B9) is simplified to

$$
\int_{i\epsilon}^{i\infty} x^{\alpha-2}e^{ixt}dx = -it\Gamma(-1,\epsilon t),
\tag{B19}
$$

which diverges logarithmically when $\epsilon \to 0$. However, as the incomplete Gamma function is always real, this term is purely imaginary and vanishes when we add the complex conjugate. The only contribution is from the I_ϵ integration,

$$
I_x + I_x^* = I_\epsilon + I_\epsilon^* = 2\epsilon^{-1} - \pi t,
\tag{B20}
$$

which we can insert back into Eq. (B3) to obtain

$$
I_J = \frac{1}{\pi}\int_0^1 (2\epsilon^{-1} - \pi t)\frac{dt}{\sqrt{1-t^2}} = \epsilon^{-1} - 1.
\tag{B21}
$$

Canceling the divergence from Eq. (B2), the result is simply

$$
\kappa_{\alpha=0} = I_D - I_J = 1.
\tag{B22}
$$

This is also what one would obtain by taking the limit $\alpha \to 0$ in the general result from Eq. (B17).

APPENDIX C: COMBINING THE PREFACTORS

The dimensionless prefactor to the power-law tail distribution is

$$
\begin{aligned}
P &= \frac{\kappa\lambda}{\pi}\Gamma(3-\alpha)e^{i\pi(1-\alpha)/2} \\
&= -\frac{1}{\pi^2}\sin\frac{\pi\alpha}{2}CGB,
\end{aligned}
\tag{C1}
$$

where C collects the complex number factors, G collects the Gamma functions, and B collects the Beta functions. The complex numbers combine to

$$
C = -\frac{i}{2}(1+e^{i\pi\alpha})e^{i\pi(1-\alpha)/2} = \cos\frac{\pi\alpha}{2},
\tag{C2}
$$

so that

$$
C\sin\frac{\pi\alpha}{2} = \frac{1}{2}\sin\pi\alpha.
\tag{C3}
$$

For the Gamma functions, we use the well-known properties

$$
\Gamma(x+1) = x\Gamma(x), \quad \Gamma(x)\Gamma(1-x) = \frac{\pi}{\sin\pi x}
\tag{C4}
$$

in order to write

$$
\begin{aligned}
G &= \Gamma(3-\alpha)\Gamma(\alpha-1) \\
&= \frac{(2-\alpha)(1-\alpha)}{\alpha-1}\Gamma(1-\alpha)\Gamma(\alpha) \\
&= -(2-\alpha)\frac{\pi}{\sin\pi\alpha}.
\end{aligned}
\tag{C5}
$$

The Beta function satisfies

$$
B(a,b) = \frac{\Gamma(a)\Gamma(b)}{\Gamma(a+b)},
\tag{C6}
$$

so we can simplify the B factor to

$$
\begin{aligned}
B &= B\left(1-\frac{\alpha}{2},\frac{1}{2}\right)B\left(\frac{3-\alpha}{2},\frac{1}{2}\right) \\
&= \frac{\Gamma\left(1-\frac{\alpha}{2}\right)\Gamma\left(\frac{1}{2}\right)}{\Gamma\left(\frac{3-\alpha}{2}\right)}\frac{\Gamma\left(\frac{3-\alpha}{2}\right)\Gamma\left(\frac{1}{2}\right)}{\Gamma\left(2-\frac{\alpha}{2}\right)} \\
&= \pi\frac{\Gamma\left(1-\frac{\alpha}{2}\right)}{\left(1-\frac{\alpha}{2}\right)\Gamma\left(1-\frac{\alpha}{2}\right)} = \frac{2\pi}{2-\alpha},
\end{aligned}
\tag{C7}
$$

where we also used that $\Gamma(1/2) = \sqrt{\pi}$. Combining everything we see that the various factors cancel each other, so in total we have

$$
P = 1.
\tag{C8}
$$

[1] R. H. Kraichnan, Phys. Fluids **10**, 1417 (1967).

[2] P. Tabeling, Phys. Rep. **362**, 1 (2002).

[3] L. Onsager, Nuovo Cimento **6**, 279 (1949).

[4] T. W. Neely, A. S. Bradley, E. C. Samson, S. J. Rooney, E. M. Wright, K. J. H. Law, R. Carretero-González, P. G. Kevrekidis, M. J. Davis, and B. P. Anderson, Phys. Rev. Lett. **111**, 235301 (2013).

[5] A. S. Bradley and B. P. Anderson, Phys. Rev. X **2**, 041001 (2012).

[6] M. T. Reeves, T. P. Billam, B. P. Anderson, and A. S. Bradley, Phys. Rev. Lett. **110**, 104501 (2013).

[7] M. T. Reeves, T. P. Billam, B. P. Anderson, and A. S. Bradley, Phys. Rev. A **89**, 053631 (2014).

[8] A. Skaugen and L. Angheluta, Phys. Rev. E **93**, 032106 (2016).

[9] E. A. Novikov, Zh. Eksp. Teor. Fiz. **68**, 1868 (1975) [Sov. Phys. JETP **41**, 937 (1975)].

[10] P.-H. Chavanis and C. Sire, Phys. Rev. E **62**, 490 (2000).

[11] P.-H. Chavanis, Eur. Phys. J. B **70**, 413 (2009).

[12] S. Chandrasekhar, Rev. Mod. Phys. **15**, 1 (1943).

[13] M. S. Paoletti, M. E. Fisher, K. R. Sreenivasan, and D. P. Lathrop, Phys. Rev. Lett. **101**, 154501 (2008).

[14] A. C. White, C. F. Barenghi, N. P. Proukakis, A. J. Youd, and D. H. Wacks, Phys. Rev. Lett. **104**, 075301 (2010).

[15] A. W. Baggaley and C. F. Barenghi, Phys. Rev. E **84**, 067301 (2011).

Paper III

III

Origin of the inverse energy cascade in two-dimensional quantum turbulence

Audun Skaugen[*] and Luiza Angheluta

Department of Physics, University of Oslo, P.O. 1048 Blindern, 0316 Oslo, Norway
(Received 28 September 2016; revised manuscript received 30 March 2017; published 30 May 2017)

We establish a statistical relationship between the inverse energy cascade and the spatial correlations of clustered vortices in two-dimensional quantum turbulence. The Kolmogorov spectrum $k^{-5/3}$ on inertial scales r corresponds to a pair correlation function between the vortices with different signs that decays as a power law with the pair distance given as $r^{-4/3}$. To test these scaling relations, we propose a forced and dissipative point vortex model that captures the turbulent dynamics of quantized vortices by the emergent clustering of same-sign vortices. The inverse energy cascade developing in a statistically neutral system originates from this vortex clustering that evolves with time.

I. INTRODUCTION

The condensation of energy into large-scale coherent structures and the prevailing flow of energy from small to large scales referred to as the inverse energy cascade [1] are two important signatures of two-dimensional (2D) classical flows. The inverse energy cascade is associated with the statistical conservation laws of energy and enstrophy (mean-square vorticity). This is in stark contrast to three-dimensional turbulence where energy cascades towards small dissipative length scales by the proliferation of vorticity. Quantum turbulence (QT) in highly oblate Bose Einstein condensates (BECs) provides a close experimental realization of 2D turbulence through the dynamics of quantized vortices and a well-defined theoretical framework to study turbulence from the statistical properties of a quantized vortex gas. In recent years, there have been indirect experimental evidence [2] and tantalizing numerical results [3–5] of the existence of an inverse energy cascade that follows the Kolmogorov scaling analogously to the classical turbulence. The condensation of energy on large scales has also been investigated in decaying quantum turbulence [6–8]. A crucial link between these two phenomena is that there is a net transport of energy from small to large scales and this happens in quantum turbulence due to the spatial clustering of quantized vortices of the same circulation. Here we show that this vortex interaction leading to clustering implies that the energy spectrum is directly related to spatial correlation functions, in particular to the vorticity correlation.

Large-scale vortices were first predicted by Onsager [9] as the negative temperature equilibrium configuration of point vortices in a statistical description of 2D turbulence bounded in a finite domain. These vortex condensates are formed by clustering of vortices of the same sign and occur through an SO(2) symmetry-breaking phase transition with negative critical temperature [10]. Recent studies of decaying QT propose that such negative temperature states can be achieved dynamically by an evaporative heating process through the annihilation of vortex dipoles (effective heating of vortices by removing the coldest ones, i.e., the smallest dipoles) [6]. Clustering of vortices is also at the origin of an inverse energy cascade in *driven QT* [3,5,11], but in this case the mere existence of vortex

clusters is not enough; their structure is crucially important and different from the equilibrium Onsager vortices emerging in decaying turbulence. Novikov [12] showed that, in principle, an inverse energy cascade with the Kolmogorov spectrum can be produced by a single cluster of same-sign vortices when there are long-range correlations in their spatial distribution such that the pair distribution function decays as a power law $r^{-4/3}$ with the separation distance r. The dependence of the energy spectrum on the vortex configuration was further explored in this idealized case of same-sign point vortices [4,13]. However, any realistic model of driven QT needs to include both vortex signs, which complicates this idealized picture.

Our aim is to show that the inverse energy cascade in driven QT is the result of the interaction between diverse clusters of corotating and counterrotating vortices. The largest of these clusters will be the nonequilibrium analog of Onsager vortices, in the sense that they will dominate the large-scale rotating flow. However, there is a spectrum of vortex clusters of various sizes and their interactions and internal structures lead to persistent long-range fluctuations in the vorticity field, measured by the weighted pair correlation function. Moreover, we show that the Kolmogorov spectrum is related to scale-free two-point statistics of quantized vorticity $\langle \omega(0)\omega(\vec{r}) \rangle \sim r^{-4/3}$, similar to Novikov's prediction for the idealized same-sign vortices. This would be analogous to the Kraichnan-Kolmogorov scaling argument for the classical coarse-grained vorticity on an inertial scale r, $\omega_r \sim v_r/r$, with the eddy velocity $v_r \sim r^{1/3}$ [1]. To investigate the origin of the inverse energy cascade in driven quantum turbulence without having to concern ourselves with the compressibility effects in quantum fluids [2], we propose a driven and dissipative point vortex model as described below.

The structure of the paper is as follows. In Sec. II we describe the point vortex model as applied to quantum turbulence. In Sec. III we give a statistical argument relating the energy spectrum to the vorticity correlation. This connection is further explored numerically within a driven and dissipative point vortex model, which is introduced in Sec. IV. We show that this model develops a turbulent steady state in Sec. V. In Sec. VI we discuss the numerical results on the vorticity correlation function and in Sec. VII we show that this is associated with a negative spectral energy flux and a Kolmogorov $k^{-5/3}$ energy spectrum. Conclusions and a discussion are presented in Sec. VIII.

―――――――
[*]audun.skaugen@fys.uio.no

II. POINT VORTEX MODEL

Point vortices in BECs are realized as codimension-2 topological defects in the complex order parameter representing the many-particle wave function. These vortices have a characteristic core structure determined by the balance of kinetic energy and distortion energy, leading to a core size on the order of the healing length ξ [4,14]. Vortices with overlapping cores have complicated dynamics that couple the vortex gas to phonon excitations in the BEC and lead to the annihilation of vortex-antivortex pairs. On the other hand, well-separated vortices will move according to the point vortex model. A collection of vortices with circulation signs $\{q_i\}$ and positions $\{\vec{r}_i\}$ in a bounded container of size R set up a velocity field characterized by the stream function $\psi(\vec{r},t)$, given by a superposition of contributions from each vortex [15]

$$\psi(\vec{r},t) = -\sum_{j=1}^{N} q_j \ln |\vec{r} - \vec{r}_j| + \sum_{j=1}^{N} q_j \ln \left(|\vec{r} - \vec{r}_j^v| r_j \right). \quad (1)$$

The second sum gives the contributions from image vortices located at $\vec{r}_j^v = \frac{R^2}{r_j^2} \vec{r}_j$, which are necessary in order to ensure the no-flux boundary condition at $r = R$, as well as image vortices located at the origin giving the extra factor of $r_j = |\vec{r}_j|$ in the logarithm. Note that the winding number $q_j = \pm 1$ is constant for quantized vortices in 2D QT, unlike the continuously varying circulation of classical vortices subjected to merging rules in vortex models for 2D CT [16]. Well-separated vortices follow this velocity field passively,

$$\dot{\vec{r}}_i = \vec{\nabla}^{\perp} \psi^{(i)}(\vec{r}_i), \quad (2)$$

where $\vec{\nabla}^{\perp} = (-\partial_y, \partial_x)$ and the (i) superscript indicates that we omit the singular self-interaction from the $i = j$ term of the stream function (although we keep the $i = j$ term in the image sum, which gives a nonsingular interaction between a vortex and its image). This is equivalent to a conservative dynamics described by the Hamiltonian

$$\mathcal{H} = \frac{1}{2} \sum_i q_i \psi^{(i)}(\vec{r}_i)$$
$$= -\frac{1}{2} \sum_{i \neq j} q_i q_j \ln |\vec{r}_i - \vec{r}_j| + \frac{1}{2} \sum_{i,j} q_i q_j \ln \left(|\vec{r}_i - \vec{r}_j^v| r_j \right), \quad (3)$$

reflecting the conservation of kinetic energy in the velocity field.

Although we can always make sure that the initial vortex positions are well separated from each other, the dynamical evolution might cause pairs of vortices to get close enough that the coupling to the phonon field becomes important. It is therefore necessary to include phenomenological rules such as dipole annihilation in order to properly represent BEC dynamics in a point vortex model.

The Hamiltonian point vortex model, describing conservative dynamics, cannot capture dynamical aspects of turbulence such as the energy cascade or the buildup of large-scale coherent structures. It is however useful for investigating equilibrium statistical properties for inertial turbulent fluctuations [17]. The phase space of the point vortex Hamiltonian

coincides with the configuration space and hence is finite for a bounded domain. This implies that the microcanonical entropy has a maximum at finite energy, giving rise to negative temperature T states at higher energies. Onsager [9] predicted that these negative-T states correspond to spatial clustering of same-sign vortices, resulting in large-scale vortices. Recently, it has been proposed that the Onsager vortices in the strongly coupled regime undergo a condensation similar to the Bose-Einstein condensation, but this requires much higher energies than those present in decaying turbulence or in the inverse energy cascade [18].

For dynamical exploration of these vortex clustered configurations from initial conditions with positive T, one needs to include phenomenological dissipation mechanisms, such as dipole annihilation rules [6] and/or thermal friction [19]. In Ref. [20] it was proposed that the annihilation of the smallest vortex dipoles acts as an effective viscous dissipation in QT. However, as pointed out in Ref. [6], this effective viscosity is not constant, but instead depends on the spatial configuration of vortices and vanishes for clusters of same-sign vortices. By removing the smallest vortex dipoles, the total energy will slowly decrease with decreasing number of vortices. Since the energy of the smallest dipole is smaller than the mean energy per vortex, the net energy per vortex keeps increasing. Hence it acts like an evaporative heating mechanism and leads to the emergence of same-sign vortex clusters in decaying turbulence [6].

III. ENERGY SPECTRUM AND VORTICITY CORRELATION

The kinetic energy spectrum of N point vortices is determined by their spatial configuration and charges as derived by Novikov [12] and in more recent studies of BEC vortices with a characteristic vortex core structure [4]. For a given vortex configuration, the energy spectrum of N vortices in an unbounded plane is given as [12]

$$E_N(k) = \frac{\pi}{k} \left(N + \sum_{i \neq j} q_i q_j J_0(k r_{ij}) \right), \quad (4)$$

where $J_0(x)$ is the zeroth-order Bessel function and $r_{ij} = |\vec{r}_{ij}| = |\vec{r}_i - \vec{r}_j|$. To study this statistically, Novikov considered a cluster of same-sign vortices and introduced the pair correlation $g(\vec{r}) = \frac{1}{\rho \langle N \rangle} \langle \sum_{i \neq j} \delta(\vec{r} - \vec{r}_{ij}) \rangle$ with the vortex number density $\rho = \langle \sum_i \delta(\vec{r} - \vec{r}_i) \rangle$. For vortices inside the given cluster the sign factors $q_i q_j$ will equal 1, so averaging the kinetic energy spectrum we find

$$\langle E_N(k) \rangle = \frac{\pi}{k} \left(\langle N \rangle + \int J_0(kr) \left\langle \sum_{i \neq j} \delta(\vec{r} - \vec{r}_{ij}) \right\rangle d^2\vec{r} \right)$$
$$= \frac{\langle N \rangle \pi}{k} \left(1 + \rho \int J_0(kr) g(\vec{r}) d^2\vec{r} \right). \quad (5)$$

A scaling $g(\vec{r}) \sim 1 + C r^{-\alpha}$ will then give rise to two new terms $\sim \delta(k)$ and $\sim k^{\alpha-3}$ in the energy spectrum, in addition to the $\sim k^{-1}$ term from the single-vortex solution. This is Novikov's statistical relationship between the scalings in energy and pair correlation of the same-sign vortex gas.

However, even if the vortices organize into clusters with a characteristic pair correlation $g(r)$, it is not clear that the

clusters would be decoupled sufficiently from each other for the energy spectrum to be a simple superposition of the spectra of each cluster. We therefore argue that simply performing the average inside a given vortex cluster does not give the complete statistical description of turbulence with two vortex signs. Instead, one should perform this derivation accounting for all the different vortex signs.

Averaging Eq. (4) and keeping all the sign factors, we find

$$\langle E_N(k)\rangle = \frac{\pi}{k}\left(\langle N\rangle + \left\langle \sum_{i\neq j} q_i q_j J_0(kr_{ij})\right\rangle\right)$$

$$= \frac{\pi}{k}\left(\langle N\rangle + \int d^2\vec{r}\, J_0(kr)\left\langle \sum_{i\neq j} q_i q_j \delta(\vec{r}-\vec{r}_{ij})\right\rangle\right)$$

$$= \frac{\langle N\rangle\pi}{k}\left(1 + \int d^2\vec{r}\, J_0(kr)\rho g_w(\vec{r})\right), \quad (6)$$

where the weighted pair correlation $\rho g_w(\vec{r})$ is defined as

$$\rho g_w(\vec{r}) = \frac{1}{\langle N\rangle}\left\langle \sum_{i\neq j} q_i q_j \delta(\vec{r}-\vec{r}_i+\vec{r}_j)\right\rangle. \quad (7)$$

This function can be interpreted as the probability of finding two same-sign vortices at a separation $\vec{r}$, minus the probability of finding two opposite-sign vortices at the same separation. For vortices of the same sign, we recover the simple pair correlation $\rho g(\vec{r})$, which decreases monotonically such that $\lim_{r\to\infty} g_w(r) = 1$, reflecting that the vortex positions are uncorrelated at large distances. However, for the neutral system the two probabilities will cancel out, giving $\lim_{r\to\infty} g_w(r) = 0$, reflecting the fact that there should be no excess of one sign over the other at large distances.

At intermediate distances the $g_w(r)$ function indicates the predominance of vortex clusters, giving positive values, and vortex dipoles, giving negative values. A characteristic scale might indicate the typical size of clusters, while a scale-free behavior might indicate either the coexistence of clusters of different sizes or a scale-free spatial structure of each cluster. Similarly to Novikov's argument, the Kolmogorov $k^{-5/3}$ energy scaling corresponds to a $Cr^{-4/3}$ scaling in the weighted pair correlation, by the relation

$$\frac{\langle E(k)\rangle}{\langle N\rangle} \sim \frac{\pi}{k} + 2\pi^2 \frac{\rho C}{k^{5/3}}\int dx\, J_0(x)x^{-1/3}. \quad (8)$$

The vanishing limit of the weighted pair correlation means that there is no singularity $\sim\delta(k)$ in the energy spectrum. The dimensionless integral equals $\frac{\sqrt{\pi}}{\Gamma(5/6)}$ in an unbounded system, but may introduce corrections in a finite-size system.

The weighted pair correlation function is related to correlations in the vorticity field $\omega(\vec{r}) = \sum_i q_i \delta(\vec{r}-\vec{r}_i)$. Assuming a statistically homogeneous system, two-point correlations in vorticity can be found as

$$\langle \omega(\vec{r})\omega(\vec{r}\,')\rangle = \left\langle \sum_{i,j} q_i q_j \delta(\vec{r}-\vec{r}_i)\delta(\vec{r}\,'-\vec{r}_j)\right\rangle$$

$$= \rho\delta(\vec{r}-\vec{r}\,') + \left\langle \sum_{i\neq j} q_i q_j \delta(\vec{r}-\vec{r}_i)\delta(\vec{r}\,'-\vec{r}_j)\right\rangle$$

$$= \rho\delta(\vec{r}-\vec{r}\,') + \rho^2 g_w(\vec{r}-\vec{r}\,'). \quad (9)$$

Hence the $r^{-4/3}$ scaling in the weighted pair correlation relates to a similar scaling in the vorticity correlation. Such a scaling in the vorticity is analogous to the Kraichnan-Kolmogorov scaling in classical turbulence, which follows from dimensional analysis based on statistical self-similarity of turbulence.

IV. DRIVEN AND DISSIPATIVE POINT VORTEX MODEL

In order to numerically investigate the relationship between the energy spectrum and vorticity correlations, we propose an extension to the point vortex model that can capture driven quantum turbulence, by adding driving and dissipation mechanisms to the equations of motion. A natural source of dissipation in QT is the nonconservative vortex motion due to thermal friction. This adds a longitudinal component in the vortex motion, with repulsion between same-sign vortices and attraction between opposite-sign vortices. Hence, the point vortices follow a non-Hamiltonian equation of motion given as

$$\dot{\vec{r}}_i = \vec{\nabla}^{\perp}\psi^{(i)}(\vec{r}_i) - \gamma q_i \vec{\nabla}\psi^{(i)}(\vec{r}_i), \quad (10)$$

where γ is the dimensionless thermal friction coefficient and the sign factor q_i is necessary in order to give different motion for same- and opposite-sign vortices. As discussed in Ref. [19], γ quantifies the main source of dissipation in the system and is directly related to the damping coefficient commonly used in Gross-Pitaevskii dynamics to account for thermal dissipation [3,4].

This dissipative evolution will cause vortex-antivortex pairs to collapse into ever tighter dipoles. To avoid a singularity we introduce a phenomenological annihilation rule for such pairs when the distance is closer than a constant l_a. This constant can, for example, represent a length scale on the order of the healing length ξ in a BEC. Vortices in a bounded disk will also be attracted to the boundary, so we need a similar rule causing vortices close to the boundary to annihilate with their image. Although same-sign vortex pairs also behave differently in BECs when they get close enough together, we do not add any phenomenological rules for this case, as we do not expect any such pair to come within a distance much smaller than l_a in our dynamics.

To generate forced turbulence, we include a small-scale stirring mechanism by spawning vortex-antivortex dipoles with a fixed separation $l_s > l_a$. This is different from the stirring mechanism with an effective negative-viscosity proposed by Siggia and Aref [21] and more relevant for QT. Our stirring mechanism is consistent with the setup for 2D QT in BECs [3,5,11], where a moving obstacle causes dipoles to be spawned into the system at a distance l_s bigger than the coherence length ξ and with annihilation occurring on the scale ξ due to phonon emission from the Gross-Pitaevskii dynamics. When the dipole spawning and evaporation happen at equal rates, the total energy will increase roughly by $\ln(l_s/l_a)$ with each event. The increase in mean energy per vortex causes the spawned dipoles to decouple into free vortices, which then form clusters of same-sign vortices. Moreover, this driving occurs on a length scale $\sim l_s$, so by choosing this distance to be small compared to the system size, we can achieve small-scale stirring. In the Supplemental Material [22] we have included

TABLE I. Parameters used in the simulations, along with some measured quantities.

Parameters		Measured quantities		
$10^3 \gamma$	c	$\langle N \rangle$	10^{-3} Re	$\langle \epsilon_d^{\text{tot}} \rangle$
10	10	144	1.20	6.59
3	10	227	5.02	5.77
1	1	100	10.0	0.541
1	2	131	11.4	1.13
1	5	187	13.7	2.79
1	10	246	15.7	5.33
1	20	320	17.9	10.5

two movies with the vortex dynamics during the transition to the steady state versus that in the statistically stationary turbulent regime.

We solve the system of ordinary differential equations given by Eq. (10) using the symplectic, fully implicit fourth-order Gauss-Legendre method for the conservative part [23]. After each time step of the symplectic method, we evolve the dissipative part using a simple forward Euler scheme, which is sufficient because $\gamma \ll 1$, so the dissipative evolution is slow compared to the conservative evolution. We use an adaptive time step based on the minimum distance d between vortices and vortex-image pairs. Since the maximum velocity is $v \sim 1/d$, the typical time until a collision $\Delta t \sim d/v \sim d^2$ is a reasonable choice for the adaptive time step. With each time-step increment, we remove all vortex dipoles with dipole moments less than l_a and any vortex within a distance less than l_a from its image vortex. Finally, we pick a random number n from a Poisson distribution with the rate parameter $c\Delta t$ (with c being the dipole injection rate) and spawn n dipoles with dipole moment l_s at random positions and dipole orientations such that neither of the spawned vortices is within l_s of another vortex.

During these simulations, we set $R = 10$, $l_s = 0.4$, and $l_a = 0.2$. The thermal friction coefficient γ and the spawning rate c were varied to generate different regimes of turbulence. The values are given in Table I, along with measured values for the mean vortex number $\langle N \rangle$ with the resulting Reynolds number (see Sec. V) and the time-averaged total energy dissipation $\langle \epsilon_d^{\text{tot}} \rangle$ (see Sec. VII).

V. STEADY-STATE TURBULENT REGIME

As a consequence of spawning and evaporation of vortex dipoles, the total number of vortices fluctuates in time. Starting from zero vortices, the number of vortices increases by spawning events dominating over dipole evaporation events. After a transient time, the number fluctuations reach a statistically steady-state regime as shown in Fig. 1 for different Re. By a rescaling of time with the crossover time t_c and of number fluctuations with their mean value $\langle N \rangle$, we find that all data collapse onto a universal curve that is nicely fitted by the $\tanh(x)$ function, i.e., the solution of the mean field kinetic equation $\dot{N} = -N^2 + 1$, written in rescaled units of t/t_c and $N/\langle N \rangle$. The first term is the leading-order contribution due to dipole annihilation and the last term is the constant spawning
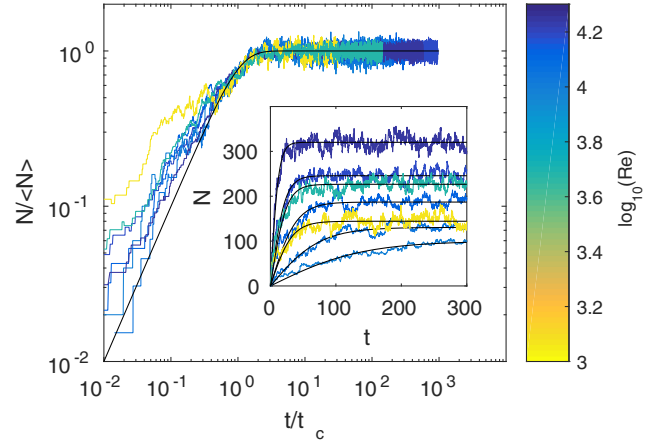

FIG. 1. Collapsed data in rescaled units plotted against $\tanh(x)$. The inset shows the temporal evolution of the total vortex number for different Re numbers. We extract the mean number $\langle N \rangle$ and the crossover time t_c by fitting each curve with the tanh function.

rate. Small deviations from this mean-field trend are the effect of higher-order terms due to collective interactions in dipole evaporation [24], but also because we neglected the small effect of a linear decay term corresponding to the evaporation of single vortices near the boundary of the disk.

After the vortex number has stabilized, the energy of the system [as measured by Eq. (3)] keeps increasing as dipoles decouple into free vortices, which then form clusters. Higher energy leads to a higher energy-dissipation rate from the dissipative evolution, eventually balancing the small-scale forcing, so the energy eventually also stabilizes. By carefully balancing the spawning and dissipation rates we can make sure that the steady-state energy is such that the system is dominated by clusters.

For the statistically stationary regime (a snapshot of the vortex configuration is illustrated in Fig. 2 and a video corresponding to this regime is included in the Supplemental Material [22]), we can define a Reynolds number Re by the balance between inertial forces (where the typical distance is
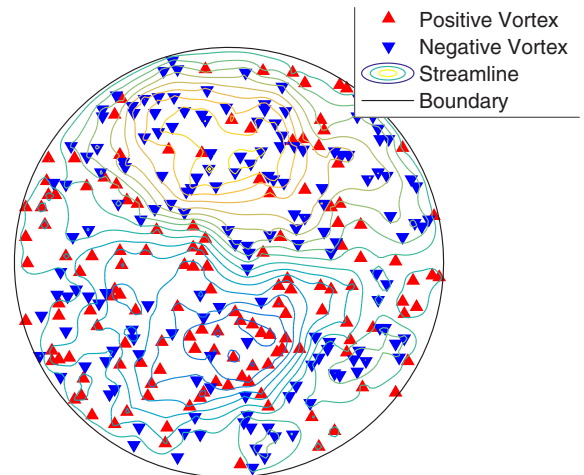

FIG. 2. Snapshot of a vortex configuration.

the disk's radius R and the typical field velocity is $U \sim 1/\langle l \rangle$ with $\langle l \rangle \sim R/\sqrt{\langle N \rangle}$) and dissipative forces (thermal friction characterized by γ), hence Re $\sim \sqrt{\langle N \rangle}/\gamma$.

VI. WEIGHTED PAIR CORRELATION FUNCTION IN A DISK

In a statistically homogeneous and isotropic system, the weighted pair correlation function defined in Eq. (7) is also isotropic and therefore is equivalent to

$$\rho g_w(r) = \frac{1}{2\pi r} \int_0^{2\pi} \rho g_w(\vec{r}) r \, d\theta$$

$$= \frac{1}{2\pi r \langle N \rangle} \sum_{i \neq j} \langle q_i q_j \delta(r - r_{ij}) \rangle, \quad (11)$$

where $r_{ij} = |\vec{r}_i - \vec{r}_j|$. For a numerical estimate of this expectation value, we can discretize the δ function into bins of width d, by $\delta_d(r) = [H(r + \frac{d}{2}) - H(r - \frac{d}{2})]/d$, where $H(x)$ is the step function. This gives the contribution $g_w^s(r)$ to the correlation function from a given realization as

$$\langle N \rangle \rho g_w^s(r) = \frac{1}{2\pi r d} \sum_{i \neq j} q_i q_j d \delta_d(r - r_{ij}). \quad (12)$$

Thus we can estimate the weighted correlation function by iterating over each vortex, counting the number of vortices that fall within a shell of radius r and width d, weighting them by whether they have equal or opposite sign, and dividing by the area of the shell. By time averaging over many vortex configurations in the statistically stationary regime, we can divide by the mean vortex number and density, giving an estimate of the correlation function.

A complication to this method arises from the fact that our system is finite with a circular boundary of radius R. This breaks homogeneity and isotropy, especially when considering particles close to the boundary. We will however still assume that the system is as homogeneous and isotropic as possible, by which we mean the following: Considering a vortex close to the boundary, the system is assumed to look the same in all directions as it would look from the center, as long as we do not see the boundary. Taking the contribution from each vortex separately,

$$\langle N \rangle \rho g_w^s(\vec{r}) = \sum_i q_i g_w^i(\vec{r}),$$

$$g_w^i(\vec{r}) = \sum_{j \neq i} q_j \frac{1}{r} \delta(r - r_{ij}) \delta(\theta - \theta_{ij}), \quad (13)$$

we assume that $g_w^i(\vec{r})$ is equal for all directions θ such that $\vec{r} + \vec{r}_i$ does not cross the boundary.

These directions go from $\theta_i^+ = \theta_i + \frac{1}{2}\Delta\theta_i$ to $2\pi + \theta_i^- = 2\pi + \theta_i - \frac{1}{2}\Delta\theta_i$ (as illustrated in Fig. 3) and by the law of cosines we have

$$R^2 = r^2 + r_i^2 + 2rr_i \cos\left(\frac{1}{2}\Delta\theta_i\right),$$

$$\Delta\theta_i = 2\arccos\frac{R^2 - r^2 - r_i^2}{2rr_i}. \quad (14)$$
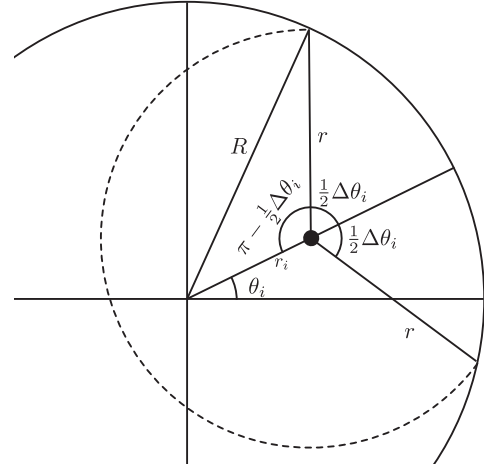

FIG. 3. Directions not crossing the boundary for a given vortex at $\vec{r}_i$ (black point). The solid circle gives the boundary, while the dashed circle gives the shell of radius r.

By our assumption of near isotropy we can integrate over the allowed directions

$$g_w^i(r) = \frac{1}{(2\pi - \Delta\theta_i)r} \int_{\theta_i^+}^{2\pi + \theta_i^-} g_w^i(\vec{r}) r \, d\theta$$

$$= \frac{1}{(2\pi - \Delta\theta_i)r} \sum_{j \neq i} q_j \delta(r - r_{ij}), \quad (15)$$

where we used that θ_{ij} certainly lies within the integration range if $r = r_{ij}$; otherwise $\vec{r}_j$ would be outside the boundary. Thus we can account for the boundary effects by estimating the correlation function in the same way as for an unbounded system, only reducing the area of the shell of radius r around vortex i from $2\pi r d$ to the area given by the directions not crossing the boundary,

$$A_i = \left(2\pi - 2\arccos\frac{R^2 - r^2 - r_i^2}{2rr_i}\right)rd. \quad$$

We measured $g_w(r)$ taking into account this boundary effect and time averaging over 10^3–10^4 statistically stationary realizations outputted at regularly spaced time intervals (about the typical time scale it takes an injected dipole to cross the disk). The resulting distribution is shown for different Re in Fig. 4, where we removed the spurious contributions of single (unclustered) vortices, using the same clustering analysis as in Ref. [11]. For the smallest Re, $g_w(r) < 0$ for most of its range, indicating that the system is dominated by dipoles. At larger Re it develops a peak around a characteristic cluster size r_c and falls off rapidly after this, which indicates that the system is dominated by small vortex clusters with similar sizes. However, at sufficiently large Re, we observe instead a scaling regime developing and approaching the power law $Cr^{-4/3}$, indicating a diverse range of different cluster sizes.

VII. ENERGY SPECTRUM IN A DISK

For N vortices, the energy spectrum from Eq. (4) can be computed in $O(N^2)$ steps straightforwardly. However, with the imposed circular boundary at radius R, there are additional
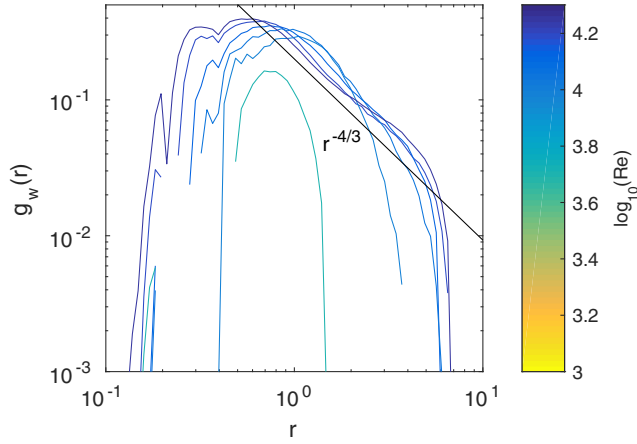
FIG. 4. Weighted pair correlation function for different Re numbers, ignoring isolated vortices. The case with the lowest Re Re ~ 1000 is excluded because this system is dominated by dipoles, so $g_w(r) < 0$ in most of its range.
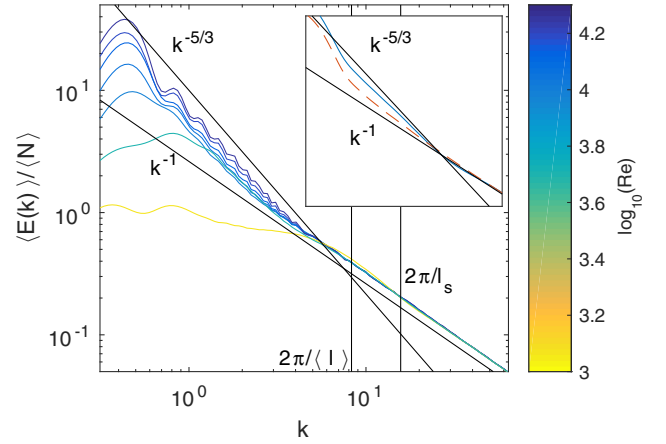

FIG. 5. Energy spectrum per vortex for different Re numbers, ignoring single vortices. The vertical lines correspond to a typical intervortex spacing $\langle l \rangle$ and the spawning length scale l_s. In the inset we compare two different energy spectra for the highest Re, where we ignore the contribution from the image vortices: including all vortices (dashed line) and excluding isolated vortices (solid line). Clearly, excluding isolated vortices is necessary to show Kolmogorov scaling.

contributions due to image vortices. With these contributions worked out in Ref. [25], the energy spectrum is given as

$$
E(k) = \frac{\pi}{k} \left\{ N + 2 \sum_{i<j} q_i q_j J_0(kr_{ij}) \right.
$$
$$
+ \sum_{l=0}^{\infty} \epsilon_l J_l(kR) \sum_{i,j} q_i q_j \left(\frac{r_i}{R}\right)^l \left[J_l(kR)\left(\frac{r_j}{R}\right)^l \right.
$$
$$
\left. \left. - 2 J_l(kr_j) \right] \cos(l\theta_{ij}) \right\}, \qquad (16)
$$

where $\epsilon_0 = 1$, $\epsilon_l = 2$ for $l \geqslant 1$, and $\theta_{ij} = \theta_i - \theta_j$ is the angle between vortices i and j.

Numerically, these extra sums are expensive to compute because they involve $N^2 L$ terms, where L is the number of terms we use in the l summation. However, the extra terms can be transformed into products of single sums over the number of vortices, decreasing the cost to NL and making it simpler to implement.

The key insight is that both the finite-size sums can almost be factored into independent sums over i and j, if not for the cosine terms coupling them. This allows us to split the sum into two new sums, which can then be decoupled,

$$
E(k) = \frac{\pi}{k} \left\{ N + 2 \sum_{i<j} q_i q_j J_0(kr_{ij}) \right.
$$
$$
+ \sum_{l=0}^{\infty} \epsilon_l J_l(kR) \left[\sum_i a_{il} \cos(l\theta_i) \sum_j b_{jl} \cos(l\theta_j) \right.
$$
$$
\left. \left. + \sum_i a_{il} \sin(l\theta_i) \sum_j b_{jl} \sin(l\theta_j) \right] \right\}, \qquad (17)
$$

where

$$
a_{il} = q_i \left(\frac{r_i}{R}\right)^l, \quad b_{il} = q_j \left[J_l(kR)\left(\frac{r_j}{R}\right)^l - 2 J_l(kr_j) \right]. \quad (18)
$$

Here all the finite-size sums over N vortices are independent, giving much faster numerical evaluation.

In Fig. 5 we show the energy spectrum per vortex $\langle E(k) \rangle / \langle N \rangle$ for the different Re, time averaged in the same way as with the correlation function. We notice that the energy spectrum transitions from the $1/k$ scaling attributed to the self-energy of a single vortex to the Kolmogorov $-5/3$ scaling law on wave numbers smaller that $2\pi/\langle l \rangle$ at high Re. As can be seen from Eq. (8), both contributions will be present in the energy spectrum and even though the $-5/3$ contribution should in principle dominate the scaling at low k, the finite-size effects may prevent this.

In order to clearly see this inertial scaling regime for both $g_w(r)$ and $\langle E_N(k) \rangle$, we removed from the statistical analysis the contribution of single (unclustered) vortices, which can hinder the collective effects for small system sizes. The inset of Fig. 5 shows the spectral analysis for the highest Re, when we include or exclude the effects of single vortices. The best inertial scaling seems to follow when we take out these effects and only look at the spectrum induced by clustered vortices. Including the contribution of the vortex images in the statistical analysis did not significantly change this picture, but merely introduced some minor oscillations around the trend line, which are visible in the main part of Fig. 5. The presence of an inverse energy cascade indicates that the energy dissipation introduced in Eq. (10) mostly acts on large scales, so energy needs to transfer from the small injection scale to the larger dissipation scale. We now turn to measuring whether this is true.

Spectral energy flux and dissipation rate

The energy fluxes can be found by time differentiating the energy spectrum from Eq. (4), giving

$$
\frac{dE(k)}{dt} = -2\pi \sum_{i<j} q_i q_j J_1(kr_{ij}) \frac{\vec{r}_{ij}}{r_{ij}} \cdot (\vec{v}_i - \vec{v}_j). \qquad (19)
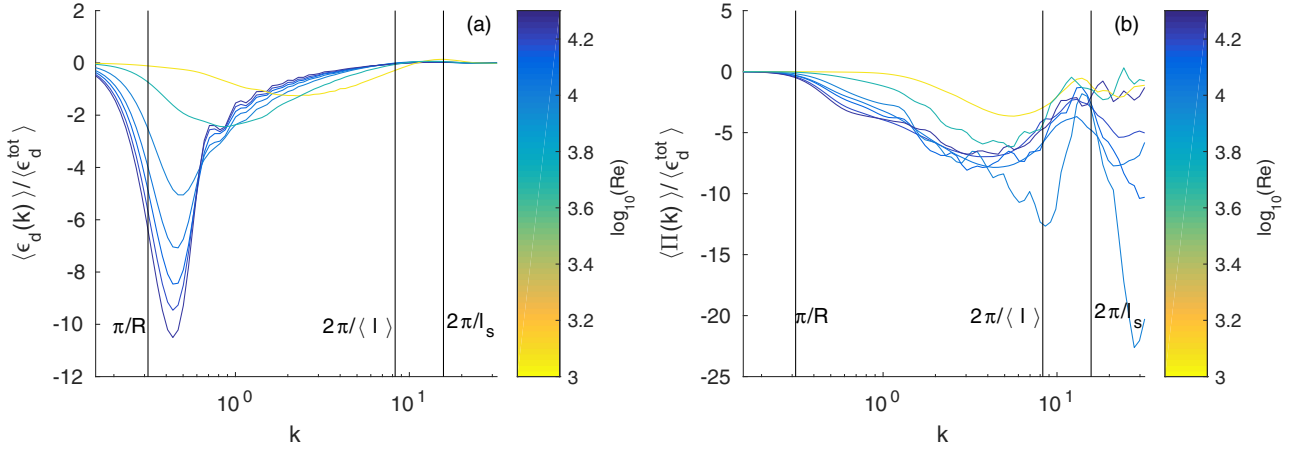$$

FIG. 6. (a) Normalized spectral dissipation rate and (b) spectral flux for different Reynolds numbers. At high Re the dissipation rate concentrates at large scales. The spectral flux is negative in the inertial range, especially for high Re.

Splitting the velocities into a dissipative part and a conservative part $\vec{v}_i = \vec{v}_i^c + \vec{v}_i^d$, we have that

$$\frac{dE(k)}{dt} = -2\pi \sum_{i<j} q_i q_j J_1(kr_{ij}) \frac{\vec{r}_{ij} \cdot \vec{v}_{ij}^d}{r_{ij}}$$
$$-2\pi \sum_{i<j} q_i q_j J_1(kr_{ij}) \frac{\vec{r}_{ij} \cdot \vec{v}_{ij}^c}{r_{ij}}$$
$$= \epsilon_d(k) + \epsilon_c(k). \tag{20}$$

The second term is due to conservative evolution and can therefore only serve to redistribute energy in the spectrum

$\int_0^\infty \epsilon_c(k)dk = 0$. Integrating this up to a given wave number k gives the spectral flux across k, $\Pi(k) = -\int_0^k \epsilon_c(k)dk$. While this integral can be carried out analytically, the finite-size contributions will make numerical integration necessary, as discussed below. The energy dissipated at a given wave number is measured by $\epsilon_d(k)$.

The spectral quantities $\epsilon_{c,d}(k)$ can be measured at a given time step by explicitly inserting the conservative or dissipative velocities and the vortex positions into Eq. (20). One can then average the quantities over different realizations or time steps.

So far, this calculation does not include the contribution from image vortices in Eq. (17). By a time differentiation of Eq. (17), we find that the finite-size correction to the spectral energy flux in Eq. (19) is

$$\frac{dE^f(k)}{dt} = \frac{\pi}{k} \sum_{l=0}^\infty \epsilon_l J_l(kR) \Bigg\{ \sum_i [\dot{a}_{il} \cos(l\theta_i) - la_{il}\dot{\theta}_i \sin(l\theta_i)] \sum_j b_{jl} \cos(l\theta_j) + \sum_i [\dot{a}_{il} \sin(l\theta_i) + la_{il}\dot{\theta}_i \cos(l\theta_{ij})] \sum_j b_{jl} \sin(l\theta_j)$$
$$+ \sum_i a_{il} \cos(l\theta_i) \sum_j [\dot{b}_{jl} \cos(l\theta_j) - lb_{jl}\dot{\theta}_j \sin(l\theta_j)] + \sum_i a_{il} \sin(l\theta_i) \sum_j [\dot{b}_{jl} \sin(l\theta_j) + lb_{jl}\dot{\theta}_j \cos(l\theta_j)] \Bigg\}, \tag{21}$$

where the remaining derivatives can be found as

$$\dot{a}_{il} = la_{il} \frac{\dot{r}_i}{r_i}, \tag{22}$$

$$\dot{b}_{jl} = lb_{jl} \frac{\dot{r}_j}{r_j} + 2k J_{l+1}(kr_j)\dot{r}_j, \tag{23}$$

$$\dot{r}_i = \frac{\vec{r}_i \cdot \vec{v}_i}{r_i}, \quad \dot{\theta}_i = \frac{\vec{r}_i^\perp \cdot \vec{v}_i}{r_i^2}. \tag{24}$$

Equation (21) is still linear in the velocities, so it can be decomposed into a dissipative and a conservative part. However, the products of several Bessel functions makes the integral $\Pi(k) = -\int_0^k \epsilon_c(k)dk$ analytically intractable. One can still measure the time-averaged $\langle\epsilon_c(k)\rangle$ and then perform the integral numerically by the trapezoidal rule.

The time-averaged spectral energy flux $\langle\Pi(k)\rangle$ and the spectral energy dissipation rate $\langle\epsilon_d(k)\rangle$, normalized by the total dissipation rate $\langle\epsilon_d^{tot}\rangle = -\langle\frac{d\mathcal{H}}{dt}\rangle$ for comparison, are shown for different Re in Fig. 6. We see that for sufficiently high Re, the dissipation is mainly localized on the largest scales, while the spectral energy flux is negative in the inertial range corresponding to an inverse energy cascade towards the large scales.

VIII. CONCLUSION

By generalizing Novikov's theory for the energy spectrum of a neutral vortex gas, we found that the Kolmogorov scaling law of the turbulent energy spectrum corresponds to the $-4/3$ scaling law of the vorticity correlation function on inertial

length scales. This is analogous to the Kraichnan-Kolmogorov scaling of the vorticity correlation in classical turbulence.

In order to explore this statistical correspondence, we proposed a forced and dissipative point vortex model that is able to produce a statistically steady-state turbulent regime, where there is a coexistence between the large-scale Onsager-like vortices of various sizes and the inverse energy cascade. We showed that in a system of two-sign vortices, the inverse energy cascade originates from the vortex clustering, which also results in persistent correlations in the vorticity field. Hence, the Kolmogorov $-5/3$ scaling law is directly connected to the scale-free statistics of vorticity, measured by the weighted pair correlation function $g_w(r) \sim r^{-4/3}$. To unify our data obtained for different values of stirring and dissipation parameters, we defined a dimensionless Re analogously to its classical definition and found that this Re for a vortex gas depends solely on the mean vortex number and thermal friction coefficient.

We studied vortex dynamics in a disk similar to the experimental setup of the highly oblate BEC, so that our results could be compared with future experiments. In particular, with the recent experimental advances in *in situ* imaging of vortices in BECs [26], it may be possible to compute the pair correlation function from experimentally obtained vortex configurations and infer the presence of an inverse energy cascade. Because of the boundary effects, we also had to carefully take into account the finite-size corrections. This way, we showed that the vortex-image interactions do not affect the scaling laws, yet they can limit substantially the scaling range, i.e., the spectral gap between the scales where energy is injected and where it is dissipated.

[1] R. H. Kraichnan, Inertial ranges in two-dimensional turbulence, Phys. Fluids **10**, 1417 (1967).

[2] T. W. Neely, A. S. Bradley, E. C. Samson, S. J. Rooney, E. M. Wright, K. J. H. Law, R. Carretero-González, P. G. Kevrekidis, M. J. Davis, and B. P. Anderson, Characteristics of Two-Dimensional Quantum Turbulence in a Compressible Superfluid, Phys. Rev. Lett. **111**, 235301 (2013).

[3] M. T. Reeves, B. P. Anderson, and A. S. Bradley, Classical and quantum regimes of two-dimensional turbulence in trapped Bose-Einstein condensates, Phys. Rev. A **86**, 053621 (2012).

[4] A. S. Bradley and B. P. Anderson, Energy Spectra of Vortex Distributions in Two-Dimensional Quantum Turbulence, Phys. Rev. X **2**, 041001 (2012).

[5] M. T. Reeves, T. P. Billam, B. P. Anderson, and A. S. Bradley, Inverse Energy Cascade in Forced Two-Dimensional Quantum Turbulence, Phys. Rev. Lett. **110**, 104501 (2013).

[6] T. Simula, M. J. Davis, and K. Helmerson, Emergence of Order from Turbulence in an Isolated Planar Superfluid, Phys. Rev. Lett. **113**, 165302 (2014).

[7] G. Moon, W. J. Kwon, H. Lee, and Y.-i. Shin, Thermal friction on quantum vortices in a Bose-Einstein condensate, Phys. Rev. A **92**, 051601 (2015).

[8] T. P. Billam, M. T. Reeves, and A. S. Bradley, Spectral energy transport in two-dimensional quantum vortex dynamics, Phys. Rev. A **91**, 023615 (2015).

[9] L. Onsager, Statistical hydrodynamics, Nuovo Cimento **6**, 279 (1949).

[10] X. Yu, T. P. Billam, J. Nian, M. T. Reeves, and A. S. Bradley, Theory of the vortex-clustering transition in a confined two-dimensional quantum fluid, Phys. Rev. A **94**, 023602 (2016).

[11] A. Skaugen and L. Angheluta, Vortex clustering and universal scaling laws in two-dimensional quantum turbulence, Phys. Rev. E **93**, 032106 (2016).

[12] E. A. Novikov, Dynamics and statistics of a system of vortices, Zh. Eksp. Teor. Fiz. **68**, 1868 (1975) [Sov. Phys. JETP **41**, 937 (1975)].

[13] A. Skaugen and L. Angheluta, Velocity statistics for nonuniform configurations of point vortices, Phys. Rev. E **93**, 042137 (2016).

[14] L. M. Pismen, *Vortices in Nonlinear Fields: From Liquid Crystals to Superfluids, From Non-equilibrium Patterns to Cosmic Strings* (Oxford University Press, Oxford, 1999), Vol. 100.

[15] P. K. Newton, *The N-vortex Problem: Analytical Techniques* (Springer Science + Business Media, Berlin, 2013), Vol. 145.

[16] R. Benzi, M. Colella, M. Briscolini, and P. Santangelo, A simple point vortex model for two-dimensional decaying turbulence, Phys. Fluids A **4**, 1036 (1992).

[17] Y. B. Pointin and T. S. Lundgren, Statistical mechanics of two-dimensional vortices in a bounded container, Phys. Fluids **19**, 1459 (1976).

[18] R. N. Valani, A. J. Groszek, and T. P. Simula, Einstein-Bose condensation of Onsager vortices, arXiv:1612.02930.

[19] J. H. Kim, W. J. Kwon, and Y. Shin, Role of thermal friction in relaxation of turbulent Bose-Einstein condensates, Phys. Rev. A **94**, 033612 (2016).

[20] L. J. Campbell and K. O'Neil, Statistics of two-dimensional point vortices and high-energy vortex states, J. Stat. Phys. **65**, 495 (1991).

[21] E. D. Siggia and H. Aref, Point-vortex simulation of the inverse energy cascade in two-dimensional turbulence, Phys. Fluids **24**, 171 (1981).

[22] See Supplemental Material at http://link.aps.org/supplemental/10.1103/PhysRevE.95.052144 for two movies illustrating the vortex dynamics during the buildup towards turbulence and the statistically stationary turbulent regime, respectively.

[23] R. I. McLachlan and P. Atela, The accuracy of symplectic integrators, Nonlinearity **5**, 541 (1992).

[24] A. J. Groszek, T. P. Simula, D. M. Paganin, and K. Helmerson, Onsager vortex formation in Bose-Einstein condensates in two-dimensional power-law traps, Phys. Rev. A **93**, 043614 (2016).

[25] T. Yoshida and M. M. Sano, Numerical simulation of vortex crystals and merging in *N*-point vortex systems with circular boundary, J. Phys. Soc. Jpn. **74**, 587 (2005).

[26] K. E. Wilson, Z. L. Newman, J. D. Lowney, and B. P. Anderson, *In situ* imaging of vortices in Bose-Einstein condensates, Phys. Rev. A **91**, 023621 (2015).

Paper IV

IV

Dislocation dynamics and crystal plasticity in the phase-field crystal model

Audun Skaugen[*] and Luiza Angheluta

Department of Physics, University of Oslo, P.O. Box 1048, Blindern, N-0316 Oslo, Norway

Jorge Viñals

School of Physics and Astronomy, University of Minnesota, 116 Church Street SE, Minneapolis, Minnesota 55455, USA

A phase-field model of a crystalline material is introduced to develop the necessary theoretical framework to study plastic flow due to dislocation motion. We first obtain the elastic stress from the phase-field crystal free energy under weak distortion and show that it obeys the stress-strain relation of linear elasticity. We focus next on dislocations in a two-dimensional hexagonal lattice. They are composite topological defects in the weakly nonlinear amplitude equation expansion of the phase field, with topological charges given by the standard Burgers vector. This allows us to introduce a formal relation between the dislocation velocity and the evolution of the slowly varying amplitudes of the phase field. Standard dissipative dynamics of the phase-field crystal model is shown to determine the velocity of the dislocations. When the amplitude expansion is valid and under additional simplifications, we find that the dislocation velocity is determined by the Peach-Koehler force. As an application, we compute the defect velocity for a dislocation dipole in two setups, pure glide and pure climb, and compare it with the analytical predictions.

I. INTRODUCTION

The description of plastic response in crystals at a mesoscale level poses fundamental challenges because of collective effects in dislocation dynamics that give rise to multiple-scale phenomena, such as spatiotemporal dislocation patterning [1,2] and intermittent deformations [3]. Different multiscale models, including discrete dislocation models, stochastic models, and cellular automata, have been proposed and used to explore various aspects of collective dislocation dynamics [4–6]. We focus here on a phase-field description of a crystalline solid, the so-called phase-field crystal, first introduced by Grant and collaborators [7–9]. This model has allowed the study of defect configurations and their kinetics that are difficult to address with either microscopic or atomistic simulation techniques or with classical continuum mechanics. Examples include large strain formulations of dislocation motion [10], creep motion mediated by diffusion [11], and defect core transformations that are seen to be key to the motion of grain boundaries [12].

A mesoscale theory is also timely given that defect imaging techniques are beginning to reveal strain and rotation fields created by one or a small number of defects in atomic detail. High-energy diffraction microscopy and Bragg coherent diffractive imaging represent the state of the art in imaging at advanced synchrotron facilities [13,14]. The former can provide three-dimensional maps of grain orientations with micron resolution, whereas the latter can determine atomic-scale displacements with $\leqslant 30$ nm resolution. Advanced image-processing methods allow the determination of the strain-field

phase around a single defect, clearly evidencing its multivalued nature. Indeed, single dislocations have been successfully imaged, and their motion has been tracked quantitatively just recently [13]. Experiments also go beyond the determination of strain fields and determine other quantities sensitive to the topology of the defects. For example, lattice rotation has been imaged and analyzed in nanoindentation experiments [15] and in two-dimensional graphene sheets [16].

Mesoscale models aim at bridging fully atomistic descriptions and macroscopic theory based on continuum mechanics. Along these lines, we mention the so-called generalized disclination theory [17,18]. This theory is a fully resolved nanoscale yet continuum dynamical description of dislocations that preserves all topological constraints necessary in the kinematic evolution of the singular fields. Singularities are replaced by topologically equivalent but smooth local fields that allow a full derivation of the governing dynamical equations following the principles of irreversible thermodynamics. The newly introduced fields are similar to a phase-field model, except that they are constructed to satisfy all conservation laws, including those of topological origin. On the other hand, the dynamical part of the theory requires constitutive input for both the free energy at the mesoscale functional of the smooth fields and mobility relations for their motion.

Conventional phase-field models have also become one of the tools of choice in the study of dislocation and grain boundary motion in a wide variety of circumstances. Contrary to kinematic models, a phenomenological set of dynamical laws for the phase field are introduced, with topological invariants appearing as derived quantities. There are two different classes of phase-field models in the plasticity literature. In one approach, the elementary dislocation is described as an eigenstrain, which is then mapped onto a set of phase

---

[*]audun.skaugen@fys.uio.no

fields [19–21]. If **b** is the Burgers vector of the dislocation and **n** is the normal to the dislocation line, then the corresponding eigenstrain is defined as

$$u_{ij}^* = \frac{b_i n_j + b_j n_i}{2a}, \tag{1}$$

where a is the crystal lattice spacing. The connection to the phase fields $\phi_\alpha(\mathbf{x})$, where α label all the slip systems of a particular lattice, is made through the decomposition

$$u_{ij}^* = \sum_\alpha \epsilon_{ij}^{*\alpha} \phi_\alpha(\mathbf{r}). \tag{2}$$

The phase fields are assumed to relax according to purely dissipative dynamics driven by minimization of a phenomenological free energy. This free energy includes a nonconvex Ginzburg-Landau-type contribution that has the same functional form as in related studies in fluids [22]. This contribution is supplemented by an elastic interaction energy that depends only on the incompatibility fields associated with the eigenstrains [23–25] and hence, ultimately, on the phase fields themselves [19–21].

The second approach, which we adopt here, is based on a physical interpretation of the phase field as a temporally coarse grained representation of the molecular density in the crystalline phase. Such as model is also known as the phase-field crystal (PFC) model [8,9]. The evolution of the phase field is diffusive and governed by a Swift-Hohenberg-like free-energy functional, which is minimized by a spatially modulated equilibrium phase with the periodicity of the crystal lattice. The chosen free energy determines not only the crystal symmetry of the equilibrium phase but all other thermodynamics quantities and response functions such as its elastic constants [8]. As is generally the case with phenomenological free energies, it is only a function of a few free parameters, and hence, the range of physical properties that can be attributed to the resulting macroscopic phase is somewhat limited. Nevertheless, the PFC model has been used in numerous numerical studies, including crystal growth, grain boundaries and polycrystalline coarse-graining phenomena [12,26–29], strained epitaxial films [30], fracture propagation [8], plasticity avalanches from dislocation dynamics [31,32], and edge dislocation dynamics [9]. It appears to us that this second approach is more natural from a physical point of view in that once the mesoscopic order parameter and the corresponding free energy are introduced, defect variables such as the Burgers vector and slip systems emerge as derived quantities. This seems preferable to introducing Ginzburg-Landau dynamics for slip-system amplitudes defined *a priori*. Also, this second approach can nominally describe highly defected configurations in which a slip system, even in a coarse-grained sense, can be difficult to define.

In this paper, we address the important theoretical question of to what extent the PFC model is actually capable of capturing mesoscopic plasticity mediated by dislocation dynamics. Although previous numerical simulations of dislocation dynamics [9,32] suggest that dislocation motion is controlled by local stress, a theoretical derivation from the PFC model is still lacking. To address this question, we consider the PFC model and its amplitude expansion formulation, where we can show that the complex amplitudes are order parameters that support topological defects corresponding to dislocations in

the crystal ordered phase. This allows us to accurately define a Burgers vector density field from the topological charges and predict the dislocation velocity directly from the dissipative relaxation of the amplitudes. We show that elastic stresses can be obtained from the PFC free-energy functional through standard variational means and recover known expressions for the linear elastic constants of the medium. Furthermore, we show that the dislocation velocity, near the bifurcation from the disordered state, follows Peach-Koehler's force and is given by the product of the Burgers vector and the elastic stress. Our theoretical predictions are consistent with previous numerical PFC studies of dislocation dynamics [9,33].

The rest of the paper is organized as follows: In Sec. II, the phase-field crystal model and its elastic equilibrium properties are discussed for the two-dimensional case. Here, we also derive the elastic stress by variation of the free-energy functional and express it in terms of the crystal density field. Plastic motion mediated by dislocation dynamics is treated in Sec. III, where we use the amplitude expansion and the connection to an order parameter that supports topological defects. In Sec. IV, we verify the theoretical results by direct numerical simulations of the PFC model for a hexagonal lattice with a dislocation dipole. A summary and concluding remarks are presented in Sec. V.

II. LINEAR ELASTICITY IN THE PHASE-FIELD CRYSTAL MODEL

The phase-field crystal model that we employ involves a single scalar field $\psi(\mathbf{r},t)$, a function of space $\mathbf{r}$ in two dimensions (2D) and time t, and a phenomenological free energy given by [9]

$$\mathcal{F}[\psi] = \int d^2\mathbf{r} \, f(\psi, \nabla^2\psi)$$
$$= \int d^2\mathbf{r} \left\{ \frac{1}{2}[(\nabla^2 + 1)\psi]^2 + \frac{r}{2}\psi^2 + \frac{1}{4}\psi^4 \right\}, \tag{3}$$

where r is a dimensionless parameter. In equilibrium, the free-energy functional (3) is minimized with respect to ψ while keeping the average density constantly equal to ψ_0, so that $\left(\frac{\delta\mathcal{F}}{\delta\psi}\right)_0 = \mu_0$, where μ_0 is a constant Lagrange multiplier. When $r > 0$, $\psi = \psi_0$ is the only stable solution, whereas for $r < 0$, equilibrium periodic solutions of unit wave number are possible for stripes and hexagonal patterns in 2D [8]. The crystalline phase with density distribution $n(\mathbf{r})$ is related to the phase-field crystal through $\psi(\mathbf{r},t) = n(\mathbf{r},t)/n_0 - 1$, where $n(\mathbf{r},t) = \sum_i \langle \delta(\mathbf{r} - \mathbf{r}_i) \rangle$ is the statistical average number density of the equivalent crystal and n_0 is its spatially averaged density.

We focus below on the range of parameters for which a 2D hexagonal lattice is the equilibrium solution [8],

$$\psi = \psi_0 + \sum_{\mathbf{g}} A_{\mathbf{g}}^{(0)} e^{i\mathbf{g}\cdot\mathbf{r}}, \tag{4}$$

where the sum extends over all reciprocal lattice vectors **g** of a hexagonal lattice. We distinguish below three reciprocal lattice wave vectors $\mathbf{q}_n$, of unit length in the dimensionless units of

Eq. (3), which are given in Cartesian coordinates by

$$\mathbf{q}_1 = \mathbf{j}, \; \mathbf{q}_2 = \frac{\sqrt{3}}{2}\mathbf{i} - \frac{1}{2}\mathbf{j}, \; \mathbf{q}_3 = -\frac{\sqrt{3}}{2}\mathbf{i} - \frac{1}{2}\mathbf{j}, \qquad (5)$$

which fixes the lattice constant $a = \frac{4\pi}{\sqrt{3}}$. These three vectors satisfy the resonance condition $\sum_{n=1}^{3} \mathbf{q}_n = 0$. The corresponding amplitudes $A_n^{(0)}$ are all constant and equal.

We first examine the change in free energy $\Delta \mathcal{F} = \mathcal{F}[\psi(\mathbf{r}')] - \mathcal{F}[\psi(\mathbf{r})]$ due to a small affine distortion $\mathbf{r}' = \mathbf{r} + \mathbf{u}(\mathbf{r})$. The free-energy change $\Delta \mathcal{F}[\psi, \mathbf{u}]$ associated with such a distortion is given, after a transformation of variables from $\mathbf{r}'$ to $\mathbf{r}$, by

$$\Delta \mathcal{F} = \int d^2 \mathbf{r} \{(1 + \mathbf{\nabla} \cdot \mathbf{u}) f[\psi(\mathbf{r}'), \nabla'^2 \psi(\mathbf{r}')] - f(\psi, \nabla^2 \psi)\}, \qquad (6)$$

where the transformed derivatives are given by

$$\partial_i' = \partial_i - (\partial_i u_j)\partial_j + O(|\nabla u|^2),$$
$$\partial_{ij}' \psi = \partial_{ij}\psi - \partial_i[(\partial_j u_k)\partial_k \psi] - (\partial_i u_k)\partial_{kj}\psi + O(|\nabla u|^2). \qquad (7)$$

After a Taylor expansion of Eq. (6) for small deformation gradients $\partial_i u_j$, we obtain

$$\Delta \mathcal{F} = \int d^2 \mathbf{r} \left[-\frac{\partial f}{\partial(\partial_i \psi)}(\partial_i u_j)\partial_j \psi - \frac{\partial f}{\partial(\partial_{ij}\psi)} \{\partial_i[(\partial_j u_k)\partial_k \psi] \right.$$
$$\left. + (\partial_i u_k)\partial_{kj}\psi\} + (\mathbf{\nabla} \cdot \mathbf{u})f \right] + O(|\nabla u|^2). \qquad (8)$$

Because of the translational invariance of $\mathcal{F}$, the change $\Delta \mathcal{F}$ does not depend on the distortion but depends only on its spatial gradients. Furthermore, the first term on the right-hand side vanishes since f does not depend on the gradient of ψ. The second term on the right-hand side can be transformed to a total divergence term and one proportional to the deformation gradient. Changing summation indices in order to factor the deformation gradient out and using Stokes' theorem on the divergence term, we obtain

$$\Delta \mathcal{F} = \int d^2 \mathbf{r} \, \mathcal{E} + \int dS_i \frac{\partial f}{\partial(\partial_{ij}\psi)}(\partial_j u_k)\partial_k \psi, \qquad (9)$$

where $d\mathbf{S}$ is the surface-element vector on the boundary of the integration domain and

$$\mathcal{E} = \left[-\frac{\partial f}{\partial(\partial_{ik}\psi)}\partial_{jk}\psi + \left(\partial_k \frac{\partial f}{\partial(\partial_{ik}\psi)}\right)\partial_j \psi + \delta_{ij} f \right]\partial_i u_j. \qquad (10)$$

Equation (9) yields the elastic stress defined as the conjugate to the displacement gradient,

$$\sigma_{ij} = \frac{\partial \mathcal{E}}{\partial(\partial_i u_j)}$$
$$= -\frac{\partial f}{\partial(\partial_{ik}\psi)}\partial_{jk}\psi + \left(\partial_k \frac{\partial f}{\partial(\partial_{ik}\psi)}\right)\partial_j \psi + f\delta_{ij}. \qquad (11)$$

Substituting Eq. (3), the corresponding stress is in our case

$$\sigma_{ij} = [\partial_i \mathcal{L}\psi]\partial_j \psi - [\mathcal{L}\psi]\partial_{ij}\psi + f\delta_{ij}, \qquad (12)$$

with $\mathcal{L} = 1 + \nabla^2$. Hence, the elastic stress can be straightforwardly evaluated from the phase field ψ. Below we will show that this stress gives rise to the expected stress-strain relation in the linear elasticity regime, in agreement with earlier results for modulated phases [34,35].

The stress gives rise to a body-force density $F_j = \partial_i \sigma_{ij}$ given by

$$F_j = \mathcal{L}^2 \psi \partial_j \psi - \mathcal{L}\psi \mathcal{L}(\partial_j \psi) + \partial_i f. \qquad (13)$$

For an incompressible deformation, the Jacobi determinant is unity; the second term is the gradient of $-\frac{1}{2}(\mathcal{L}\psi)^2$ and can be included in a pressure term $\partial_j p$ as a gradient force. Thus, we can write the body force up to its gradient force contributions as

$$F_j = \mu \partial_j \psi, \qquad (14)$$

as the additional terms in the chemical potential $\mu = \frac{\delta \mathcal{F}}{\delta \psi} = \mathcal{L}^2 \psi + r\psi + \psi^3$ also lead to gradient terms.

More generally, the additional contribution of a compressible deformation to the body force is

$$\partial_i(\delta_{ij} f) = \partial_j f = \mathcal{L}\psi \mathcal{L}(\partial_j \psi) + r\psi \partial_j \psi + \psi^3 \partial_j \psi. \qquad (15)$$

Hence, the body-force density induced by a deformation is the same in both the compressible and incompressible cases (up to a gradient force in the incompressible case) and is given as

$$F_j = \partial_i \sigma_{ij} = (\mathcal{L}^2 \psi + r\psi + \psi^3)\partial_j \psi = \mu \partial_j \psi. \qquad (16)$$

Thus, the body force associated with a small distortion in the phase-field crystal density is expressed, in general, as $\mu \mathbf{\nabla}\psi$. Analogous results have been derived by using microforce balances in the context of continuum mechanics [22] or invoking thermodynamic relations arising from broken symmetries [36].

In the weakly nonlinear region of $|r| \ll 1$, the order parameter ψ can be expanded in terms of the slowly varying amplitudes A_n of the resonant modes $\mathbf{q}_n$ of Eq. (5). A weakly distorted configuration relative to the reference hexagonal configuration can then be written in this expansion as [33,37]

$$\psi = \psi_0 + \sum_n A_n e^{i\mathbf{q}_n \cdot (\mathbf{r} - \mathbf{u})} + \text{c.c.}, \qquad (17)$$

where both the mean density ψ_0 and the amplitudes A_n are slowly varying on length scales much larger than the lattice spacing. After straightforward differentiation of ψ in Eq. (17), we obtain

$$\partial_i(\mathcal{L}\psi) = 2i A_0 \partial_l u_k \sum_{\mathbf{q}} q_l q_k q_i \exp[i\mathbf{q} \cdot (\mathbf{r} - \mathbf{u})],$$

$$[\partial_i(\mathcal{L}\psi)]\partial_j \psi = -2A_0^2 \partial_l u_k \sum_{\mathbf{q}, \mathbf{q}'} q_l q_k q_i q_j'$$
$$\times \exp[i(\mathbf{q} + \mathbf{q}') \cdot (\mathbf{r} - \mathbf{u})], \qquad (18)$$

where the sums involve the components of the vectors $\pm \mathbf{q}_n$, with the negative vectors included for the complex conjugate (we have dropped the subindex n for ease of notation).

Similarly, we find

$$
[\mathcal{L}\psi]\partial_{ij}\psi = -\psi_0 A_0 \sum_{\mathbf{q}} (q_i q_j - q_i q_k \partial_j u_k - q_j q_k \partial_i u_k)
$$

$$
\times \exp[i\mathbf{q}\cdot(\mathbf{r}-\mathbf{u})] - 2A_0^2 \partial_l u_k \sum_{\mathbf{q},\mathbf{q}'} q_l q_k q_i' q_j'
$$

$$
\times \exp[i(\mathbf{q}+\mathbf{q}')\cdot(\mathbf{r}-\mathbf{u})]. \tag{19}
$$

Finally, by averaging this result over a unit cell of the lattice and given that the slowly varying deformation gradients are constant over a lattice spacing, all single $\mathbf{q}$ terms vanish, whereas $\exp[i(\mathbf{q}+\mathbf{q}')\cdot(\mathbf{x}-\mathbf{u})]$ factors integrate to $\delta_{\mathbf{q},-\mathbf{q}'}$. Therefore, the averaged stress field from Eq. (12) becomes

$$
\langle\sigma_{ij}\rangle = 4A_0^2 \partial_l u_k \sum_{\mathbf{q}} q_l q_k q_i q_j. \tag{20}
$$

Since the coefficients multiplying $\partial_l u_k$ are symmetric under the interchange $l \leftrightarrow k$, we can also write the relation in terms of the symmetrized strain $u_{lk} = \frac{1}{2}(\partial_l u_k + \partial_k u_l)$. Reintroducing the vectors $\mathbf{q}_n$ and their negatives $-\mathbf{q}_n$ explicitly, we find

$$
\langle\sigma_{ij}\rangle = 8A_0^2 u_{lk} \sum_{n=1}^{3} q_i^n q_j^n q_k^n q_l^n. \tag{21}
$$

Equation (21) is a linear stress-strain relationship which depends only on three crystal reciprocal lattice vectors and the slowly varying amplitudes. For a hexagonal lattice, inserting the reciprocal lattice vectors given in Eq. (5) yields $C_{11} = C_{22} = 9A_0^2$, $C_{12} = 3A_0^2$, and $C_{44} = 3A_0^2$ (cf., e.g., Ref. [9]). This result can also be written in terms of Lamé coefficients as $\langle\sigma_{ij}\rangle = \lambda\delta_{ij}u_{kk} + 2\mu u_{ij}$, with $\lambda = \mu = 3A_0^2$, giving a Poisson's ratio of $\nu = \frac{\lambda}{2(\lambda+\mu)} = \frac{1}{4}$. This is different from the Poisson's ratio of $\frac{1}{3}$ obtained in Ref. [27], as they use the plane-stress condition, while we are assuming plane strain without loss of generality.

III. PLASTIC FLOW AND DISLOCATION DYNAMICS

At the mesoscale level, the evolution of the phase field is driven by local relaxation of the free-energy functional,

$$
\frac{\partial\psi}{\partial t} = \nabla^2 \frac{\delta\mathcal{F}}{\delta\psi}, \tag{22}
$$

where we have assumed a constant mobility coefficient (equal to unity in rescaled units). Equation (22) governs both conservation of mass and the evolution of crystal deformations. We will focus here on 2D systems, although a similar development can be applied in three dimensions.

There are no topological singularities in the phase field $\psi(\mathbf{r},t)$. However, under conditions in which the amplitude expansion of Eq. (4) is valid (mean density ψ_0 and amplitudes A_n that vary on length scales much larger than the wavelength of the reference pattern), topological defects can be identified from the location of the zeros of the complex amplitudes [38,39]. Evolution equations for ψ_0 and A_n have been derived by several techniques, such as renormalization-group methods [40] and multiple-scale analysis [41]. In the lowest derivative approximation that preserves the rotational invariance of the phase-field model [42], the resulting equations are given

as [41]

$$
\frac{\partial\psi_0}{\partial t} = \nabla^2 \Bigg[(1+\nabla^2)^2 \psi_0 + \psi_0^3 + 6\psi_0 \sum_n |A_n|^2
$$

$$
+ 6\Bigg(\prod_n A_n + \text{c.c.}\Bigg)\Bigg],
$$

$$
\frac{\partial A_n}{\partial t} = -\mathcal{L}_n^2 A_n - (3\psi_0^2 + r)A_n - 6\psi_0 \prod_{m\neq n} A_m^*
$$

$$
- 3A_n \Bigg(2\sum_m |A_m|^2 - |A_n|^2\Bigg), \tag{23}
$$

where $n = 1,2,3$, $\mathcal{L}_n = \nabla^2 + 2i\mathbf{q}_n \cdot \nabla$, and $\mathbf{q}_n$ are the three reciprocal vectors of Eq. (5). Variation of ψ_0 at constant A_n needs to be interpreted as vacancy diffusion. These amplitude equations are themselves variational and can be written as [41]

$$
\frac{\partial\psi_0}{\partial t} = \nabla^2 \frac{\delta\mathcal{F}_{CG}}{\delta\psi_0},
$$

$$
\frac{\partial A_n}{\partial t} = -\frac{\delta\mathcal{F}_{CG}}{\delta A_n^*}, \tag{24}
$$

where $\mathcal{F}_{CG}\{\psi_0, A_n\}$ is the free-energy function of the amplitudes alone. Recall that all of these equations ignore higher Fourier components $|\mathbf{q}| > 1$, so they are only valid close to the bifurcation point, $|r| \ll 1$.

A. Transformation of field singularities to dislocation coordinates

In order to make contact with the classical macroscopic description of plastic motion in terms of the velocity of a dislocation element under an imposed stress, we describe the transformation of variables that is required to relate the evolution of the phase field to the motion of the singularities associated with the amplitudes. Assume a spatial distribution of point dislocations, and define a Burgers vector density as $\mathbf{B}(\mathbf{r}) = \sum_\alpha \mathbf{b}_\alpha \delta(\mathbf{r} - \mathbf{r}_\alpha)$, where $\mathbf{r}_\alpha$ is the location of the dislocation with Burgers vector $\mathbf{b}_\alpha$ in some element of volume. For each Burgers vector $\mathbf{b}_\alpha$ we define the three integers $s_n^\alpha = \frac{1}{2\pi}(\mathbf{q}_n \cdot \mathbf{b}_\alpha)$, which satisfy the relation $\sum_{n=1}^3 s_n^\alpha = \frac{1}{2\pi}\mathbf{b}_\alpha \cdot \sum_{n=1}^3 \mathbf{q}_n = 0$.

A dislocation at $\mathbf{r}_\alpha$ corresponds to a discontinuous deformation field $\mathbf{u}(\mathbf{r})$ with $\oint d\mathbf{u} = \mathbf{b}_\alpha$ around a contour containing only $\mathbf{r}_\alpha$. This deformation field is associated with a phase factor in the complex amplitudes, given by $A_n(\mathbf{r}) = |A_n|e^{-i\mathbf{q}_n\cdot\mathbf{u}+i\phi}$, with $\phi(\mathbf{r})$ smooth inside the contour. The phase circulation of the amplitude around the same contour can then be found as

$$
\oint d(\arg A_n) = -q_j^n \oint \partial_k u_j dr_k + \oint \partial_k \phi dr_k
$$

$$
= -q_j^n b_j^\alpha = -2\pi s_n^\alpha, \tag{25}
$$

using the fact that ϕ has no circulation, being smooth inside the contour. Thus, the amplitude A_n has a vortex with winding number $-s_n^\alpha$ at $\mathbf{r} = \mathbf{r}_\alpha$. This induces the following

transformation of δ functions [43–46]:

$$D_n \delta(A_n) = -\sum_\alpha s_n^\alpha \delta(\mathbf{r} - \mathbf{r}_\alpha)$$

$$= -\frac{1}{2\pi} \sum_\alpha (\mathbf{q}_n \cdot \mathbf{b}_\alpha) \delta(\mathbf{r} - \mathbf{r}_\alpha) \quad (26)$$

for a given amplitude A_n, where

$$D_n = \text{Im}(\partial_x A_n^* \partial_y A_n) = \frac{1}{2i} \epsilon_{ij} \partial_i A_n^* \partial_j A_n \quad (27)$$

is the Jacobian of the transformation from complex amplitudes A_n to vortex coordinates $\mathbf{r}_\alpha$ and ϵ_{ij} is the antisymmetric tensor. Multiplying the above expression with a reciprocal vector $\mathbf{q}_n$ and summing over n, we find the dislocation density is

$$\mathbf{B}(\mathbf{r}) = -\frac{4\pi}{3} \sum_{n=1}^3 \mathbf{q}_n D_n \delta(A_n) \quad (28)$$

by making use of the fact that $\sum_{n=1}^3 q_i^n q_j^n = \frac{3}{2} \delta_{ij}$ (see the Appendix for why we use reciprocal lattice vectors in this expansion rather than real-space lattice vectors).

In order to obtain the equation governing the motion of the Burgers vector density, we use that the determinant fields D_n have conserved currents given by [46]

$$J_k^{(n)} = \frac{1}{2i} \epsilon_{kl} \left(\frac{\partial A_n}{\partial t} \partial_l A_n^* - \frac{\partial A_n^*}{\partial t} \partial_l A_n \right) = \epsilon_{kl} \, \text{Im} \left(\frac{\partial A_n}{\partial t} \partial_l A_n^* \right), \quad (29)$$

so that $\frac{\partial D_n}{\partial t} = -\partial_k J_k^{(n)}$, as can be verified by substitution. The amplitude evolution at the vortex location $\frac{\partial A_n}{\partial t}$ can be found from an amplitude expansion of $\frac{\partial \psi}{\partial t}$, such as Eq. (23).

We also have a similar continuity equation for the delta functions,

$$D_n \frac{\partial}{\partial t} \delta(A_n) = -J_i^{(n)} \partial_i \delta(A_n), \quad (30)$$

which can be proved by differentiating through the delta functions and inserting for D_n and $J_i^{(n)}$. Hence, differentiating the dislocation density with time, we find the Burgers vector current

$$\frac{\partial B_i}{\partial t} = -\frac{4\pi}{3} \sum_{n=1}^3 q_i^n \left[\frac{\partial D_n}{\partial t} \delta(A_n) + D_n \frac{\partial}{\partial t} \delta(A_n) \right]$$

$$= \frac{4\pi}{3} \sum_{n=1}^3 q_i^n \left[\partial_j J_j^{(n)} \delta(A_n) + J_j^{(n)} \partial_j \delta(A_n) \right]$$

$$= \partial_j \left[\frac{4\pi}{3} \sum_{n=1}^3 q_i^n J_j^{(n)} \delta(A_n) \right] = -\partial_j \mathcal{J}_{ij}. \quad (31)$$

Whenever $D_n = 0$, we have $\delta(A_n) = 0$; otherwise, we can transform back to physical coordinates using Eq. (26),

$$\mathcal{J}_{ij} = -\frac{4\pi}{3} \sum_{n=1}^3 q_i^n J_j^{(n)} \delta(A_n)$$

$$= \frac{2}{3} \sum_{n=1}^3 q_i^n J_j^{(n)} \sum_\alpha \frac{\mathbf{q}_n \cdot \mathbf{b}_\alpha}{D_n} \delta(\mathbf{r} - \mathbf{r}_\alpha). \quad (32)$$

On the other hand, if the dislocations are moving with velocity $\mathbf{v}_\alpha$, we have

$$\mathcal{J}_{ij} = \sum_\alpha b_i^\alpha v_j^\alpha \delta(\mathbf{r} - \mathbf{r}_\alpha). \quad (33)$$

Hence, equating the two expressions for $\mathcal{J}_{ij}$ at $\mathbf{r} = \mathbf{r}_\alpha$ and contracting with the Burgers vector $\mathbf{b}_\alpha$, we find

$$v_j^\alpha = \frac{2}{3} \sum_{n=1}^3 \frac{(\mathbf{q}_n \cdot \mathbf{b}_\alpha)^2}{|\mathbf{b}_\alpha|^2} \frac{J_j^{(n)}}{D_n} = \frac{1}{S_\alpha^2} \sum_{n=1}^3 (s_n^\alpha)^2 \frac{J_j^{(n)}}{D_n}, \quad (34)$$

where we set $S_\alpha^2 = \sum_{n=1}^3 (s_n^\alpha)^2$ and used that $|\mathbf{b}_\alpha|^2 = \frac{8}{3}\pi^2 S_\alpha^2$. This is a general result and the central relation between the velocity of a point singularity and the equation governing the evolution of the phase-field amplitudes. We apply this expression below to obtain an estimate of the velocity response of a single point dislocation under an applied strain.

B. Dislocation motion

At a dislocation core, assumed at $\mathbf{r} = 0$, the amplitude A_n will vanish as long as $2\pi s_n = \mathbf{q}_n \cdot \mathbf{b} \neq 0$. Since $s_1 + s_2 + s_3 = 0$, any dislocation must give rise to vortices in at least two of the three amplitudes, so these two amplitudes vanish. This means that the amplitude evolution equation (23) for vanishing amplitudes at the dislocation position reduces to

$$\frac{\partial A_n(\mathbf{r} = 0)}{\partial t} \approx -\mathcal{L}_n^2 A_n \Big|_{\mathbf{r}=0} \quad (35)$$

whenever $s_n \neq 0$. The equations governing the defect amplitudes entering Eq. (34) decouple, and hence, we can study the motion of each amplitude independently.

We now consider a dislocation which would be stationary in the absence of any externally imposed stress, $\mathcal{L}_n^2 A_n \big|_{\mathbf{r}=0} = 0$. If a smooth deformation $\tilde{\mathbf{u}}$ is imposed in addition to the singular deformation field associated with the stationary dislocation, the total displacement field can be written as $\mathbf{u} = \mathbf{u}^{\text{sing}} + \tilde{\mathbf{u}}$. This displacement includes the singular deformation $\mathbf{u}^{\text{sing}}$ for the stationary dislocation described by the amplitudes A_n and a smooth "phonon" part (e.g., as described in Eq. (2.8a) of Ref. [24]). The defect amplitude under this distortion is $\tilde{A}_n = A_n e^{-i\mathbf{q}_n \cdot \tilde{\mathbf{u}} + h_n(\mathbf{r})}$, where the unknown function h_n models how the defect core responds to the deformation [45]. We assume that these core perturbations are small compared to the driving force due to the deformation gradient, $|\nabla h_n| \ll |\nabla \tilde{\mathbf{u}}|$ and neglect them. The applied smooth deformation will cause the dislocation to move,

$$\partial_t \tilde{A}_n = -\mathcal{L}_n^2 \tilde{A}_n \neq 0, \quad (36)$$

and our aim is to compute how the resulting dislocation motion depends on the imposed deformation.

Let us focus on one particular n and write $\tilde{A} = A e^{-i\mathbf{q} \cdot \tilde{\mathbf{u}}}$, with its associated wave vector $\mathbf{q}$. Then,

$$\partial_i \tilde{A} = (\partial_i A - i A q_k \partial_i \tilde{u}_k) e^{-i\mathbf{q} \cdot \tilde{\mathbf{u}}},$$

$$\partial_{ij} \tilde{A} = (\partial_{ij} A - i \partial_i A q_k \partial_j \tilde{u}_k - i \partial_j A q_k \partial_i \tilde{u}_k) e^{-i\mathbf{q} \cdot \tilde{\mathbf{u}}}. \quad (37)$$

Continuing in this manner and using the fact that A is the stationary vortex solution ($\mathcal{L}^2 A = 0$), we then have that

$$\partial_t \tilde{A} = -\mathcal{L}^2 \tilde{A} = 4i q_j [(\partial_i + iq_i)\mathcal{L}A] \partial_i \tilde{u}_j e^{-i\mathbf{q} \cdot \tilde{\mathbf{u}}}. \quad (38)$$

If $s = \pm 1$, one solution of $\mathcal{L}^2 A = 0$ is the isotropic vortex solution $A \propto x - isy$. We will assume the vortex takes this form, although other solutions are possible. For this solution, we have $\mathcal{L}A = 2iq_k \partial_k A$ and $\partial_i \mathcal{L}A = 0$. Hence, $\partial_t \tilde{A}$ simplifies to

$$\partial_t \tilde{A} = -8iq_i q_j q_k \partial_k A \partial_i \tilde{u}_j e^{-i\mathbf{q}\cdot\tilde{\mathbf{u}}}. \tag{39}$$

Inserting this into the defect current in Eq. (29), we find

$$J_i = -8\epsilon_{ij} q_k q_l q_m \partial_k \tilde{u}_l \, \mathrm{Im}(i\partial_m A \partial_j A^*). \tag{40}$$

Since the defect density is unchanged under the smooth deformation, the Jacobi determinant at the dislocation position is unchanged,

$$D = \frac{1}{2i}\epsilon_{ij}\partial_i \tilde{A}^* \partial_j \tilde{A} = \frac{1}{2i}\epsilon_{ij}\partial_i A^* \partial_j A. \tag{41}$$

The isotropic vortex $A \propto x - isy$ satisfies

$$i\partial_i A = -\frac{1}{s}\epsilon_{ij}\partial_j A, \tag{42}$$

so that

$$J_i = \frac{8}{s}\epsilon_{ij}\epsilon_{mo} q_k q_l q_m \partial_k \tilde{u}_l \, \mathrm{Im}(\partial_o A \partial_j A^*). \tag{43}$$

We can show that $\mathrm{Im}(\partial_o A \partial_j A^*) = \epsilon_{jo} D$, which means that

$$J_i = \frac{8}{s}\epsilon_{ij} q_j q_k q_l \partial_k \tilde{u}_l D. \tag{44}$$

Thus, for a simple dislocation with all $|s_n| \leqslant 1$, we find that the vortex velocity from Eq. (34) is

$$
\begin{aligned}
v_i &= \frac{8\epsilon_{ij}}{S^2} \sum_{n=1}^3 s_n q_j^n q_k^n q_l^n \partial_k \tilde{u}_l \\
&= \frac{4b_m}{\pi S^2}\epsilon_{ij} \sum_{n=1}^3 q_m^n q_j^n q_k^n q_l^n \partial_k \tilde{u}_l \\
&= \frac{1}{4\pi A_0^2}\epsilon_{ij}\langle \tilde{\sigma}_{jk}\rangle b_k,
\end{aligned}
\tag{45}
$$

where we used the stress-strain relation from Eq. (21) to relate the gradient of the smooth deformation $\tilde{\mathbf{u}}$ to its associated stress $\tilde{\sigma}_{ij}$.

Thus, we obtain an expression for the dislocation velocity which agrees with the Peach-Koehler force of classical dislocation theory [4] and gives an explicit form of the dislocation mobility. The derivation has excluded the singular deformation $\mathbf{u}^{\mathrm{sing}}$ associated with the dislocation, as well as any defect core variations in the amplitudes which would be contained in the functions $h_n(\mathbf{r})$. Within our approximations, the mobility coefficient is isotropic. This probably follows from our assumption that the vortex solution of $\mathcal{L}_n^2 A_n = 0$ is isotropic.

In what follows, we calculate numerically the dislocation velocity by tracking the position of the dislocation and compare it with the velocity determined by Eq. (34) from the topological defect currents. We also discuss the numerical challenge to verify overdamped motion with isotropic mobility, the Peach-Kohler force Eq. (45), as well as the extent to which we expect our analysis to be valid.

IV. NUMERICAL RESULTS

We test our predictions by directly simulating a perfect hexagonal crystal containing a dislocation dipole in two scenarios of pure glide and pure climb, respectively. The dislocations move under the mutual interaction force between them until they annihilate.

We use two parameter sets $r = -0.01$ and $\psi_0 = -0.04$ (small amplitude near the bifurcation) and $r = -0.8$ and $\psi_0 = -0.43$ (finite amplitude). The initial state is prepared by setting $\psi(\mathbf{r}) = \psi_0 + \sum_n A_n e^{i\mathbf{q}_n \cdot \mathbf{r}} + \text{c.c.}$, where the amplitudes contain vortices with the appropriate charges for each dislocation $A_n = A_0 \exp[-\sum_\alpha i s_n^\alpha \theta(\mathbf{r} - \mathbf{r}_\alpha)]$. We use two different initial geometries for measuring glide and climb motion. For the glide case, we put two dislocations with opposite Burgers vectors pointing along the x direction, i.e., $\mathbf{b} = (\pm a, 0)$, and located in the same glide plane on the x axis with some initial separation. For climb, we place the same dislocations directly above each other on the y axis on different glide planes. We then evolve Eq. (22) using an exponential time differencing method [47] and track the motion of dislocations as topological defects.

The amplitudes of the phase field are computed by performing a local amplitude decomposition, which corresponds to averaging $\psi e^{-i\mathbf{q}\cdot\mathbf{r}}$ over a region roughly corresponding to a lattice unit cell [48]. For numerical stability we use a convolution with a Gaussian of width $a = 4\pi/\sqrt{3}$ instead of hard limits to the averaging region. This convolution is most efficiently evaluated in Fourier space, using the expression

$$A_n(\mathbf{r}) = e^{-i\mathbf{q}_n \cdot \mathbf{r}} F^{-1}\{e^{-\frac{8}{3}\pi^2(\mathbf{k}-\mathbf{q}_n)^2} F[\psi]\}, \tag{46}$$

where F and F^{-1} denote the Fourier and inverse Fourier transforms, respectively. Similarly, the time evolution of the amplitude can be extracted from the PFC dynamics as

$$\frac{\partial A_n(\mathbf{r})}{\partial t} = e^{-i\mathbf{q}_n \cdot \mathbf{r}} F^{-1}\left\{e^{-\frac{8}{3}\pi^2(\mathbf{k}-\mathbf{q}_n)^2} F\left[\frac{\partial \psi}{\partial t}\right]\right\}. \tag{47}$$

Figures 1(a) and 1(b) show the magnitude and phase of the complex amplitude A_2 for the initial dislocation dipole after a short period of relaxation.

From the amplitudes we can calculate a Gaussian approximation to the $\delta(A_n)$ function as

$$\delta(A_n) = \frac{1}{2\pi w^2}e^{-\frac{|A_n|^2}{2w^2}}, \tag{48}$$

where smaller w's give sharper δ functions. Along with the D_n fields obtained by numerically differentiating the amplitudes [Fig. 1(c)], we obtain approximations to the Burgers vector density from Eq. (28), shown in Fig. 1(d).

The total displacement field away from defect cores can be obtained by writing $A_n = |A_n|e^{-i\mathbf{q}_n \cdot \mathbf{u}}$, so that

$$\mathrm{Im}\frac{\partial_j A_n}{A_n} = -q_k^n \partial_j u_k. \tag{49}$$

This relation can be inverted to find

$$\partial_j u_k = -\frac{2}{3}\sum_n q_k^n \, \mathrm{Im}\frac{\partial_j A_n}{A_n}, \tag{50}$$

thus giving numerical values for the total strain. Figure 2 summarizes our results. We show the distortion $\partial_y u_x$ given
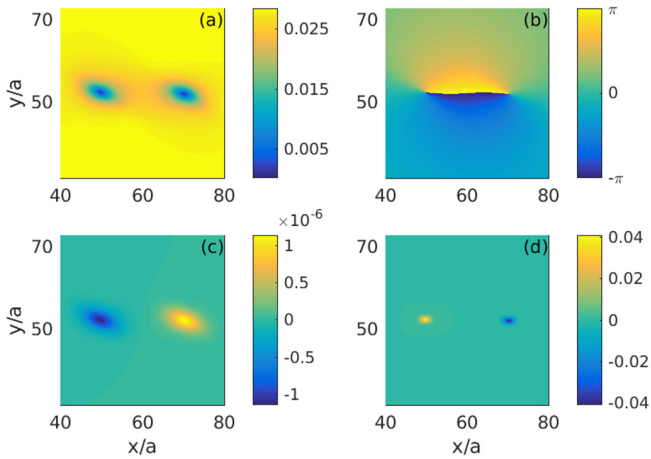
FIG. 1. (a) Magnitude and (b) phase of the A_2 amplitude, showing the initial vortices corresponding to the initial dislocations. (c) The D_2 field showing the sign of the vortex charge. (d) The resulting B_x dislocation density in the x direction, with $w = A_0/5$. Here x and y are given in units of the lattice constant $a = \frac{4\pi}{\sqrt{3}q_0}$.

by Eq. (50) along with the corresponding stress field evaluated from Eq. (12) with a Gaussian average. Of course, this stress-strain relation is not expected to hold near the defect cores where the distortion is large. However, we also plot the shear stress as a function of y along the line shown in Fig. 2 and show that the linear stress-strain relation, Eq. (21), does hold away from the cores.

Properties of a given dislocation can be computed by taking averages weighted by the Burgers vector density $\mathbf{B}(\mathbf{r})$ inside a thresholded region. Thus, we compute the location of each
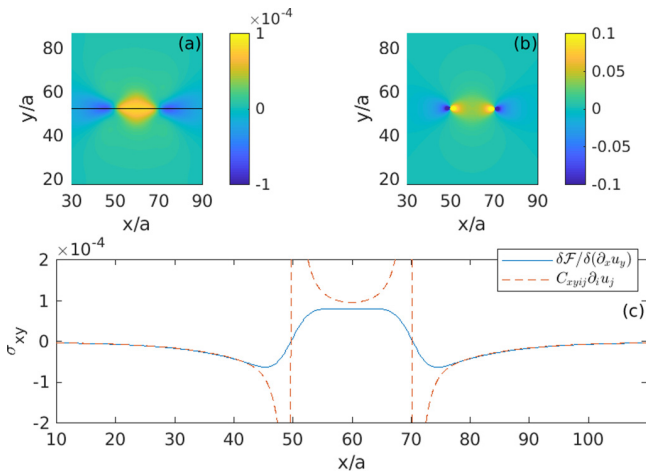

FIG. 2. (a) Map of the stress field $\langle \sigma_{xy} \rangle$, as computed directly from the formula in Eq. (12), with a Gaussian average. (b) Map of the strain field $\partial_y u_x$, computed from the amplitudes by Eq. (50). Note that the color scale is saturated, and the measured strain field diverges at the dislocation. (c) Comparison of the stress computed along the indicated horizontal line in two different ways: Using the direct expression for the stress in Eq. (12) (solid line) and using the stress-strain relation from Eq. (21) (dashed line). Both expressions agree in the crystal bulk but break down close to the dislocation.
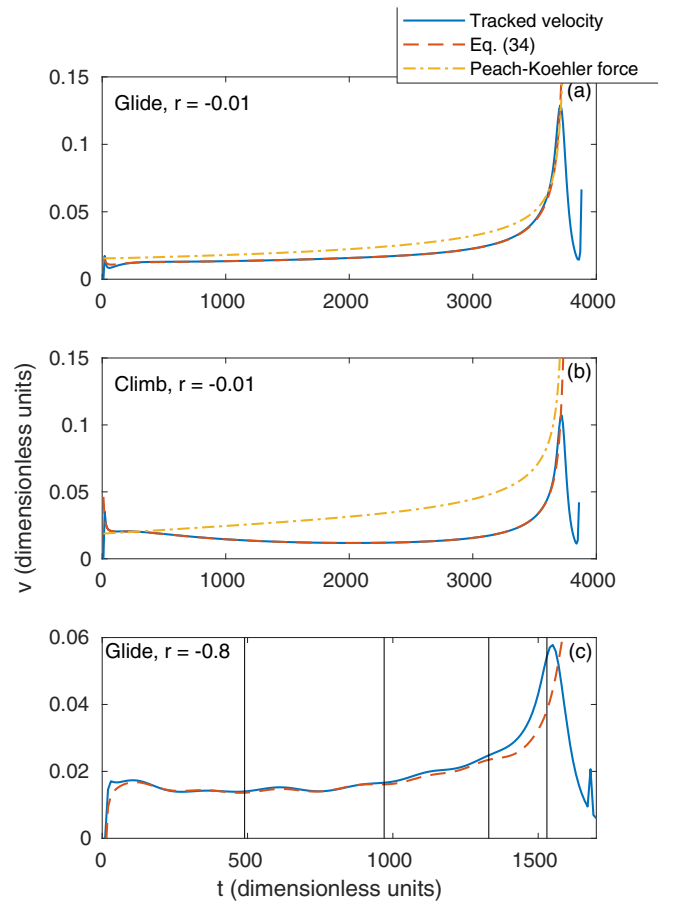

FIG. 3. The dislocation velocity as a function of time until the annihilation time for (a) and (b) low quenches versus (c) deep quenches, given in the dimensionless units of Eq. (22). In (c), vertical lines indicate points in time when the dislocation has traveled a distance a from its initial point.

dislocation by taking centers of mass of the Burgers vector density and dislocation speeds by averaging the topological defect currents of Eq. (34). In Fig. 3, we compare glide and climb velocities predicted from Eq. (34) and a direct numerical determination of the velocities by performing a finite-time difference between successive dislocation positions. In Figs. 3(a) and 3(b), the glide and climb velocities are presented for small $|r|$, showing excellent agreement. The glide velocity for finite r is presented in Fig. 3(c) and shows a stick-and-slip-like behavior with periodicity related to the lattice constant a, consistent with previous numerical simulations from Ref. [9]. These are lattice effects affecting the motion of the amplitudes when r is not small due to nonlinear couplings, the phase-field analog of Peierls pinning stresses [49]. Note that we observe no climb motion at the deep quench parameter $r = -0.8$.

The velocity computations shown are robust with respect to the δ function width parameter w from Eq. (48). However, the dislocation center-of-mass location used in the tracked velocity shows artificial fluctuations for width parameters larger than $\approx A_0/20$.

Directly verifying Eq. (45) is more difficult due to the required separation of stress fields into a singular part and

a phonon part $\tilde{\sigma}_{ij}$. As an indirect test, one can assume as a first approximation that the stress field on each dislocation is due only to the other, and it is approximately given by the equilibrium shear stress induced by an edge dislocation in an infinite space,

$$\sigma_{xy} = \frac{b}{2\pi} \frac{2\mu(\lambda + \mu)}{\lambda + 2\mu} \frac{\cos\phi\cos 2\phi}{d},$$

$$\sigma_{xx} = -\frac{b}{2\pi} \frac{2\mu(\lambda + \mu)}{\lambda + 2\mu} \frac{\sin\phi(2 + \cos 2\phi)}{d}, \qquad (51)$$

where d and ϕ are the instantaneous distance and angle between the dislocations, respectively. Inserting this expression into Eq. (45) and using appropriate values for the angle ϕ for the glide and climb geometries, we find

$$v_x^{\text{glide}} = v_y^{\text{climb}} = \pm \frac{a^2}{2\pi^2 d}, \qquad (52)$$

with the sign depending on which of the two dislocations we are considering. This equilibrium velocity is denoted as the "Peach-Koehler force" in Figs. 3(a) and 3(b). For glide velocity we find a reasonable agreement with the measured velocity, but the climb velocity shows a different functional form. The deviations from the predicted evolution from Eq. (52) are due to simplifying assumptions used in deriving the Peach-Koehler force, the most important being the isotropic solution of the stationary vortex structure. In practice, the profile of the vortex near the core may be anisotropic and dependent on the driving force. This means that the core structure would deform in the presence of external forces, which would be described by having the $h_n(\mathbf{r})$ functions depend on $\tilde{\mathbf{u}}$. Note that the decoupling of the amplitude equations and the assumption of an isotropic vortex solution were what allowed us to ignore the effect of vacancies. It is known that vacancy diffusion is important for climb motion, and therefore, we expect greater deviations from the theoretical prediction in the case of climb, as is evidenced in Fig. 3(c).

V. CONCLUSIONS AND DISCUSSION

We have introduced a phase-field model of a crystalline phase to describe the topological singularity that corresponds to isolated dislocations. The phase field itself is regular (nonsingular) at defect cores. The singularity appears through consideration of the slowly varying amplitudes or envelopes of the phase field in a macroscopically defected configuration. These amplitudes allow the computation of local stresses near the defect, as well as the velocity of the point defect from the kinetic equations governing the evolution of the phase field. The combination of both results allows the derivation of the classical Peach-Koehler force on the defect as well as an explicit calculation of the defect mobility, although these depend sensitively on the dislocation core structure. Our main results have been verified by direct numerical solution of the equation governing the evolution of the phase field for the case of a dislocation dipole in a two-dimensional hexagonal lattice.

Phase-field crystal models of the type discussed in this paper lack a dependence on lattice deformation as an independent variable. However, we have shown explicitly that it is possible to calculate the *elastic* stress directly from the phase-field free

energy by considering its variation with respect to a suitably chosen phase-field distortion. The stress thus derived is consistent with linear elasticity and leads to known expressions for the elastic constants of the phase-field crystal. Furthermore, the phase-field description can also describe defected configurations. While the phase field remains nonsingular no matter how large the local distortion of the reference configuration is, the location of any isolated singularities can be accomplished through the determination of the zeros of a slowly varying (on the scale of the periodicity of the field) complex amplitude or envelope of the phase field. Such a coarse graining is essential to defining singular fields from the regular phase field. On this slow scale, we have then derived the Peach-Koehler force on a topological defect, subject to some simplifying assumptions. As expected, this force depends only on a slowly varying stress (distortion) and not on other fast variations of the phase field near the defect that constitute the singular strain field. However, more work is needed to fully understand the effect of the core structure and vacancy diffusion on this Peach-Kohler force.

Our results also clarify the relationship between dissipative relaxation of the phase field and plastic motion. Equation (45) relates the velocity of a dislocation with its Burgers vector and the *slowly* varying stress $\langle\tilde{\sigma}_{ij}\rangle$. Such a relation follows directly from the equation governing the relaxation of the phase field, Eq. (22), in the range of $r \ll 1$, in which it can be described by an amplitude equation. This equation also gives an explicit expression for the dislocation mobility which depends on the specific functional form of the free energy considered. More generally, the role of the free-energy functional introduced includes the definition of a Burgers vector scale and topological charge conservation over large length scales. Of course, any fast variations of the phase field near defects are still described and very much included in Eq. (22). Short-scale effects such as dislocation creation and annihilation and any nonlinearities of both elastic and plastic origin evolve according to the dissipative evolution of the phase field.

APPENDIX: CALCULATION OF THE DISLOCATION CURRENT

Equation (28) gives an expression for the dislocation density in terms of the three reciprocal lattice vectors $\mathbf{q}_n$. Since the Burgers vector is a vector in the real-space lattice, it would seem more natural to express the dislocation density in terms of the two real-space lattice vectors $\mathbf{a}_n$, where $\mathbf{q}_n \cdot \mathbf{a}_m = 2\pi\delta_{mn}$ (for $n,m = 1,2$). Indeed, using that $\sum_{n=1}^2 a_i^n q_j^n = 2\pi\delta_{ij}$, we find the alternative expression

$$\mathbf{B}(\mathbf{r}) = -\sum_{n=1}^2 \mathbf{a}_n D_n \delta(A_n), \qquad (A1)$$

which, of course, is equal to Eq. (28). Going through the same derivation as in Sec. III A leads to a Burgers vector current

$$\mathcal{J}_{ij} = -\sum_{n=1}^{2} a_i^n J_j^{(n)} \delta(A_n). \tag{A2}$$

However, this current does not agree with the current in Eq. (32).

The missing point is that the conservation equation for the field $D_n \delta(A_n)$,

$$\partial_t [D_n \delta(A_n)] + \partial_i [J_i^{(n)} \delta(A_n)] = 0, \tag{A3}$$

determines its current $I_j^{(n)}$ only up to an unknown divergence-free vector field $K_j^{(n)}$, i.e.,

$$I_i^{(n)} = J_i^{(n)} \delta(A_n) + K_i^{(n)}, \tag{A4}$$

where $\partial_i K_i^{(n)} = 0$. To determine this residual current, we observe that

$$\sum_{n=1}^{3} D_n \delta(A_n) = -\frac{1}{2\pi} \sum_{\alpha} b_i^{\alpha} \delta(\mathbf{r} - \mathbf{r}_{\alpha}) \sum_{n=1}^{3} q_i^n = 0 \tag{A5}$$

due to the resonance condition $\sum_n \mathbf{q}_n = 0$. Hence, it is natural to require that the current of this field vanishes identically,

$$\sum_{n=1}^{3} I_i^{(n)} = \sum_{n=1}^{3} J_i^{(n)} \delta(A_n) + \sum_{n=1}^{3} K_i^{(n)} = 0. \tag{A6}$$

This condition is fulfilled by setting $K_i^{(n)} = -\frac{1}{3} \sum_{m=1}^{3} J_i^{(m)} \delta(A_m)$, which has vanishing divergence. With this choice, the dislocation current in Eq. (32) is modified to

$$\mathcal{J}_{ij} = -\frac{4\pi}{3} \sum_{n=1}^{3} q_i^n J_j^{(n)} \delta(A_n) + \frac{4\pi}{9} \sum_{n=1}^{3} q_i^n \sum_{m=1}^{3} J_j^{(m)} \delta(A_m),$$

$$\tag{A7}$$

where the second term vanishes due to resonance. Hence, the additional fields $K_i^{(n)}$ give no contribution when we express $\mathbf{B}(\mathbf{r})$ in terms of the three reciprocal lattice vectors. On the other hand, if we used real lattice vectors $\mathbf{a}_n$ instead, the extra term would not vanish.

---

[1] J. Weiss and D. Marsan, Science **299**, 89 (2003).

[2] M. Zaiser and P. Moretti, J. Stat. Mech. (2005) P08004.

[3] J. Weiss, W. B. Rhouma, T. Richeton, S. Dechanel, F. Louchet, and L. Truskinovsky, Phys. Rev. Lett. **114**, 105504 (2015).

[4] I. Groma, in *Multiscale Modelling of Plasticity and Fracture by Means of Dislocation Mechanics* (Springer, New York, 2010), pp. 213–270.

[5] O. U. Salman and L. Truskinovsky, Phys. Rev. Lett. **106**, 175503 (2011).

[6] P. D. Ispánovity, L. Laurson, M. Zaiser, I. Groma, S. Zapperi, and M. J. Alava, Phys. Rev. Lett. **112**, 235501 (2014).

[7] M. Haataja, J. Müller, A. D. Rutenberg, and M. Grant, Phys. Rev. B **65**, 165414 (2002).

[8] K. R. Elder, M. Katakowski, M. Haataja, and M. Grant, Phys. Rev. Lett. **88**, 245701 (2002).

[9] K. R. Elder, N. Provatas, J. Berry, P. Stefanovic, and M. Grant, Phys. Rev. B **75**, 064107 (2007).

[10] V. I. Levitas and M. Javanbakht, Phys. Rev. B **86**, 140101 (2012).

[11] J. Berry, J. Rottler, C. W. Sinclair, and N. Provatas, Phys. Rev. B **92**, 134103 (2015).

[12] D. Taha, S. K. Mkhonta, K. R. Elder, and Z.-F. Huang, Phys. Rev. Lett. **118**, 255501 (2017).

[13] A. Yau, W. Cha, M. Kanan, G. Stephenson, and A. Ulvestad, Science **356**, 739 (2017).

[14] R. Suter, Science **356**, 704 (2017).

[15] A. Sarac, M. Oztop, C. Dahlberg, and J. Kysar, Int. J. Plast. **85**, 110 (2016).

[16] L. L. Bonilla, A. Carpio, C. Gong, and J. H. Warner, Phys. Rev. B **92**, 155417 (2015).

[17] A. Acharya and C. Fressengeas, Int. J. Fract. **174**, 87 (2012).

[18] A. Acharya and C. Fressengeas, in *Differential Geometry and Continuum Mechanics* (Springer, New York, 2015).

[19] Y. Wang, Y. Jin, A. Cuitino, and A. Khachaturyan, Acta Mater. **49**, 1847 (2001).

[20] M. Koslowski, A. M. Cuitino, and M. Ortiz, J. Mech. Phys. Solids **50**, 2597 (2002).

[21] V. Bulatov and W. Cai, *Computer Simulations of Dislocations* (Oxford University Press, Oxford, 2006).

[22] M. E. Gurtin, D. Polignone, and J. Viñals, Math. Models Methods Appl. Sci. **06**, 815 (1996).

[23] A. M. Kosevich, in *Dislocations in Solids*, edited by F. R. N. Nabarro (North-Holland, New York, 1979), Vol. 1, p. 33.

[24] D. R. Nelson and J. Toner, Phys. Rev. B **24**, 363 (1981).

[25] J. M. Rickman and J. Viñals, Philos. Mag. A **75**, 1251 (1997).

[26] J. J. Eggleston, G. B. McFadden, and P. W. Voorhees, Phys. D (Amsterdam, Neth.) **150**, 91 (2001).

[27] K. R. Elder and M. Grant, Phys. Rev. E **70**, 051605 (2004).

[28] K.-A. Wu and P. W. Voorhees, Phys. Rev. B **80**, 125408 (2009).

[29] M. Bjerre, J. M. Tarp, L. Angheluta, and J. Mathiesen, Phys. Rev. E **88**, 020401 (2013).

[30] Z.-F. Huang and K. R. Elder, Phys. Rev. Lett. **101**, 158701 (2008).

[31] P. Y. Chan, G. Tsekenis, J. Dantzig, K. A. Dahmen, and N. Goldenfeld, Phys. Rev. Lett. **105**, 015502 (2010).

[32] J. M. Tarp, L. Angheluta, J. Mathiesen, and N. Goldenfeld, Phys. Rev. Lett. **113**, 265503 (2014).

[33] V. Heinonen, C. V. Achim, K. R. Elder, S. Buyukdagli, and T. Ala-Nissila, Phys. Rev. E **89**, 032411 (2014).

[34] K. Kawasaki and T. Ohta, Physica **139**, 223 (1986).

[35] R. Tamate, K. Yamada, J. Viñals, and T. Ohta, J. Phys. Soc. Jpn. **77**, 034802 (2008).

[36] P. Martin, O. Parodi, and P. Pershan, Phys. Rev. A **6**, 2401 (1972).

[37] K. R. Elder, Z.-F. Huang, and N. Provatas, Phys. Rev. E **81**, 011602 (2010).

[38] E. D. Siggia and A. Zippelius, Phys. Rev. A **24**, 1036 (1981).

[39] Y. Shiwa and K. Kawasaki, J. Phys. A **19**, 1387 (1986).

[40] B. P. Athreya, N. Goldenfeld, and J. A. Dantzig, Phys. Rev. E **74**, 011601 (2006).

[41] D.-H. Yeon, Z.-F. Huang, K. R. Elder, and K. Thornton, Philos. Mag. **90**, 237 (2010).

[42] G. H. Gunaratne, Q. Ouyang, and H. L. Swinney, Phys. Rev. E **50**, 2802 (1994).

[43] B. Halperin, in *Physics of Defects*, edited by R. Balian, M. Kléman, and J.-P. Poirier (North Holland, Amsterdam, 1981), pp. 813–857.

[44] G. F. Mazenko, Phys. Rev. Lett. **78**, 401 (1997).

[45] G. F. Mazenko, Phys. Rev. E **64**, 016110 (2001).

[46] L. Angheluta, P. Jeraldo, and N. Goldenfeld, Phys. Rev. E **85**, 011153 (2012).

[47] S. M. Cox and P. C. Matthews, J. Comput. Phys. **176**, 430 (2002).

[48] Y. Guo, J. Wang, Z. Wang, J. Li, S. Tang, F. Liu, and Y. Zhou, Philos. Mag. **95**, 973 (2015).

[49] D. Boyer and J. Viñals, Phys. Rev. Lett. **89**, 055501 (2002).

Paper V

V

Mesoscale model of dislocation motion and crystal plasticity

Audun Skaugen* and Luiza Angheluta

Njord Center, Department of Physics, University of Oslo, P.O. 1048 Blindern, 0316 Oslo, Norway

Jorge Viñals

School of Physics and Astronomy, University of Minnesota,
116 Church St. SE, Minneapolis, MN 55455, USA
(Dated: July 10, 2018)

A consistent, small scale description of plastic motion in a crystalline solid is presented based on a phase field description. By allowing for independent mass motion given by the phase field, and lattice distortion, the solid can remain in mechanical equilibrium on the timescale of plastic motion. Singular (incompatible) strains are determined by the phase field, to which smooth distortions are added to satisfy mechanical equilibrium. A numerical implementation of the model is presented, and used to study a benchmark problem: the motion of an edge dislocation dipole in a hexagonal lattice. The time dependence of the dipole separation agrees with classical elasticity without any adjustable parameters.

A phase field theory of a crystalline solid is one of the contending approaches to model defect mediated plastic motion at the nanoscale [1, 2]. Due to the diffusive nature of the evolution of the phase field, existing formulations do not maintain mechanical equilibrium during defect motion, and hence are not adequate models of plastic motion. We reinterpret the phase field as the source for singular strains in defected configurations, and add smooth distortions to maintain mechanical equilibrium at all times. The relative motion of two edge dislocations of opposite Burger's vectors under each other's stress field is studied in a hexagonal lattice. In contrast with a direct solution of the phase field equations, we recover the classical law in which the dipole separation scales with time as $\sqrt{t_0 - t}$.

Crystal plasticity theory assumes coarse grained volumes that contain a large number of defects, and hence is valid at scales on the order of microns or larger. On the other hand, recent theoretical efforts [1, 3–11] focus on the nanoscale, as new high resolution experiments and large scale simulations are producing a wealth of information about defect motion at the atomic scale. State of the art Bragg Coherent Diffractive Imaging can determine atomic scale displacements with ≤ 30 nm resolution [12, 13]. Advanced image processing methods allow the determination of the strain field phase around a single defect, clearly evidencing its multivalued nature. Indeed, single dislocations have been successfully imaged and their motion tracked quantitatively just recently [14]. At the same time, nanoscale experiments are revealing new phenomenology that shows that plastic distortion is a rather complex process, characterized by strain bursts and dislocation avalanches [15–21]. These phenomena lie

squarely outside of classical crystal plasticity theory.

A continuum theory of plasticity starts from the statement of incompatibility of the deformation gradient tensor

$$\epsilon_{ilm}\partial_l w_{mk} = \alpha_{ik}, \quad w_{mk} = \partial_m u_k \tag{1}$$

where ϵ_{ilm} is the anti symmetric Levi-Civita tensor, α_{ik} the dislocation density tensor, and w_{mk} the distortion tensor [22, 23]. The integral of α_{ik} over a surface is the sum of the Burger's vectors **b** corresponding to all the dislocation lines n that pierce the surface $\int_S \alpha_{ij} dS_j = \sum_n b_i^n$. For any given distribution of topological defects in the material, α is fixed, but not the distortion, which can be decomposed into a singular part, the curl of which yields α_{ij}, and a smooth strain which we denote by u_{ij}^δ. The smooth strain is compatible $\epsilon_{ikm}\epsilon_{jln}\partial_{kl}u_{mn}^\delta = 0$. Regardless of the state of distortion, plastic motion is slow on the scale of lattice vibration, and occurs in mechanical equilibrium, as the stress σ_{ij} adiabatically follows the instantaneous distribution of dislocations, $\partial_j\sigma_{ij} = 0$. Closure generally requires a constitutive relation involving the stress and the smooth deformation. These considerations and appropriate boundary conditions are sufficient to specify the static problem. Dynamically, over the time scale appropriate for plastic flow, an evolution equation needs to be introduced for the dislocation density tensor [3, 7, 24]. In field dislocation dynamics theories, its evolution is kinematically related to the velocity of the dislocation lines, which in turn require a constitutive definition in terms of a local free energy and a dissipation function [25]. The phase field crystal model of defect motion, as currently formulated [1, 6, 26, 27], can be used to specify most of the static and dynamic features just described, but not all, as discussed below.

The phase field, a scalar function of space and time, is a physical order parameter that describes the dimen-

*audun.skaugen@fys.uio.no

sionless mass density of the crystalline phase $\psi(\mathbf{r}) = \psi_0 + \sum_{\mathbf{g}} A_{\mathbf{g}} e^{i\mathbf{g}\cdot\mathbf{r}}$, where the sum extends over all reciprocal lattice vectors $\mathbf{g}$ of the lattice. A non convex free energy functional for an isothermal system $\mathcal{F}$ is introduced so that its minimizer ψ^* has the desired symmetry of the crystalline phase. Lattice constants appear as parameters. In dimensionless units, we use $\mathcal{F}[\psi] = \int d\mathbf{r} f(\psi, \nabla^2\psi)$ with $f(\psi, \nabla^2\psi) = (\mathcal{L}\psi)^2/2 + r^2\psi^2/2 + \psi^4/4$, and $\mathcal{L} = 1 + \nabla^2$ [1, 8, 28]. The only remaining constant parameter r is the dimensionless distance away from the symmetry breaking bifurcation. For $r > 0$, $\psi^* = 0$ is the only stable solution. For $r < 0$, and depending on the conserved spatial average ψ_0, ψ^* is periodic with wavenumber unity in our dimensionless units, but of various symmetries. For simplicity, we consider here a two dimensional system where the equilibrium configuration is a hexagonal phase with lattice constant $a = 4\pi/\sqrt{3}$. The Burger's vector density in 2D is $B_k(\mathbf{r}) = \alpha_{3,k}(\mathbf{r}), k = 1, 2$. Our results, however, can be readily extended to three dimensions. The temporal evolution of the phase field ψ is defined to be relaxational and driven by free energy reduction

$$\partial_t \psi(\mathbf{r}, t) = \nabla^2 \frac{\delta\mathcal{F}}{\delta\psi(\mathbf{r}, t)} \qquad (2)$$

where $\delta/\delta\psi(\mathbf{r}, t)$ stands for the variational derivative with respect to the phase field.

For smooth distortions of ψ^*, the free energy $\mathcal{F}$ suffices to determine the stress-strain relation [6]. For small distortions, we define a non-singular stress σ^ψ [29]

$$\sigma_{ij}^\psi = \left\langle \tilde{\sigma}_{ij}^\psi \right\rangle_c, \quad \tilde{\sigma}_{ij}^\psi = [\partial_i \mathcal{L}\psi] \partial_j \psi - [\mathcal{L}\psi] \partial_{ij}\psi + f\delta_{ij}, \quad (3)$$

with $\tilde{\sigma}_{ij}^\psi = \partial f/\partial(\partial_i u_j)$, and $\langle\cdot\rangle_c$ denoting a spatial average across a region roughly corresponding to a unit cell. σ_{ij}^ψ is symmetric and related to the strain field $u_{ij} = (\partial_i u_j + \partial_j u_i)/2$ according to linear elasticity. For the hexagonal phase under discussion, the relation is that of isotropic elasticity

$$\sigma_{ij}^\psi = \lambda\delta_{ij}u_{kk} + 2\mu u_{ij} \qquad (4)$$

with Lamé coefficients $\lambda = \mu = 3A_0^2$ [29]. The quantity A_0 is the amplitude of the uniform mode in a multiple scale amplitude expansion of ψ^*.

The phase field model has been used extensively to describe static and dynamic defected configurations. Following early work on dislocation motion and grain boundaries in roll patterns [30, 31], the phase field crystal theory has been used to study dislocation [7, 26] and grain boundary motion [32, 33]. Strain fields have been explicitly extracted [34], or imposed to analyze strained film epitaxy [35], and considered as the limiting case of phonon degrees of freedom [27]. More complex properties of defect motion such as specification of slip systems, defect mobilities, and Peierls barriers are also given by

phase field kinetics [29, 36, 37] thus opening the door to the study of defect pinning, bursts, and avalanches. However, whereas for a specified and fixed defected configuration minimizers of $\mathcal{F}$ with appropriate boundary conditions can be found that are in mechanical equilibrium, any local deformation of $\psi(\mathbf{r}, t)$ propagates only diffusively according to Eq. (2). The relevant transverse diffusion constant is small, and can even vanish [38]. This is not physical for a crystalline solid, as has been already recognized [26, 27, 39, 40]. In ordinary crystals, unlike the phase field model, elastic equilibrium compatible with a transient distribution $\alpha_{ik}(\mathbf{r}, t)$ and boundary conditions is established quickly, in a time scale determined by damping of elastic waves in the medium.

To overcome this difficulty, we propose to use the phase field $\psi(\mathbf{r}, t)$ only as an indicator function of defect location and topology, as well as governing local relaxation near defect cores. The field $\psi(\mathbf{r}, t)$ determines the source for lattice incompatibility in Eq. (1), the solution of which is only a *particular singular solution* for the deformation field. A smooth distortion $\mathbf{u}^\delta$ (in the null space of the curl) must be added to this particular solution to enforce elastic equilibrium. Equation (2) for the newly displaced phase field $\psi'(\mathbf{r}) = \psi(\mathbf{r}+\mathbf{u}^\delta)$ provides for defect motion in a manner that is consistent with the Peach-Kohler force [29]. Plastic motion is uniquely specified, with the only constitutive input being the free energy functional $\mathcal{F}$. We discuss in what follows the details of our computational implementation, and specifically address the relative motion of a dislocation dipole in a 2D hexagonal phase.

We decompose the stress field into a singular part arising from the current phase field configuration, σ^ψ, and a small contribution arising from the smooth distortion σ^δ, so that $\sigma = \sigma^\psi + \sigma^\delta$ is in mechanical equilibrium $\nabla\cdot\sigma = 0$. This condition is satisfied by introducing the Airy function χ, which in two dimensions reads $\sigma_{ij} = \epsilon_{ik}\epsilon_{jl}\partial_{kl}\chi$. Inverting Eq. (4), we have in 2D

$$u_{ij} = \frac{1}{2}(\partial_i u_j + \partial_j u_i) = \frac{1}{2\mu}\left(\sigma_{ij} - \kappa\delta_{ij}\sigma_{kk}\right), \qquad (5)$$

where $\kappa = \frac{\lambda}{2(\lambda+\mu)}$. Inserting Eq. (5) into the incompatibility relation in 2D $\epsilon_{ik}\epsilon_{jl}\partial_{kl}u_{ij} = \epsilon_{ij}\partial_i B_j(\mathbf{r})$ (e.g. [22]) and expressing the stress in terms of χ-function, we obtain that

$$\frac{1-\kappa}{2\mu}\nabla^4\chi = \epsilon_{ij}\partial_i B_j(\mathbf{r}), \qquad (6)$$

where $B_j(\mathbf{r}) = \sum_\alpha b_j^n \delta(\mathbf{r} - \mathbf{r}_n)$ is the dislocation density in 2D for a configuration of dislocations with Burgers vector $\mathbf{b}^n$ at locations $\mathbf{r}_n$. In Ref. [29], we explicitly computed $\mathbf{B}(\mathbf{r})$ through complex demodulation of the phase field $\psi(\mathbf{r}, t)$. Demodulation yields both the amplitude and phase of the deformation field; the former going to zero at the defect core, the latter undergoing a discontinuity across a line that terminates at the core. Figure

1(a) shows a dislocation dipole in a 2D hexagonal lattice, and Figure 1(d) the right hand side of Eq. (6)) obtained by demodulation. We proceed differently here and introduce a more efficient numerical procedure that does not require demodulation. The smooth strain u_{ij}^δ is compatible ($\epsilon_{ik}\epsilon_{jl}\partial_{ij}u_{kl}^\delta = 0$) and therefore, with Eq. (5), the corresponding stress satisfies,

$$\epsilon_{ik}\epsilon_{jl}\partial_{ij}\left(\sigma_{kl}^\delta - \kappa\delta_{kl}\sigma_{ll}^\delta\right) = 0. \tag{7}$$

We now proceed as if the linear decomposition $\sigma = \sigma^\psi + \sigma^\delta$ holds everywhere, including near dislocation cores as defined by the phase field. This is not strictly correct, but this decomposition results in a distortion u_{ij}^δ which is everywhere compatible. However, as discussed below, the computed stress field σ will be divergence free only away from any defect core. Given this decomposition $\sigma_{ij}^\delta = \epsilon_{ik}\epsilon_{jl}\partial_{ij}\chi - \sigma_{ij}^\psi$, we find an analogous result to Eq. (6),

$$(1 - \kappa)\nabla^4\chi = \left(\epsilon_{ik}\epsilon_{jl}\partial_{ij}\sigma_{kl}^\psi - \kappa\nabla^2\sigma_{kk}^\psi\right). \tag{8}$$

Note that the stress σ^ψ (as defined in Eq. (3)) is smooth and bounded, so the right-hand side of Eq. (8) can only give a nonsingular approximation to the singular right hand side of Eq. (6). Figure 1(c) shows the right-hand side of Eq. (8) obtained numerically for the dislocation dipole which is in good agreement Eq. (6) obtained through demodulation (Fig. 1(d)). Both methods act as regularizations of the singular density at defect cores.

From a given phase field configuration at time t, $\psi(\mathbf{r}, t)$, we compute σ^ψ from Eq. (3), and then solve Eq. (8) to obtain χ and therefore σ. The difference $\sigma_{ij}^\delta = \epsilon_{ik}\epsilon_{jl}\partial_{ij}\chi - \sigma_{ij}^\delta$ leads to the smooth strain $u_{ij}^\delta = \frac{1}{2\mu}(\sigma_{ij}^\delta - \nu\sigma_{kk}^\delta\delta_{ij})$ which is, by construction, compatible. It can, therefore, be integrated to obtain a compatible deformation $\mathbf{u}^\delta$. The final step in the computation is to redefine the phase field $\psi'(\mathbf{r}, t) = \psi(\mathbf{r} + \mathbf{u}^\delta, t)$.

Both the stress-strain relation and stress superposition only hold far from defect cores. We define the stress of this newly deformed configuration everywhere as

$$\sigma_{ij} = \sigma_{ij}^\psi + \sigma_{ij}^\delta = \sigma_{ij}^\psi + \lambda\delta_{ij}u_{kk}^\delta + 2\mu u_{ij}^\delta, \tag{9}$$

which satisfies $\partial_j\sigma_{ij} = 0$ only far from defect cores, not at short distances. This is not a problem as standard diffusive evolution of the phase field suffices to equilibrate the stress near cores in time. We discuss this further below, and in Fig. 2.

The integration of the compatible strain u_{ij}^δ to obtain $\mathbf{u}^\delta$ is carried out through a Helmholtz decomposition into curl-free and divergence-free parts $u_i^\delta = \partial_i V + \epsilon_{ij}\partial_j A$. Applying the divergence to this expression, one obtains a Poisson equation for the potential V, $\partial_i u_i^\delta = u_{ii}^\delta = \nabla^2 V$, which is easily solved by spectral methods. On the other hand, taking the curl we find $\epsilon_{ij}\partial_i u_j^\delta = \epsilon_{ij}\epsilon_{jk}\partial_{ik}A =$
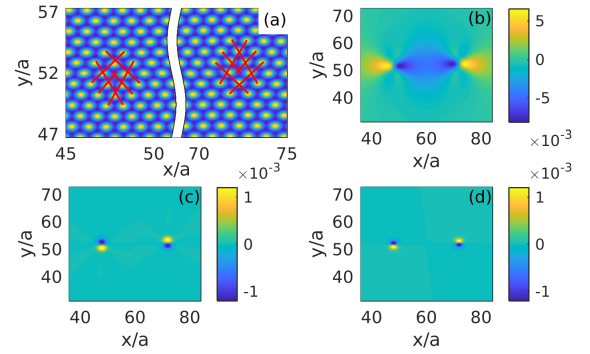

FIG. 1: (a): Phase field ψ for an initial condition comprising two dislocations with opposite Burger's vectors on the same glide plane. Crystal planes in the [11] and [$\bar{1}$1] directions are indicated to illustrate the structure of the dislocations in the hexagonal lattice. (b): Coarse-grained shear stress σ_{xy}^ψ showing two characteristic stress dipoles. (c): Right side of Eq. (8), divided by 2μ, showing dipolar sources at the dislocation positions. (d): Curl of the Burger's vector density as computed by demodulation in ref. [29], showing good agreement with (c).

$-\nabla^2 A$, which is a Poisson equation for A. Unfortunately the source term depends on the antisymmetric part of the smooth deformation gradient, which we do not obtain directly from the elastic stress, as this only depends on the symmetric part. We therefore apply another Laplacian operator to the equation, and use the compatibility relation $\epsilon_{ij}\partial_{ij}u_k^\delta = 0$ to find

$$\nabla^4 A = -\epsilon_{ij}\partial_{ik}(\partial_k u_j^\delta + \partial_j u_k^\delta) = -2\epsilon_{ij}\partial_{ik}u_{jk}^\delta. \tag{10}$$

This is a biharmonic equation for A with a known source term, which is again easily solved by spectral methods. In particular, if k_i are the components of the $\mathbf{k}$ vector and $\hat{u}_{ij}^\delta$ are the Fourier components of the residual strain, the Fourier components of the residual deformation can be expressed as

$$\hat{u}_i^\delta = -\frac{ik_i}{k^2}\hat{u}_{jj}^\delta + 2i\epsilon_{ij}\epsilon_{rs}\frac{k_j k_r k_l}{k^4}\hat{u}_{sl}^\delta, \tag{11}$$

with the $k = 0$ component chosen to be zero to avoid rigid body displacements. We then compute the distorted phase field $\psi'(\mathbf{r}) = \psi(\mathbf{r} + \mathbf{u}^\delta)$ on the original grid $\mathbf{r}$ by expanding in Taylor series up to fifth order in $\mathbf{u}^\delta$.

We present next the results of a numerical study of a benchmark configuration: the relative motion of two edge dislocations along their glide plane, Fig. 1(a). The computational domain is assumed periodic containing 120x120 unit cells with a spatial resolution of $a/8 = \pi/2\sqrt{3}$ in the x direction, and $2\pi/7$ in the y direction. The initial distance between dislocations is $24a$, and we consider two sets of values $r = -0.2, \psi_0 = 0.265$ and $r = -0.8, \psi_0 = -0.43$. We prepare the initial condition in the same way as in Ref. [29], and numerically solve
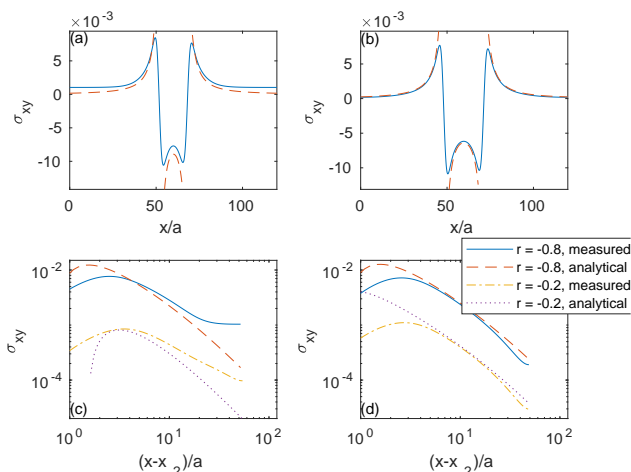
FIG. 2: (a) Shear stress σ_{xy}^{ψ} along the line joining the two dislocation cores from direct integration of Eq. (2) (solid line) compared with Eq. (12) (dashed line). (b) Constrained stress according to the simultaneous solution of Eqs. (2), (8), and (9), also compared with Eq. (12). (c) and (d) are the enlarged tail regions of (a) and (b) respectively.
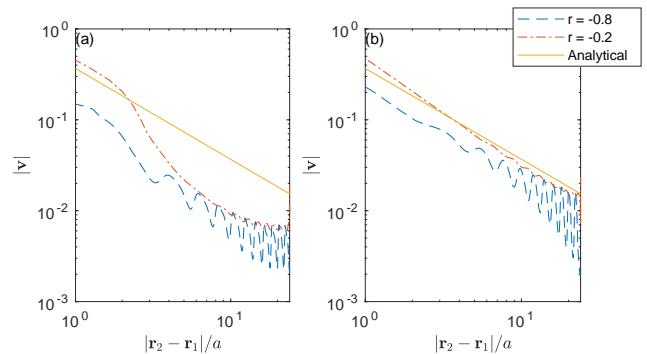

FIG. 3: Dislocation velocity as a function of dipole separation. Velocities from the numerical computations are obtained from the locations of the zeros of the complex amplitudes of ψ as described in Ref. [29]. The analytic result follows from the Peach-Kohler force with stress given by Eq. (12), and mobility computed from $\mathcal{F}$ as given in [29]. There are no adjustable parameters in this calculation. (a), Numerically computed velocity by direct integration of Eq. (2). (b), Velocity given by our model.

Eq. (2) using an exponential time differencing method with a time step of $\Delta t = 0.1$ [41]. According to linear elasticity theory for an isotropic medium, the shear stress in such a configuration is,

$$\sigma_{xy} = \frac{2\mu(\lambda + \mu)}{\lambda + 2\mu} \sum_{\alpha} \frac{b_x^n}{2\pi} \frac{\cos \phi_n \cos(2\phi_n)}{|\mathbf{r} - \mathbf{r}_n|}, \qquad (12)$$

where ϕ_n is the azimuth relative to dislocation n. Figures (2)(a,c) show σ^{ψ} along a line that includes the two dislocation cores at time $t = 700$ obtained by direct integration of Eq. (2), and compares it to Eq. (12). Divergences in Eq. (12) are regularized by the phase field, and the stress near the cores is relatively well described by σ^{ψ}. Far from the cores, however, the two stresses show qualitatively different asymptotic dependence. Figures (2)(b,d) show the stress in a configuration in which the smooth distortion (11) has been applied between time steps. The stress is still regularized near defect cores, yet, by construction, agrees with linear elasticity away from them.

Figure 3 shows the time dependence of the dislocation velocity as a function of dipole separation as given by direct integration of the phase field model, Eq. (2), Fig. 3(a), and by our model, Fig. 3(b). For reference, we also show the expected result from elasticity theory by using the Peach-Kohler force with stress (12), and mobility derived from $\mathcal{F}$ (Eq. (45) in Ref. [29]). There are no adjustable parameters in the calculation of the analytic velocity. The two dislocations move towards each other until they annihilate, with a velocity inversely proportional to their separation. Our model captures this result well for a range of parameters r, with slight stick-

slip motion observed at larger $|r|$, visible as oscillations in the dislocation velocity.

To summarize, we have argued that the phase field crystal model currently in use lacks deformation as an independent variable, and as a consequence fails to maintain proper mechanical equilibrium during plastic motion. We retain the model because it provides for lattice and topological defect structures as derived properties from the phenomenological free energy. It also allows regularization of defect cores and singular stresses. Phase field kinetics is also consistent with the classical Peach-Kohler force, with mobility that is again specified by the free energy $\mathcal{F}$. We take the view, however, that the phase field is not adequate to describe the distortion of the lattice away from moving defect cores, and hence supplement it with a smooth distortion field, compatible with the topological content of the phase field, but defined so as to maintain mechanical equilibrium everywhere away from defect cores. When the evolution of $\psi'(\mathbf{r}, t)$ is thus constrained to satisfy mechanical equilibrium at all times, we show numerically that our model agrees with the classical law of motion for a dislocation dipole in isotropic, linear elasticity. These results put the phase field crystal model on firmer ground to study more complex defected configurations at the nanoscale.

[1] K. R. Elder, M. Katakowski, M. Haataja, and M. Grant, Phys. Rev. Lett. **88**, 245701 (2002).

[2] H. Emmerich, H. Lwen, R. Wittkowski, T. Gruhn, G. I. Tth, G. Tegze, and L. Grnsy, Advances in Physics **61**, 665 (2012).

[3] A. Acharya, J. Mech. Phys. Solids **49**, 761 (2001).

[4] M. Haataja, J. Müller, A. D. Rutenberg, and M. Grant, Phys. Rev. B **65**, 165414 (2002).

[5] M. Koslowski, A. M. Cuitino, and M. Ortiz, J. Mech. Phys. Solids **50**, 2597 (2002).

[6] K. R. Elder and M. Grant, Phys. Rev. E **70**, 051605 (2004).

[7] S. Limkumnerd and J. P. Sethna, Phys. Rev. Lett. **96**, 095503 (2006).

[8] K. R. Elder, N. Provatas, J. Berry, P. Stefanovic, and M. Grant, Phys. Rev. B **75**, 064107 (2007).

[9] A. Acharya and C. Fressengeas, Int. J. of fracture **174**, 87 (2012).

[10] A. Acharya and C. Fressengeas, in *Differential Geometry and Continuum Mechanics* (Springer, New York, 2015).

[11] I. Groma, Z. Vandrus, and P. D. Ispánovity, Phys. Rev. Lett. **114**, 015503 (2015).

[12] A. D. Rollett, R. Suter, and J. Almer, Annu. Rev. Mater. Research **47** (2017).

[13] R. Suter, Science **356**, 704 (2017).

[14] A. Yau, W. Cha, M. Kanan, G. Stephenson, and A. Ulvestad, Science **356**, 739 (2017).

[15] J. Weiss and D. Marsan, Science **299**, 89 (2003).

[16] M. Koslowski, R. LeSar, and R. Thomson, Phys. Rev. Lett. **93**, 125502 (2004).

[17] F. F. Csikor, C. Motz, D. Weygand, M. Zaiser, and S. Zapperi, Science **318**, 251 (2007).

[18] P. D. Ispánovity, I. Groma, G. Györgyi, F. F. Csikor, and D. Weygand, Phys. Rev. Lett. **105**, 085503 (2010).

[19] P. D. Ispánovity, L. Laurson, M. Zaiser, I. Groma, S. Zapperi, and M. J. Alava, Phys. Rev. Lett. **112**, 235501 (2014).

[20] J. M. Tarp, L. Angheluta, J. Mathiesen, and N. Goldenfeld, Phys. Rev. Lett. **113**, 265503 (2014).

[21] Y. Cui, G. Po, and N. Ghoniem, Phys. Rev. Lett. **117**, 155502 (2016).

[22] A. M. Kosevich, in *Dislocations in Solids*, Vol. 1, edited by F. R. N. Nabarro (North-Holland, New York, 1979) p. 33.

[23] D. R. Nelson and J. Toner, Phys. Rev. B **24**, 363 (1981).

[24] J. M. Rickman and J. Viñals, Phil. Mag. A **75**, 1251 (1997).

[25] A. Acharya, J. Mech. Phys. Solids **52**, 301 (2004).

[26] J. Berry, M. Grant, and K. R. Elder, Phys. Rev. E **73**, 031609 (2006).

[27] V. Heinonen, C. V. Achim, J. M. Kosterlitz, S.-C. Ying, J. Lowengrub, and T. Ala-Nissila, Phys. Rev. Lett. **116**, 024303 (2016).

[28] S. van Teeffelen, R. Backofen, A. Voigt, and H. Löwen, Phys. Rev. E **79**, 051404 (2009).

[29] A. Skaugen, L. Angheluta, and J. Viñals, Phys. Rev. B **97**, 054113 (2018).

[30] E. D. Siggia and A. Zippelius, Phys. Rev. A **24**, 1036 (1981).

[31] G. Tesauro and M. C. Cross, Phil. Mag. A **56**, 703 (1987).

[32] A. Adland, Y. Xu, and A. Karma, Phys. Rev. Lett. **110**, 265504 (2013).

[33] D. Taha, S. K. Mkhonta, K. R. Elder, and Z.-F. Huang, Phys. Rev. Lett. **118**, 255501 (2017).

[34] E. J. Schwalbach, J. A. Warren, K.-A. Wu, and P. W. Voorhees, Phys. Rev. E **88**, 023306 (2013).

[35] Z.-F. Huang and K. R. Elder, Phys. Rev. Lett. **101**, 158701 (2008).

[36] D. Boyer and J. Viñals, Phys. Rev. Lett. **89**, 055501 (2002).

[37] B. Perreault, J. Viñals, and J. M. Rickman, Phys. Rev. B **93**, 014107 (2016).

[38] M. C. Cross and D. I. Meiron, Phys. Rev. Lett. **75**, 2152 (1995).

[39] V. Heinonen, C. V. Achim, K. R. Elder, S. Buyukdagli, and T. Ala-Nissila, Phys. Rev. E **89**, 032411 (2014).

[40] P. Stefanovic, M. Haataja, and N. Provatas, Phys. Rev. Lett. **96**, 225504 (2006).

[41] S. M. Cox and P. C. Matthews, Journal of Computational Physics **176**, 430 (2002).